Tailoring the activity and stability of oxygen evolution electrocatalysts

Tailoring the activity and stability of oxygen evolution electrocatalysts

PROEFSCHRIFT

ter verkrijging van de graad van doctor aan de Technische Universiteit Eindhoven,
op gezag van de rector magnificus prof.dr.ir. F.P.T. Baaijens,
voor een commissie aangewezen door het College voor Promoties, in het
openbaar te verdedigen op donderdag 10 december 2020 om 11:00 uur

door

Marco Etzi Coller Pascuzzi

geboren te Turijn, Italië

Dit proefschrift is goedgekeurd door de promotoren en de samenstelling van de promotiecommissie is als volgt:

voorzitter:	prof.dr.ir. R. Tuinier
1e promotor:	prof.dr.ir. E.J.M. Hensen
copromotor:	prof.dr.rer.nat. J.P. Hofmann (Technical University of Darmstadt)
leden:	dr.ir. M.T. de Groot (Nouryon)
	prof.dr. P.P. Pescarmona (Rijksuniversiteit Groningen)
	prof.dr.ir. J. van der Schaaf
	prof.dr. H. Over (Justus Liebig University Giessen)
adviseur:	dr. M.C. Costa Figueiredo

Het onderzoek of ontwerp dat in dit proefschrift wordt beschreven is uitgevoerd in overeenstemming met de TU/e Gedragscode Wetenschapsbeoefening.

To the ones
who believed in me

Marco Etzi Coller Pascuzzi

Tailoring the activity and stability of oxygen evolution electrocatalysts

A catalogue record is available from the Eindhoven University of Technology Library.

ISBN: 978-90-386-5179-8

The work described in this thesis has been carried out at the Laboratory of Inorganic Materials and Catalysis, Eindhoven University of Technology, The Netherlands. This project was funded by a Graduate School program from the Netherlands Organization for Scientific Research (NWO).

Printed by: Ipskamp Printing

Cover design: Laura Ceccarelli

Contents

Chapter 1

Introduction and scope

1.1. Introduction

Since the Industrial Revolution more than two centuries ago, global energy demand has only been increasing (e.g., 2.3% in 2018).[1] We depend on cheap abundant energy for nearly all human activities such as transportation, residential and commercial activities, and industrial production. Global energy demand will continue to rise due to an increasing world population and higher levels of gross domestic product, mostly in developing countries. This higher demand for energy has mostly been covered by burning more fossil fuels. The associated emission of the greenhouse gas CO_2 into the atmosphere has led to grave concerns about its impact on the environment. The Paris agreement aims for a concerted global response to this threat by keeping the Earth's temperature rise well below 2 degrees Celsius. The agreement implies a carbon budget to respect for limiting the impact of global warming on climate change, biodiversity, and humanity.[2] Therefore, it is a must to replace fossil sources of energy and materials with renewable ones.

The potential of renewable energy from the sun is enormous: as an example, the solar energy irradiated on Earth in just 1 hour is higher than the global annual energy consumption.[3,4] Despite this, renewable sources are not uniformly distributed in place and time. Especially, the intermittency of solar and wind requires the development of technologies to store renewable energy and convert it back into a usable form when needed.[5,6] Electrochemical processes are ideally suited to convert renewable electricity into chemicals for energy storage and/or the production of building blocks for other chemicals.[7] In this context, electrochemical water splitting for H_2 generation,[8] CO_2 reduction for the production of hydrocarbons (e.g., as energy-dense energy carriers),[9] and N_2 reduction to obtain NH_3 (an essential bulk chemical but also a prospective energy carrier)[10] can (partially) replace current processes based on fossil resources such as steam reforming, oil refining, and Haber-Bosch ammonia synthesis. However, many of these technologies require the development of better catalysts, preferably based on Earth-abundant elements, cheap materials for reactors, and optimization of electrochemical reactors in order to arrive at a cost-competitive production of storage solutions.

Hydrogen is an obvious energy carrier to store energy for its successive use. Figure 1.1 shows the various applications of H_2. It can be applied as such in hydrogen fuel cells for the generation of electrical energy in stationary applications or portable devices,[11] or as reactant in CO or CO_2 methanation, CO_2 hydrogenation to methanol, Fischer-Tropsch synthesis of hydrocarbons, and NH_3 synthesis.[12–15] Currently, steam reforming of natural gas is the main source of H_2 (mostly used in NH_3 synthesis and oil refining) but this process contributes to global warming by emitting significant amounts of CO_2.[8] H_2 can also be produced electrochemically *via* water splitting, which involves the cleavage of H-O bonds in water to form molecular hydrogen and oxygen using electricity.[4] Water splitting thus allows to use excess renewable electricity, decreasing the amount of CO_2 emitted because of the displacement of conventional fossil resources.

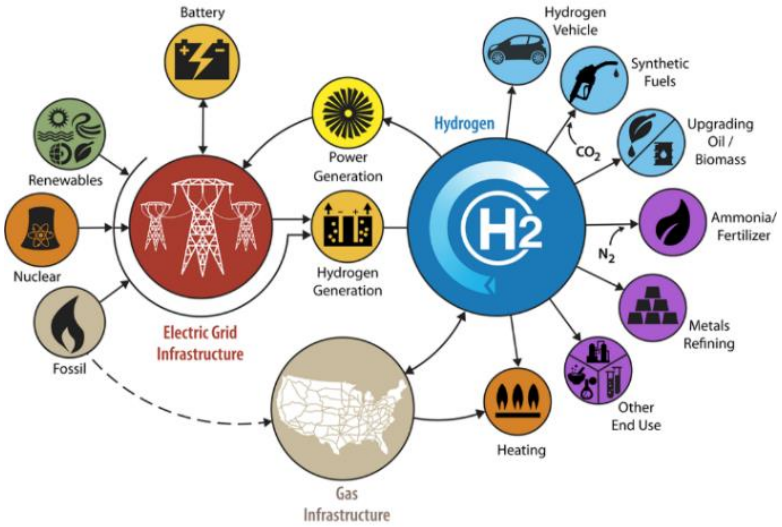

Figure 1.1. Integration of H_2 as energy carrier.[16]

The first experiment on water electrolysis was performed in 1789 by Deiman and Van Troostwijk in a glass tube.[17] For more than two centuries, water electrolysis has been optimized in terms of materials and processes. The use of electrocatalysts has allowed lowering the energy losses. With respect to electrochemical reactors, we distinguish three main types of water electrolyzers:[18]

- *Alkaline Electrolysis Cells (AEC):* the electrolyte is a concentrated alkaline solution (≈30 wt% KOH) and the electrodes are metal plates (Ni) separated by a diaphragm. Operating temperatures are 70-80 °C. Currently, AECs represent the majority of

electrolyzers employed at industrial scale: advantages are design simplicity and low cost, although their efficiency is relatively low (because of low operating pressures), especially when they work in dynamic operation (frequent starts and stops or partial load);[19]

- *Proton-Exchange Membrane Electrolysis Cells (PEMEC):* the electrolyte is a solid polymeric membrane and the electrodes are usually titanium plates loaded with noble metal-based catalysts (Pt, IrO_2). Operating temperatures are 50-80 °C. The main advantages of these electrolyzers are high overall efficiencies, high operating pressures, low ohmic drops, and high flexibility in working dynamically; the main disadvantages are their high complexity and cost of the required noble metal-based catalysts. PEMEC is currently a less mature technology compared to AEC and is mainly used in small-scale applications. Nonetheless, it would be an ideal solution for coupling with photovoltaic or wind generation of renewable electricity due to the rapid system response and the high efficiency at partial load operation;[20,21]

- *Solid Oxide Electrolysis Cells (SOEC):* the electrolyte is a ceramic material (doped ZrO_2, CeO_2, $LaGaO_3$) with high ionic conductivity which allows the transport of O^{2-} ions from the cathodic to the anodic side of the cell. These devices usually operate at high temperatures (800-1000 °C). The advantages of these devices are high efficiency and the possibility to operate them in a reverse mode (as fuel cells). This technology is still at the demonstration scale; commercialization is hindered by rapid materials degradation due to high operating temperatures.[22] To overcome these limitations, the use of proton-conducting oxides as electrolyte materials is also under investigation.[23]

1.2. Water splitting: reaction and catalysis

Water splitting is a non-spontaneous reaction (ΔG^0 = +237 kJ mol^{-1}) given by the sum of two half-reactions, the hydrogen evolution reaction (HER) and the oxygen evolution reaction (OER) taking place at the cathode and anode, respectively.[24]

In acidic environment, the two half-reactions can be written as follows:

Anode (+): $2H_2O \longrightarrow O_2 + 4H^+(aq) + 4e^-$ $E°$= +1.23 V_{SHE}

Cathode (−): $2H^+(aq) + 2e^- \longrightarrow H_2$ $E°$= +0.00 V_{SHE}

In alkaline environment:

Anode (+): $4OH^-$ (aq) ⟶ $O_2 + 2H_2O + 4e^-$ $E°$= +0.40 V_{SHE}

Cathode (−): $2H_2O + 2e^-$ ⟶ $H_2 + 2OH^-$ (aq) $E°$= −0.83 V_{SHE}

Sum: $2H_2O$ ⟶ $2H_2 + O_2$ $E°_{cell}$ = −1.23 V

While the thermodynamic potentials of the half-reactions are pH-sensitive, the potential of the cell remains equal to −1.23 V irrespective of the pH. Practically, higher potentials are needed; the difference between the applied potential and the reversible potential is the overpotential (η), caused by activation, concentration, and resistance limitations. The total overpotential needed to drive water splitting is given by the sum of cathodic (η_{cath}) and anodic (η_{an}) overpotentials. Between the two half-reactions, the OER typically requires higher overpotential than the simpler HER, because OER involves the transfer of four protons and four electrons.[24,25] Lowering the anodic overpotential is thus of primary importance for increasing the efficiency of water-splitting devices.[24,26,27]

Catalysis plays an essential role in reducing the kinetic barriers, allowing the reaction to proceed through lower free energy pathways and, for electrochemical reactions, reduce the overpotentials. Catalysts are substances that are not consumed during a chemical reaction, yet they increase the rate of a chemical reaction by interacting with the reactants. For electrochemical reactions, electrocatalysts are materials that assist in transferring electrons between the electrode and reactants and/or facilitate an intermediate electrochemical reaction step. For heterogeneously catalyzed electrochemical reactions, the reaction steps can be listed as follows:

- Transport of the reactants from the solution to the electrode surface;
- Adsorption of the reactants on the electrode surface;
- Electron transfer between reactants and the electrode surface and bond breaking and making in and between adsorbed intermediates (reaction);
- Desorption of the products;
- Transport of the products from the electrode surface to the solution.

At low current densities, *i.e.* at low reaction rates, the reaction is usually limited by one or more of the elementary reaction steps occurring at the surface, because mass transport is fast enough to ensure the supply of reactants and removal of products to and from the electrode surface, respectively. At high current densities, mass transport can become a rate-

determining step, because the diffusion rate is not sufficient to ensure the supply of reactants or removal of the products. To enhance the overall rate, it is possible to lower the transport limitations (e.g., by using higher supporting electrolyte concentration, stirring the solution, or using a rotating disk electrode), or to change the thermodynamics (by modifying temperature and concentrations).

Ideal electrocatalysts should exhibit optimal bond strength with respect to the reaction intermediates, not too weak nor too strong (Sabatier's principle).[28] For OER electrocatalysts that bind oxygen intermediates too weakly, the adsorption and activation steps determine the reaction rate, while too strong binding of oxygen intermediates results in product desorption being the rate-determining step.[29] The theoretical OER activity can be plotted *versus* the adsorption energy on the electrode surface for many oxide surfaces: the resulting graph resembles a volcano, where the materials with optimum binding energetics for the oxygen intermediates sit at the top (maximum activity).[30,31]

The OER activity is often expressed in terms of the overpotential needed to reach a specific current density (typically 10 mA cm^{-2}) or by the current density measured at a specific overpotential. Although lower overpotential and higher current densities are considered indicators of better electrocatalytic properties, these parameters cannot be used to judge whether the higher activity is governed solely by electrocatalytic aspects. For example, a higher surface area or a higher number of active sites also lead to lower overpotential or higher current densities without implying a real intrinsic electrocatalytic effect. By measuring the electrochemical surface area (ECSA) and normalizing the current densities with ECSA values, it is possible to evaluate the intrinsic (or specific) catalytic activity regardless of the different number of actives sites exposed to the electrolyte.

The Tafel plot is a common tool to study the kinetics of OER. The kinetics of an electrode can be described using the Butler-Volmer equation:

$$j = j_0 \{\exp[\alpha z F \eta / RT] - \exp[-(1-\alpha) z F \eta / RT]\} \quad (1.1)$$

In equation (*1.1*), j is the current density, j_0 the exchange current density, α the electron-transfer coefficient, z the number of electrons transferred in the reaction, F the Faraday constant, η the overpotential, R the universal gas constant, and T the absolute temperature. At high cathodic or anodic overpotential, one of the two exponential terms can be neglected. It is then possible to derive the Tafel equation for anodic reactions in the kinetic regime:

$$\eta = a + b \log(j) \quad (1.2)$$

In equation (*1.2*), *a* is proportional to the logarithm of the exchange current density (j_0) and *b* represents the Tafel slope. The Tafel slope is an intrinsic parameter that gives insight into the reaction mechanism: changes in Tafel slope can be indicative of changes in the rate-determining step of the reaction or of different adsorptive properties of the electrode surface with respect to the reaction intermediates.

Besides high electrocatalytic activity, ideal electrode materials should also have:[32]

- High (electro)chemical, thermal, and mechanical stabilities under reaction conditions;
- High selectivity (when side-reactions are possible);
- High electrical conductivity;
- High surface area;
- Earth-abundancy and low cost;
- Non-toxicity.

Noble metal oxides, especially RuO_2 and IrO_2, are excellent electrocatalysts for the oxygen evolution reaction.[33,34] However, Ru and Ir are scarce and expensive metals, and it would be desirable to replace these oxides with those based on cheaper and more abundant metals.[27,35]

In alkaline environments, relevant to AECs, first-row transition metal oxides and (oxy)hydroxides are the preferred OER electrocatalysts because of their high activity, long durability at high pH, and also because of their abundance. Ni-oxide and (oxy)hydroxide are the most investigated OER catalysts for the alkaline regime due to their excellent performance.[36–38] Their electrocatalytic activity can be further enhanced through doping with Co,[39–41] Mn,[42,43] or Fe.[44–46] The activity of Fe-doped Ni oxide and (oxy)hydroxide is so high that in some cases it outperformed that of IrO_2 and RuO_2.[47–49] The synergistic effect between Ni and Fe for the water oxidation reaction was already reported in 1987 by Corrigan.[50] Further research efforts focused on understanding the role of Fe[51–56] and designing catalysts with higher surface area to maximize the mass activity.[57–59] These electrocatalysts can be easily (electro)deposited on Ni meshes or Ni plates, which constitute the anodes of AECs. Co-based catalysts (oxides and hydroxides) also exhibit good electrocatalytic performance in the alkaline water oxidation, but their activities are lower than those of NiFe-based catalysts. Co is also more expensive than Ni.[60–67] The development of Fe-[68–72] and Mn-based[73–77] catalysts would offer advantages in terms of metal scarcity and toxicity, but these catalysts cannot achieve the same electrocatalytic activity of Ni- and Co-based systems.[25]

In PEM electrolyzers, due to the acidic environment, noble metal oxides (IrO_2 and RuO_2) are required in the anodes for providing sufficient activity and stability.[78] RuO_2 is considered the most active metal oxide for OER.[29,32] However, anode corrosion and dissolution of active phase occur under applied anodic potentials. RuO_2 dissolution involves the formation of volatile RuO_4: this compound can either dissociate and redeposit on the electrode surface, or dissolve in form of soluble ruthenate ions into the electrolyte.[79,80] The critical anode potential (E_{crit}) is defined as the onset potential of anode corrosion and is related to the oxidation RuO_2/RuO_4.[81] The onset potential of RuO_2 dissolution experimentally matches the onset of OER. For this reason, it was suggested that these two processes are closely correlated.[82,83] At potentials higher than E_{crit}, massive anodic dissolution occurs as a thermodynamically-driven process. However, dissolution can occur also at potentials lower than E_{crit} in the form of transient dissolution. This degradation phenomenon is related to the insertion/removal of oxygen atoms in the crystal structure during oxidation/reduction of the metal/metal oxide surface, which can result in the exposure of a low coordination site to the electrolyte, and its successive dissolution.[84,85]

Despite being slightly less active, IrO_2 is more stable than RuO_2 and, thus, its use is preferred in PEM electrolyzers to ensure sufficient durability.[86,87] Differences in activity and stability of IrO_2 are found depending on the preparation method.[88] Thermal Ir-oxides prepared at high calcination temperatures that display a high degree of crystallinity have lower activities but higher stabilities than amorphous or low-crystalline Ir-oxides prepared at low calcination temperatures.[89,90] Typically, a dissolution pathway involves the oxidation of IrO_2 to IrO_3, which then decomposes or reacts with water to form IrO_4^{2-}.[91] This reaction is competitive to oxygen evolution and is the main reason for dissolution for thermal rutile IrO_2. For amorphous IrO_2, an additional dissolution pathway can occur involving lattice oxygen in the OER mechanism.[85,92] Activated lattice oxygen in amorphous IrO_2 can be attacked by water and form O_2, leaving an oxygen vacancy in the lattice;[93] this leads to the formation of low-coordinated Ir atoms that are prone to dissolve. This additional mechanism, which was shown by isotopic-labeling experiments, explains the superior catalytic OER activity and lower stability of amorphous IrO_2 than rutile IrO_2.[93] A major challenge in the development of IrO_2-based OER catalysts is thus balancing activity and stability in the same material.[94] Maximizing the mass activity of crystalline IrO_2 and stabilizing amorphous IrO_2 are possible ways to achieve better OER performance for IrO_2-based anodes together with a reduction in the Ir content of the electrodes.

The scarcity and high price of Ir hinder the scalability of PEM electrolyzers at the TW scale.[27,35] For this reason, replacing this element with cheaper, more abundant metals represents a viable approach to the scale-up of the PEM technology, provided that sufficient

durability is achieved.[95–98] First-row transition metals are abundant and, therefore, suitable candidates for this purpose. The main source of instability for first-row transition metal oxides lies in the formation of soluble species at low pH and under applied anodic potentials, which leads to the dissolution of the active phase. Among the Earth-abundant materials, Mn- and Co-based electrocatalysts are currently under investigation as potential candidates to (partially) replace Ir as anodic catalyst in acidic environment. Mn-oxide catalysts can be used in acid up to moderate current densities (~1 mA cm^{-2}), but they dissolve in form of permanganates at higher current densities.[75,99] Co-oxides are more active OER catalysts than Mn-oxides and also moderately stable at low pH.[100] Ensuring a high material crystallinity or mixing active Co-oxide with a structural phase (e.g. $CoFePbO_x$) have been identified as effective strategies to improve the stability of CoO_x under strongly acidic conditions.[98,101]

1.3. Chlorine evolution

To overcome the sluggish OER kinetics, a possible strategy consists in replacing OER with other simpler anodic half-reactions. The chlorine evolution reaction (CER) is an alternative anodic reaction occurring in the presence of chloride ions.[102] The CER can be written as follows:

$$2Cl^- \longrightarrow Cl_2 + 2e^- \qquad E° = +1.36\ V_{SHE}$$

This is a pH-independent, two-electron transfer process. Although CER is thermodynamically less favorable than OER in the whole pH range, due to its faster kinetics, it is the dominant anodic reaction in seawater electrolysis on metal oxide surfaces.[103] Compared to OER, CER leads to the production of a higher value product (Cl_2) than O_2. Cl_2 is industrially used in a wide variety of applications, including polymerization, metallurgy, water treatment, and organic synthesis.[104] Moreover, CER allows for the direct use of seawater, which represents the majority of water on Earth, without any additional cost related to water purification.[105] On the other hand, due to the high corrosiveness and toxicity of Cl_2, more expensive materials and special precautions for its storage and handling are required. For these reasons, while Cl_2 evolution is appealing in large-scale applications, the production of O_2 is preferred in small- and medium-scale applications. An example of a large-scale application of CER is the chlor-alkali process, which is the largest source of Cl_2 produced annually (*ca.* 60-70 million tonnes). Other than Cl_2, NaOH and H_2 are also produced, according to the following overall reaction:

$2NaCl + 2H_2O \longrightarrow Cl_2 + H_2 + 2NaOH$

Three different chlor-alkali processes are used, which differ in the separation between the anodic and cathodic compartments: the diaphragm process, the mercury amalgam process, and the membrane process. The first two were developed at the end of the 19th century and have been used for more than 100 years for the production of Cl_2 and NaOH. Nonetheless, these are among the most environmentally stressing processes of the chemical industry, as they require the use of asbestos in the diaphragm or mercury in the amalgam. The third process is the membrane process, first developed in the 1950s, which employs an ion-selective membrane to separate the anodic and cathodic compartments. In the last decades, legislation has required the conversion of most plants based on the diaphragm or mercury amalgam to the membrane process, which does not produce any hazardous wastes.[106]

The cathode of the chlor-alkali process is typically made of Ni, stainless steel, or graphite. The anode is the electrode that suffers most from the corrosion due to the evolution of Cl_2. Historically, graphite electrodes have been used as anodes. After Beer's invention of Dimensionally Stable Anodes (DSA®), graphite has been gradually abandoned and DSA® anodes have become the preferred choice due to their exceptionally high electrocatalytic CER performances at high current densities.[107] DSA® anodes are formed by a valve-metal plate (usually Ti) coated with a TiO_2-RuO_2 film (typically in a 70:30 molar ratio). TiO_2 provides a stabilizing matrix and dilutes the expensive active phase (RuO_2). These two metal oxides form a solid solution with a rutile structure with excellent activity and stability.[108] TiO_2 can be replaced by Ta_2O_5 or ZrO_2, while RuO_2 can be replaced by IrO_2; nonetheless, TiO_2-RuO_2 is by far the most used composition in the fabrication of DSA® anodes employed in the chlorine manufacturing industry.[109–111] As DSA® anodes are also very active catalysts for OER,[112–115] high concentration of chlorides (≈5 M) and low pH (≈2) are used to tailor the selectivity towards CER and suppress OER.[102,116]

1.4. Scope of the thesis

This thesis aims at exploring strategies for tailoring the electrocatalytic performance of oxygen evolution catalysts and at gaining insight into their activity and stability. A crucial goal for scaling up of water splitting devices is combining high catalytic activity and stability with a reduction of the noble-metal content in the anodes for a better price-sustainability.

Stability represents an issue for both oxygen- and chlorine-evolution anodes. The electrochemical stability of a model electrode under OER and competitive OER-CER conditions is examined in **Chapter 2.** RuO_2 typically constitutes the active phase in industrial catalysts for Cl_2 production and is also a very active OER electrocatalyst. Epitaxially-grown films of RuO_2(110) on a Ru(0001) substrate are subjected to electrochemical treatments in H_2SO_4 or HCl in order to evaluate differences and similarities in the corrosion mechanisms of this model system under OER and CER/OER conditions. Online Electrochemical Mass Spectrometry (OLEMS) is used to evaluate the onset potentials and selectivities of OER and CER. A comprehensive set of lab-based and synchrotron-based techniques allows for a comparison of the impact of electrochemical treatments on the crystallinity, morphology, and structure of the electrodes. A corrosion mechanism is derived for this model system applicable to both OER and CER reactions.

Chapter 3 introduces a strategy to lower the noble-metal content in TiO_2-RuO_2 anodes for water oxidation under acidic conditions. TiO_2 and RuO_2 form a solid solution with the rutile structure where RuO_2 is the OER active phase and TiO_2 acts as a stabilizer. We explore the impact of Mn addition on the electrocatalytic activity and stability of the anodes and the crystalline structure and morphology. Mn was chosen as it is a cheap and abundant element that can also crystallize in its oxide form in the rutile structure. This strategy allows obtaining a catalyst with very low Ru content outperforming TiO_2-RuO_2 and RuO_2 reference systems. The stability and degradation of the electrodes have been investigated to gain insight into the structural and compositional anode modifications occurring upon prolonged electrolysis.

A similar approach has been used in **Chapter 4** to fine-tune the activity and stability of IrO_2, which is the state-of-the-art OER catalyst in acidic media. IrO_2 crystallizes in the rutile structure like RuO_2 and TiO_2. This chapter studies the electronic and crystalline changes induced by Mn addition to IrO_2, providing structure-performance relationships for IrO_2-based anodes. This is achieved by monitoring the overall and intrinsic activity and stability of the anodes at different Mn loadings and by linking the findings with the results of the structural and spectroscopic characterization.

The following part of the thesis deals with the use of non-noble metal-based catalysts for the oxygen evolution reaction. **Chapter 5** focuses on the stability issue of $NiFeO_xH_y$ electrodes in conditions relevant to the industrial alkaline water electrolysis. $NiFeO_xH_y$ is one of the most active catalysts in alkaline media. The high temperature and high KOH concentration used in industrial operations could however impact the electrocatalytic performances of the anodes. Nonetheless, most of the lab-based research experiments are

performed under standard conditions (25 °C, 1 M KOH). This chapter aims at describing the influence of more realistic harsh testing conditions on the structural and catalytic behavior of $NiFeO_xH_y$ anodes. Also, the impact of an anodic polarization at industrially relevant conditions on the structure and performance of NiO_xH_y and $NiFeO_xH_y$ are investigated and compared.

The use of noble-metal free OER electrocatalysts in acidic environment is still hampered by their insufficient stability. **Chapter 6** investigates the stability behavior of Co_3O_4 anodes for the acidic water oxidation. This chapter aims at clarifying the reasons for catalyst deactivation under prolonged electrochemical treatment in acid electrolyte: emphasis is given to the role of substrate, composition (in terms of Li doping), and dissolution in the deactivation of Co_3O_4. Li doping is used to tune the crystallinity and electronic properties of Co_3O_4, factors aiming at optimizing the catalytic activity and stability.

1.5. References

(1) IEA. *World Energy Outlook 2019* **2019**.

(2) Hone, D. In *Putting the Genie Back*; 2017; pp 121–159.

(3) Barber, J.; Tran, P. D. *J. R. Soc. Interface* **2016**, *10* (81), 20120984.

(4) Nocera, D. G.; Lewis, N. S. *Proc. Natl. Acad. Sci. U. S. A.* **2006**, *103* (43), 15729–15735.

(5) Beaudin, M.; Zareipour, H.; Schellenberglabe, A.; Rosehart, W. *Energy Sustain. Dev.* **2010**, *14* (4), 302–314.

(6) Akinyele, D. O.; Rayudu, R. K. *Sustain. Energy Technol. Assessments* **2014**, *8*, 74–91.

(7) Seh, Z. W.; Kibsgaard, J.; Dickens, C. F.; Chorkendorff, I.; Nørskov, J. K.; Jaramillo, T. F. *Science* **2017**, *355*, eaad4998.

(8) Dincer, I.; Acar, C. *Int. J. Hydrogen Energy* **2014**, *40* (34), 11094–11111.

(9) Nitopi, S.; Bertheussen, E.; Scott, S. B.; Liu, X.; Engstfeld, A. K.; Horch, S.; Seger, B.; Stephens, I. E. L.; Chan, K.; Hahn, C.; Nørskov, J. K.; Jaramillo, T. F.; Chorkendorff, I. *Chem. Rev.* **2019**, *119* (12), 7610–7672.

(10) Liu, H.; Wei, L.; Liu, F.; Pei, Z.; Shi, J.; Wang, Z. J.; He, D.; Chen, Y. *ACS Catal.* **2019**, 5245–5267.

(11) Kirubakaran, A.; Jain, S.; Nema, R. K. *Renew. Sustain. Energy Rev.* **2009**, *13* (9), 2430–2440.

(12) Schulz, H. *Appl. Catal. A Gen.* **1999**, *186*, 3–12.

(13) Jiang, X.; Nie, X.; Guo, X.; Song, C.; Chen, J. G. *Chem. Rev.* **2020**.

(14) Rönsch, S.; Schneider, J.; Matthischke, S.; Schlüter, M.; Götz, M.; Lefebvre, J.; Prabhakaran, P.; Bajohr, S. *Fuel* **2016**, *166*, 276–296.

(15) Smith, C.; Hill, A. K.; Torrente-Murciano, L. *Energy Environ. Sci.* **2020**, *13* (2), 331–344.

(16) H2@Scale | Department of Energy https://www.energy.gov/eere/fuelcells/h2scale (accessed Aug 13, 2020).

(17) de Levie, R. *J. Electroanal. Chem.* **1999**, *476* (2), 92–93.

(18) Schmidt, O.; Gambhir, A.; Staffell, I.; Hawkes, A.; Nelson, J.; Few, S. *Int. J. Hydrogen Energy* **2017**, *42* (52), 30470–30492.

(19) Zeng, K.; Zhang, D. *Prog. Energy Combust. Sci.* **2010**, *36* (3), 307–326.

(20) Carmo, M.; Fritz, D. L.; Mergel, J.; Stolten, D. *Int. J. Hydrogen Energy* **2013**, *38* (12), 4901–4934.

(21) Babic, U.; Suermann, M.; Büchi, F. N.; Gubler, L.; Schmidt, T. J. *J. Electrochem. Soc.* **2017**, *164* (4), F387–F399.
(22) Laguna-Bercero, M. A. *J. Power Sources* **2012**, *203*, 4–16.
(23) Bi, L.; Boulfrad, S.; Traversa, E. *Chem. Soc. Rev.* **2014**, *43* (24), 8255–8270.
(24) Walter, M. G.; Warren, E. L.; McKone, J. R.; Boettcher, S. W.; Mi, Q.; Santori, E. A.; Lewis, N. S. *Chem. Rev.* **2010**, *110* (11), 6446–6473.
(25) McCrory, C. C. L.; Jung, S.; Ferrer, I. M.; Chatman, S. M.; Peters, J. C.; Jaramillo, T. F. *J. Am. Chem. Soc.* **2015**, *137* (13), 4347–4357.
(26) Eftekhari, A. *Mater. Today Energy* **2017**, *5*, 37–57.
(27) Kibsgaard, J.; Chorkendorff, I. *Nat. Energy* **2019**, *4* (6), 430–433.
(28) Sabatier, P. *Berichte der Dtsch. Chem. Gesellschaft* **1911**, *44* (3), 1984–2001.
(29) Fabbri, E.; Habereder, A.; Waltar, K.; Kötz, R.; Schmidt, T. J. *Catal. Sci. Technol.* **2014**, *4* (11), 3800–3821.
(30) Rossmeisl, J.; Qu, Z. W.; Zhu, H.; Kroes, G. J.; Nørskov, J. K. *J. Electroanal. Chem.* **2007**, *607* (1–2), 83–89.
(31) Man, I. C.; Su, H.-Y.; Calle-Vallejo, F.; Hansen, H. A.; Martínez, J. I.; Inoglu, N. G.; Kitchin, J.; Jaramillo, T. F.; Nørskov, J. K.; Rossmeisl, J. *ChemCatChem* **2011**, *3*, 1159–1165.
(32) Trasatti, S. *Electrochim. Acta* **1984**, *29* (11), 1503–1512.
(33) McCrory, C. C. L.; Jung, S.; Peters, J. C.; Jaramillo, T. F. *J. Am. Chem. Soc.* **2013**, *135* (45), 16977–16987.
(34) Jung, S.; McCrory, C. C. L.; Ferrer, I. M.; Peters, J. C.; Jaramillo, T. F. *J. Mater. Chem. A* **2016**, *4* (8), 3068–3076.
(35) Vesborg, P. C. K.; Jaramillo, T. F. *RSC Adv.* **2012**, *2* (21), 7933–7947.
(36) Hall, D. S.; Lockwood, D. J.; Bock, C.; MacDougall, B. R. *Proc. R. Soc. A* **2015**, *471*, 2174.
(37) Lyons, M. E. G.; Brandon, M. P. *Int. J. Electrochem. Sci.* **2008**, *3* (12), 1386–1424.
(38) Roger, I.; Symes, M. D. *J. Am. Chem. Soc.* **2015**, *137* (43), 13980–13988.
(39) Castro, E. B.; Gervasi, C. A. *Int. J. Hydrogen Energy* **2000**, *25* (12), 1163–1170.
(40) Lambert, T. N.; Vigil, J. A.; White, S. E.; Davis, D. J.; Limmer, S. J.; Burton, P. D.; Coker, E. N.; Beechem, T. E.; Brumbach, M. T. *Chem. Commun.* **2015**, *51* (46), 9511–9514.
(41) Wu, G.; Li, N.; Zhou, D. R.; Mitsuo, K.; Xu, B. Q. *J. Solid State Chem.* **2004**, *177* (10), 3682–3692.
(42) Menezes, P.; Indra, A.; Levy, O.; Kailasam, K.; Pfrommer, J.; Gutkin, V. *Chem. Commun.* **2015**, *51*, 5005–5008.
(43) Chen, Z.; Wang, Z.; Cai, R.; Xie, Y.; Yu, J.; Long, X.; Yang, B.; Yang, S. *Nanoscale* **2020**, *12* (4), 2472–2478.
(44) Gong, M.; Dai, H. *Nano Res.* **2015**, *8* (1), 23–39.
(45) Wang, Y.; Yan, D.; El Hankari, S.; Zou, Y.; Wang, S. *Adv. Sci.* **2018**, *5* (8).
(46) Dionigi, F.; Strasser, P. *Adv. Energy Mater.* **2016**, *6*, 1600621.
(47) Trotochaud, L.; Ranney, J. K.; Williams, K. N.; Boettcher, S. W. *J. Am. Chem. Soc.* **2012**, *134* (41), 17253–17261.
(48) Zhou, T.; Cao, Z.; Zhang, P.; Ma, H.; Gao, Z.; Wang, H.; Lu, Y.; He, J.; Zhao, Y. *Sci. Rep.* **2017**, *7* (46154), 1–9.
(49) Gong, M.; Li, Y.; Wang, H.; Liang, Y.; Wu, J. Z.; Zhou, J.; Wang, J.; Regier, T.; Wei, F.; Dai, H. *J. Am. Chem. Soc.* **2013**, *135*, 8452–8455.
(50) Corrigan, D. A. *J. Electrochem. Soc.* **1987**, *134* (2), 377–384.
(51) Louie, M. W.; Bell, A. T. *J. Am. Chem. Soc.* **2013**, *135* (33), 12329–12337.
(52) Li, N.; Bediako, D. K.; Hadt, R. G.; Hayes, D.; Kempa, T. J.; von Cube, F.; Bell, D. C.; Chen, L. X.; Nocera, D. G. *Proc. Natl. Acad. Sci.* **2017**, *114* (7), 1486–1491.
(53) Klaus, S.; Cai, Y.; Louie, M. W.; Trotochaud, L.; Bell, A. T. *J. Phys. Chem. C* **2015**, *119* (13), 7243–7254.
(54) Stevens, M. B.; Trang, C. D. M.; Enman, L. J.; Deng, J.; Boettcher, S. W. *J. Am. Chem. Soc.* **2017**, *139* (33), 11361–11364.

(55) Ahn, H. S.; Bard, A. J. *J. Am. Chem. Soc.* **2016**, *138* (1), 313–318.
(56) Friebel, D.; Louie, M. W.; Bajdich, M.; Sanwald, K. E.; Cai, Y.; Wise, A. M.; Cheng, M. J.; Sokaras, D.; Weng, T. C.; Alonso-Mori, R.; Davis, R. C.; Bargar, J. R.; Nørskov, J. K.; Nilsson, A.; Bell, A. T. *J. Am. Chem. Soc.* **2015**, *137* (3), 1305–1313.
(57) Lu, X.; Zhao, C. *Nat. Commun.* **2015**, *6*, 6616.
(58) Fominykh, K.; Chernev, P.; Zaharieva, I.; Sicklinger, J.; Stefanic, G.; Döblinger, M.; Müller, A.; Pokharel, A.; Böcklein, S.; Scheu, C.; Bein, T.; Fattakhova-Rohlfing, D. *ACS Nano* **2015**, *9* (5), 5180–5188.
(59) Kim, K. H.; Zheng, J. Y.; Shin, W.; Kang, Y. S. *RSC Adv.* **2012**, *2* (11), 4759.
(60) Chou, N. H.; Ross, P. N.; Bell, A. T.; Tilley, T. D. *ChemSusChem* **2011**, *4* (11), 1566–1569.
(61) Klingan, K.; Ringleb, F.; Zaharieva, I.; Heidkamp, J.; Chernev, P.; Gonzalez-Flores, D.; Risch, M.; Fischer, A.; Dau, H. *ChemSusChem* **2014**, *7* (5), 1301–1310.
(62) Deng, X.; Tuysuz, H. *ACS Catal.* **2014**, *4*, 3701–3714.
(63) Liu, Y. C.; Koza, J. A.; Switzer, J. A. *Electrochim. Acta* **2014**, *140*, 359–365.
(64) Menezes, P. W.; Indra, A.; Gonzalez-Flores, D.; Sahraie, N. R.; Zaharieva, I.; Schwarze, M.; Strasser, P.; Dau, H.; Driess, M. *ACS Catal.* **2015**, *5* (4), 2017–2027.
(65) Burke, M. S.; Kast, M. G.; Trotochaud, L.; Smith, A. M.; Boettcher, S. W. *J. Am. Chem. Soc.* **2015**, *137* (10), 3638–3648.
(66) Huang, J.; Chen, J.; Yao, T.; He, J.; Jiang, S.; Sun, Z.; Liu, Q.; Cheng, W.; Hu, F.; Jiang, Y.; Pan, Z.; Wei, S. *Angew. Chemie - Int. Ed.* **2015**, *54* (30), 8722–8727.
(67) Wang, J.; Cui, W.; Liu, Q.; Xing, Z.; Asiri, A. M.; Sun, X. *Adv. Mater.* **2016**, *28* (2), 215–230.
(68) Zou, S.; Burke, M. S.; Kast, M. G.; Fan, J.; Danilovic, N.; Boettcher, S. W. *Chem. Mater.* **2015**, *27* (23), 8011–8020.
(69) Chen, J. Y. C.; Dang, L.; Liang, H.; Bi, W.; Gerken, J. B.; Jin, S.; Alp, E. E.; Stahl, S. S. *J. Am. Chem. Soc.* **2015**, *137* (48), 15090–15093.
(70) Park, G.; Kim, Y. Il; Kim, Y. H.; Park, M.; Jang, K. Y.; Song, H.; Nam, K. M. *Nanoscale* **2017**, *9* (14), 4751–4758.
(71) Luo, W.; Jiang, C.; Li, Y.; Shevlin, S. A.; Han, X.; Qiu, K.; Cheng, Y.; Guo, Z.; Huang, W.; Tang, J. *J. Mater. Chem. A* **2017**, *5* (5), 2021–2028.
(72) Babar, P. T.; Pawar, B. S.; Lokhande, A. C.; Gang, M. G.; Jang, J. S.; Suryawanshi, M. P.; Pawar, S. M.; Kim, J. H. *J. Energy Chem.* **2017**, *26* (4), 757–761.
(73) Takashima, T.; Hashimoto, K.; Nakamura, R. *J. Am. Chem. Soc.* **2012**, *134* (3), 1519–1527.
(74) Ramírez, A.; Hillebrand, P.; Stellmach, D.; May, M. M.; Bogdanoff, P.; Fiechter, S. *J. Phys. Chem. C* **2014**, *118* (26), 14073–14081.
(75) Huynh, M.; Shi, C.; Billinge, S. J. L.; Nocera, D. G. *J. Am. Chem. Soc.* **2015**, *137* (47), 14887–14904.
(76) Zhou, F.; Izgorodin, A.; Hocking, R. K.; Armel, V.; Spiccia, L.; MacFarlane, D. R. *ChemSusChem* **2013**, *6* (4), 643–651.
(77) Meng, Y.; Song, W.; Huang, H.; Ren, Z.; Chen, S.; Suib, S. L. *J. Am. Chem. Soc.* **2014**, *136*, 11452–11464.
(78) Feng, Q.; Yuan, X. Z.; Liu, G.; Wei, B.; Zhang, Z.; Li, H.; Wang, H. *J. Power Sources* **2017**, *366*, 33–55.
(79) Iwakura, C.; Hirao, K.; Tamura, H. *Electrochim. Acta* **1977**, *22* (4), 329–334.
(80) Kötz, R.; Stucki, S.; Scherson, D.; Kolb, D. M. *J. Electroanal. Chem. Interfacial Electrochem.* **1984**, *172* (1–2), 211–219.
(81) Veselovskaya, I. E.; Khodkevich, S. D.; Malkina, R. I.; Yakimenko, L. M. *Elektrokhimiya* **1974**, *10*, 74–77.
(82) Kotz, R.; Lewerenz, H. J.; Stucki, S. *J. Electrochem. Soc.* **1983**, *130*, 825–829.
(83) Wohlfahrt-Mehrens, M.; Heitbaum, J. *J. Electroanal. Chem. Interfacial Electrochem.* **1987**, *237* (2), 251–260.
(84) Hodnik, N.; Jovanovič, P.; Pavlišič, A.; Jozinović, B.; Zorko, M.; Bele, M.; Šelih, V. S.; Šala, M.; Hočevar, S.;

Gaberšček, M. *J. Phys. Chem. C* **2015**, *119* (18), 10140–10147.
(85) Cherevko, S.; Zeradjanin, A. R.; Topalov, A. A.; Kulyk, N.; Katsounaros, I.; Mayrhofer, K. J. J. *ChemCatChem* **2014**, *6* (8), 2219–2223.
(86) Antolini, E. *ACS Catal.* **2014**, *4* (5), 1426–1440.
(87) Rozain, C.; Mayousse, E.; Guillet, N.; Millet, P. *Appl. Catal. B Environ.* **2016**, *182*, 153–160.
(88) Johnson, B.; Girgsdies, F.; Weinberg, G.; Rosenthal, D.; Knop-Gericke, A.; Schlögl, R.; Reier, T.; Strasser, P. *J. Phys. Chem. C* **2013**, *117* (48), 25443–25450.
(89) Geiger, S.; Kasian, O.; Shrestha, B. R.; Mingers, A. M.; Mayrhofer, K. J. J.; Cherevko, S. *J. Electrochem. Soc.* **2016**, *163* (11), F3132–F3138.
(90) Cherevko, S.; Reier, T.; Zeradjanin, A. R.; Pawolek, Z.; Strasser, P.; Mayrhofer, K. J. J. *Electrochem. commun.* **2014**, *48*, 81–85.
(91) Kasian, O.; Grote, J. P.; Geiger, S.; Cherevko, S.; Mayrhofer, K. J. J. *Angew. Chemie - Int. Ed.* **2018**, *57* (9), 2488–2491.
(92) Grimaud, A.; Diaz-Morales, O.; Han, B.; Hong, W. T.; Lee, Y.-L.; Giordano, L.; Stoerzinger, K. A.; Koper, M. T. M.; Shao-Horn, Y. *Nat. Chem.* **2017**, *9* (5), 457–465.
(93) Oellers, T.; Fruchter, L.; Pizzutilo, E.; Geiger, S.; Kasian, O.; Ledendecker, M.; Mingers, A. M.; Cherevko, S.; Koper, M. T. M.; Mayrhofer, K. J. J.; Li, Z.; Diaz-Morales, O.; Ludwig, A.; Fu, W. T. *Nat. Catal.* **2018**, *1* (7), 508–515.
(94) Kim, Y.; Lopes, P. P.; Park, S.; Lee, A.; Lim, J.; Lee, H.; Back, S.; Jung, Y.; Danilovic, N.; Stamenkovic, V.; Erlebacher, J.; Snyder, J.; Markovic, N. M. *Nat. Commun.* **2017**, *8*, 1449.
(95) Ledendecker, M.; Geiger, S.; Hengge, K.; Lim, J.; Cherevko, S.; Mingers, A. M.; Göhl, D.; Fortunato, G. V.; Jalalpoor, D.; Schüth, F.; Scheu, C.; Mayrhofer, K. J. J. *Nano Res.* **2019**, *12* (9), 2275–2280.
(96) Oakton, E.; Lebedev, D.; Povia, M.; Abbott, D. F.; Fabbri, E.; Fedorov, A.; Nachtegaal, M.; Copéret, C.; Schmidt, T. J. *ACS Catal.* **2017**, *7* (4), 2346–2352.
(97) Strickler, A. L.; Flores, R. A.; King, L. A.; Nørskov, J. K.; Bajdich, M.; Jaramillo, T. F. *ACS Appl. Mater. Interfaces* **2019**, *11* (37), 34059–34066.
(98) Huynh, M.; Ozel, T.; Liu, C.; Lau, E. C.; Nocera, D. G. *Chem. Sci.* **2017**, *8* (7), 4779–4794.
(99) Huynh, M.; Bediako, D. K.; Nocera, D. G. *J. Am. Chem. Soc.* **2014**, *136* (16), 6002–6010.
(100) Burke, M. S.; Zou, S.; Enman, L. J.; Kellon, J. E.; Gabor, C. A.; Pledger, E.; Boettcher, S. W. *J. Phys. Chem. Lett.* **2015**, *6* (18), 3737–3742.
(101) Mondschein, J. S.; Callejas, J. F.; Read, C. G.; Chen, J. Y. C.; Holder, C. F.; Badding, C. K.; Schaak, R. E. *Chem. Mater.* **2017**, *29* (3), 950–957.
(102) Karlsson, R. K. B.; Cornell, A. *Chem. Rev.* **2016**, *116* (5), 2982–3028.
(103) Goryachev, A.; Etzi Coller Pascuzzi, M.; Carlà, F.; Weber, T.; Over, H.; Hensen, E. J. M.; Hofmann, J. P. *Electrochim. Acta* **2020**, *336*, 135713.
(104) Fauvarque, J. *Pure Appl. Chem.* **1996**, *68*, 1713–1720.
(105) Dionigi, F.; Reier, T.; Pawolek, Z.; Gliech, M.; Strasser, P. *ChemSusChem* **2016**, *9* (9), 962–972.
(106) Crook, J.; Mousavi, A. *Environ. Forensics* **2016**, *17* (3), 211–217.
(107) Beer, H. B. *J. Electrochem. Soc.* **1980**, *127* (8), 303C.
(108) Trasatti, S. *Electrochim. Acta* **2000**, *45* (15–16), 2377–2385.
(109) Comninellis, C.; Vercesi, G. P. *J. Appl. Electrochem.* **1991**, *21*, 335–345.
(110) Comninellis, C.; Vercesi, G. P. *J. Appl. Electrochem.* **1991**, *21* (2), 136–142.
(111) Trieu, V.; Schley, B.; Natter, H.; Kintrup, J.; Bulan, A.; Hempelmann, R. *Electrochim. Acta* **2012**, *78*, 188–194.
(112) Martelli, G. N.; Ornelas, R.; Faita, G. *Electrochim. Acta* **1994**, *39* (11–12), 1551–1558.
(113) Naslund, L.-A.; Sanchez-Sanchez, C. M.; Ingason, A. S.; Backstrom, J.; Herrero, E.; Rosen, J.; Holmin, S. *J.*

Phys. Chem. C **2013**, *117* (12), 6126–6135.

(114) Hu, J.-M.; Zhang, J.-Q.; Cao, C.-N. *Int J Hydrog. Energy* **1994**, *29*, 355–361.

(115) Etzi Coller Pascuzzi, M.; Goryachev, A.; Hofmann, J. P.; Hensen, E. J. M. *Appl. Catal. B Environ.* **2020**, *261*, 118225.

(116) Bennett, J. E. *Int. J. Hydrogen Energy* **1980**, *5* (4), 401–408.

Chapter 2

Electrochemical stability of RuO_2(110)/Ru(0001) model electrodes in the oxygen and chlorine evolution reactions

Abstract

RuO_2 is commercially employed as an anodic catalyst in the chlor-alkali process. It is also one of the most active electrocatalysts for the oxidation of water, relevant to electrochemical water splitting. However, the use of RuO_2 is limited by its low anodic stability under acidic conditions, especially at high overpotentials. In the present work, the electrochemical stability of model RuO_2(110)/Ru(0001) anodes was investigated in order to gain a deeper understanding of the relation between structure and performance in Cl_2 and O_2 evolution reactions (CER and OER, respectively). Online electrochemical mass spectrometry was used to determine the onset potential of CER and OER in HCl and H_2SO_4 electrolytes, respectively. The onset potential of OER was higher in HCl than in H_2SO_4 due to competition with the kinetically more favorable CER. A detailed stability evaluation revealed pitting corrosion of the electrode surface with exposure of Ru(0001) metal substrate concomitant with the formation of a hydrous RuO_2 in some areas regardless of the applied electrochemical treatment. However, despite local pitting, the RuO_2(110) layer preserves its thickness in most areas. Degradation of the electrode was found to be less severe in 0.5 M HCl due to a decrease in the faradaic efficiency of RuO_2 oxidation caused by competition with the kinetically more favorable CER.

This chapter has been published as:

Goryachev, A.[$]; Etzi Coller Pascuzzi, M.[$]; Carlà, F.; Weber, T.; Over, H.; Hensen, E. J. M.; Hofmann, J. P. *Electrochim. Acta* **2020**, *336*, 135713.

[$] The authors contributed equally.

2.1. Introduction

RuO_2 is a common electrocatalyst which is primarily used for large-scale electrochemical production of Cl_2 as a part of mixed oxide anodes (Dimensionally Stable Anodes, DSA®).[1–4] Nearly all chlorine is produced by electrolysis of concentrated NaCl solution (brine) in the chlor-alkali process with an annual global production of ca. 70 million tons of Cl_2.[5,6] Chlorine is used as a base chemical for a wide range of applications including metallurgy, polymerization, and organic synthesis.[7] Besides the production of Cl_2, the chlor-alkali process yields NaOH and H_2 as by-products, which are typically used in oil refineries, the manufacture of paper, soap, and textiles.[8]

A major challenge with the use of RuO_2 is the competition of the desired anodic oxidation of Cl^- with the formation of gaseous oxygen as a result of water oxidation. Although the oxygen evolution reaction (OER) is thermodynamically favored over the CER in all the pH range due to its lower standard potential (E^0 (O_2/H_2O) = +1.23 V *vs*. the standard hydrogen electrode (SHE) and E^0 (Cl_2/Cl^-) = +1.36 V *vs*. SHE, respectively), CER occurs at a higher rate and has a lower onset potential than OER because of its faster kinetics.[8] Unlike CER, OER is pH-dependent (*i.e.,* E_{OER} decreases with increasing pH). Accordingly, acidic conditions are utilized in the chlor-alkali process to minimize the OER rate and thus its selectivity. In industry, operation at pH ≤ 2 is inconvenient because of the limited stability of the employed membrane materials. Due to the formation of molecular oxygen as a side-product, a significant fraction of the process costs are related to the separation of O_2 from the Cl_2 product stream. Selectivity and stability of the CER and OER anodes have therefore been studied in great detail in the last decades.[9–13] To increase the stability of RuO_2, it is commonly used in a mixture with other oxides such as TiO_2, ZrO_2, and Ta_2O_5.[3,14,15] This strategy, which results in improved corrosion resistance, was first applied in the fabrication of the so-called Dimensionally Stable Anodes (DSA®), which show enhanced activity and structural stability during operation under corrosive electrochemical conditions.[16] DSAs® are typically composed of a solid solution of rutile TiO_2 and RuO_2 (Ti:Ru atomic ratio ~ 70:30) deposited on a Ti substrate. The mixing of the two components to form a solid solution of the oxides is a key to combine activity and conductivity, provided by RuO_2, with a sufficient stability provided by TiO_2.[17–19] However, upon prolonged use under harsh industrial CER/OER conditions, even DSAs® suffer from corrosion, which leads to the dissolution of RuO_2. RuO_2 dissolution at anodic potentials can proceed in three ways: (i) oxidation of RuO_2 to volatile RuO_4, (ii) formation of soluble (per)ruthenates and (iii) physical detachment and loss of solid RuO_2 particles.[20,21] The critical anode potential (E_{crit}) is defined as the onset potential of corrosion and is usually ascribed to the oxidation of RuO_2 to RuO_4 (*2.1*), which

is estimated to occur at about +1.45 V_{SHE}.[22] It has also been noted by various authors that $E_{crit.}$ matches the onset potential of OER, suggesting that the underlying mechanisms of the two processes are closely related.[23–26]

$$RuO_4 + 4H^+ + 4e^- \rightarrow RuO_2 + 2H_2O \qquad (E^0 = +1.387\ V) \qquad (2.1)$$

RuO_2 corrosion can occur as transient or steady-state dissolution.[15] The latter is a thermodynamically controlled process and occurs when $E \geq E_{crit}$, while transient dissolution can already occur at much lower overpotential, when low-coordination sites or metastable transition states are exposed to the electrolyte.[27] Transient dissolution was observed for both Ru and RuO_2 electrodes.[27,28] It has also been observed that the lower stability of electrochemically prepared amorphous (hydrous) RuO_2 and the higher stability of thermally prepared crystalline RuO_2 show an inverse relationship with OER activity.[27] This is consistent with the observed correlation of the OER activity and the dissolution rate for a set of transition metals and their oxides.[28] The presence of Cl^- ions has a positive effect on RuO_2 stability. Particularly, RuO_2 and Ru^0 dissolution are slowed down at higher Cl^- concentrations.[6] Since a high concentration of Cl^- is necessary to kinetically promote CER over OER, this stabilization can be explained by a lower rate of the OER. However, it has also been shown that an excess of Cl^- in combination with low pH (< 2) opens an alternative corrosion route of RuO_2, which is related to the formation of soluble ruthenium chlorides.[29]

In the present study, we compare the stability of well-defined RuO_2(110)/Ru(0001) single crystal model anodes under pure OER and competitive CER/OER conditions. The use of model electrodes allows to precise monitoring of structural, morphological and chemical changes of the electrode surface for a selected facet of the active catalyst phase. Besides electrochemical methods, we employed lab- and synchrotron-based characterization techniques, including surface X-ray scattering (SXS) and X-ray reflectivity (XRR), X-ray photoelectron spectroscopy (XPS), inductively-coupled plasma optical emission spectroscopy (ICP-OES), and atomic force microscopy (AFM) to evaluate the degree and type of corrosion occurring during OER and CER treatments. Our multi-technique approach allowed us to follow the structural and compositional changes of the model electrode upon electrochemical treatment in different conditions, enabling a deeper understanding of the nature of the underlying physicochemical processes involved in anodic corrosion.

2.2. Experimental Section

2.2.1. Preparation of RuO_2(110)/Ru(0001)

An ultra-thin RuO_2(110) film was grown epitaxially on sputter-cleaned Ru(0001) single crystals (Surface Preparation Laboratories, Zaandam, NL) with diameters of 7 and 10 mm under ultra-high vacuum (UHV) conditions according to a procedure described elsewhere.[30] In brief, the substrate was cleaned by sequential sputtering/annealing steps until low energy electron diffraction (LEED) showed the pattern characteristic for a clean Ru(0001) surface. Sputtering was carried out at room temperature, p(Ar) = $1 \cdot 10^{-6}$ mbar and 600 eV beam energy for a maximum of 15 min in order to prevent crystal damage. Flash annealing was performed by heating the sample with an electron beam heater to 930 °C. The target temperature was maintained for 1 min, after that, the sample was allowed to cool down naturally in the absence of O_2. The cleaning step was followed by a roasting procedure ($p(O_2)$ = $1 \cdot 10^{-7}$ mbar, T = 780 °C, 20 min) to remove carbon impurities. Then, the growth of RuO_2(110) was carried out at 380 °C for 120 min while $3 \cdot 10^{-5}$ mbar O_2 were supplied to the preparation chamber via a leak valve. Uniformness of the film and absence of impurities were checked by LEED and XPS, respectively.

2.2.2. Stability evaluation

The electrochemical (EC) stability of RuO_2(110)/Ru(0001) electrodes under O_2 and Cl_2 evolution conditions was evaluated by subjecting the electrodes to continuous potential treatment (E = +1.50 V) for 60 min. All potentials reported in this work are plotted versus reversible hydrogen electrode (RHE) if not mentioned otherwise. The potential was chosen to be above the expected critical potential of RuO_2 in order to induce possible electrode degradation, which was assumed to be different under pure OER and competitive OER/CER conditions.[6] The EC treatment was performed in hanging meniscus mode in a standard three-electrode cell filled with 0.5 M H_2SO_4 or 0.5 M HCl (Sigma Aldrich, > 99.99%). Milli-Q (18.2 MΩ·cm) water was used in all operations. For simplicity, the experiments conducted in H_2SO_4 and HCl will be further referred to as OER and CER, respectively. Platinum foil (area = 10 cm^2) and Red Rod electrodes (Radiometer Analytical, E_{RE} = +0.215 V) were utilized as counter (CE) and reference (RE) electrodes, respectively.

The values of the overpotential (η) were calculated using the following equations:

for OER: $\eta_{OER} = E_{meas} + E_{Ag/AgCl} + 0.059\ pH - E^0_{OER}$ (*2.2*)

for CER: $\eta_{CER} = E_{meas} + E_{Ag/AgCl} - E^0_{CER}$ (*2.3*)

where E_{meas} is the electrode potential measured against the reference electrode, $E_{Ag/AgCl}$ is the potential of the reference electrode vs. the Standard Hydrogen Electrode (SHE), and E^0 is the standard electrode potentials for the reactions.

Before and after the EC treatment, electrochemical impedance spectroscopy (EIS) measurements were conducted at the open circuit potential in the frequency range of 0.1 Hz to 100 kHz with an amplitude of 10 mV. The double-layer capacitances were evaluated from the Nyquist plots by fitting the system with an $R_1(R_2C)$ circuit using Nova Software (version 1.10), where C represents the double-layer capacitance of the samples. The values of the Electrochemical Surface Area (ECSA) were estimated by dividing the values of the double-layer capacitance with the constant value of specific capacitance for ideally flat surfaces in acidic solution (35 μF cm^{-2}).[31] The corresponding roughness factors were then calculated dividing the values of ECSA with the values of geometric area of the electrodes.

2.2.3. Online electrochemical mass spectrometry (OLEMS)

OLEMS measurements were carried out in a three-electrode EC cell in a configuration similar to the one described above. RuO_2(110)/Ru(0001) single crystals were mounted into the PEEK sample holder with a bottom contact and used as working electrodes. The holder was additionally covered by several layers of Teflon™ tape (Swagelok) to prevent electrolyte interaction with the contact wire. EC treatment was performed using an Ivium Compactstat potentiostat (Ivium Technologies). OLEMS measurements were conducted with a quadrupole mass spectrometer (Balzers Quadstar, Prisma QME 200) at an operating pressure of approximately $5 \cdot 10^{-7}$ mbar. A more detailed description of the utilized OLEMS setup is given elsewhere.[30,32] In order to evaluate the onset potentials of OER and CER and to derive Faraday plots (see Appendix A for details), OLEMS measurements were conducted in 0.5 M H_2SO_4 and 0.5 M HCl, respectively. In the case of 0.5 M H_2SO_4, potential pulses (duration 10 s) were alternated with pulses at the resting potential (t = 90 s, E = +0.70 V). Ion currents of m/z = 32 (O_2^+) and m/z = 34 ($H_2O_2^+$) were continuously recorded throughout the experiment. The resting time was necessary to achieve temporal separation of individual OLEMS peaks. A similar procedure was applied in 0.5 M HCl with a slightly different duration and value of the resting potential (E = +0.80 V, 300 s). In CER, a longer resting time was necessary due to an increased tailing time of Cl_2 in the OLEMS system. The presence of HCl^+ and Cl^+ rather than Cl_2^+ signals in the mass spectrometer points to dissociation of Cl_2 and recombination with H^+ from water, the main component in the mass spectrometer vacuum chamber.[30]

2.2.4. Surface X-ray scattering

Fresh and EC-treated model electrodes were characterized by surface X-ray scattering (SXS) techniques. Ex-situ SXS measurements were performed at the surface diffraction beamline ID03 of the European Synchrotron Radiation Facility (ESRF, Grenoble, France). In this study, we utilized hard X-ray radiation with an energy of 22 keV (λ = 0.564 Å) focused to a spot size of 370 µm × 30 µm (horizontal × vertical relative to the plane of the sample surface) at the sample position. The measures were conducted using a reference surface unit cell based on the Ru hcp primitive unit cell, where the h and k vectors are laying parallel to the sample surface and l is normal to the surface and the lattice parameters are: a = b = 2.706Å, c = 4.282Å, α = β = 90°, γ= 120°. All the diffraction data reported in this work are referred to as the reciprocal space coordinates of such a cell. Structure and crystallinity were evaluated by recording the diffracted intensities along in-plane (*h* scans) and out of plane crystallographic directions (*l* scans) at the positions of Ru(0001) and RuO_2(110) crystal truncation rods (CTRs). XRR (X-ray reflectivity) measurements were used to evaluate surface roughening. The experiments were conducted using a MAXIPIX[33] installed on the diffractometer arm at a distance of 709 mm from the sample. Visualization, data reduction and fitting of the SXS data were done by the BINoculars script and PyMCA software. Measurement errors were determined from the noise level of the separate patterns.

2.2.5. Other characterization methods

XPS measurements of as-prepared samples were carried out on a SPECS XPS spectrometer equipped with a monochromatic small-spot (300 µm) X-ray source, an Al anode (Al *K*α = 1486.6 eV) and a 180° double-focusing hemispherical analyzer working with a 144-channel delay-line detector. The background pressure inside the analysis chamber was kept below 10^{-8} mbar. No additional charge neutralization was applied due to the metallic conductivity of the Ru(0001) substrates. High-resolution and survey spectra were recorded at constant pass energies of 20 eV and 40 eV, respectively. Spectra were calibrated by setting the binding energy of the Ru^0 ($3d_{5/2}$) component equal to 280.1 eV.[34] XPS spectra were taken at different positions on the surface to average the obtained quantitative results. LEED patterns were recorded with a 4-grid LEED optics (SPECS GmbH) integrated into the UHV preparation chamber of a SPECS NAP-XPS system.

XPS measurements of tested samples were carried out on a K-Alpha XP spectrometer (Thermo Scientific). A different spectrometer was used to allow mapping of the surface with a built-in top-view video microscope. Differences from the previously described XPS machine include spot size (400 µm), number of delay line detector channels (128) and pass energy (50 eV for high-resolution spectra, 200 eV for survey spectra).

Non-contact (tapping mode) atomic force microscopy (AFM) measurements were carried out on an NT-MDT Next microscope. Micrographs were recorded using gold-coated Si probes with a curvature radius of 10 nm (NSG10, NT-MDT). Scanning electron micrographs (SEM) and energy-dispersive X-ray spectra (EDXS) were taken on a FEI Quanta 3D FEG microscope at an accelerating voltage of 15 kV without any additional coating of the surface.

Inductively Coupled Plasma Optical Emission Spectrometry (ICP-OES) measurements were performed on a SPECTROBLUE EOP spectrometer equipped with an axial plasma source (Ar). The sample uptake rate was set to 2 mL/min. The emission intensity of dissolved Ru ions was measured at 240.3 and 267.9 nm.

2.3. Results and Discussion

2.3.1. Preparation of fresh RuO_2(110)/Ru(0001) model electrodes

Single crystal RuO_2(110)/Ru(0001) model anodes were prepared by thermal oxidation according to a procedure described elsewhere.[30] Ru(0001) single crystals were repeatedly subjected to a sequence of sputtering/annealing steps followed by a roasting procedure prior to thermal oxidation to RuO_2. The cleanliness of the Ru(0001) single crystals was evaluated by LEED. RuO_2(110) was prepared by thermal oxidation of Ru(0001) at T = 380°C and $p(O_2) = 3 \cdot 10^{-5}$ mbar for 120 min until LEED revealed the disappearance of Ru(0001) reflections and the appearance of three rotational domains characteristic for RuO_2(110) (Figure 2.1).[30] Then, crystals were UHV-transferred to a SPECS XP spectrometer connected to the preparation chamber and both Ru 3d and survey XP spectra were recorded. Both spectra contain only Ru^0 and RuO_2 -related peaks and no additional (in)organic impurities were observed (Figure 2.2a, b). The analysis of the Ru 3d spectra (Figure 2.2b) shows the presence of three doublets attributable to Ru^0 (BE(Ru $3d_{5/2}$) = 280.1 eV), RuO_2 (BE(Ru $3d_{5/2}$) = 280.7 eV) and RuO_2 shake-ups (BE(Ru $3d_{5/2}$) = 282.5 eV).[34] Based on these three components, the RuO_2 related species amount to 63.4 ± 0.9 at% and 47.7 ± 0.8 at% of the total Ru $3d_{5/2}$ peak area for the two different RuO_2(110)/Ru(0001) samples, respectively. The observed difference in the RuO_2 component areas for the two crystals likely relates to the presence of differently thick RuO_2(110) layers. The first sample was subsequently used for CER and the second for OER experiments. Considering the XPS probing depth of a few nm in the measured range of binding energies (BE), the composition corresponds to surface RuO_2 while some bulk Ru^0 remains visible. The thickness of the thermally grown RuO_2(110) layer is estimated to be similar to reported values.[35] SEM analysis of Ru(0001) surface before

and after oxidation shows an absence of any noticeable microscopic (µm scale) defects (Figure 2.2c, d).

AF micrographs (Figure A1a-d) show the presence of agglomerates of flat islands (CER fresh sample) or petals (OER fresh sample). The difference in morphology can be explained by microscopic differences of the initial metal surfaces. However, since the LEED patterns of both oxide samples showed the same crystallographic phase (*i.e.* RuO_2(110)) while the reflexes of the Ru(0001) substrate being absent, we assumed to have prepared covering layers of RuO_2(110).

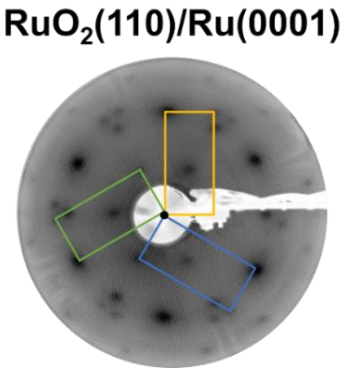

Figure 2.1. LEED pattern of as-prepared RuO_2(110)/Ru(0001) taken at 65 eV electron energy. The rectangles display the rotational domains of RuO_2(110).

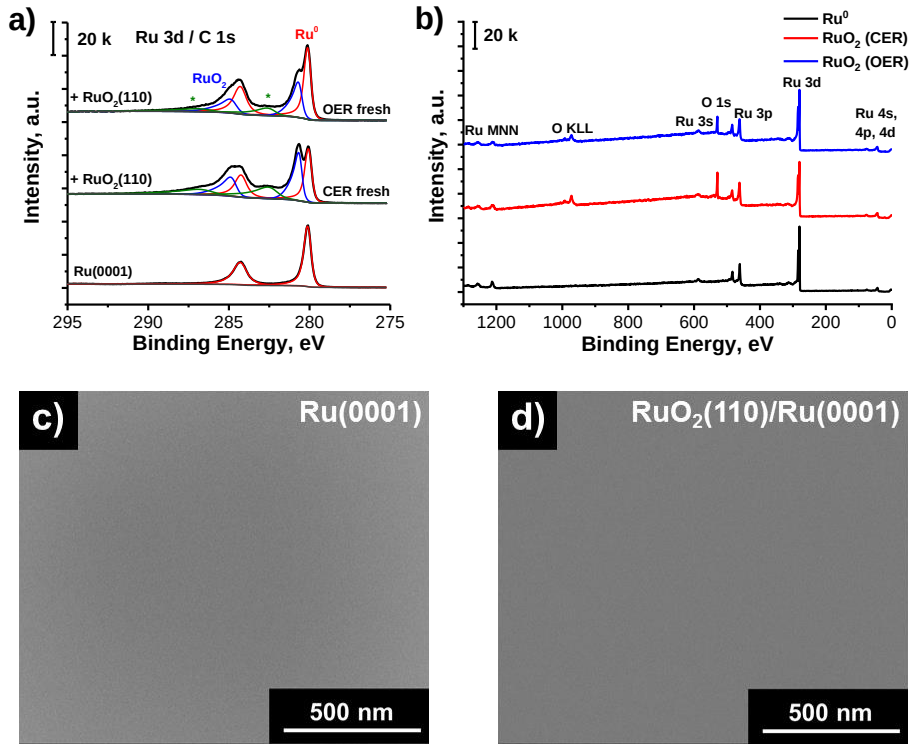

Figure 2.2. a) Ru 3d and b) survey XPS spectra of sputter-cleaned Ru(0001) and as-prepared RuO_2(110)/Ru(0001); c, d) corresponding SEM images of the surfaces.

2.3.2. CER and OER performance of RuO_2(110)/Ru(0001)

The performance and selectivity of the RuO_2(110)/Ru(0001) model anodes were evaluated using on-line electrochemical mass spectrometry (OLEMS) in 0.5 M H_2SO_4 and 0.5 M HCl solutions. The results of the OLEMS measurements can be represented as a three-dimensional plot which reports the gas production versus the charge and the applied potential (Figure A2). The two-dimensional plots of gas production versus charge, the so-called Faraday plots, shown in the main text, are projections of those 3D plots. Each data point belongs to a separate potential applied. Faraday plots can be used for the detection of side-reactions, such as electrode degradation and formation of by-products.[36] In the ideal case of a single reaction on a stable electrode, the amount of detected gaseous product is directly proportional to the passed charge, according to the Faraday law of electrolysis. Assuming a constant gas collection efficiency, a change in the slope of the Faraday plot α

can be attributed to the presence of side-reactions which contribute to the measured faradaic charge, resulting in a decrease of the faradaic efficiency (FE) of the main reaction.

In 0.5 M H_2SO_4, where OER is expected to be the dominant reaction, oxygen was first detected at +1.45 V (η = 220 mV) during a positive potential scan (Figure 2.3a). The entire data set is reported in Figure A3. Upon further increase of the potential, a proportional increase in O_2 production was observed in line with Faraday's law (Figure 2.3b). However, at E > +1.53 V, the charge spent in the O_2 production decreased nearly two times, as can be seen from the change of α. This can be attributed to the onset of electrochemical oxidation of RuO_2 to RuO_4 (*2.1*), which is expected to start at the critical potential.[22] In the studied model system RuO_2(110)/Ru(0001), the metallic substrate will be exposed subsequently, opening new routes of corrosion, as we discuss later in the text. The fact that the OLEMS-measured value of the critical potential is more positive than the values obtained from radiochemical analysis[6] can be explained by the lower sensitivity of OLEMS. To exclude the possibility that H_2O_2 formation contributed to the observed decrease in O_2 production, we monitored its signal (Figure 2.3c). H_2O_2 formation was detected by OLEMS at $E \geq$ +1.49 V, which is below the observed critical potential,[37,38] and its Faraday plot shows a comparable change in the FE as it was observed for O_2. This result indicates that H_2O_2 production was also affected at the critical potential, and hence can be excluded as the main reason for the observed change of Faraday slope.

The OER performance was further evaluated by a Tafel plot analysis (Figure 2.3d). The OLEMS-based Tafel plot was constructed from the potential-dependent O_2^+ (m/z = 32) ion current.[24] Unlike current density, the OLEMS m/z = 32 signal is specific for O_2 only and does not account for products of possible side-reactions, such as RuO_2 oxidation. Tafel slopes of both current- and OLEMS-derived Tafel plots were found to match: the value of 40 mV/dec indicates that a second-electron transfer-process is the rate-determining step of the OER,[39] and no deviations due to surface rearrangement are observed.[40] A value of 40 mV/dec is intermediate between Tafel slopes expected for RuO_2(110) (~60 mV/dec)[39,41] and metallic Ru (30 mV/dec),[20,42] indicating that the exposure of the underneath substrate to the electrolyte took place, as we will discuss further below.

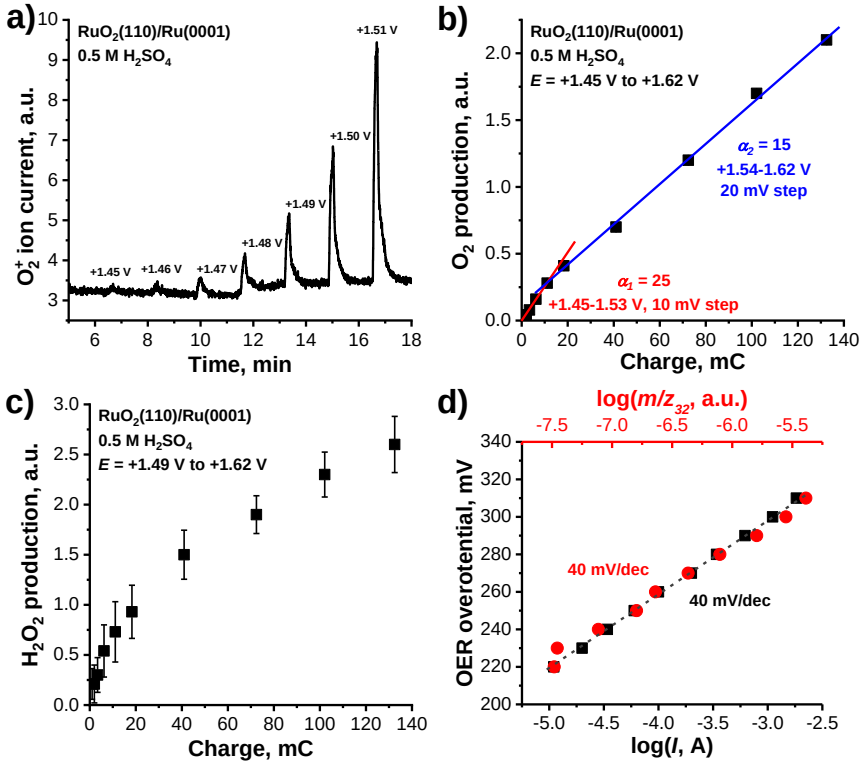

Figure 2.3. Potential-dependent ion currents of a) O_2^+ (m/z = 32) and corresponding Faraday plots of b) O_2 and c) H_2O_2 evolution; d) Tafel plots derived from voltammograms (black) and m/z = 32 (O_2^+) ion current (red) yelding similar Tafel slopes. All plots correspond to RuO_2(110)/Ru(0001) subjected to anodic potential pulses in 0.5 M H_2SO_4.

A similar testing protocol was applied to RuO_2(110)/Ru(0001) in 0.5 M HCl, where Cl_2 evolution is expected to occur along with OER. Indeed, Cl_2 gas was detected for $E \geq +1.44$ V (η_{CER} = 80 mV), which matches well with the reported values of the CER onset potential for RuO_2 (Figure 2.4a).[6,43] In the presence of Cl^-, O_2 evolution was only observed at $E \geq +1.50$ V (η_{OER} = 270 mV) which is 50 mV more positive than the OER onset potential in 0.5 M H_2SO_4 (Figure 2.4a, c). The origin of this shift has to be found in the competitive adsorption of Cl^- ions on the on-top oxygen species on undercoordinated Ru atom (Ru-O_{ot}), which is regarded as the active surface phase on RuO_2(110) for both the CER and OER.[41] The start of the competition between these two reactions can also be observed in the corresponding Faraday plots of Cl_2 and O_2. In the Cl_2 Faraday plot (Figure 2.4b), we can observe a change in the slope similar to the case of O_2 production in 0.5 M H_2SO_4. While the change is located

at a similar potential as in the previous experiment, the onset of OER is shifted anodically. This observation indicates that the onset of RuO_2 dissolution is not affected by the OER rate. Unfortunately, we were not able to evidence a change in the O_2 Faraday plot in the 0.5 M HCl experiment, because of the insufficient number of points between the onset of OER and the critical potential, caused by the later onset of OER in this case.

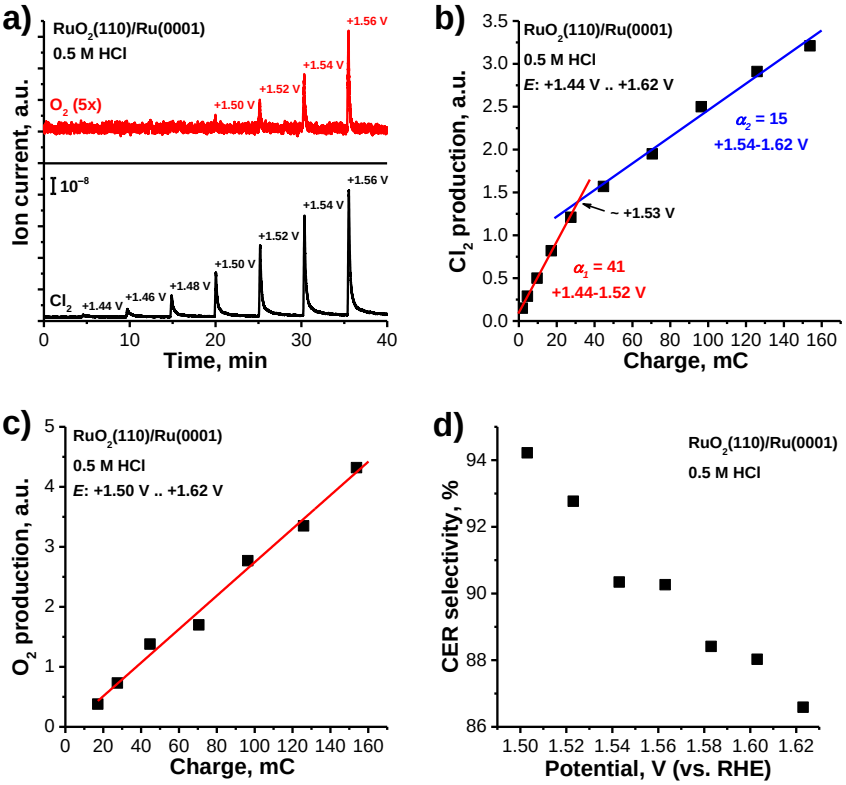

Figure 2.4. a) O_2^+ (*m/z* = 32) and $H^{35}Cl^+$ (*m/z* = 36) ion currents and corresponding Faraday plots of potential-dependent b) Cl_2 and c) O_2 evolution under applied anodic pulses recorded on RuO_2(110)/Ru(0001) in 0.5 M HCl; d) estimated selectivity of the CER vs. OER as a function of applied potential.

A discrepancy regarding the correlation between the RuO_2 corrosion and OER is present in the literature, where some works found their onset potentials should necessarily coincide,[26,44] while in other more recent papers OER and RuO_2 dissolution were not found to be in tradeoff correlation.[27,45,46] In our experiments, we show that the onset potential of

the OER is not necessarily matching this critical potential. For instance, the onset potential of OER can be shifted by increasing selectivity towards CER, while at the same time the critical potential remains independent from the major reaction (Table 2.1). Thus, we conclude that the critical potential for RuO_2 corrosion and the onset potential of the OER are not linked to each other. Our results support the conclusion of Hodnik et al.[27] that the onsets of OER and of RuO_2 dissolution do not coincide.

Table 2.1. Dependence of the critical potential on OER/CER selectivity and the OER onset potential.

[a]OER selectivity = $\frac{\text{OLEMS signal}(O_2)}{\text{OLEMS signal}(O_2)+\text{OLEMS signal}(Cl_2)}100\%$

	0.5 M HCl	**0.5 M H_2SO_4**
Onset potential of Cl_2 production, V	+1.44	n/a
Onset potential of O_2 production, V	+1.50	+1.45
Critical potential, V	+1.53	+1.53
OER selectivity[a] at *E* = +1.53 V, %	< 8	~98

Because of the presence of the metallic Ru substrate in our system the corrosion mechanism at higher potentials involves two corrosion routes: the dissolution of RuO_2 and, at the same time, the dissolution of metallic Ru.[28] When metallic Ru gets exposed, the dissolution can be accelerated, as reported in previous works,[47] because corrosion, in this case, can also take place as a result of direct anodic dissolution of the Ru metal.[27]

The potential-dependent CER selectivity was found to decrease by 5.9 ± 0.4% per 0.1 V at *E* > +1.50 V (Figure 2.4d). It should be noted that, for a more accurate assessment of the electrode selectivity, the actual RuO_2 corrosion rate must be taken into account, which could be achieved by complementary online ICP-MS measurements.[15,28,48]

2.3.3. Stability of RuO_2(110)/Ru(0001) under CER and OER

In order to study the stability of the model electrodes with respect to the dominant reaction being either OER or CER, a potentiostatic treatment was conducted in 0.5 M H_2SO_4 and 0.5 M HCl, respectively. In both cases, the electrodes were mounted in a hanging-meniscus

configuration to avoid contact of electrolyte with the sides of the crystals and subjected to a potentiostatic treatment (E = +1.50 V) for 60 min (Figure A4). A variety of different characterization techniques was utilized before and after the electrochemical treatment to evaluate structural, morphological and compositional changes of the model electrode surfaces.

Diffracted intensities along the (10*l*) rod of RuO_2 films were recorded for the fresh and tested electrodes. From the variation of the intensities of the Bragg reflections of the film along the *l* direction, it is possible to extract information about the impact of the EC treatment on the out-of-plane domain size of the RuO_2 crystallites composing the RuO_2(110) film (Figure 2.5a and Table 2.2). The FWHM of the relevant reflections was used to determine the out-of-plane crystallite domain size (*i.e*. the thickness of the RuO_2(110) films) via the Scherrer equation (see equation A3). These sizes were determined to be 2.0 ± 0.1 nm and 1.7 ± 0.1 nm for the samples exposed to testing in HCl and H_2SO_4, respectively, and remained nearly unaffected by the EC treatment.[35] The difference in the thickness of the RuO_2(110) layers in the fresh crystals is in line with XPS spectra (Figure 2.2a), which pointed at a higher oxide content on the crystal used in the CER experiment. The comparison of the results between fresh and tested samples indicate an overall preservation of the RuO_2(110) thickness upon electrochemical treatment.

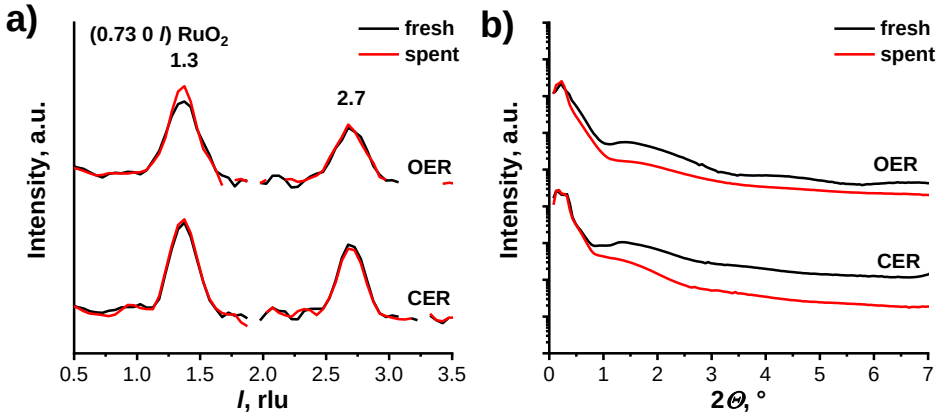

Figure 2.5. a) Diffracted intensity of RuO_2 film along the (10*l*) rod, recorded at (0.73 0 *l*) respect to the Ru(0001) surface unit cell and b) XRR profiles of fresh and treated RuO_2(110)/Ru(0001) electrodes.

Table 2.2. RuO_2(110) crystallographic changes upon EC treatment.

RuO_2(110)	CER (0.5 M HCl)		OER (0.5 M H_2SO_4)	
	fresh	spent	fresh	spent
Crystallite size[a] (out-of-plane, *l*), nm	2.0 ± 0.1	2.0 ± 0.1	1.7 ± 0.1	1.8 ± 0.1

[a] Determined from the FWHM of RuO_2 (110) peak.

XRR experiments allow determining the roughness of the samples independently from their crystallinity. While the intensity along the RuO_2 rod remains largely unchanged upon EC treatment, XRR data presented in Figure 2.5b show a slightly increased roughness of the surface, as evident from a steeper decrease of the reflectivity profiles of the spent electrodes accompanied by a decrease of Kiessig fringes.[49] From the minima and maxima positions in the XRR plots, the RuO_2(110) layer of the CER sample was found to be slightly thicker than that of the OER sample. Along the same lines, preservation of the RuO_2(110) phase is visible in *hk* maps (Figure A5 and Figure A6a, b). Taken the SXS and XRR results together, we can conclude that, apart from the expected degradation of RuO_2(110)/Ru(0001) model electrodes under OER and CER conditions, most of the RuO_2(110) layer is stable.

The SE micrographs of the spent electrodes (Figure 2.6a-d) reveal the presence of features with an average diameter of 1 µm on the surfaces of the tested electrodes, differently from the surfaces of the samples prior to the electrochemical treatments (Figure 2.2c, d). These features appear in the form of pits with a hole in the middle of each individual feature, which are assumed to be the centers of the initial corrosion. The islands are prone to form agglomerates located mostly along with defect sites of the crystal (*e.g.* nano-scratches, centers of mismatch between rotational domains of RuO_2(110)).[50] These features were observed both in HCl and H_2SO_4. However, the area of the surface covered with such islands (R1) was found to be dependent on the performed EC treatment. Particularly, in the case of the OER treatment, 58 ± 3% of the electrode surface was found to be covered with islands, while for CER this was only 16.5 ± 0.6%. EDXS analysis of the chemical composition of both island-covered (R1) and island-free (R2) surfaces points towards higher O content in R1 relative to R2 (Figure A7a).

For the OER-treated sample, Ru 3d XPS spectra taken at R1 areas show a significantly higher RuO_2 to Ru ratio compared to that of R2. In the case of the OER treatment, an overall

increase of the RuO_2-related XPS peak area in contrast to the fresh electrode was found to be 17 ± 4% (R1) and 6 ± 2% (R2). The X-ray spot size of the XPS spectrometer was too large to distinguish between R1 and R2 of the CER-treated sample. Thus, the observed increase of RuO_2 peaks (2.3 ± 0.6%) was attributed to a combination of contributions from R1 and R2. As from the RuO_2 rods we observed a similar thickness of the RuO_2(110) layer, we can conclude that regions R1 correspond to corroded areas where an electrochemically grown, hydrous RuO_2 was formed (Figure 2.7). The analysis of the O 1s spectra of the corroded regions reveal an increased area of the hydroxyl-related component in respect of the fresh electrode, indicative of the hydrous nature of the oxide formed upon electrochemical treatment (Figure A7c, d).[51] We emphasize that this change is relatively small as most of the signal is arising from intact RuO_2 (110) still present in the corroded regions.

Morphology analysis of the spent electrodes by AFM confirms the presence of holes on both CER- and OER-treated samples. Particularly, loosely distributed pits with a depth variation of 20-120 nm were found on the surface of CER-treated sample (Figure A8a, c and Figure A9), while OER treatment yields a large number of smaller and shallower pits with an average depth of 6 ± 2 nm (Figure A8b, d). These pits can be attributed to the centers of corrosion previously observed in the SEM images (Figure 2.6a-d).

Elemental analysis of the electrolytes after electrochemical testing by ICP-OES showed that Ru dissolved from the anodes in both HCl and H_2SO_4. Overall Ru dissolution rates were determined and showed that the anode operated in H_2SO_4 resulted in a much higher dissolution rate (6.27 ± 0.08 $\mu mol \cdot h^{-1} \cdot cm^{-2}$) compared to the anode operated in HCl (3.01 ± 0.08 $\mu mol \cdot h^{-1} \cdot cm^{-2}$). This difference in dissolution rates is consistent with values found in the literature.[6] The amount of dissolved Ru detected with ICP-OES after exposing the samples for 1 hour at E = 1.50 V (1 and 5 µmol in the CER and OER experiments, respectively) is orders of magnitude higher than expected from the dissolution of the RuO_2(110) layer only, which would be less than 10 nmol. Thus, it is reasonable to state that the dissolution of bulk Ru(0001) has significantly contributed to the leaching of Ru by pitting corrosion. Moreover, the difference between OER and CER-caused Ru dissolution, measured by ICP-OES, was found to be smaller (2.1 x) than that estimated from the surface coverage of corroded domains (SEM, 3.6 x) (Table 2.3). The reason for this is that CER leads to the formation of fewer but deeper corrosion pits, as observed in the AFM profiles. The pitting corrosion mechanism, which led to the exposure of the underlying, is similar to what has been recently observed in the case of an IrO_2(110) layer deposited on RuO_2(110/Ru(0001) template under OER conditions.[52]

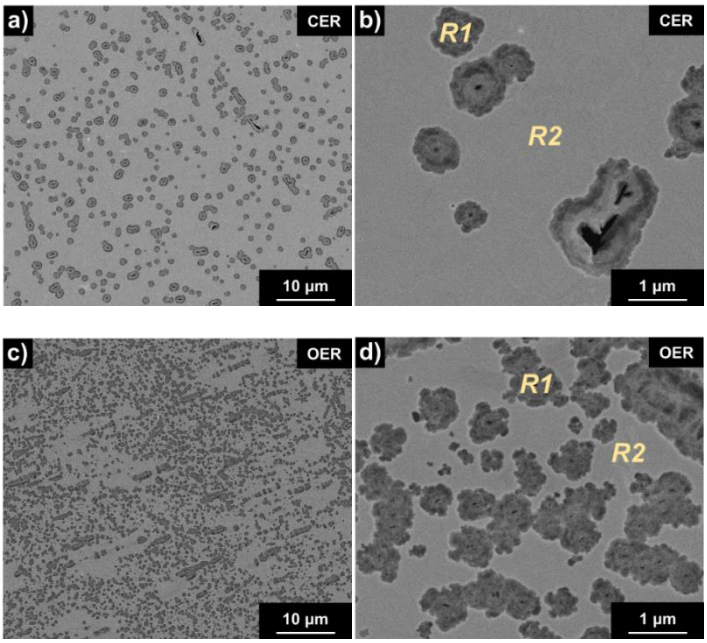

Figure 2.6. SE micrographs of RuO_2(110)/Ru(0001) electrodes treated at E = + 1.5 V for 60 min in a-b) 0.5 M HCl, c-d) 0.5 M H_2SO_4.

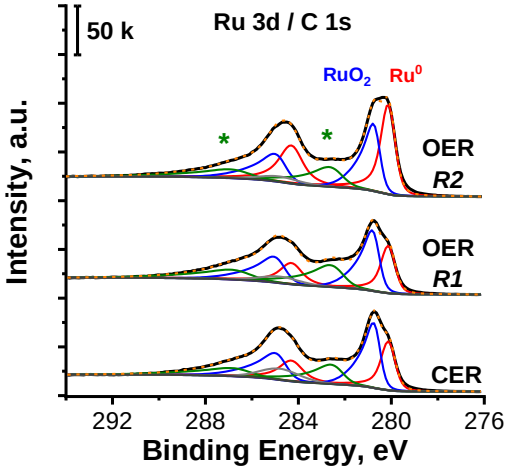

Figure 2.7. XPS spectra of combined Ru 3d/C 1s region of the spent electrodes. Components denoted with * represent the satellite peaks of RuO_2.

Table 2.3. Estimation of Ru leaching based on ICP-OES and SEM results.

	CER (0.5 M HCl)	**OER (0.5 M H_2SO_4)**	**Ratio OER/CER**
Corroded area[a] (R1, SEM), %	16 ± 1	58 ± 3	3.6
Ru dissolution rate (ICP-OES), µmol·h^{-1}·cm^{-2}	3.01 ± 0.08	6.27 ± 0.08	2.1

[a] Area covered with corrosion domains (Figure 2.6).

UV-Vis spectra of the spent electrolytes suggest that etched Ru is most likely present in form of Ru(III) chloride aqua complexes with the general formula $[RuCl_n(H_2O)_{6-n}]^{(3-n)+}$ as well as (per)ruthenates, in the case of CER and OER, respectively (Figure A10).[26,29,53–55] Thus, ICP-OES and UV-Vis analyses confirm the electrochemically induced ruthenium leaching at the critical potential, which is likely the reason for the change in the faradaic efficiency of both OER and CER observed by OLEMS.

In order to relate the long-term stability of the model electrodes at the critical potential ($E_{crit.}$ = +1.50 V) with their EC activity, a sequence of anodic pulses was applied, while measuring the gas evolution by OLEMS. By combining these data with the results described above, we can correlate the stability of the model RuO_2(110)/Ru(0001) anodes with their activity. For both types of acidic electrolytes, similar dependencies were observed (Figure 2.8a, b). Firstly, repeated potential pulsing led to an increase of the electrocatalytic activity of the electrode reflected in a current increase. Secondly, both Cl_2 and O_2 production increased roughly proportionally with the current, in accordance with Faraday's law. The correlation between gas production and total charge points towards constant selectivity of the major reaction at constant potential. From this, we can conclude that the corrosion rate was not changing over time and is only altered by changing the potential. A similar conclusion was drawn for the corrosion of IrO_2(110) on RuO_2(110)/Ru(0001) in H_2SO_4 solution.[56]

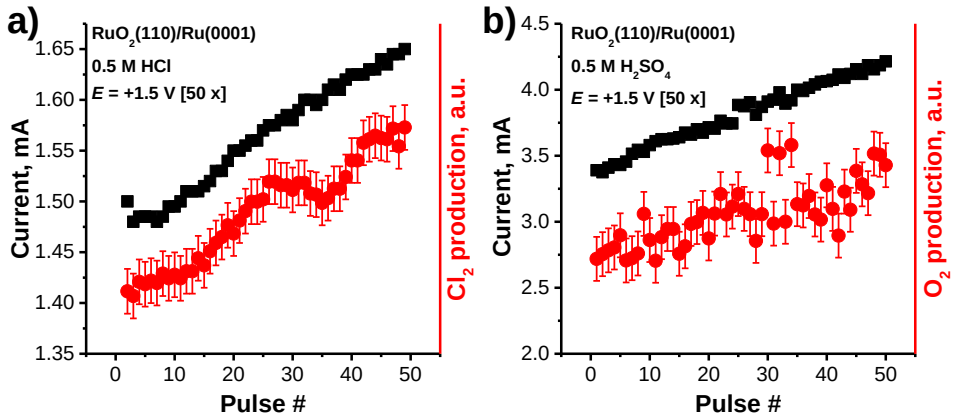

Figure 2.8. Electric current and gas production probed under repeated potential pulsing at +1.50 V in a) 0.5 M HCl (product - Cl_2) and b) 0.5 M H_2SO_4 (product - O_2).

An increase of electrode performance, observed in the form of the proportionally increasing current and gas production, can be caused either by an increase of the surface area or by the formation of catalytic sites with higher activity (*e.g.* Ru^0 or electrochemically grown oxide). Higher values of the double-layer capacitance and of the calculated Electrochemical Surface Area (ECSA) were indeed observed in the electrodes after being exposed for 1 h at 1.50 V in 0.5 M HCl and 0.5 M H_2SO_4 (Table 2.4). These results can be interpreted as an increase of the roughness factor after the electrochemical treatments (particularly in the case of the sample tested in 0.5 M H_2SO_4), supporting the results of XRR, AFM, and SEM, which highlighted an increased roughness of the spent electrodes. However, we highlight that the formation of hydrous oxide formed in the pits of corrosion could also contribute to higher the values of the capacitance of the tested samples with its enhanced proton mobility.[50] The increased capacitive current is also reflected in the CVs of the tested samples, especially in the case of H_2SO_4 electrolyte (Figure A11). We can neglect the impact of metallic Ru on the observed increase in the catalytic activity since it would rapidly oxidize at E = +1.50 V.[6,57] Indeed, no Ru^0 related peaks were observed in the CV scans of the tested electrodes (Figure A11a, b).[58] Apart from the larger roughness, the increase in the catalytic activity during time can also be a consequence of the observed formation of electrochemically grown hydrous RuO_2, which is reported to be more active than thermal RuO_2.[27]

Table 2.4. Values of double-layer capacitance and roughness factors of the samples.

	CER (0.5 M HCl)	**OER (0.5 M H_2SO_4)**
Double-layer capacitance, µF	15 (fresh) 92 (tested)	24 (fresh) 334 (tested)
Roughness factor	1.12 (fresh) 6.84 (tested)	0.87 (fresh) 12.15 (tested)

2.4. Conclusions

RuO_2(110)/Ru(0001) single crystal model electrodes were prepared and employed for the evaluation of the stability of RuO_2(110) under acidic CER and OER conditions in 0.5 M HCl and 0.5 M H_2SO_4 electrolytes, respectively. The onset potential of OER is shifted to higher anodic potentials in HCl electrolyte due to the competing CER, while at the same time the critical potential (*i.e.* the onset of RuO_2 oxidation) remains independent from the primary electrochemical reaction, indicating that OER and RuO_2 dissolution are not coupled.

When electrodes were subjected to the critical potential, a significant dissolution of Ru was observed by elemental analysis of the electrolyte after testing. Pitting corrosion of bulk Ru(0001) can be considered as the main source of dissolved Ru. Despite the observed dissolution, electrode corrosion was found to be accompanied by the growth of hydrous RuO_2 due to exposure of the bulk Ru(0001) substrate upon the corrosive treatment. Morphology evaluation of spent electrodes reveals that the corroded areas correspond to the formation of micrometer-sized features (pits), which contain a sub-micrometer pit in the center surrounded by randomly oriented flat petals. The corroded areas revealed significantly higher O content and a higher RuO_2/Ru ratio, indicating an additional growth of electrochemically grown, i.e. hydrous, RuO_2. ICP-OES, SEM, XPS, and EDX analyses all confirmed that the degree of corrosion was higher in the OER case (in H_2SO_4) than in the CER case (in HCl), because the latter reaction reduces the faradaic efficiency of O_2 formation as well as anodic RuO_2 oxidation. The areas not covered with pits showed a similar RuO_2/Ru ratio compared with the fresh samples, indicating that the homogeneous RuO_2(110) layer protects the underlying Ru(0001) from fast corrosion, and its thickness remains to a large extent unchanged after the electrochemical treatment (as seen from the RuO_2 *I*-scans). The mechanism of RuO_2(110)/Ru(0001) corrosion is proposed to consist of the following steps. Initially, the surface of RuO_2(110) starts dissolving at the critical potential by the formation

of anionic Ru compounds in a higher oxidation state, preferably at surface defects (such as points where rotational domains of RuO_2(110) meet). Then, the corrosion of the RuO_2(110) layer causes the exposure of the bulk Ru(0001) substrate, which is more prone to corrosion than the RuO_2(110) surface. Along with the dissolution, the exposed Ru(0001) is oxidized yielding the growth of additional hydrous RuO_2 in the corroded areas. We emphasize that our findings relate to the corrosion behavior of the RuO_2(110) layer on Ru(0001) system, while the corrosion of the underlying metallic substrate is observed as a side reaction and is only related to the nature of the model system. An inert substrate would be necessary to study the mechanism of corrosion of the RuO_2(110) overlayer separately from the underlying substrate.

2.5. References

(1) Trasatti, S. *Electrochim. Acta* **2000**, *45* (15–16), 2377–2385.

(2) Beer, H. B. *J. Electrochem. Soc.* **1980**, *127* (8), 303C-307C.

(3) Trasatti, S. *Electrochim. Acta* **1984**, *29* (11), 1503–1512.

(4) Reier, T.; Teschner, D.; Lunkenbein, T.; Bergmann, a; Selve, S.; Kraehnert, R.; Schlögl, R.; Strasser, P. *J. Electrochem. Soc.* **2014**, *161* (9), F876–F882.

(5) Schmittinger, P.; Florkiewicz, T.; Curlin, L. C.; Luke, B.; Scannell, R.; Navin, T.; Zelfel, E.; Bartsch, R. *Ullmann's Encyclopedia of Industrial Chemistry*; 2012.

(6) Karlsson, R. K. B.; Cornell, A. *Chem. Rev.* **2016**, *116* (5), 2982–3028.

(7) Fauvarque, J. *Pure Appl. Chem.* **1996**, *68*, 1713–1720.

(8) Moussallem, I.; Jörissen, J.; Kunz, U.; Pinnow, S.; Turek, T. *J. Appl. Electrochem.* **2008**, *38* (9), 1177–1194.

(9) Petrykin, V.; Macounova, K.; Shlyakhtin, O. A.; Krtil, P. *Angew. Chemie - Int. Ed.* **2010**, *49* (28), 4813–4815.

(10) Petrykin, V.; MacOunova, K.; Franc, J.; Shlyakhtin, O.; Klementova, M.; Mukerjee, S.; Krtil, P. *Chem. Mater.* **2011**, *23* (2), 200–207.

(11) Zeradjanin, A. R.; Menzel, N.; Schuhmann, W.; Strasser, P. *Phys. Chem. Chem. Phys.* **2014**, *16* (27), 13741–13747.

(12) Macounová, K.; Makarova, M.; Jirkovský, J.; Franc, J.; Krtil, P. *Electrochim. Acta* **2008**, *53* (21), 6126–6134.

(13) Petrykin, V.; MacOunová, K.; Okube, M.; Mukerjee, S.; Krtil, P. *Catal. Today* **2013**, *202* (1), 63–69.

(14) Comninellis, C.; Vercesi, G. P. *J. Appl. Electrochem.* **1991**, *21*, 335–345.

(15) Cherevko, S.; Zeradjanin, A. R.; Topalov, A. A.; Kulyk, N.; Katsounaros, I.; Mayrhofer, K. J. J. *ChemCatChem* **2014**, *6* (8), 2219–2223.

(16) Duby, P. *JOM* **1993**, *45* (3), 41–43.

(17) Trasatti, S. *Electrochim. Acta* **1991**, *36* (2), 225–241.

(18) Hine, F.; Yasuda, M.; Yoshida, T. *J. Electrochem. Soc.* **1977**, *124* (4), 500–505.

(19) Etzi Coller Pascuzzi, M.; Goryachev, A.; Hofmann, J. P.; Hensen, E. J. M. *Appl. Catal. B Environ.* **2020**, *261*, 118225.

(20) Iwakura, C.; Hirao, K.; Tamura, H. *Electrochim. Acta* **1977**, *22* (4), 329–334.

(21) Uzbekov, A. A.; Lambrev, V. G.; Yazikov, I. F.; Rodin, N. N.; Zabrodskaya, L. M.; Klement'eva, V. S.; Vlodov, Y. M. *Elektrokhimiya* **1978**, *14*, 1150–1159.

(22) Veselovskaya, I. E.; Khodkevich, S. D.; Malkina, R. I.; Yakimenko, L. M. *Elektrokhimiya* **1974**, *10*, 74–77.

(23) Kötz, R.; Lewerenz, H. J.; Stucki, S. *J. Electrochem. Soc.* **1983**, *130* (4), 825.
(24) Wohlfahrt-Mehrens, M.; Heitbaum, J. *J. Electroanal. Chem. Interfacial Electrochem.* **1987**, *237* (2), 251–260.
(25) Fabbri, E.; Habereder, A.; Waltar, K.; Kötz, R.; Schmidt, T. J. *Catal. Sci. Technol.* **2014**, *4* (11), 3800–3821.
(26) Kötz, R.; Stucki, S.; Scherson, D.; Kolb, D. M. *J. Electroanal. Chem. Interfacial Electrochem.* **1984**, *172* (1–2), 211–219.
(27) Hodnik, N.; Jovanovič, P.; Pavlišič, A.; Jozinović, B.; Zorko, M.; Bele, M.; Šelih, V. S.; Šala, M.; Hočevar, S.; Gaberšček, M. *J. Phys. Chem. C* **2015**, *119* (18), 10140–10147.
(28) Cherevko, S.; Geiger, S.; Kasian, O.; Kulyk, N.; Grote, J. P.; Savan, A.; Shrestha, B. R.; Merzlikin, S.; Breitbach, B.; Ludwig, A.; Mayrhofer, K. J. J. *Catal. Today* **2016**, *262*, 170–180.
(29) Loučka, T. *J. Appl. Electrochem.* **1990**, *20* (3), 522–523.
(30) Sohrabnejad-Eskan, I.; Goryachev, A. E.; Exner, K. S.; Kibler, L. A.; Hensen, E. J. M.; Hofmann, J. P.; Over, H. *ACS Catal.* **2017**, *7*, 2403–2411.
(31) Goryachev, A.; Etzi Coller Pascuzzi, M.; Carlà, F.; Weber, T.; Over, H.; Hensen, E. J. M.; Hofmann, J. P. *Electrochim. Acta* **2020**, *336*, 135713.
(32) Wonders, A. H.; Housmans, T. H. M.; Rosca, V.; Koper, M. T. M. *J. Appl. Electrochem.* **2006**, *36* (11), 1215–1221.
(33) Ponchut, C.; Rigal, J. M.; Clément, J.; Papillon, E.; Homs, A.; Petitdemange, S. *J. Instrum.* **2011**, *6* (01), C01069–C01069.
(34) Morgan, D. J. *Surf. Interface Anal.* **2015**, *47* (11), 1072–1079.
(35) He, Y. B.; Knapp, M.; Lundgren, E.; Over, H. *J. Phys. Chem. B* **2005**, *109* (46), 21825–21830.
(36) Goryachev, A.; Gao, L.; Zhang, Y.; Rohling, R. Y.; Vervuurt, R. H. J.; Bol, A. A.; Hofmann, J. P.; Hensen, E. J. M. *ChemElectroChem* **2018**, *5* (8), 1230–1239.
(37) Gerischer, R.; Gerischer, H. *Zeitschrift für Phys. Chemie* **1956**, *6* (3_4), 178–200.
(38) Burke, L. D.; Murphy, O. J.; O'Neill, J. F.; Venkatesan, S. *J. Chem. Soc. Faraday Trans. 1 Phys. Chem. Condens. Phases* **1977**, *73*, 1659.
(39) Fang, Y. H.; Liu, Z. P. *J. Am. Chem. Soc.* **2010**, *132* (51), 18214–18222.
(40) Castelli, P.; Trasatti, S. *J. Electroanal. Chem.* **1986**, *210*, 189–194.
(41) Exner, K. S.; Sohrabnejad-Eskan, I.; Over, H. *ACS Catal.* **2018**, *8* (3), 1864–1879.
(42) Tamura, H.; Iwakura, C. *Int. J. Hydrogen Energy* **1982**, *7* (11), 857–865.
(43) Arikawa, T.; Murakami, Y.; Takasu, Y. *J. Appl. Electrochem.* **1998**, *28* (5), 511–516.
(44) Kotz, R.; Lewerenz, H. J.; Stucki, S. *J. Electrochem. Soc.* **1983**, *130*, 825–829.
(45) Danilovic, N.; Subbaraman, R.; Chang, K. C.; Chang, S. H.; Kang, Y.; Snyder, J.; Paulikas, A. P.; Strmcnik, D.; Kim, Y. T.; Myers, D.; Stamenkovic, V. R.; Markovic, N. M. *Angew. Chemie Int. Ed.* **2014**, *53* (51), 14016–14021.
(46) Zeradjanin, A. R.; Topalov, A. A.; Van Overmeere, Q.; Cherevko, S.; Chen, X.; Ventosa, E.; Schuhmann, W.; Mayrhofer, K. J. J. *RSC Adv.* **2014**, *4* (19), 9579.
(47) Danilovic, N.; Subbaraman, R.; Chang, K. C.; Chang, S. H.; Kang, Y. J.; Snyder, J.; Paulikas, A. P.; Strmcnik, D.; Kim, Y. T.; Myers, D.; Stamenkovic, V. R.; Markovic, N. M. *J. Phys. Chem. Lett.* **2014**, *5* (14), 2474–2478.
(48) Cherevko, S. *J. Electroanal. Chem.* **2017**, *787*, 11–13.
(49) Chason, E.; Mayer, T. M. *Crit. Rev. Solid State Mater. Sci.* **1997**, *22* (1), 1–67.
(50) Over, H. *Chem. Rev.* **2012**, *112* (6), 3356–3426.
(51) Krause, P. P. T.; Camuka, H.; Leichtweiss, T.; Over, H. *Nanoscale* **2016**, *8* (29), 13944–13953.
(52) Weber, T.; Pfrommer, J.; Abb, M. J. S.; Herd, B.; Khalid, O.; Rohnke, M.; Lakner, P. H.; Evertsson, J.; Volkov, S.; Bertram, F.; Znaiguia, R.; Carla, F.; Vonk, V.; Lundgren, E.; Stierle, A.; Over, H. *ACS Catal.* **2019**, *9* (7), 6530–6539.

(53) Chen, J.-Y.; Hsieh, Y.-C.; Wang, L.-Y.; Wu, P.-W. *J. Electrochem. Soc.* **2011**, *158* (8), D463.

(54) Mercer, E. E.; McAllister, W. A. *Inorg. Chem.* **1965**, *4* (10), 1414–1416.

(55) Connick, R. E.; Hurley, C. R. *J. Am. Chem. Soc.* **1952**, *74* (20), 5012–5015.

(56) Weber, T.; Ortmann, T.; Escalera-López, D.; Abb, M. J. S.; Mogwitz, B.; Cherevko, S.; Rohnke, M.; Over, H. *ChemCatChem* **2019**, *11*, 1–13.

(57) Pourbaix, M. *Atlas of electrochemical equilibria in aqueous solutions.*; Pourbaix, M., Ed.; Oxford, New York, Pergamon Press, 1966.

(58) Hadzi-Jordanov, S.; Angerstein-Kozlowska, H.; Vuković, M.; Conway, B. E. *J. Phys. Chem.* **1977**, *81* (24), 2271–2279.

Appendix A

Supporting information for Chapter 2

A.1. Atomic Force Microscopy (AFM) – fresh electrodes

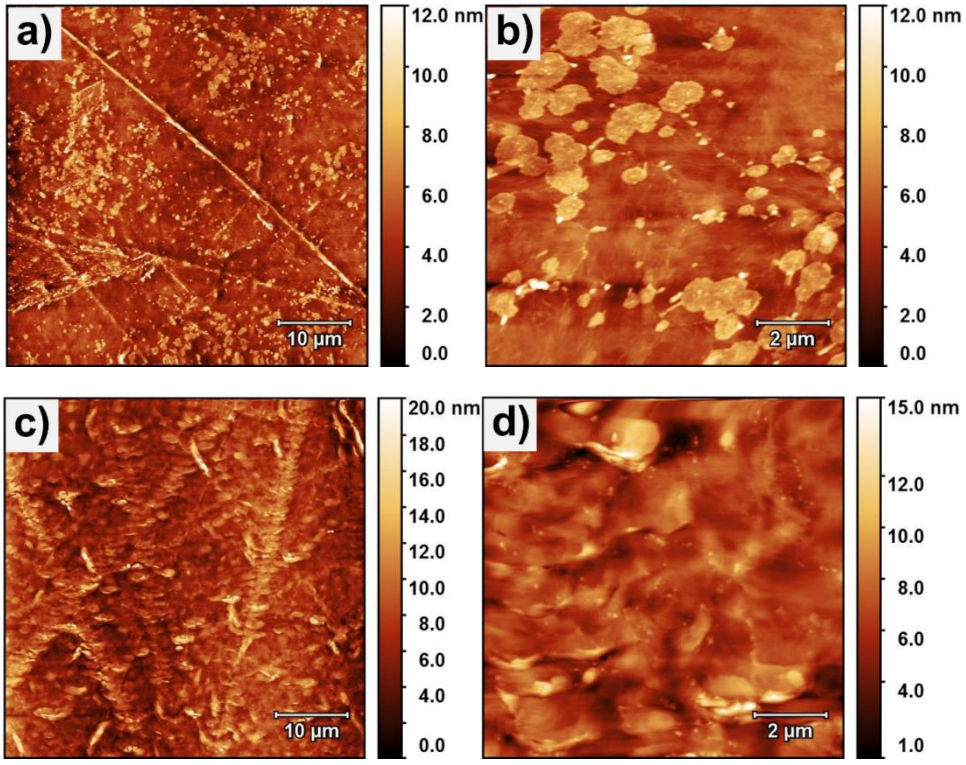

Figure A1. AFM images acquired in non-contact mode of as-prepared RuO_2(110)/Ru(0001) of a-b) CER fresh and c-d) OER fresh samples at different magnifications.

A.2. Online Electrochemical Mass Spectrometry (OLEMS)

The ion current of fragment *m/z* ($I_{m/z}$), observed in OLEMS, relates to the faradaic charge of a single reaction *i*, where *m/z* is the fragment of a product *i*, via the set of equations *A1a-c*. Equation (*A1a*) describes the dependence of the ion current on the partial pressure of the fragment *m/z* ($p_{m/z}$), and eventually its proportionality to the amount of product *i* (n_i). I_E is the electron emission current, λ_m is the mean free path of electrons, $s_{m/z}$ is the differential ionization parameter, γ_i is the pressure-to-amount conversion factor, β is the OLEMS collection efficiency. The collection efficiency depends on multiple parameters, such as: effective tip-to-WE distance, permeability of gases, porosity of membrane, etc. Due to its complexity, β of each OLEMS tip cannot be quantitatively determined apart from reaction. The Faraday's law of electrolysis (A*1b*) describes the proportionality between the faradaic charge supplied in a single faradaic reaction *i* (Q_i) and the amount of evolved product *i*. *z* is the number of electrons involved in the reaction and *F* is the Faraday constant. Combining equations (*A1a*) and (*A1b*) results in equation (*A1c*), which describes proportionality between faradaic charge of reaction *i* and the ion current of the fragment *m/z* detected by OLEMS. α is the proportionality constant.

$$I_{m/z} = \beta \cdot \gamma_i \cdot I_E \cdot \lambda_m \cdot p_{m/z} \cdot s_{m/z} \propto n_i \qquad (A1a)$$

$$n_i = \frac{Q_i}{zF} \qquad (A1b)$$

$$I_{m/z} \propto \alpha \cdot Q_i, \quad \text{where } \alpha = \frac{\beta \cdot \gamma_i \cdot I_E \cdot \lambda_m \cdot s_{m/z}}{zF} \qquad (A1c)$$

The results of such a pulse experiment performed with OLEMS can be reported via a three dimensional representation of the gas production versus the potential and the charge (see Figure A2a, b). The Faraday plots reported in the main text correspond to the projection of the gas production versus the charge at a given potential.

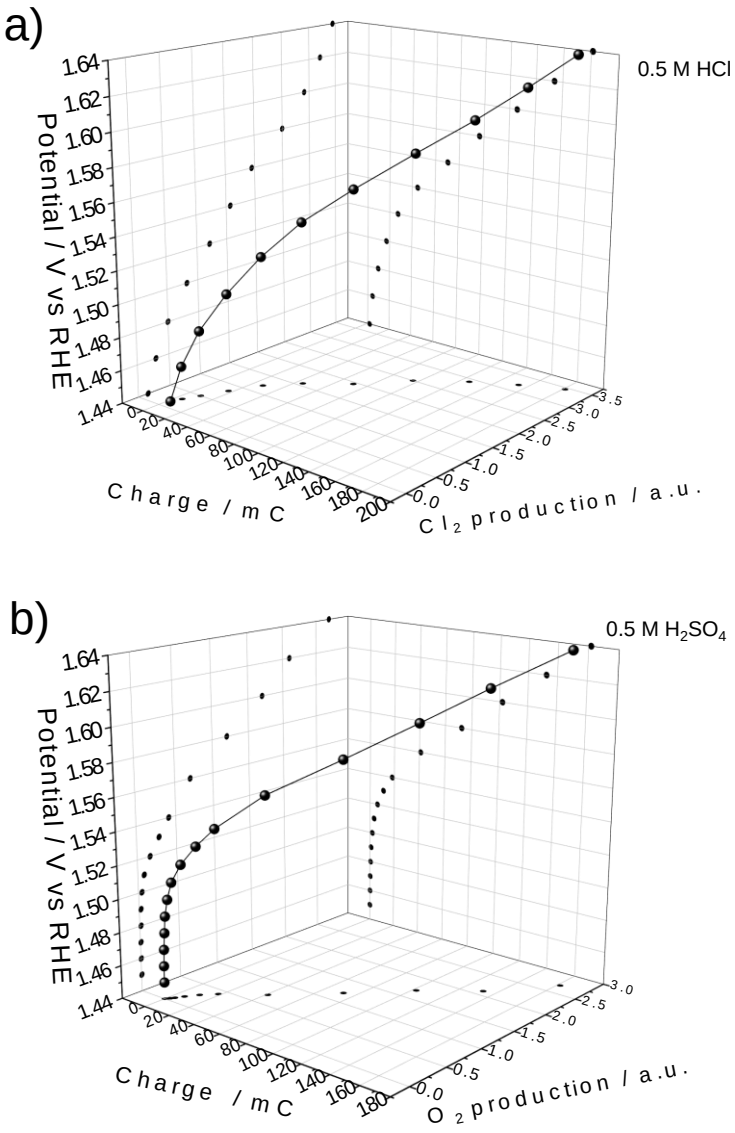

Figure A2. Three-dimensional representations of the results of OLEMS experiments conducted in a) 0.5 M HCl and b) 0.5 M H_2SO_4, which report the gas production versus the applied potential and charge.

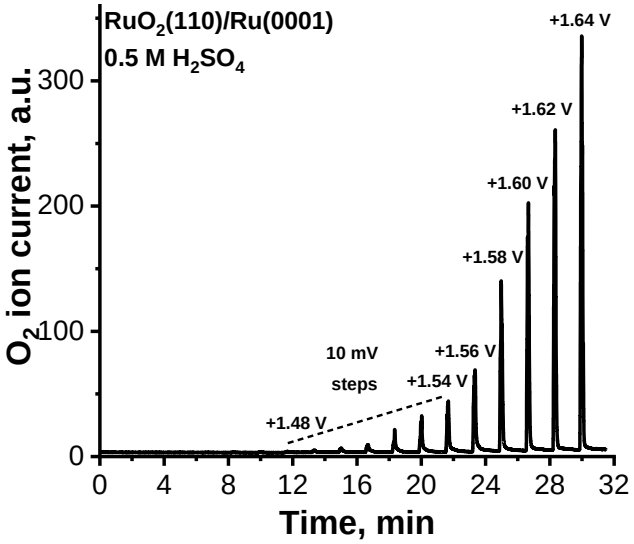

Figure A3. Potential-dependent ion currents of a) O_2^+ (*m/z* = 32) recorded for the sample RuO_2(110)/Ru(0001) subjected to anodic potential pulses in 0.5 M H_2SO_4. The onset potential of OER is better displayed in Figure 2.3a, which corresponds to a magnification of the left part of this figure.

The OER selectivity in the case of competitive CER/OER (Table 2.1, Figure 2.4d) was determined from the OLEMS data in the following way:

$$S_{OER} = \frac{100 * m/z_{32}}{m/z_{32} + m/z_{36} + m/z_{34}} \qquad (A2)$$

where *S* is the OER selectivity and m/z_i is the area of the fragment *i*. *i* = 32 corresponds to O_2^+, *i* = 36 corresponds to $H^{35}Cl^+$ and *i* = 34 corresponds to $H_2O_2^+$. Although this formula does not include all possible products of the involved faradaic reactions (*e.g.* Ru^0 and RuO_2 oxidation), it allows to evaluate how much faradaic charge was spent on formation of O_2 from all gaseous products.

A.3. Electrochemical treatment

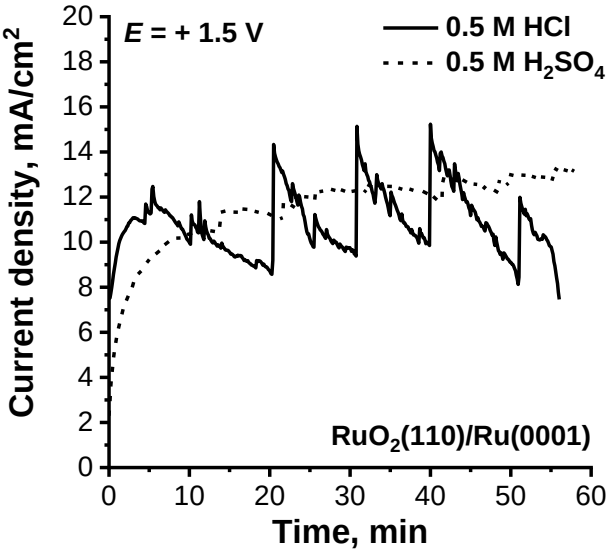

Figure A4. Chronoamperograms recorded on RuO_2(110)/Ru(0001) electrodes subjected to E = +1.5 V for 60 min in two different electrolytes. Currents are normalized on the geometric surface area of the electrodes. Variations in current density are caused by bubbles formation.

A.4. Surface X-ray Scattering

The Scherrer equation was used for determination of the crystalline size from SXRD patterns reported in Figure 2.5a:

$$d = \frac{K\lambda}{\beta cos\theta} \qquad (A3)$$

where: d = coherent diffraction domain size, λ = the wavelength of the X-rays, β = the reflection width (2ϑ), ϑ = the Bragg angle and K = the shape constant.

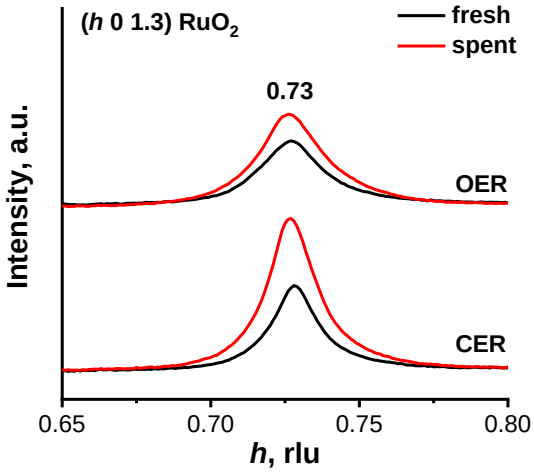

Figure A5. Diffracted intensity of RuO_2 film along the (*h* 0 1) rod recorded at (*h* 0 1.3) respect to the Ru(0001) surface unit cell.

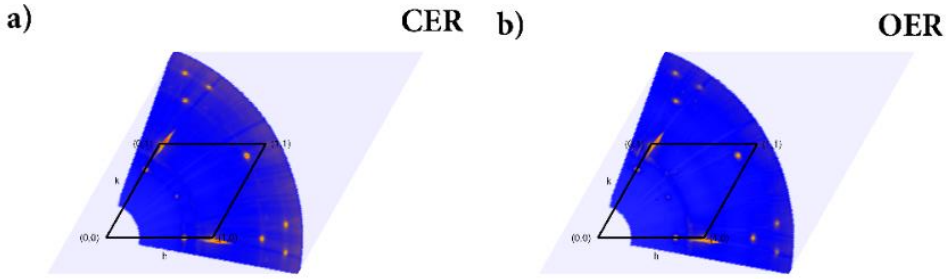

Figure A6. *hk* maps of RuO_2(110)/Ru(0001) electrodes treated at *E* = +1.5 V for 60 min in a) 0.5 M HCl, and b) 0.5 M H_2SO_4.

From the analysis of *hk* maps we can observe a preservation of RuO_2(110) phase (Figure A6a, b). This conclusion can be made based on the fact that the maps look similar to the initial LEED patterns (Figure 2.1). Particularly, we can observe the presence of RuO_2(110)-specific reflections (*e.g.* $H \approx 1.6 \pm 0.1$, $K \approx 0.0 \pm 0.1$ and $H = 0.73$, $K = 0.0$). A wide band at $H \approx 1.0$, $K = 0.0$ can be attributed to the polycrystalline Ru(0001) impurities which were also observed on the fresh single crystals.

A.5. X-ray Photoelectron Spectroscopy (XPS)

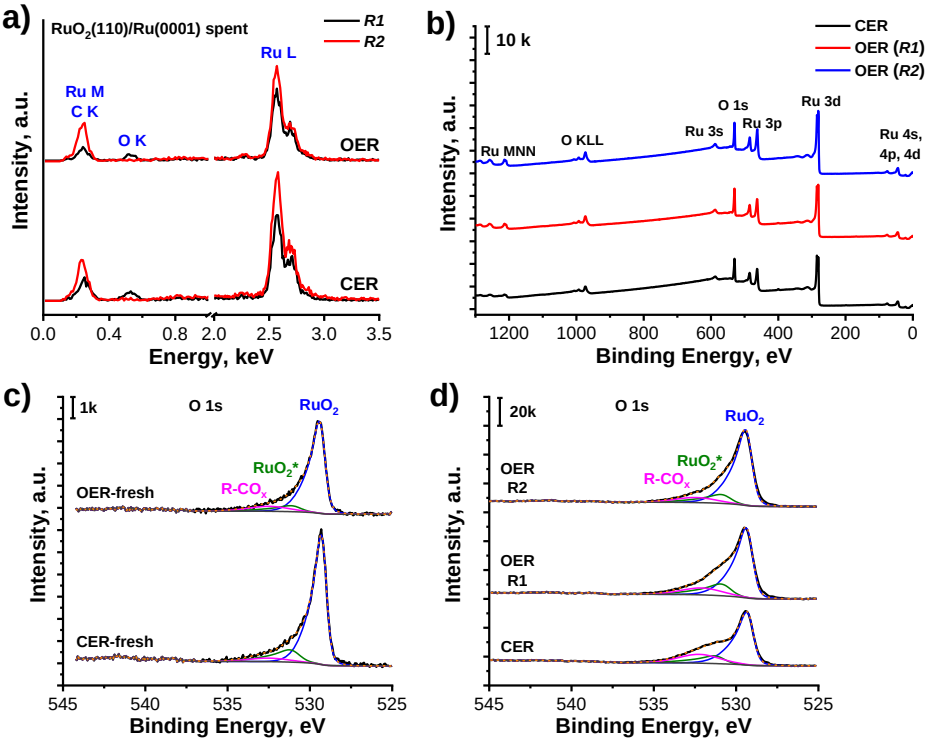

Figure A7. Spectroscopic analyses of the spent RuO_2(110)/Ru(0001) electrodes: a) EDX spectra, b) XPS survey; c) O 1s (fresh) and d) O 1s (spent) XPS spectra. Components denoted with * indicate the satellite peak of RuO_2 and OH-groups of hydrous RuO_2 (same binding energy).

A.6. Atomic Force Microscopy (AFM) – spent electrodes

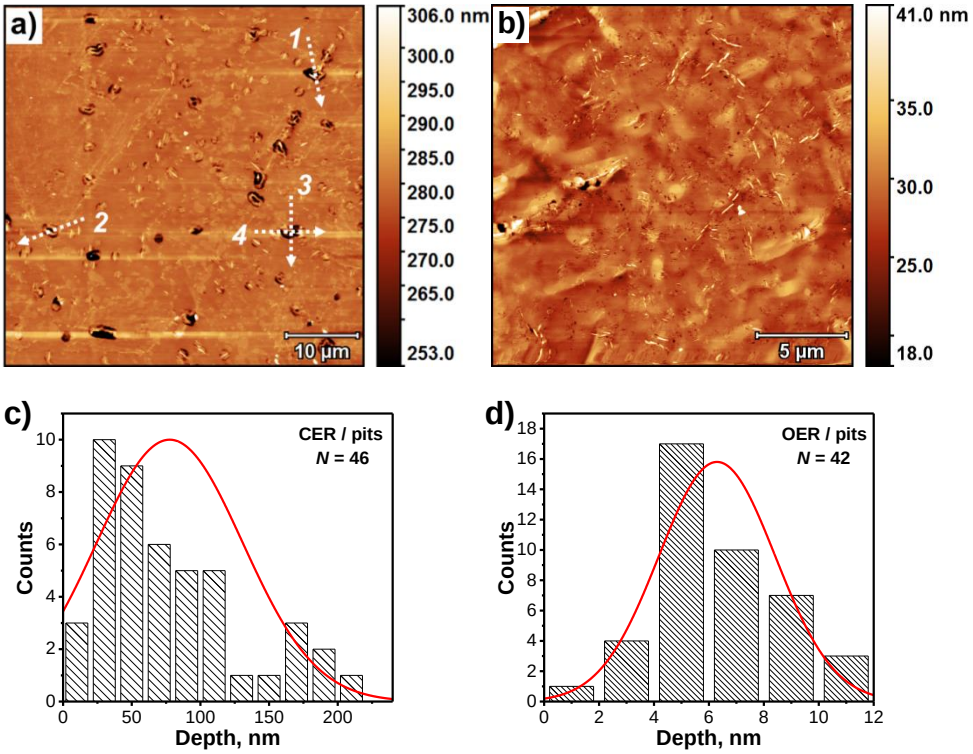

Figure A8. AF micrographs of spent RuO_2(110)/Ru(0001) subjected to a) CER and b) OER treatments; c, d) corresponding histograms of depth distribution of pits.

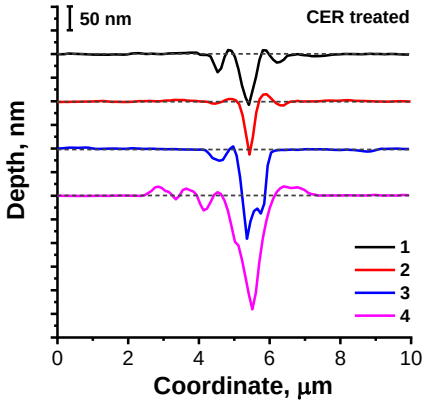

Figure A9. Selected linear depth profiles of Figure A8a (dashed lines correspond to surface plane).

A.7. Analysis of spent electrolytes

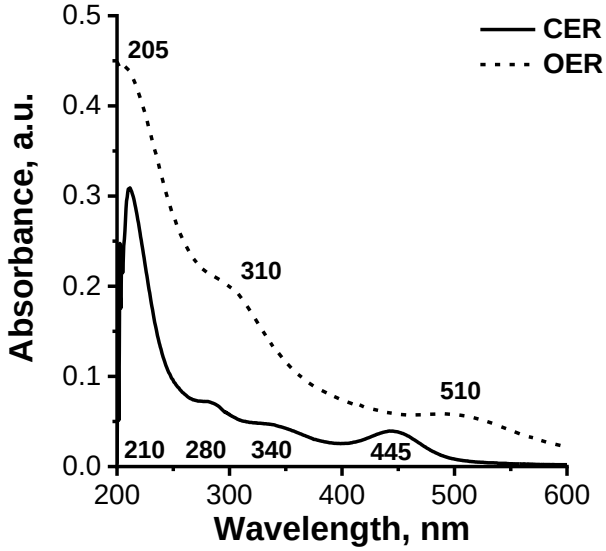

Figure A10. UV-Vis spectra of 0.5 M HCl and 0.5 M H_2SO_4 electrolytes containing dissolved Ru after electrochemical treatments.[1–6]

A.8. Cyclic Voltammetry (CV)

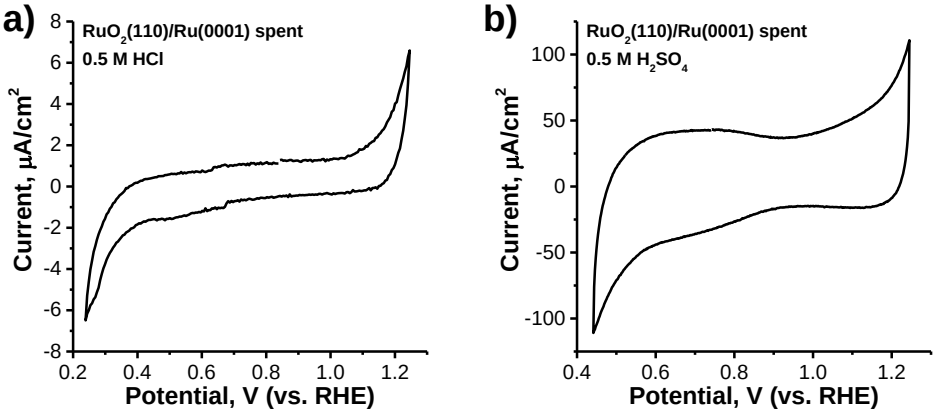

Figure A11. Cyclic voltammograms of spent RuO_2(110)/Ru(0001) electrodes subjected to E = +1.5 V pulses in a) 0.5 M HCl and b) 0.5 M H_2SO_4 electrolytes. Scan rates are 50 mV/s in both cases.

A.9. References

(1) Chen, J.-Y.; Hsieh, Y.-C.; Wang, L.-Y.; Wu, P.-W. *J. Electrochem. Soc.* **2011**, *158* (8), D463.

(2) Kötz, R.; Stucki, S.; Scherson, D.; Kolb, D. M. *J. Electroanal. Chem. Interfacial Electrochem.* **1984**, *172* (1–2), 211–219.

(3) Viljoen, K. Ruthenium (III) aqua-chloro complex chemistry: The Interconversion of the Hexachlororuthenate(III) and Aquapentachlororuthenate(III) Species, 2003.

(4) Loučka, T. *J. Appl. Electrochem.* **1990**, *20* (3), 522–523.

(5) Mercer, E. E.; McAllister, W. A. *Inorg. Chem.* **1965**, *4* (10), 1414–1416.

(6) Connick, R. E.; Hurley, C. R. *J. Am. Chem. Soc.* **1952**, *74* (20), 5012–5015.

Appendix A

Chapter 3

Mn promotion of rutile TiO_2-RuO_2 anodes for water oxidation in acidic media

Abstract

A method to reduce noble metal content in oxygen-evolving electrocatalysts suitable to work in acidic media is presented. TiO_2-RuO_2 anodes can be promoted by Mn, resulting in increased activity and stability. The most active composition displayed an overpotential of 386 mV at a current density of 10 mA cm^{-2}, and a Tafel slope of 50 mV dec^{-1}. This anode only included 17 at% Ru out of the total amount of metals included in the film. We investigated the influence of Mn addition to TiO_2-RuO_2 on the structure, morphology, and surface area, and related differences to catalytic activity and stability. We found that increased porosity of the anode film by Mn addition and Mn inclusion in the TiO_2-RuO_2 lattice can explain the enhanced catalytic activity. A detailed characterization of fresh and used anodes provided insight into structural modifications induced by electrochemical treatment.

This chapter has been published as:
Etzi Coller Pascuzzi, M.; Goryachev, A.; Hofmann, J. P.; Hensen, E. J. M. *Appl. Catal. B Environ.* **2020**, *261,* 118225.

3.1. Introduction

Concerns about CO_2 emissions associated with burning fossil fuels to cover the ever-increasing global energy demand require breakthroughs in renewable energy solutions.[1] Clean energy from wind turbines and solar photovoltaics will increasingly contribute to the global energy supply. As these sources are highly variable and cannot be predicted well, there is a growing need to store electricity for successive use. Among the available energy carriers, hydrogen has attracted a lot of interest because of its high gravimetric energy density and the possibility to use it as a fuel in electrochemical cells with important applications for transportation and stationary power generation.

As the direct conversion of sunlight into hydrogen is still limited by the relatively low efficiency and stability of photoelectrochemical devices or photocatalysts,[2–4] a promising alternative is to use electrolysis of water to convert (clean) electricity into chemical energy.[5] In a water electrolyzer, water is split into hydrogen and oxygen. Of the two half-reactions, the oxygen evolution reaction (OER), which takes place at the anode, is considered a bottleneck because of its slow kinetics due to the involvement of four protons and four electrons in the reaction mechanism.[6,7] Anodic overpotentials are usually around three times higher than the overpotentials at the cathode, where the relatively simple and fast hydrogen evolution reaction (HER) takes place.[8] The development of active and stable catalysts for anodic OER is crucial in order to improve the efficiency of the whole water splitting process. In the case of alkaline electrolysis, first-row transition metals, and particularly their oxides and oxyhydroxides, are promising OER electrocatalysts.[9–11] The use of Ni,[12–16] Co,[17–21] and Mn[22–26] has been investigated in depth, and the preparation and development of such electrocatalysts has been optimized so well that in some cases their performance is even better than that of IrO_2 and RuO_2 in alkaline environment.[8,27–29]

However, in acidic media, relevant primarily to Proton Exchange Membrane (PEM) electrolyzers,[30,31] the activity and stability of 3d metal oxides/oxyhydroxides are insufficient for large-scale applications. In these cases, only the rutile oxides IrO_2 and RuO_2 display sufficient stability, in particular when they are mixed with (rutile) TiO_2, acting as a stabilizer. These so-called Dimensionally Stable Anodes (DSA®) are employed for the large-scale electrochemical production of chlorine (chlor-alkali process) and oxygen.[32–34] However, in a hydrogen economy, it would be desirable to have anodes with the same performance but at a lower cost. Many strategies have been applied to reduce the noble metal content in the composition of DSAs®. The fabrication of IrO_2 and RuO_2 nanoparticles has been investigated as it allows for exposure of a larger number of active sites to the electrolyte while keeping the amount of active phase constant.[35–39] Another promising option is to add

first-row transition metals in the composition of the electrodes. Ni,[40,41] Co,[42] Fe,[43] and Zn[44] have been used in most of the cases as dopants for RuO_2. Typically, only small amounts of these elements are added to iso-structurally replace Ru atoms in the rutile lattice of RuO_2. In the case of manganese, instead, mixed ruthenium and manganese oxides have been shown to be active and stable electrocatalysts for the oxygen evolution reaction in alkaline media.[45,46] Only in a few studies, the effect of Mn addition on the performance of DSA®-type electrodes in the acidic OER has been reported,[47–49] but a comprehensive structural and electrochemical characterization is needed to understand the reasons behind the activity and stability changes. In the present work, we addressed this issue by studying the influence of manganese on mixed Ti-Ru oxide electrodes in acidic water oxidation, establishing composition and activity trends. We emphasize the impact of manganese on the structure and the catalytic performance of TiO_2-RuO_2 anodes.

3.2. Experimental

3.2.1. Preparation of mixed TiO_2-RuO_2 electrodes

The preparation of TiO_2-RuO_2 anodes was carried out according to a procedure reported elsewhere.[50] Briefly, titanium tetraisopropoxide (Sigma-Aldrich, 97%) and ruthenium(III) chloride hydrate (Sigma-Aldrich, ruthenium content 38% minimum) were used as precursors. Ti to Ru atomic ratio was kept close to the composition of industrial DSA® anodes (70:30). 2,4-pentanedione (Alfa Aesar, 99%), a chelating agent, was added to the solution (2.5 $mmol/mmol_{Ti+Ru}$) in order to prevent a fast hydrolysis of the precursors. The concentration of the precursor salts was then adjusted to 1 M by dilution with a 2:1 by volume ethanol/water mixture. The resulting solution was then stirred overnight prior to deposition.

Titanium foil (Advent, purity 99.6+ %, thickness 0.25 mm) was used as a substrate. Before deposition, the Ti foils were washed in acetone and sonicated for 15 min and, finally, rinsed with ethanol and deionized water. The solution was deposited on the cleaned Ti substrates by using a spin coater (SPS-Europe). Spin coating was performed at 4000 rpm for 15 s. The deposition area was limited to 1 cm^2. As-prepared anodes were dried in air at 80 °C for 10 min and calcined at 500 °C in static air for 2 h.

3.2.2. Mn incorporation

In order to investigate the effect of Mn addition on the electrocatalytic performance of the DSA® anodes, manganese chloride tetrahydrate (Sigma-Aldrich, ACS reagent ≥ 98%) was

added to the previously described 1 M solution of the Ti-Ru precursor. The concentration of Mn^{2+} was chosen to be either 0.1, 0.5, 0.8, or 1.5 mol/L. Further preparation of Mn-containing anodes was done in the same manner as described above. The composition of the precursor solutions, the atomic composition of the as-prepared anodes, and sample names are summarized in Table 3.1.

Table 3.1. Sample names, concentrations of the precursors in the starting solutions and nominal atomic ratio of the metals.

Sample	Intended loading			Nominal metal composition		
	$Ti(i\text{-}OPr)_4$, mol/L	$RuCl_3$, mol/L	$MnCl_2$, mol/L	Ti, at%	Ru, at%	Mn, at%
Mn00	0.7	0.3	0.0	70	30	0
Mn09	0.7	0.3	0.1	64	27	9
Mn33	0.7	0.3	0.5	47	20	33
Mn44	0.7	0.3	0.8	39	17	44
Mn60	0.7	0.3	1.5	28	12	60

3.2.3. Characterization of MnO_x-TiO_2-RuO_2 electrodes

X-ray diffraction (XRD) patterns were obtained using a Bruker D2 Phaser diffractometer equipped with a Cu K_α radiation source. The diffractograms were recorded with a step size of 0.02° and an acquisition time of 1 s, in the 2θ range of 10° to 70°.

Field-emission scanning electron micrographs (FESEM) were taken using a FEI Quanta 3D FEG microscope at an accelerating voltage of 5 kV without additional coating of the surface.

Energy dispersive X-Ray (EDX) spectrometry was performed in a Phenom Pro-X microscope with an accelerating voltage of 15 kV.

X-ray photoelectron spectroscopy (XPS) measurements were carried out on a K-Alpha XPS spectrometer (Thermo Scientific) equipped with a monochromatic Al K_α (1486.6 eV) X-ray source. The spot size was 400 µm and the pass energy was set at 200 eV and 50 eV for survey and region scans, respectively. Spectra were calibrated by setting the binding energy of the RuO_2 (Ru $3d_{5/2}$) component equal to 280.6 eV.[51] Fitting of the XPS spectra was performed using CasaXPS software.

XPS depth profiles were recorded on the same spectrometer by Ar^+ ion sputtering (3 kV, high-current). The duration of the sputtering steps was 4 min and XPS spectra were taken

after each sputtering cycle. The depth profiles of each element were normalized to the highest intensity. In-plane and out-of-plane homogeneity of the samples was checked by XPS mapping and XPS depth profiling, respectively (see Appendix B). Ru 3d, Mn 2p, and Ti 3p regions were used to determine the content of RuO_2, MnO_x, and Ti^0, respectively. Due to the high reducibility of RuO_2 under ion sputtering conditions, no deconvolution of the Ru 3d region was performed and the area of the entire region was used to construct a profile. Profiles of MnO_x were constructed in the same way. The Ti 3p region was used instead of the Ti 2p region due to the overlap of the latter with Ru 3p peaks. The Ti^0 peaks (binding energy, BE ≈ 32.9 eV) were used to track the location of the titanium substrate.

3.2.4. Electrochemical characterization

Electrochemical measurements were carried out in a standard three-electrode cell at room temperature with an Autolab PGSTAT302N potentiostat (Metrohm Autolab B.V.). Ti-supported films with a geometric area of 1 cm^2 were used as working electrodes (WE). Anodic currents of the bare Ti foil were found to be negligible in the range of the applied potentials (Figure B1a, b), making it unnecessary to mask the back of the working electrodes. A platinum foil (area: 5 cm^2) was used as a counter electrode and an Ag/AgCl electrode (Radiometer Analytical, E_{RE} = +0.24 V) was used as a reference electrode, if not mentioned otherwise. 0.1 M H_2SO_4 (H_2SO_4 Sigma Aldrich, 99.999%) was used as electrolyte in all the tests. Milli-Q water (18.2 MΩ·cm) was used in all the cleaning and dilution steps. All potentials are *iR*-corrected and reported versus the Reversible Hydrogen Electrode (RHE). Current densities are normalized using the geometric areas, if not mentioned otherwise.

The catalytic activity was evaluated by linear sweep voltammetry (LSV) recorded with a scan rate of 0.5 mV s^{-1} in the anodic direction. The values of overpotential at current densities of 1 and 10 mA cm^{-2} were used to compare the activity of the catalysts. Overpotentials (η) were calculated using the following equation:

$$\eta_{OER} = V_{meas} + V_{Ag/AgCl} + 0.059\ pH - E^0_{OER} \qquad (3.1)$$

where V_{meas} is the measured potential, $V_{Ag/AgCl}$ is the potential of the reference electrode, and E^0_{OER} = +1.23 V is the standard electrode potential for the Oxygen Evolution Reaction. The as-recorded voltammograms were used to construct Tafel plots, where we evaluated the Tafel slopes (with an error ± 1 mV dec^{-1}).

Chronopotentiometry (CP) at a constant current density of 1 mA cm^{-2} and duration of 6 h was employed to assess the stability of the catalysts. The solutions were stirred during the measurements to avoid the accumulation of bubbles on the electrode surface.

Electrochemical impedance spectroscopy (EIS) was carried out in a frequency range of 10^{-1} to 10^5 Hz with an amplitude of 10 mV at the open circuit potential. The system was simulated with an $R_s(R_{ct}C_{dl})$ circuit using Nova 1.10 software, where R_s represents the electrolyte resistance, R_{ct} the charge transfer resistance, and C_{dl} the double layer capacitance of the electrode. The values of the Electrochemical Surface Area (ECSA) were calculated from the ratio of the double layer capacitances with the specific capacitance. For the latter, we employed a constant value of 35 µF cm^{-2} for all prepared electrodes, in accordance with literature.[8,27]

When current densities were normalized using the values of ECSA, this is specifically mentioned reporting the values in "mA cm^{-2}_{ECSA}".

Long-term electrochemical stability of the samples Mn00 and Mn44 was evaluated by chronoamperometry at E = +1.80 V_{RHE} for 17 h. The amounts of dissolved Ru, Ti and Mn were determined by ICP-OES measurement of the spent electrolytes.

3.2.5. Characterization of spent electrolytes

The amount of Ru, Mn and Ti ions in the spent electrolytes was determined by ICP analysis. Inductively coupled plasma optical emission spectrometry (ICP-OES) was performed on a SPECTROBLUE EOP spectrometer equipped with an axial plasma source (Ar). The following emission lines were used: 240.3 nm and 267.9 nm (Ru), 257.6 nm and 259.4 nm (Mn), 334.9 nm and 336.1 nm (Ti).

3.2.6. Online Electrochemical Mass Spectrometry (OLEMS) measurements

OLEMS measurements were carried out in a three-electrode EC glass cell equipped with a Red Rod reference electrode (Radiometer Analytical, E_{RE} = +0.225 V) and a Pt plate counter electrode. The working electrode slides with an average size of 0.5 cm^2 were mounted into a PEEK holder and contacted from the top by a gold wire enclosed in a quartz tube. Ar-purged 0.1 M H_2SO_4 (H_2SO_4 Sigma Aldrich, 99.999 %) was used as electrolyte. The temperature of the cell was maintained at 25 °C by a thermostat. EC treatment was performed using an Ivium Compactstat potentiostat (Ivium Technologies). OLEMS measurements were conducted on a quadrupole mass spectrometer (Balzers Quadstar, Prisma QME 200) at an operating pressure of approximately $4 \cdot 10^{-7}$ mbar. The OLEMS tip was equipped with a porous PTFE plug with a probing area of 0.79 mm^2. The tip was

approached to the surface of the working electrode at a distance of ca. 20 µm by a micrometer screw with the help of a video microscope. The working electrode (WE)-tip distance was optimized for the highest intensity of the O_2^+ ion current (m/z = 32) measured during the OER. A more detailed description of the utilized OLEMS setup is given elsewhere.[52,53]

Faraday plots[52,53] (*i.e.* gas production vs. faradaic charge) were constructed by plotting integrated ion currents of relevant ions (proportional to the amount of evolved gases) versus anodic charge supplied in the form of potential pulses (step size: 10 mV). Ion currents of m/z = 32 (O_2^+) and m/z = 34 ($H_2O_2^+$) were continuously recorded throughout the experiments. Potential pulses were separated by resting periods (open circuit, j = 0 mA cm^{-2}), necessary to achieve temporal separation of individual OLEMS peaks.

3.3. Results and discussion

3.3.1. Structural characterization of fresh electrodes

The influence of Mn addition on the phase composition of the electrodes was evaluated by XRD (Figure 3.1). The reflections of the Ti substrate remain visible in all XRD patterns. Sample Mn00 contains a single rutile phase, demonstrating that a solid solution of TiO_2 and RuO_2 was formed.[50,54] Upon addition of Mn, a gradual shift of the rutile peaks towards higher diffraction angles is seen, which can be explained by a contraction of the unit cell. This change is due to the incorporation of Mn(IV) in the solid TiO_2-RuO_2 solution.[49] The ionic radii of Mn(IV), Ti(IV) and Ru(IV) are 67 pm, 74.5 pm, and 76 pm, respectively. As the differences in ionic radii among the elements are less than 15%, we can expect that Mn can easily enter into the solid solution of TiO_2-RuO_2. For Mn09 and Mn33 with a low Mn content, no diffraction patterns characteristic of Mn-oxides could be observed. This does not exclude the presence of very small domains of Mn-oxides or amorphous Mn-oxides. Samples with a higher Mn content (Mn44 and Mn60) exhibit diffraction peaks of Mn_3O_4 and Mn_2O_3. Thus, part of the Mn has segregated into separate Mn-oxide phases. The XRD patterns also show that a Mn content of the film higher than 9 at% results in a decrease of the rutile peak intensities, suggesting that the film becomes increasingly disordered due to the presence of Mn, as previously reported for RuO_2 – MnO_x electrodes.[45]

The oxidation state of manganese was investigated by XPS. As Mn 2p region of mixed MnO_x compounds is composed of broad overlapping features with nearly similar BE (binding energy) values due to the multiplet splitting of Mn 2p (*e.g.* Mn(II) – 641.4 eV, Mn(III) – 641.4

eV, Mn(IV) – 641.8 eV),[55] we focused on Mn 3s spectra to determine the chemical composition and oxidation state of Mn in the samples (Figure B2a). The Mn 3s peak is split due to exchange coupling between the 3s hole and the 3d electrons of Mn.[56] For the interpretation of these spectra, we followed the relevant literature.[24,56–59] The observed splitting values for samples Mn33, Mn44, and Mn60 range from 5.22 to 5.40 eV (Table B1), typical for Mn(II) and Mn(III).[56–58] This is in keeping with the presence of Mn_3O_4 and Mn_2O_3 derived by XRD patterns of these samples. The lower splitting for sample Mn09 (5.05 eV) indicates an overall increase in the oxidation state of Mn, which can be attributed to the additional presence of Mn in higher oxidation state (Mn(IV), splitting value 4.5 eV). This result is consistent with the insertion of part of the Mn in the TiO_2 – RuO_2 solid solution as Mn(IV), as discussed above.

For two selected samples, Mn00 and Mn44, survey spectra and fitted Ru 3d spectra are reported (Figure 3.2a, b). The analysis of the Ru 3d spectra of Mn00 and Mn44 samples, done in accordance with the model proposed by Morgan,[51] shows that Ru is present in form of RuO_2 (BE $Ru3d_{5/2}$ = 280.6 ± 0.2 eV). Apart from the two RuO_2 main peaks (Ru $3d_{5/2}$ and Ru $3d_{3/2}$), we can also see two characteristic features (BE $Ru3d_{5/2\ sat.}$ ≈ 282.5 eV) which can be ascribed to RuO_2 satellite peaks.[51] The asymmetry of the RuO_2 lines is due to its metallic conductive nature. The absence of Cl-related peaks in Ru 3d ($RuCl_3 \cdot xH_2O$, BE Ru $3d_{5/2}$ = 282.2 eV) and survey spectra (BE Cl 2p ≈ 200 eV) indicates that the Ru and Mn precursors were completely converted into oxides. Survey spectra show that the samples contain Ti, Ru, O, C and Mn (the latter only for Mn44), with no other elements present in detectable amounts. The presence of adventitious carbon (visible in the Ru 3d spectra) can be explained by the fact that the samples were handled in air.[60] The metal content at the surface of samples Mn00 and Mn44 are reported in Table B2. Mn00 shows the same Ti:Ru ratio at the surface as the nominal composition of the sample. For Mn44, an enrichment of Mn is observed, which suggests that the Mn-oxides present in this sample tend to segregate toward the surface of the electrode.

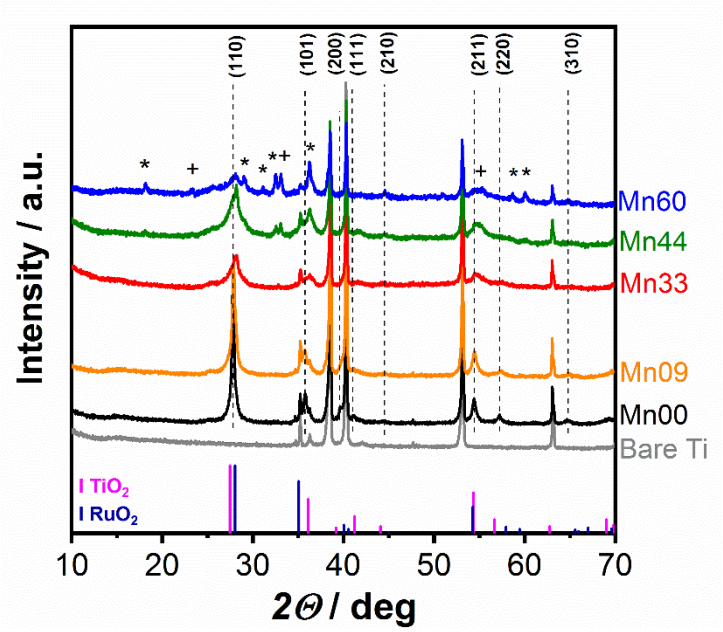

Figure 3.1. X-ray diffractograms of the mixed TiO_2-RuO_2 samples. Dashed lines indicate the rutile peaks of the solid solution formed by TiO_2 (JCPDS#21-1276) and RuO_2 (JCPDS#40-1290). [*] Mn_3O_4 (JCPDS#24-0734), [+] Mn_2O_3 (JCPDS#41-1442) peaks.

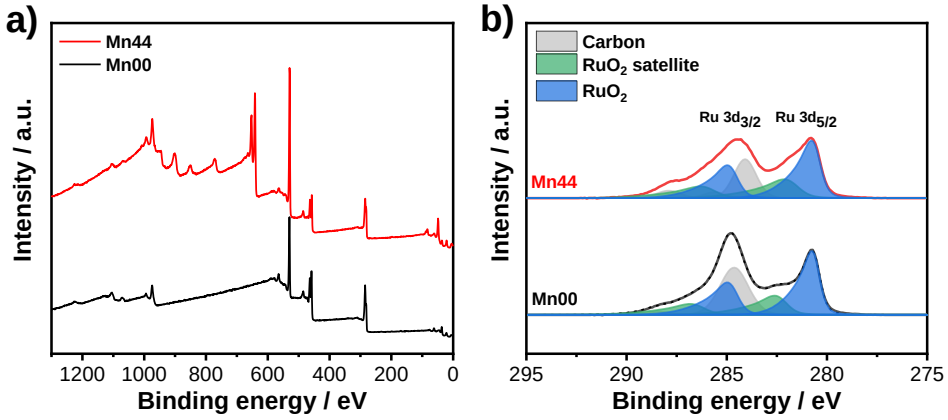

Figure 3.2. a) Survey and b) Ru 3d XPS spectra of samples Mn00 and Mn44. Grey components in the Ru 3d region are related to C 1s peaks.

The effect of Mn addition on the morphology of the anodes was investigated by means of Field-Emission Scanning Electron Microscopy (FESEM). The images at low magnification (Figure B3) give an idea of how manganese modifies the surface morphology. In Figure 3.3, micrographs acquired both in SE (secondary electrons) and BSE (backscattered secondary electrons) are reported for all the investigated samples. TiO_2-RuO_2 anodes exhibit a mud-cracked morphology (Figure B3a), well-known for this kind of materials[45,54,61,62] and ascribed to the tensile stress induced by the applied thermal treatment.[54,62] Indeed, Mn00 and Mn09 (Figure B3a, b and Figure 3.3a, b) show a similar morphology, with a lower degree of roughness and fewer fractures on the outermost layer. In Mn09, a slight increase of the roughness can be seen compared to Mn00. By taking advantage of the compositional contrast arising from the BSE, it is possible to get an impression of the ruthenium dispersion (*i.e.*, Ru has a higher atomic number than both Ti and Mn). Ruthenium-rich particles are observed both on the plain surface and in the cracks of the electrode (Figure 3.3f, g). This is in agreement with EDX elemental mapping of the sample Mn00 (Figure B4); for this reason, all other samples are discussed referring to micrographs acquired using the BSE detector.

The sample morphology drastically changes when the Mn content is further increased (Mn33, Mn44, and Mn60): the structures become rougher and more porous (Figure B3c, d, e). In sample Mn33, some porous areas with smaller and more irregular cracks than observed for Mn00 and Mn09 are interconnected by a three-dimensional network of "sunflower"-like structures (Figure 3.3c). By looking at the compositional contrast (Figure 3.3h), the sample appears quite homogeneous and Ru-rich particles disappear. This suggests that the cracks observed for the first two samples, Mn00 and Mn09, are mainly due to the crystalline growth and slight segregation of RuO_2 particles. This effect is not observed for Mn33 sample, partially because of the reduced loading of ruthenium. A similar effect is found for samples Mn44 and Mn60 (Figure 3.3d, e): in these two samples, the porous surface of the electrodes presents some craters. Sample Mn60 also exhibits deep fractures of the film and a homogeneous Ru dispersion (Figure 3.3i, j), with a slight enrichment in Ru mainly in the rims of the circular craters.

The porous structure of samples Mn33, Mn44, Mn60, with bubble-like features, is most likely due to differences in surface tension of the Mn-containing solution, a parameter that is well known to influence the morphology of the final material in DSA® anodes by changing the rate of evaporation.[34] The addition of Mn chloride can alter the surface tension of the solution, promoting the formation of bubbles due to released gases during precursor decomposition.

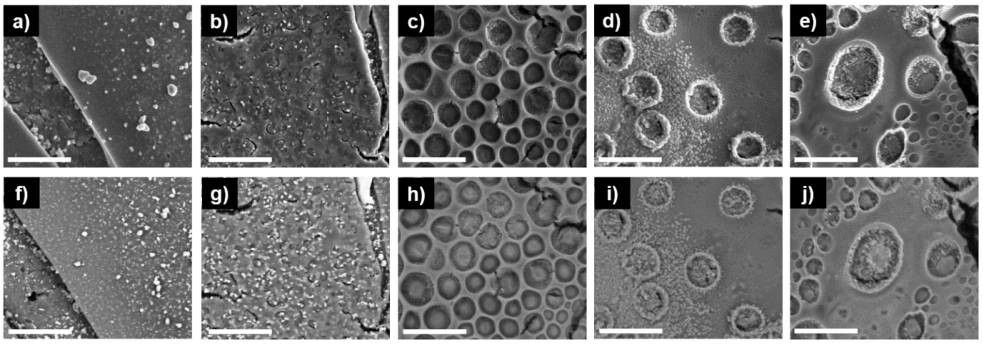

Figure 3.3. Electron micrographs acquired in normal detection mode using secondary electrons (top) and back-scattered electron (BSE) mode (bottom) of samples: a, f) Mn00; b, g) Mn09; c, h) Mn33; d, i) Mn44; e, j) Mn60. Scale bars are 2 μm.

3.3.2. Electrochemical characterization

The catalytic activity was assessed by linear sweep voltammetry (LSV) at a scan rate of 0.5 mV s^{-1} (Figure 3.4a). This low scan rate was chosen to minimize the amount of current generated by the capacitive effect and in order to obtain the corresponding Tafel plots reported in Figure 3.4b. The bare titanium substrate exhibits negligible current densities in all potential ranges applied in this work (Figure B1a, b), and thus its contribution to the catalytic activity for OER can be ignored.

The addition of manganese led to a significant cathodic shift of the voltammograms. Already the sample with the lowest Mn content (Mn09) showed a significant increase in the recorded current density compared to the Mn-free sample (Figure 3.4 and Table 3.2). This sample is also more active than a pure RuO_2 sample prepared with the same method. For samples Mn33, Mn44, and Mn60, a further increase of the catalytic activity is observed. Before, it has been shown that the inclusion of Mn in the RuO_2 lattice enhanced the catalytic activity of $Ru_xMn_{1-x}O_2$ anodes in water oxidation under acidic conditions and the synergy was most pronounced for x = 0.30.[49] We demonstrate in this work that Mn also promotes the electrocatalytic performance of TiO_2-RuO_2 mixed anodes. Even though at higher content Mn addition leads to segregation of Mn-oxides, this is not detrimental to the synergistic effect between Mn and these dimensionally stabilized TiO_2-RuO_2 anodes.

To confirm that the increased activity is due to a synergistic effect between Mn and Ru and not to Mn itself, we evaluated the activity of a Ru-free sample prepared from a solution containing 70% titanium and 30% manganese precursors (Ti0.7Mn0.3). This sample showed

negligible current densities compared to those recorded for Ru-containing samples (Figure B5).

The performance of the electrodes was evaluated from the overpotential (η) required to reach a current density of 1 mA cm^{-2} or 10 mA cm^{-2}. Clearly, η was significantly lowered, nearly proportionally with the Mn loading (Table 3.2 and Figure 3.5). The lowest overpotential at j = 10 mA cm^{-2} is observed for the Mn44 electrode (η = 386 mV). Its overpotential (386 mV) is only 26 mV higher than the overpotential reported for a thin film of pure RuO_2 in 0.05 M H_2SO_4,[63] and 46 mV higher than the value reported for an IrO_x catalyst in 1 M H_2SO_4.[8] We stress the promising performance of sample Mn44 prepared in a simple procedure, whose activity is comparable to that of pure ruthenium- or iridium-based systems. The benefit of our composition is that the noble metal content is considerably lower. We highlight that this sample, containing only 17 at% Ru, reaches the target of activity designated to highly promising catalysts (η_{10} < 400 mV) in an acidic electrolyte.[64]

We also determined Tafel slopes for the different samples. Tafel slopes for Mn09 and Mn33 are only slightly higher (44-56 mV dec^{-1}) than for Mn00. Only sample Mn60 exhibited a slope higher than 60 mV dec^{-1}. Mn44 exhibited a Tafel slope of 50 mV dec^{-1}, close to the value determined for Mn00 (44 mV dec^{-1}). The changes in the Tafel slopes are indicative of different reaction mechanisms. While Tafel slopes of about 40 mV dec^{-1} are typical for a second electron transfer being the rate-determining step of the reaction, values of about 60 mV dec^{-1} indicate that a chemical step is taking place before the OER.[65] For the sample Mn60, we speculate that electro-oxidation of Mn^{2+} as a chemical step prior to oxygen evolution, as already identified as the rate-determining step in pure MnO_x-catalyzed water oxidation at pH < 8.[25] The value of the Tafel slope of sample Mn44 of 50 mV dec^{-1} is in line with values reported for Ru-based OER catalysts, i.e. in the 30 – 60 mV dec^{-1} range,[66,67] and lower than the Tafel slopes reported for Ir-based catalysts (typically 55- 65 mV dec^{-1} range).[68,69]

As the very different morphologies of the films can influence the current densities exposing more active sites, we also determined the electrochemical surface area (ECSA). Higher surface areas contribute to higher the observed current densities;[70] it is therefore relevant to normalize the results based on the ECSA to gain insights into the intrinsic activity. The normalization with the geometric area only does not allow to distinguish whether an activity change is caused by extrinsic (different surface areas) or intrinsic factors ("real" electrocatalysis). The ECSA was evaluated from the ratio between the double-layer capacitance obtained by EIS and the specific capacitance of metal oxides in acidic electrolytes (35 µF cm^{-2}), following the approach described by McCrory *et al*.[27] We refer to

their work for the explanation of the assumptions and accuracy of the method.[27] As follows from Table 3.2, the ECSA substantially increases when the Mn content is raised. The effect on the ECSA is most pronounced when the Mn content is increased from 0 to 33 at%. The nearly one order of magnitude increase shows a strong textural influence of Mn on the catalytic performance. The ECSA differences are in qualitative agreement with the FESEM images.

However, even after normalization of the Tafel plots with the values of the ECSA instead of the geometric areas (Figure 3.4c), we can still observe a shift of the curves towards higher current densities. In particular, the trend in the low overpotential region is similar to the trend observed for the current densities normalized with the geometric area, where the catalytic activity increases with the Mn content. This finding shows that a higher content also affects the intrinsic activity of the anodes. In the high overpotential region, the sample with the highest intrinsic activity is Mn09. This may find its origin in the mass transport limitations for the samples Mn33, Mn44 and Mn60 by vigorous oxygen bubble formation at the surface.

In Table 3.2 we evaluated the specific current densities normalized with the values of ECSA for all the samples at a fixed overpotential of 300 mV. The results show an increase of the specific activity upon Mn addition up to sample Mn44, which displayed the best performance. The recorded specific current density for sample Mn44 (3.85 µA cm^{-2}_{ECSA}) is substantially higher compared to Mn00 (1.31 µA cm^{-2}_{ECSA}). A further increase in Mn content did not yield to a further increase in the specific activity. To the best of our knowledge, no ECSA-normalized results of the catalytic performances of similar systems (*i.e.*, RuO_2 –MnO_x) have been previously reported. Thus, our findings show that, in addition to the positive influence of manganese on the dispersion of Ru, there is also a qualitative influence of the Mn promoter on the Ru active sites. The activity enhancement can be due to the presence of defects in the rutile structure resulting from Mn insertion into the TiO_2-RuO_2 solid solution, as observed by XRD. The presence of disordered surface structures can lead to increased OER performance, because the higher density of unsaturated sites enhances reactant adsorption and the higher structural flexibility of the active sites stabilizes the formation of intermediates. This is for instance observed for RuO_2, the amorphous form exhibiting a higher OER activity than its crystalline counterpart.[71] The enhanced activity of catalysts with a high number of oxygen vacancies finds origin in the participation of lattice oxygen atoms in the oxygen evolution, which is also the reason of the higher dissolution rates usually recorded for these materials.[72]

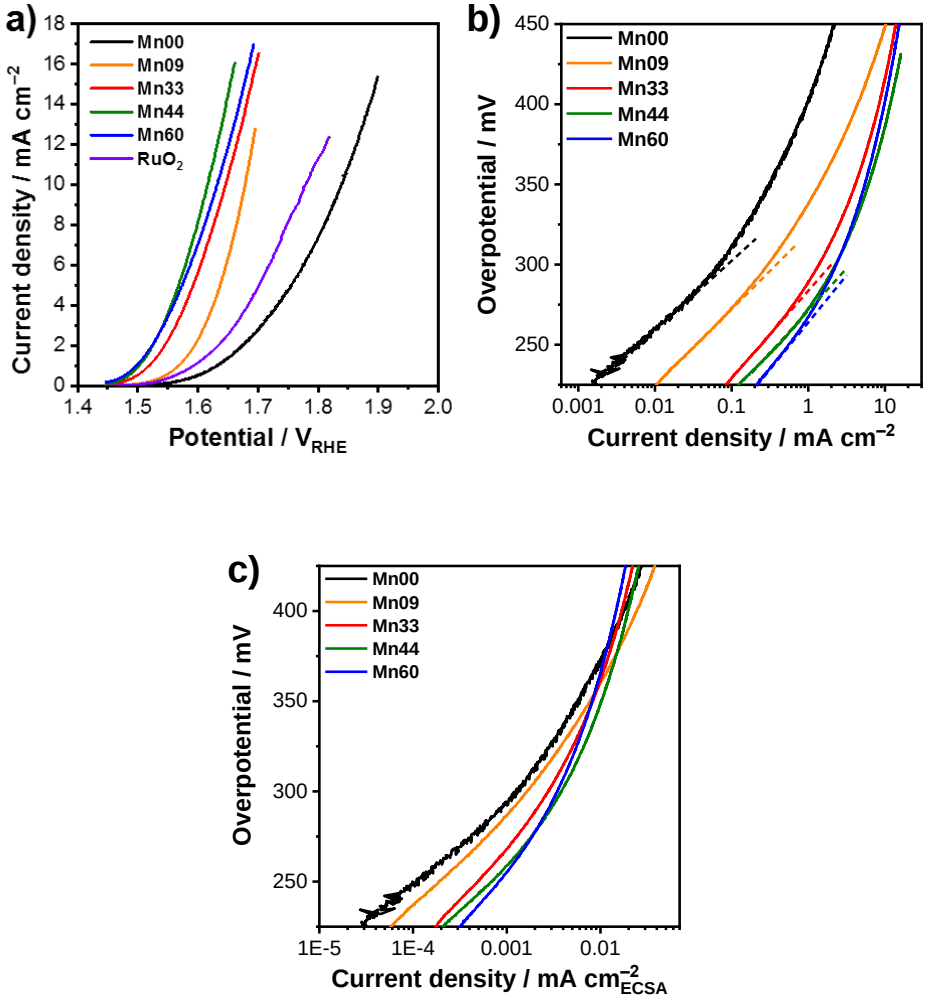

Figure 3.4. a) Linear sweep voltammetries and b) corresponding Tafel plots of the anodes recorded in 0.1 M H_2SO_4. Linear Tafel regions are indicated by dashed lines. c) Tafel plots of the electrodes normalized with ECSA.

Table 3.2. Summary of overpotentials at 1 and 10 mA cm^{-2}_{geo} (η_1, η_{10}), Tafel slopes, ECSA values, and specific current densities at an overpotential of 300 mV normalized with ECSA ($j_{spec,\ \eta=300\ mV}$).

Sample ID	η_1, mV	η_{10}, mV	Tafel slope, mV dec^{-1}	ECSA, cm^2	$j_{spec,\ \eta=300\ mV}$, µA cm^{-2}_{ECSA}
Mn00	404	609	44	54	1.31
Mn09	338	448	50	180	1.65
Mn33	290	416	56	497	2.78
Mn44	273	386	50	594	3.85
Mn60	268	402	61	669	3.51

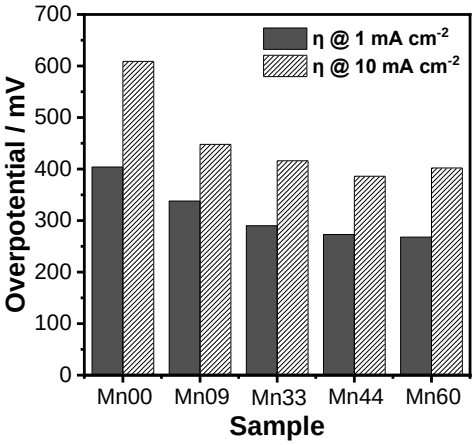

Figure 3.5. Overpotentials of mixed TiO_2-RuO_2-MnO_x anodes required to reach current densities of 1 mA cm^{-2} and 10 mA cm^{-2} determined by LSV in a 0.1 M H_2SO_4 solution at 25 °C. Current densities are normalized on the geometric areas of the electrodes.

The stability of the catalysts was evaluated by chronopotentiometry (CP) conducted for 6 h in 0.1 M H_2SO_4 at a current density of 1 mA cm^{-2}. The addition of Mn not only results in increased electrocatalytic activity but also in improved stability (Figure 3.6). This improved stability is already evident at a Mn content of 9 at%. The overpotential remains nearly constant during the CP measurement, in contrast to sample Mn00. Sample Mn33 shows an increase in the overpotential during time, yet still exhibiting lower values at the end of the test compared to the samples with a lower Mn content. We ascribe the increase of overpotential for this sample to its three-dimensional porous structure, which is substantially altered during the electrochemical treatment as will be shown below. Sample

Mn44 is not only the most active sample but also displays the highest stability, *i.e.* the overpotential remains below 300 mV after 6 h. A similar value was recorded for the sample with the highest Mn content (Mn60).

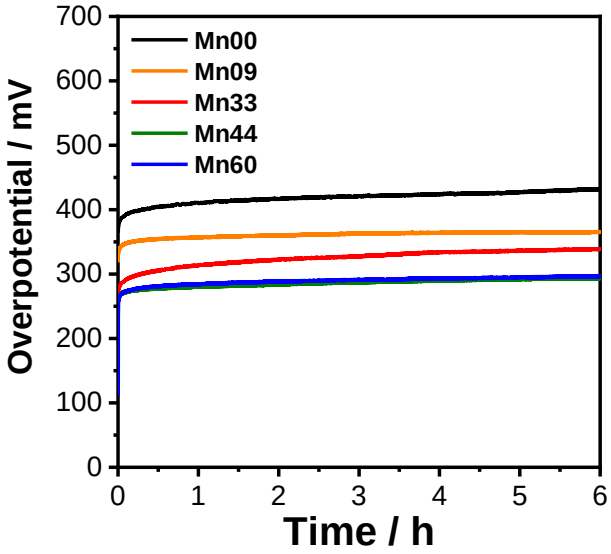

Figure 3.6. Chronopotentiometries of mixed TiO_2-RuO_2-MnO_x anodes recorded in 0.1 M H_2SO_4 at a constant current density of 1 mA cm^{-2}.

3.3.3. Effect of electrochemical treatment on the electrodes

The influence of a prolonged electrochemical treatment on the electrode morphology was analyzed by means of FESEM. Micrographs of the anodes at high magnification are reported for all the samples in Figure 3.7 (micrographs at low magnification in Figure B3). The morphology of samples with no Mn or a low Mn content (Mn00 and Mn09) does not substantially change upon electrochemical treatment (Figure B3f, g, and Figure 3.7a, b, f, g). Mostly, a flattening of the surface and a reduced number of cracks are noticed. A severe morphology change is visible for sample Mn33, which can explain the substantial change in performance during the treatment. The ordered and porous structure characterizing the fresh sample Mn33 is unstable under OER conditions, as it is converted and replaced by a disordered and rougher structure (Figure B3h and Figure 3.7c, h) after the electrochemical treatment. The samples with a high Mn content (Mn44 and Mn60) maintain a morphology

with craters (Figure B3i, j and Figure 3.7d, e) with a homogenous dispersion of the elements (Figure 3.7i, j).

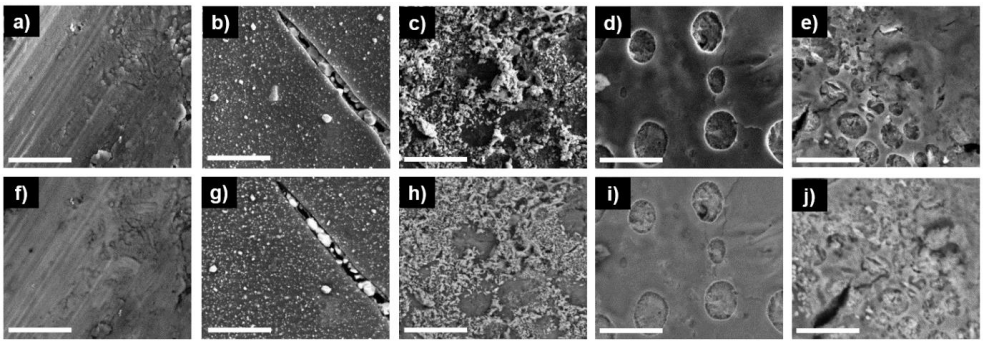

Figure 3.7. Electron micrographs acquired in normal detection mode using secondary electrons (top) and back-scattered electron (BSE) mode (bottom) of samples after 6 h of electrolysis at 1 mA cm^{-2} in 0.1 M H_2SO_4: a, f) Mn00; b, g) Mn09; c, h) Mn33; d, i) Mn44; e, j) Mn60. Scale bars are 2 µm.

X-ray diffractograms of the tested samples (Figure B6) show for all the samples a decrease in peak intensities, which is an evidence of a lowered crystallinity of the electrodes due to the electrochemical treatment. The sharp peaks originating from the Mn-oxides observed in fresh Mn44 and Mn60 samples are absent in the spectra of the used anodes. Thus, the electrochemical treatment causes a substantial decrease in the crystallinity and, possibly, leaching of Mn from the anode surface. As the overpotential at the end of the stability tests remains lower for the Mn samples from which crystalline Mn-oxides were removed, it is likely that their higher catalytic activity originates from the inclusion of Mn in the lattice of the mixed TiO_2-RuO_2 rutile phase and the porous structure with a better Ru dispersion.

XPS results (Table B2) show that the Mn content of sample Mn44 at the surface dramatically decreased from 71 at% in the fresh sample to 14 at% after electrochemical treatment. The peak splitting of the samples with a higher Mn content decreased significantly (Figure B2b, Table B1). From the values for the used catalysts, we infer that the remaining Mn is mainly present as Mn(IV),[56–58] likely as a substituent in the TiO_2-RuO_2 lattice. The Mn(II) and Mn(III) species present in the fresh samples as segregated oxides were further oxidized during electrochemical oxidation and eventually dissolved in the solution as MnO_4^-.[73] The aspect of stability is further investigated in the remainder of this work. Based on the activity and stability results, we selected sample Mn44 for these further investigations, because this sample had the lowest overpotential at a current density of 10 mA cm^{-2} during the LSV, the

lowest overpotential at the end of the chronopotentiometry, lower Tafel slope compared to Mn60, and the highest specific current density at an overpotential of 300 mV.

3.3.4. Online Electrochemical Mass Spectrometry (OLEMS)

In contrast to conventional electrochemical analysis, OLEMS provides semi-quantitative information on the gases evolving at the electrode. A low detection limit and fast response enable instantaneous detection of reaction products during dynamic electrochemical treatment. We employed OLEMS to determine the OER onset potentials for samples Mn00 and Mn44 by measuring the O_2 signal as a function of the applied potential (Figure 3.8a, b). Surprisingly, the onset potentials of the O_2 production were nearly similar for these two samples, *i.e.*, 250 ± 10 mV and 260 ± 10 mV, respectively. Although this seems to be in disagreement with the overpotentials reported in Table 3.2, we suspect that, at this initial stage, a part of the charge is used to oxidize Mn, as we will discuss below.

OLEMS can also be used for studying competitive reactions by means of Faraday plots.[52] In Figure B7 we report the three-dimensional representations of the gas production versus potential applied and charge for both the samples Mn00 and Mn44. The projections in two dimensions of the gas productions versus the charge result in the Faraday plots, reported in Figure 3.8c, d. Faraday plots represent the potential dependence of the amount of product formed per amount of supplied faradaic charge, in accordance with the Faraday's law of electrolysis. Linearity between the gas production and faradaic charge is expected for systems where only a single faradaic reaction occurs in the studied potential range. Deviations can occur when more than one faradaic reaction is involved. Figure 3.8c shows a linear behavior of O_2 production against faradaic charge for sample Mn00, suggesting that the OER is the major electrochemical reaction occurring at E = +1.50 ÷ 1.63 V. On the contrary, a Faraday plot for sample Mn44 exhibits two distinct regions in E_1 = +1.50 ÷ 1.54 V and E_2 = +1.54 ÷ 1.63 V with different slopes (Figure 3.8d). The lower slope in region E_1 compared to region E_2 indicates that part of the charge is used for another reaction than the OER. Considering the Pourbaix diagram of Mn in water,[74] we surmise that, at E_1, part of the charge is consumed to oxidize Mn^{2+} and Mn^{3+} to Mn(IV) and Mn(VII) in accordance with XPS analysis (Figure B2 and Table B1). The formation of MnO_4^- leads to partial dissolution of Mn into the electrolyte.[25]

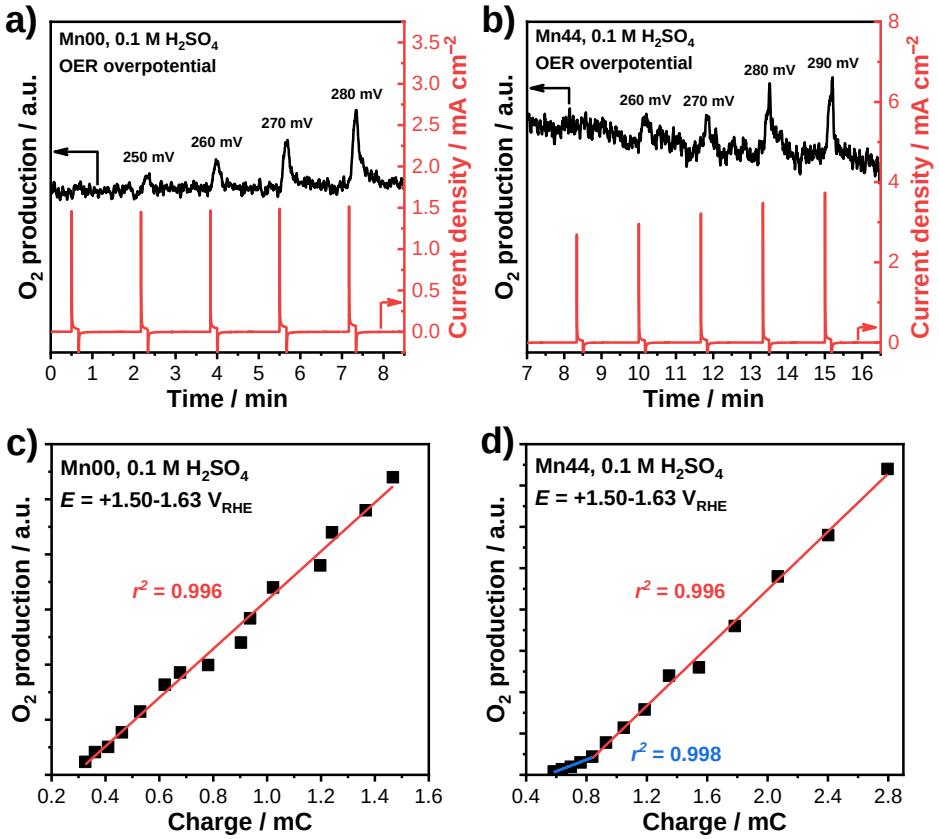

Figure 3.8. Potential-dependent O_2^+ (m/z = 32) ion currents of a) Mn00 and b) Mn44 samples recorded at low overpotential values (η > 240 mV); corresponding Faraday plots of c) Mn00 and d) Mn44 recorded at E = 1.50-1.63 V.

During the OLEMS experiment, we also monitored the signal of the fragment m/z = 34 ($H_2O_2^+$). At the highest potential applied in our experiment (E = 1.63 V_{RHE}, i.e. η_{OER} = 400 mV), this signal accounted for 0.4 ± 0.2 % of the sum between O_2^+ and $H_2O_2^+$ for both Mn00 and Mn44. However, as the thermodynamic potential of the oxidation of water to H_2O_2 is +1.77 V_{RHE}, the formation of H_2O_2 has to be ascribed to the recombination of molecular H_2 and O_2 present in the solution.[75]

3.3.5. Stability evaluation: XPS depth profiles and ICP-OES

To compare the stability of sample Mn44 with sample Mn00 under more severe conditions, we subjected the two samples to a constant electrolysis at E = +1.8 V_{RHE} for 17 h. These tests aimed to provide insights about the structural modifications occurring to the anodes during prolonged electrolysis. The chronoamperograms (Figure B8) show a significant decrease of the current density for the sample Mn44 at the beginning of the test. After this rapid decrease, the current density stabilizes and even after 17 h the recorded current density remains higher than for Mn00. To better understand the degradation process occurring during long-term electrolysis, we performed XPS depth profiling for fresh samples and those subjected to 3 h or 17 h electrolysis at E = +1.8 V_{RHE}. XPS depth profiling analysis comprises cycles of high-energy ion sputtering alternated with XPS measurements. The sputtering time is proportional to the thickness of the layer removed during a sputtering cycle. As a direct correlation between sputtering time and thickness can only be obtained for systems with known sputtering constants, the thickness of the analyzed sample is usually only given in terms of sputtering times. Figure 3.9 shows XPS depth profiles for Mn00 and Mn44 before and after electrolysis for 3 and 17 h (more data in Figure B9). The changes in the depth profiles were more pronounced for Mn44 than for Mn00. For Mn44, leaching of Ru- and Mn-oxides is pronounced after 3 h with only limited changes after further electrolysis. From this, we conclude that the EC-induced dissolution of RuO_2 occurs mostly at the initial stage of electrolysis, in keeping with literature.[76–78] Mn leaching is much more severe than Ru leaching, indicative of the lower stability of the former in the film. The thickness of the films can be semi-quantitatively evaluated from the sputtering times needed to remove Ru and obtain the pure Ti^0 substrate signal. Clearly, this sputtering time is much longer for Mn44 (t_s ≈ 3.5 h) than for Mn00 (t_s ≈ 2 h), confirming that Mn addition increases the thickness of the film by modifying its morphology.

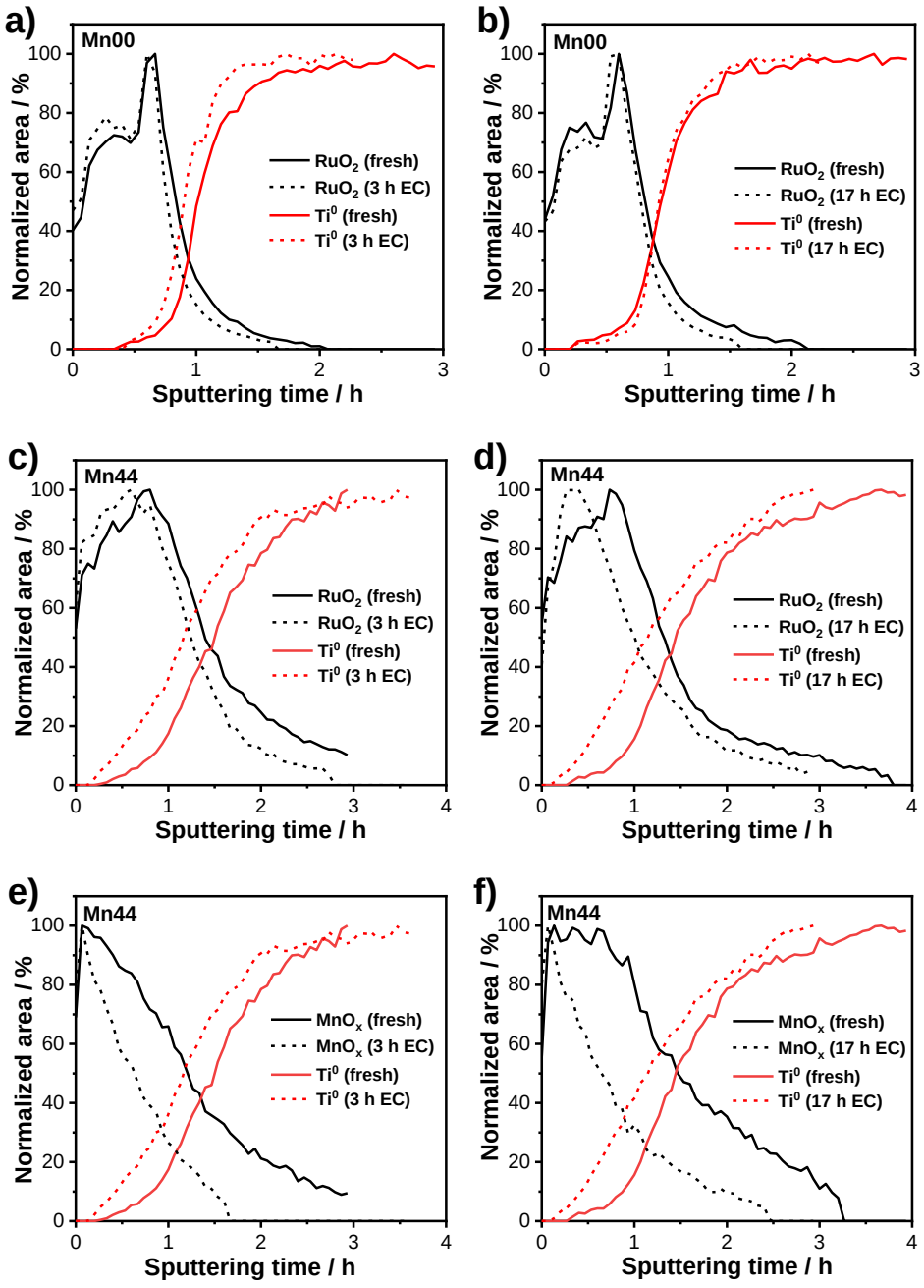

Figure 3.9. XPS depth profiles of a, b) Mn00 and: c, d, e, f) Mn44 subjected to E = 1.8 V_{RHE} in 0.1 M H_2SO_4 for 3 h (a, c, e) and 17 h (b, d, f).

We also measured the elemental composition of the used electrolytes by ICP-OES after 17 h electrolysis (Table 3.3).

The potential applied in the chronoamperometry is higher than the thermodynamic potentials of Ru and Mn dissolution. Ru anodic dissolution involves the formation of RuO_4 thorough the following reaction:

$$RuO_2 + 2H_2O \rightarrow RuO_4 + 4H^+ + 4e^- \quad (3.2)$$

The formation of RuO_4 has a thermodynamic potential of 1.387 V_{SHE}[36,79] and its onset is typically observed close to the OER onset.[80,81]

The dissolution of Mn_2O_3 and Mn_3O_4 in H_2SO_4 includes the formation of an oxyhydroxide,[82] which undergoes disproportionation through the following reaction:

$$2MnOOH + 2H^+ \rightarrow MnO_2 + Mn^{2+} + 2H_2O \quad (3.3)$$

At potentials higher than 1.7 V_{RHE}, MnO_2 is oxidized to MnO_4^- through the following reaction:

$$MnO_2 + 2H_2O \rightarrow MnO_4^- + 4H^+ + 3e^- \quad (3.4)$$

The amount of dissolved metals and the dissolution rates normalized to the geometric surface area listed in Table 3.3 confirm that leaching of Ru, Mn and Ti is more pronounced for Mn44 than for Mn00. This higher dissolution rate can derive from the approximately one-order of magnitude higher ECSA of Mn44 in comparison to Mn00. The ruthenium dissolution rate for sample Mn44 (5.04 nmol cm^{-2} h^{-1}), even though higher than for sample Mn00, is lower than what previously reported for pure RuO_2.[63] This implies that this novel anode composition presents an increased activity compared to standard DSA®, still benefiting from the stabilizing effect of TiO_2.

To take into account the different electrochemical surface areas exposed, we normalized the dissolution rates on the ECSA. The resulting data also given in Table 3.3 show that the surface-normalized Ru dissolution rate in Mn44 (0.008 nmol h^{-1} cm^{-2}_{ECSA}) is two times lower than in Mn00 (0.019 nmol h^{-1} cm^{-2}_{ECSA}). However, as the Ru content in the Mn00 is twice that in Mn44, we conclude that the dissolution rates are nearly similar.

The Ti dissolution rate is higher for Mn44 than for Mn00, which is most likely due to the more extensive exposure of the Ti substrate in the more open Mn-containing film. Therefore, we infer from these data that dissolution of Ru is mainly more severe in the

porous film due to the higher surface area and also that Mn does not influence the intrinsic stability of the films.

The elemental analysis results obtained by ICP-OES can be used to calculate the charge spent in metal dissolution processes by applying Faraday's law and to derive the Faradic efficiencies of these reactions. Assuming that (*3.2*) and (*3.4*) are the oxidation reactions of ruthenium and manganese in sample Mn44, the Faradaic efficiencies of the dissolution of ruthenium and manganese are 0.007% and 0.025%. These extremely low values, in combination with the low selectivity of H_2O_2 measured by OLEMS (0.4 ± 0.2 %), led us to conclude that OER is the main reaction taking place at the anode.

Table 3.3. Amount of metals dissolved during 17 h of constant electrolysis at E = 1.8 V_{RHE} and leaching rates normalized with ECSA (metal content determined by ICP-OES elemental analysis).

	Mn00	**Mn44**
Ru, nmol cm^{-2}	17.8 ± 0.4	85.6 ± 0.5
Mn, nmol cm^{-2}	n/a	412 ± 1
Ti, nmol cm^{-2}	42.1 ± 0.1	711.1 ± 0.9
Ru, nmol h^{-1} cm^{-2}	1.05 ± 0.02	5.04 ± 0.03
Mn, nmol h^{-1} cm^{-2}	n/a	24.26 ± 0.07
Ti, nmol h^{-1} cm^{-2}	2.47 ± 0.01	41.8 ± 0.1
Ru, nmol h^{-1} cm^{-2} $_{ECSA}$	0.019 ± 0.001	0.008 ± 0.001
Mn, nmol h^{-1} cm^{-2} $_{ECSA}$	n/a	0.041 ± 0.001
Ti, nmol h^{-1} cm^{-2} $_{ECSA}$	0.046 ± 0.001	0.070 ± 0.001

3.4. Conclusions

In this work, we synthesized mixed TiO_2-RuO_2 electrodes for acidic water electrolysis by a sol-gel method and investigated the influence of Mn addition on the structure, morphology, activity, and stability of the electrodes for the oxygen evolution reaction. The presence of Mn in the preparation led to a more open structure of the mixed oxide film, evident from a strong increase of the electrochemical surface area. Surface-area corrected current densities suggest that Mn inclusion in the film results in a higher intrinsic electrochemical activity of the mixed oxide compared to TiO_2-RuO_2. Detailed characterization shows that Mn is predominantly inserted into the rutile phase, while the segregation of Mn-oxides is evident at higher Mn content. The most active sample contains 44 at% Mn and reaches an overpotential of 386 mV at a current density at 10 mA cm^{-2}, and proved to be stable during electrolysis for 6 h. Its Tafel slope was 50 mV dec^{-1}, close to the value recorded for Mn00 (44 mV dec^{-1}). This performance is high considering that the catalyst was obtained by a simple preparation method and the final film only contained 17 at% Ru. The presence of Mn not only contributes to boosting the electrochemical OER performance of TiO_2-RuO_2 but, at the same time, drastically decreases the precious metal content and thus the price of the anodes. As the segregated Mn-oxides are removed during long-term electrolysis, it is reasonable to conclude that the synergistic effect is due to the inclusion of Mn in mixed TiO_2-RuO_2 anodes. Detailed analysis of the anode surface during long-term electrolysis shows that Ru dissolution is higher in the more porous Mn-promoted film than for the TiO_2-RuO_2 one. Normalization of dissolution rates suggests that the intrinsic dissolution rate of Ru is independent of the morphology and also does not depend on the presence of Mn.

3.5. References

(1) Nocera, D. G.; Lewis, N. S. *Proc. Natl. Acad. Sci. U. S. A.* **2006**, *103* (43), 15729–15735.

(2) Reece, S. Y.; Hamel, J. A.; Sung, K.; Jarvi, T. D.; Esswein, a. J.; Pijpers, J. J. H.; Nocera, D. G. *Science* **2011**, *334*, 645–648.

(3) Cox, C. R.; Lee, J. Z.; Nocera, D. G.; Buonassisi, T. *Proc. Natl. Acad. Sci.* **2014**, *111* (39), 14057–14061.

(4) Luo, J.; Im, J. H.; Mayer, M. T.; Schreier, M.; Nazeeruddin, M. K.; Park, N. G.; Tilley, S. D.; Fan, H. J.; Grätzel, M. *Science* **2014**, *345* (6204), 1593–1596.

(5) Ibrahim, H.; Ilinca, A.; Perron, J. *Renew. Sustain. Energy Rev.* **2008**, *12* (5), 1221–1250.

(6) Suen, N.-T.; Hung, S.-F.; Quan, Q.; Zhang, N.; Xu, Y.-J.; Chen, H. M. *Chem. Soc. Rev.* **2017**, *46* (2), 337–365.

(7) Scarr, R. F. *J. Electrochem. Soc.* **1969**, *116* (11), 1526.

(8) McCrory, C. C. L.; Jung, S.; Ferrer, I. M.; Chatman, S. M.; Peters, J. C.; Jaramillo, T. F. *J. Am. Chem. Soc.* **2015**, *137* (13), 4347–4357.

(9) Yagi, M.; Kaneko, M. *Chem. Rev.* **2001**, *101* (1), 21–36.

(10) Roger, I.; Shipman, M. A.; Symes, M. D. *Nat. Rev. Chem.* **2017**, *1*, 1–13.

(11) Burke, M. S.; Enman, L. J.; Batchellor, A. S.; Zou, S.; Boettcher, S. W. *Chem. Mater.* **2015**, *27* (22), 7549–7558.
(12) Gong, M.; Dai, H. *Nano Res.* **2015**, *8* (1), 23–39.
(13) Li, X.; Walsh, F. C.; Pletcher, D. *Phys. Chem. Chem. Phys.* **2011**, *13* (3), 1162–1167.
(14) Gong, M.; Li, Y.; Wang, H.; Liang, Y.; Wu, J. Z.; Zhou, J.; Wang, J.; Regier, T.; Wei, F.; Dai, H. *J. Am. Chem. Soc.* **2013**, *135*, 8452–8455.
(15) Gao, M.; Sheng, W.; Zhuang, Z.; Fang, Q.; Gu, S.; Jiang, J.; Yan, Y. *J. Am. Chem. Soc.* **2014**, *136* (19), 7077–7084.
(16) Lu, X.; Zhao, C. *Nat. Commun.* **2015**, *6*, 6616.
(17) Deng, X.; Tuysuz, H. *ACS Catal.* **2014**, *4*, 3701–3714.
(18) Kanan, M. W.; Nocera, D. G. *Science* **2008**, *321* (5892), 1072–1075.
(19) Surendranath, Y.; Kanan, M. W.; Nocera, D. G. *J. Am. Chem. Soc.* **2010**, *132* (14), 16501–16509.
(20) Esswein, A. J.; Surendranath, Y.; Reece, S. Y.; Nocera, D. G. *Energy Environ. Sci.* **2011**, *4* (2), 499–504.
(21) Surendranath, Y.; Lutterman, D. A.; Liu, Y.; Nocera, D. G. *J. Am. Chem. Soc.* **2012**, *134* (14), 6326–6336.
(22) Zaharieva, I.; Chernev, P.; Risch, M.; Klingan, K.; Kohlhoff, M.; Fischer, A.; Dau, H. *Energy Environ. Sci.* **2012**, *5* (5), 7081–7089.
(23) Bergmann, A.; Zaharieva, I.; Dau, H.; Strasser, P. *Energy Environ. Sci.* **2013**, *6* (9), 2745–2755.
(24) Huynh, M.; Shi, C.; Billinge, S. J. L.; Nocera, D. G. *J. Am. Chem. Soc.* **2015**, *137* (47), 14887–14904.
(25) Takashima, T.; Hashimoto, K.; Nakamura, R. *J. Am. Chem. Soc.* **2012**, *134* (3), 1519–1527.
(26) Etzi Coller Pascuzzi, M.; Selinger, E.; Sacco, A.; Castellino, M.; Rivolo, P.; Hernández, S.; Lopinski, G.; Tamblyn, I.; Nasi, R.; Esposito, S.; Manzoli, M.; Bonelli, B.; Armandi, M. *Electrochim. Acta* **2018**, *284*.
(27) McCrory, C. C. L.; Jung, S.; Peters, J. C.; Jaramillo, T. F. *J. Am. Chem. Soc.* **2013**, *135* (45), 16977–16987.
(28) Jung, S.; McCrory, C. C. L.; Ferrer, I. M.; Peters, J. C.; Jaramillo, T. F. *J. Mater. Chem. A* **2016**, *4* (8), 3068–3076.
(29) Trotochaud, L.; Ranney, J. K.; Williams, K. N.; Boettcher, S. W. *J. Am. Chem. Soc.* **2012**, *134* (41), 17253–17261.
(30) Carmo, M.; Fritz, D. L.; Mergel, J.; Stolten, D. *Int. J. Hydrogen Energy* **2013**, *38* (12), 4901–4934.
(31) Ayers, K. E.; Anderson, E. B.; Capuano, C.; Carter, B.; Dalton, L.; Hanlon, G.; Manco, J.; Niedzwiecki, M. *ECS Trans.* **2010**, *33* (1), 3–15.
(32) Beer, H. B. *J. Electrochem. Soc.* **1980**, *127* (8), 303C-307C.
(33) Trasatti, S. *Electrochim. Acta* **2000**, *45* (15–16), 2377–2385.
(34) Comninellis, C.; Vercesi, G. P. *J. Appl. Electrochem.* **1991**, *21* (4), 335–345.
(35) Lee, Y.; Suntivich, J.; May, K. J.; Perry, E. E.; Shao-Horn, Y. *J. Phys. Chem. Lett.* **2012**, *3*, 399–404.
(36) Hodnik, N.; Jovanovič, P.; Pavlišič, A.; Jozinović, B.; Zorko, M.; Bele, M.; Šelih, V. S.; Šala, M.; Hočevar, S.; Gaberšček, M. *J. Phys. Chem. C* **2015**, *119* (18), 10140–10147.
(37) Nguyen, T. D.; Scherer, G. G.; Xu, Z. J. *Electrocatalysis* **2016**, *7* (5), 420–427.
(38) Paoli, E. A.; Masini, F.; Frydendal, R.; Deiana, D.; Schlaup, C.; Malizia, M.; Hansen, T. W.; Horch, S.; Stephens, I. E. L.; Chorkendorff, I. *Chem. Sci.* **2015**, *6* (1), 190–196.
(39) Reier, T.; Oezaslan, M.; Strasser, P. *ACS Catal.* **2012**, *2* (8), 1765–1772.
(40) Macounova, K.; Jirkovsky, J.; Makarova, M.; Franc, J.; Krtil, P. *J. Solid State Electrochem.* **2009**, *13* (6), 959–965.
(41) Macounová, K.; Makarova, M.; Jirkovský, J.; Franc, J.; Krtil, P. *Electrochim. Acta* **2008**, *53* (21), 6126–6134.
(42) Jirkovský, J.; Hoffmannová, H.; Klementová, M.; Krtil, P. *J. Electrochem. Soc.* **2006**, *153* (6), E111–E118.
(43) Macounová, K.; Makarova, M.; Franc, J.; Jirkovský, J.; Krtil, P. *Electrochem. Solid-State Lett.* **2008**, *11* (12), F27.
(44) Petrykin, V.; MacOunova, K.; Franc, J.; Shlyakhtin, O.; Klementova, M.; Mukerjee, S.; Krtil, P. *Chem.*

Mater. **2011**, *23* (2), 200–207.
(45) Browne, M. P.; Nolan, H.; Duesberg, G. S.; Colavita, P. E.; Lyons, M. E. G. *ACS Catal.* **2016**, *6* (4), 2408–2415.
(46) Browne, M. P.; Nolan, H.; Twamley, B.; Duesberg, G. S.; Colavita, P. E.; Lyons, M. E. G. *ChemElectroChem* **2016**, *3* (11), 1847–1855.
(47) Cipris, D.; Pouli, D. *J. Electroanal. Chem.* **1976**, *73*, 125–128.
(48) Morita, M.; Iwakura, C.; Tamura, H. *Electrochim. Acta* **1978**, *23* (4), 331–335.
(49) Fernandez, J. L.; Chialvo, M. R. G. DE; Chialvo, A. C. *J. Appl. Electrochem.* **2002**, *2* (3), 513–520.
(50) Guglielmi, M.; Colombo, P.; Rigato, V. *J. Electrochem. Soc.* **1992**, *139* (6), 1655–1661.
(51) Morgan, D. J. *Surf. Interface Anal.* **2015**, *47* (11), 1072–1079.
(52) Goryachev, A.; Gao, L.; Zhang, Y.; Rohling, R. Y.; Vervuurt, R. H. J.; Bol, A. A.; Hofmann, J. P.; Hensen, E. J. M. *ChemElectroChem* **2018**, *5* (8), 1230–1239.
(53) Goryachev, A.; Gao, L.; van Veldhoven, R. P. J.; Haverkort, J. E. M.; Hofmann, J. P.; Hensen, E. J. M. *Phys. Chem. Chem. Phys.* **2018**, *20*, 14242–14250.
(54) Aparicio, M.; Klein, L. *J. Sol-Gel Sci. Technol.* **2004**, *29* (2), 81–88.
(55) Biesinger, M. C.; Payne, B. P.; Grosvenor, A. P.; Lau, L. W. M.; Gerson, A. R.; Smart, R. S. C. *Appl. Surf. Sci.* **2011**, *257* (7), 2717–2730.
(56) Galakhov, V. R.; Demeter, M.; Bartkowski, S.; Neumann, M.; Ovechkina, N. A.; Kurmaev, E. Z.; Lobachevskaya, N. I.; Mukovskii, Y. M.; Mitchell, J.; Ederer, D. L. *Phys. Rev. B - Condens. Matter Mater. Phys.* **2002**, *65* (11), 1–4.
(57) Chigane, M.; Ishikawa, M. *J. Electrochem. Soc.* **2000**, *147* (6), 2246.
(58) Gorlin, Y.; Jaramillo, T. F. *J. Am. Chem. Soc.* **2010**, *132* (39), 13612–13614.
(59) Nelson, A. J.; Reynolds, J. G.; Roos, J. W. *J. Vac. Sci. Technol. A* **2000**, *18* (4), 1072–1076.
(60) Barr, T. L.; Seal, S. *J. Vac. Sci. Technol. A Vacuum, Surfaces, Film.* **1995**, *13* (3), 1239–1246.
(61) Shrivastava, P.; Moats, M. S. *J. Appl. Electrochem.* **2009**, *39* (1), 107–116.
(62) Trieu, V.; Schley, B.; Natter, H.; Kintrup, J.; Bulan, A.; Hempelmann, R. *Electrochim. Acta* **2012**, *78*, 188–194.
(63) Frydendal, R.; Paoli, E. A.; Knudsen, B. P.; Wickman, B.; Malacrida, P.; Stephens, I. E. L.; Chorkendorff, I. *ChemElectroChem* **2014**, *1* (12), 2075–2081.
(64) Tahir, M.; Pan, L.; Idrees, F.; Zhang, X.; Wang, L.; Zou, J. J.; Wang, Z. L. *Nano Energy* **2017**, *37*, 136–157.
(65) Doyle, R. L.; Godwin, I. J.; Brandon, M. P.; Lyons, M. E. G. *Phys. Chem. Chem. Phys.* **2013**, *15* (33), 13737.
(66) Kim, J.; Shih, P. C.; Tsao, K. C.; Pan, Y. T.; Yin, X.; Sun, C. J.; Yang, H. *J. Am. Chem. Soc.* **2017**, *139* (34), 12076–12083.
(67) Fang, Y. H.; Liu, Z. P. *J. Am. Chem. Soc.* **2010**, *132* (51), 18214–18222.
(68) Oh, H. S.; Nong, H. N.; Reier, T.; Bergmann, A.; Gliech, M.; Ferreira De Araújo, J.; Willinger, E.; Schlögl, R.; Teschner, D.; Strasser, P. *J. Am. Chem. Soc.* **2016**, *138* (38), 12552–12563.
(69) Diaz-Morales, O.; Raaijman, S.; Kortlever, R.; Kooyman, P. J.; Wezendonk, T.; Gascon, J.; Fu, W. T.; Koper, M. T. M. *Nat. Commun.* **2016**, *7*, 12363.
(70) Sun, S.; Li, H.; Xu, Z. J. *Joule* **2018**, *2* (6), 1024–1027.
(71) Tsuji, E.; Imanishi, A.; Fukui, K. I.; Nakato, Y. *Electrochim. Acta* **2011**, *56* (5), 2009–2016.
(72) Oellers, T.; Fruchter, L.; Pizzutilo, E.; Geiger, S.; Kasian, O.; Ledendecker, M.; Mingers, A. M.; Cherevko, S.; Koper, M. T. M.; Mayrhofer, K. J. J.; Li, Z.; Diaz-Morales, O.; Ludwig, A.; Fu, W. T. *Nat. Catal.* **2018**, *1* (7), 508–515.
(73) Huynh, M.; Ozel, T.; Liu, C.; Lau, E. C.; Nocera, D. G. *Chem. Sci.* **2017**, *8* (7), 4779–4794.
(74) Boytsova, O. V.; Shekunova, T. O.; Baranchikov, A. E. *Russ. J. Inorg. Chem.* **2015**, *60* (5), 546–551.
(75) Shi, X.; Siahrostami, S.; Li, G.-L.; Zhang, Y.; Chakthranont, P.; Studt, F.; Jaramillo, T. F.; Zheng, X.; Nørskov,

J. K. *Nat. Commun.* **2017**, *8*, 701.

(76) Cherevko, S. *J. Electroanal. Chem.* **2017**, *787*, 11–13.

(77) Cherevko, S.; Zeradjanin, A. R.; Topalov, A. A.; Kulyk, N.; Katsounaros, I.; Mayrhofer, K. J. J. *ChemCatChem* **2014**, *6* (8), 2219–2223.

(78) Cherevko, S.; Geiger, S.; Kasian, O.; Kulyk, N.; Grote, J. P.; Savan, A.; Shrestha, B. R.; Merzlikin, S.; Breitbach, B.; Ludwig, A.; Mayrhofer, K. J. J. *Catal. Today* **2016**, *262*, 170–180.

(79) Fabbri, E.; Habereder, A.; Waltar, K.; Kötz, R.; Schmidt, T. J. *Catal. Sci. Technol.* **2014**, *4* (11), 3800–3821.

(80) Kötz, R.; Stucki, S.; Scherson, D.; Kolb, D. M. *J. Electroanal. Chem. Interfacial Electrochem.* **1984**, *172* (1–2), 211–219.

(81) Wohlfahrt-Mehrens, M.; Heitbaum, J. *J. Electroanal. Chem. Interfacial Electrochem.* **1987**, *237* (2), 251–260.

(82) Artamonova, I. V.; Gorichev, I. G.; Godunov, E. B. *Engineering* **2013**, *05* (09), 714–719.

Appendix B

Supporting Information for Chapter 3

B.1. Electrochemical performance of Ti substrate

The impact of anodic current densities of Ti substrate was evaluated in the wide range of anodic potentials used in this work (Figure B1a). Even at highest anodic potential (E = +1.8 V_{RHE}) the current density of the Ti substrate was found to be negligible ($j_{Ti} \approx 1.4$ µA cm^{-2}, Figure B1b) compared to the observed current densities of the tested electrodes ($j > 1$ mA cm^{-2}, e.g. Figure 3.4a).

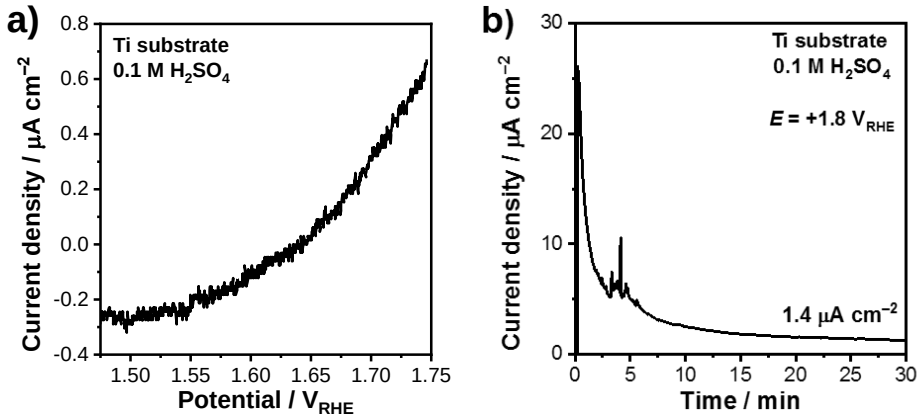

Figure B1. a) Linear Sweep Voltammogram and b) chronoamperogram (E = +1.8 V_{RHE}) of bare Ti substrate recorded in 0.1 M H_2SO_4.

B.2. XPS analysis of Mn-doped anodes

Table B1. Values of Mn 3s splitting (± 0.05 eV) for the electrocatalysts.

Sample ID	Δ Mn 3s (eV)	
	Fresh anodes	After 6 hours at j = 1 mA cm^{-2}
Mn09	5.05	5.05
Mn33	5.29	5.16
Mn44	5.22	4.85
Mn60	5.40	4.81

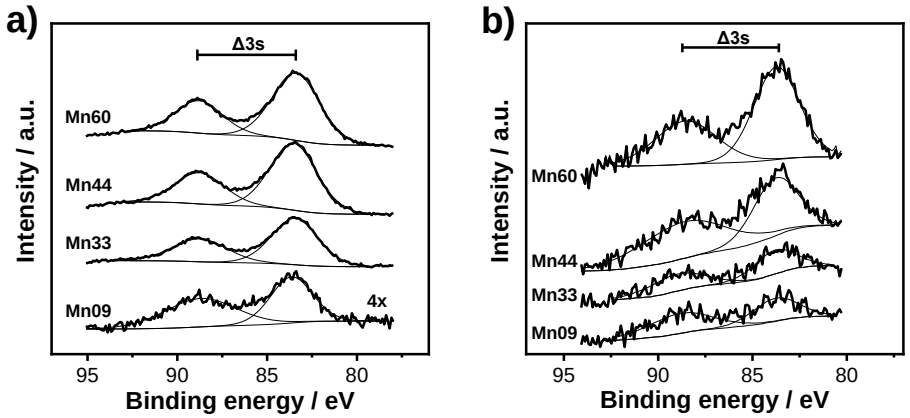

Figure B2. Mn 3s spectra of the samples subjected to 6 hours of electrolysis in 0.1 M H_2SO_4 at j = 1 mA cm^{-2}.

Table B2. Surface fraction of metals in samples Mn00 and Mn44 determined by XPS. Values in brackets indicate the values after the samples were tested at 1 mA cm^{-2} for 6 h in 0.1 M H_2SO_4.

Sample ID	Ti, at%	Ru, at%	Mn, at%
Mn00	70 (68)	30 (32)	-
Mn44	18 (49)	11 (34)	71 (17)

B.3. Morphology of electrodes

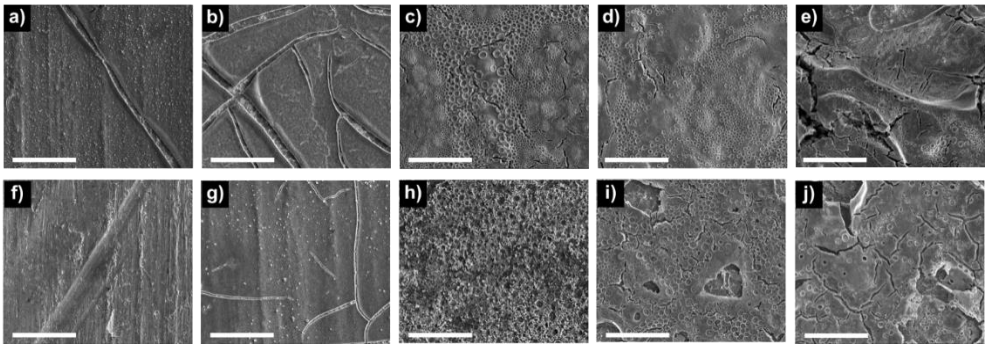

Figure B3. Low magnification electron micrographs acquired in normal detection mode using secondary electrons for fresh samples (top) and samples after 6 h of electrolysis in 0.1 M H_2SO_4 at j = 1 mA cm^{-2} (bottom): a, f) Mn00; b, g) Mn09; c, h) Mn33; d, i) Mn44; e, j) Mn60. Scale bars are 20 µm.

B.4. Elemental distribution in Mn00 sample

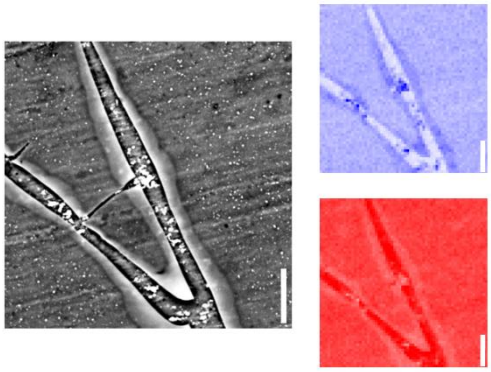

Figure B4. EDX elemental mapping of fresh sample Mn00 of titanium (red) and ruthenium (blue). Scale bars are equal to 10 µm.

B.5. Electrochemical performance of sample $Ti_{0.7}Mn_{0.3}$

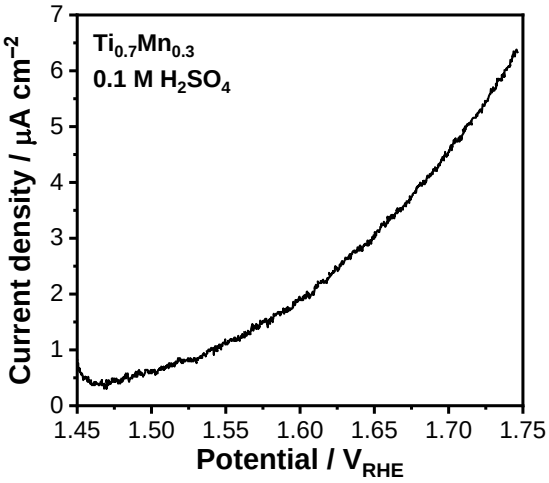

Figure B5. Linear sweep voltammogram of sample $Ti_{0.7}Mn_{0.3}$ recorded in 0.1 M H_2SO_4.

B.6. XRD of electrochemically tested samples

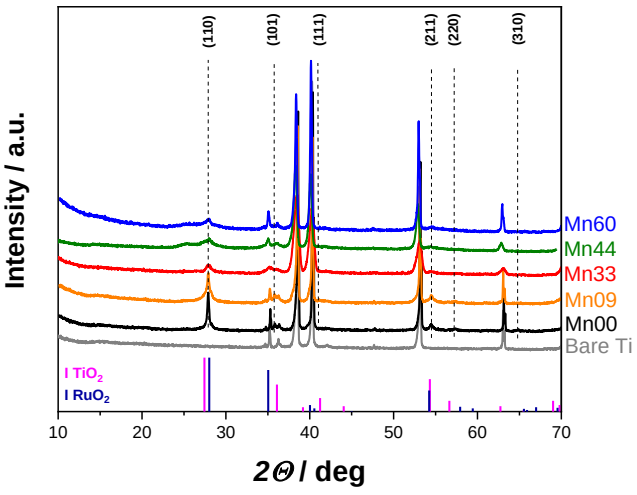

Figure B6. X-ray diffractograms of the samples after 6 hours of electrolysis at 1 mA cm^{-2} in 0.1 M H_2SO_4. Dashed lines indicate the rutile peaks of the solid solution formed by TiO_2 (JCPDS#21-1276) and RuO_2 (JCPDS#40-1290).

B.7. Online Electrochemical Mass Spectrometry (OLEMS)

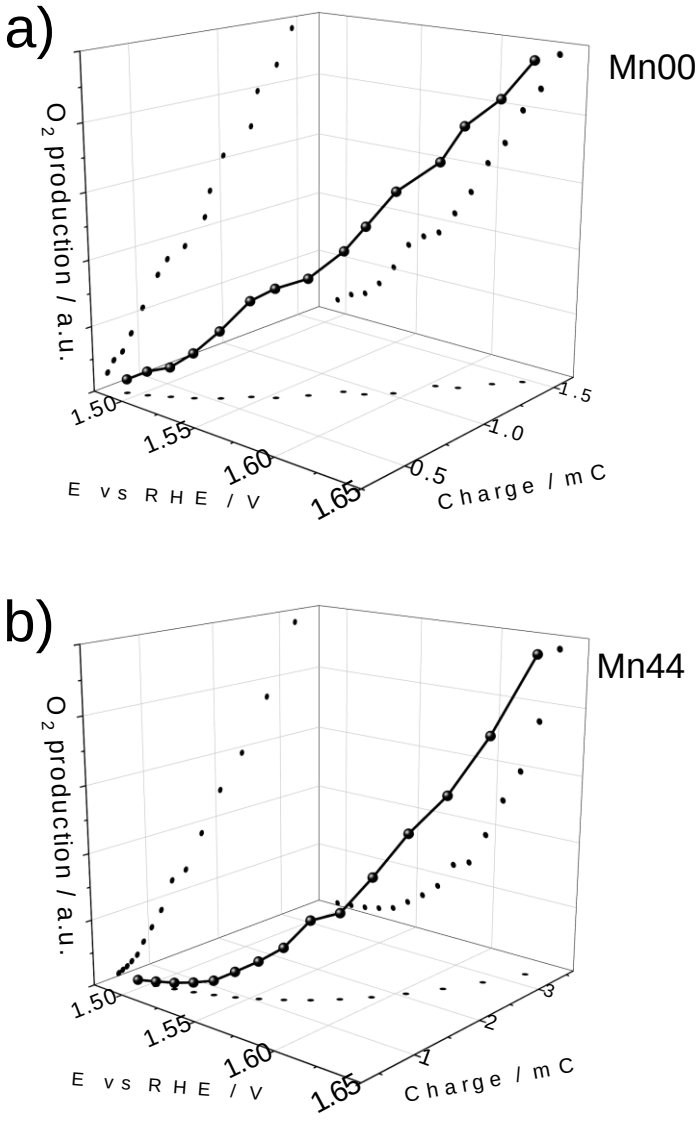

Figure B7. Three-dimensional representations correlating the O_2 production with potential and charge for samples a) Mn00 and b) Mn44 in 0.1 M H_2SO_4. The projections of the O_2 production versus charge result in the Faraday plots, which are reported in Figure 3.8c,d in the main text.

B.8. Stability evaluation of the anodes

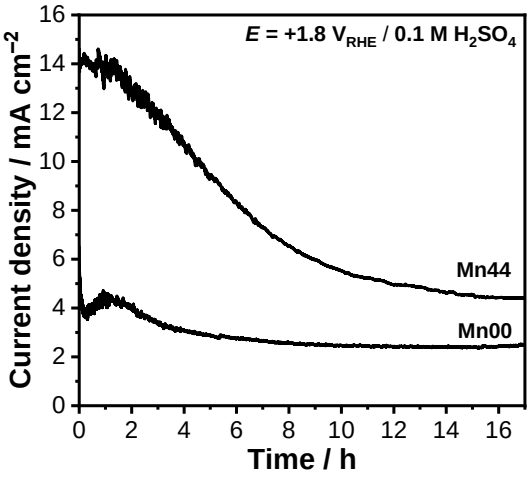

Figure B8. Chronoamperograms of the samples subjected to long-term stability test (E = +1.8 V_{RHE}, 0.1 M H_2SO_4, 17 h).

B.9. Homogeneity of the elemental distribution in the anodes

In order to evaluate the homogeneity of the as-prepared Mn00 and Mn44 films, XPS depth profiles were taken at different spots on the surface of the fresh anodes. To construct the depth profiles (DPs) for Ru, Ti and Mn, we used the integrated areas of Ru 3d, Ti 2p and Mn 2p core levels, respectively. No additional deconvolution of the spectral regions was performed due to the artificial changes in oxidation states induced by high-energy Ar^+ sputtering. Thus, the areas of Ti 2p and Ru 3p core levels were integrated as a single region due to their significant overlap.

The differences in sputtering times within the sample were then compared to detect any possible deviation in bulk elemental distribution. Only slight changes in the bulk elemental distribution were observed for Mn00. Particularly, at the sputtering times higher than 50 min (*i.e.* 42 % of the film thickness) some variations in Ru distribution were observed and did not exceed 5 % (Figure B9a). The same behavior was found for Ti distribution in this sample (Figure B9b). Mn44 electrode demonstrates a slightly higher degree of inhomogeneity, reaching 5-10% of DPs mismatch at most (Figure B9c, d).

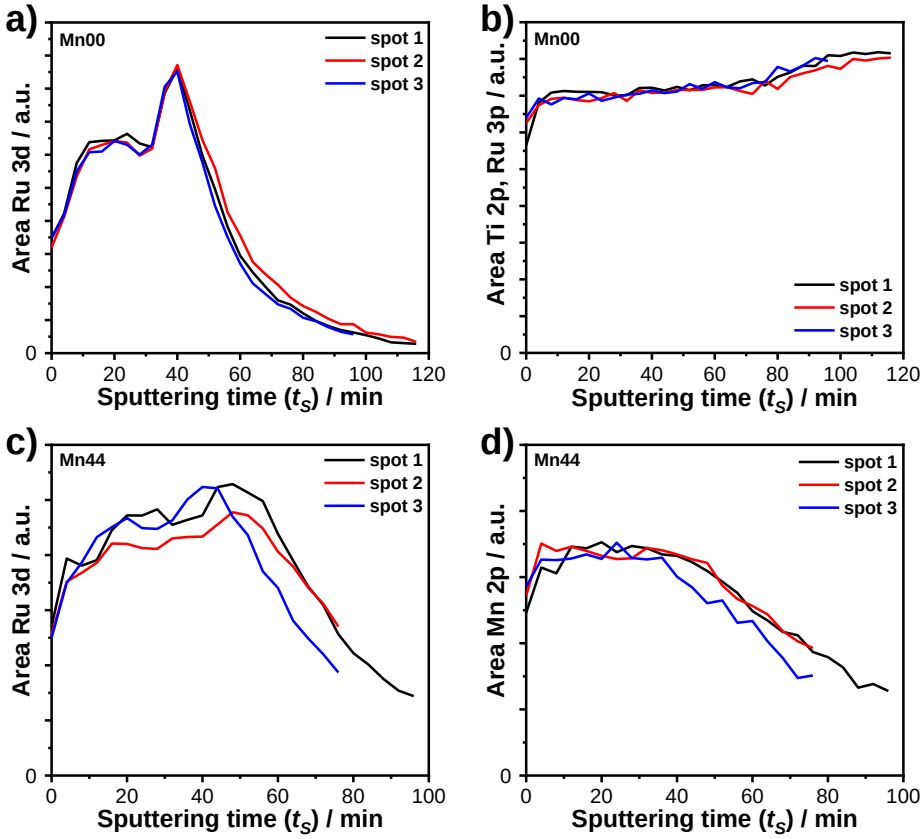

Figure B9. XPS depth profiles of fresh a-b) Mn00 and c-d) Mn44 samples taken in different spots of the sample.

Chapter 4

Promoting oxygen evolution of IrO_2 in acid electrolyte by Mn

Abstract

IrO_2 is considered one of the most active electrocatalysts for the oxygen evolution reaction (OER) relevant to electrochemical water splitting in, for instance, proton-exchange membrane electrolyzers. Scaling up of such catalysts is hampered by the high price of Ir. We demonstrate in this work that IrO_2 can be promoted by Mn in terms of electrochemical performance at nearly similar stability. The enhancement in electrochemical performance can be attributed to a higher electrochemically active surface and a higher intrinsic activity of the Ir-Mn oxide surface. Mn promotion led to lower Tafel slopes and higher surface-normalized current densities and can be related to the introduction of Mn in the crystalline structure of IrO_2. Specifically, the introduction of Mn led to an increased amount of Ir^{3+} species at the surface, which are thought to be involved in the OER. Extensive characterization showed that the fresh anodes consisted of Mn-doped IrO_2 with Mn_3O_4 at higher Mn content. The latter spinel oxides were easily removed during initial anodic polarization. The synergy between Ir and Mn is maintained during chronopotentiometric stability test.

This chapter has been published as:
Etzi Coller Pascuzzi, M.; Hofmann, J. P.; Hensen, E. J. M. *Electrochim. Acta* **2020**, accepted.

4.1. Introduction

The increasing supply of energy obtained from fluctuating renewable sources requires proper solutions to store the excess of mostly electric energy for successive use. Water splitting is a promising technology to convert energy from intermittent sources into hydrogen, which can be used as fuel or chemical.[1] The sluggish kinetics of the oxygen evolution reaction (OER) taking place at the anode constitutes a major hurdle in scaling up this process.[2] Thus, improved OER catalysts are needed to increase the reaction rate and thus to maximize the overall efficiency of electrochemical water splitting reactors.[3] The acidic conditions used in electrolyzers utilizing a proton-exchange membrane (PEM) limit the choice of suitable metals for OER catalysts.[4,5] Ir-oxide represents the state of the art in terms of activity and stability among PEM-based OER catalysts.[6] The high price of Ir, which is a by-product of Pt production, hinders the scalability of PEM water electrolysis technology.[7] Two explored methods involve the tailoring of Ir-oxides in terms of crystallinity and the addition of cheaper transition metals towards higher activity and stability in the OER.

Hydrous and amorphous IrO_2 exhibited higher OER activity in comparison to crystalline and thermally prepared IrO_2.[8,9] The high activity of hydrous IrO_2 has been attributed to bulk defects in the early work of Gottesfald and Srinivasan.[10] A lower calcination temperature for thermally prepared Ir-oxides was also found to enhance OER activity, presumably due to the higher structural flexibility of the surface.[11] More recently, Pfeifer et al. ascribed the higher activity of amorphous IrO_2 compared with rutile IrO_2 to increased amounts of Ir^{3+} and electrophilic oxygen (O^-) species at the surface.[12,13] On the other hand, less crystalline and hydrous IrO_2 suffers from lower stability, because it is prone to a faster dissolution under OER conditions.[11,14,15] With a few exceptions, a lower calcination temperature is reported to increase the activity of IrO_2, albeit that the stability is impeded.[9,14] Recently, Geiger at al. explained the low stability of amorphous Ir-oxide by the instability of Ir intermediates caused by oxygen vacancies.[16] The authors mentioned that the strategies for the improvement of IrO_2 OER catalysts should focus on the activity improvement of crystalline IrO_2 or the stabilization of amorphous IrO_2. Thus, it is important to assess the balance between activity and stability of Ir-based electrocatalysts.[16,17]

The introduction of cheaper elements in Ir-oxide represents another interesting approach to lower the Ir content of OER catalysts. A requirement is that activity and stability of the resulting bimetallic oxides are not significantly impeded. For example, mixed Ir-Ni oxide catalysts for OER[18–20] exhibited higher intrinsic activity when compared to IrO_2.[18] Despite a higher activity, these catalysts are less stable due to higher Ir dissolution rates. Recently,

Strickler et al. investigated a series of bimetallic Ir-based materials (Ir-Sn, Ir-Cr, Ir-Ti, Ir-Ni) and found that Cr is the most effective promoter for achieving a high intrinsic activity of Ir-oxide.[21] In a previous report, the use of Cr and Mn as dopants for IrO_2 was also reported to be beneficial for alkaline OER, the photo-oxidation of thiol, and CO oxidation, because it led to a higher number of vacancies at the catalytic surface.[22] Mixed rutile IrO_2-MnO_2 has also been proposed as a suitable material for acidic water splitting;[23] in two follow-up studies, the promising performance of F-doped mixed IrO_2-MnO_2 for the acidic OER was mentioned.[24,25] Similarly, it was found that Mn incorporation led to a higher activity of RuO_2[26,27] and mixed TiO_2-RuO_2 anodes,[28] which share the same crystalline rutile structure with IrO_2. Ir was also used as a dopant to increase the OER activity of cryptomelane-type Mn oxide, which does not crystallize in a rutile structure; the tunnel structure of cryptomelane facilitates water insertion into the material, which results in an enhanced OER activity.[29]

Here we present a systematic investigation of the Ir-Mn synergy in the OER. We aim at determining the overall performance of IrO_2 and Mn-doped IrO_2 anodes in acidic solutions relevant to PEM electrolyzers and establishing structural and electronic aspects that contribute to Mn promotion.

4.2. Experimental

4.2.1. Film preparation

Electrodes were prepared by spin-coating a solution containing the metal precursors on a Ti substrate, followed by a thermal treatment to form the desired oxides. Before deposition, the Ti foils (99.5%, Alfa Aesar) were sonicated in acetone for 15 min, rinsed with ethanol, and then with deionized water. Ir and Mn solutions were prepared by dissolving Ir(IV) chloride (99.95%, Alfa Aesar) and Mn(II) chloride tetrahydrate (≥ 98%, Sigma-Aldrich) in absolute ethanol at a concentration of 0.5 mol_{metal} dm^{-3}. The solutions were then mixed to give the desired atomic Ir:Mn ratios followed by spin-coating on the Ti substrates at 1500 rpm. The substrates were then spun for another 60 s at 4000 rpm to complete the deposition process. The as-prepared samples were finally calcined at 400 °C for 1 h in air. The selected Ir:Mn atomic ratios were 100:0, 75:25, 50:50, 30:70, 15:85, and 0:100. The samples are denoted by Mn*x*, in which *x* represents the atomic percentage of Mn.

4.2.2. Electrochemical characterization

Electrochemical measurements were carried out in a standard three-electrode cell at room temperature with an Autolab PGSTAT30 potentiostat (Metrohm Autolab B.V.). Ti-supported

films with a geometric area of 1 cm^2 were used as working electrodes (WE). A Pt foil (area $\simeq$ 5 cm^2) was used as counter electrode and a Ag/AgCl electrode (Radiometer Analytical, E_{RE} = +0.24 V) as reference electrode. A 0.1 M H_2SO_4 (H_2SO_4 Sigma Aldrich, 99.999%) solution was used as electrolyte in all the electrochemical tests. Milli-Q water (18.2 MΩ·cm) was used in all cleaning and dilution steps. Potentials were *iR*-corrected and reported *vs*. the Reversible Hydrogen Electrode (RHE). Current densities were normalized using the geometric areas of the electrodes unless mentioned otherwise. After immersion in the electrolyte, the samples were firstly subjected to five cycles of cyclic voltammetry at a scan rate of 50 mV s^{-1} in the OER region. The catalytic activity was then evaluated by linear sweep voltammetry (LSV) recorded at a scan rate of 1 mV s^{-1} in the anodic direction.

Step chronoamperometry was conducted by increasing the potential in 20 mV steps and applying a hold time of 30 s at each step. This method can be considered a "quasi steady-state" measurement as the hold time is long enough to neglect transient currents due to double-layer charging and oxidation state changes of the catalyst, but short enough to prevent catalyst degradation.[21,30] The current densities measured at the end of each potential step were then plotted *vs.* the overpotential (η) to construct the Tafel plots.

Cyclic voltammetry (CV) was performed at a scan rate of 50 mV s^{-1} between 0 and 1.4 V_{RHE}. The anodic charge q^* was determined by the integration of the voltammograms in the potential window 0.4-1.4 V_{RHE}. The as-obtained values of q^* were used to normalize the catalytic results on the electrochemically active surface area of the catalysts.

Electrochemical impedance spectroscopy (EIS) measurements were carried out at E = +1.58 V_{RHE} in the frequency range 0.1-10^3 Hz with an AC amplitude of 10 mV. The results were fitted with an $R_s(R_{ct}C_{dl})$ equivalent circuit in Nova 1.10 Software, where R_s corresponds to the series resistance (solution, contacts, cables), R_{ct} to the charge-transfer resistance, and C_{dl} to the double-layer capacitance of the electrodes. The values of R_s were used to *iR*-correct the potentials of the activity and stability tests, while the values of C_{dl} were used to normalize the current densities on the electrochemical surface area, where specifically mentioned.

Chronopotentiometry (CP) at a constant current density of 10 mA cm^{-2} for 16 h was employed to assess the stability of the catalysts. The solutions were stirred during the measurements to avoid the accumulation of bubbles at the electrode surface. The electrolytes were successively analyzed by ICP-OES elemental analysis (see section 4.2.3).

4.2.2. Characterization of used electrolytes

The amount of dissolved Ir and Mn species in the used electrolytes was determined by inductively coupled plasma optical emission spectrometry (ICP-OES) performed on a SPECTROBLUE spectrometer equipped with an axial plasma source (Ar).

4.2.3. Materials characterization

X-ray diffraction (XRD) patterns were obtained using a Bruker D2 Phaser diffractometer equipped with a Cu K_α radiation source. The diffractograms were recorded with a step size of 0.02° and an acquisition time of 2 s per step, in the 2θ range from 15° to 60°.

X-ray photoelectron spectroscopy (XPS) measurements were carried out on a K-alpha XPS spectrometer (Thermo Scientific) equipped with a monochromatic Al K_α (1486.6 eV) X-ray source. The spot size was 400 µm and the pass energy was set at 200 eV and 50 eV for survey and high-resolution scans, respectively. No charge correction for the energy axis was applied because of the metallic conductive nature of the samples. Depth-profiling XPS experiments were conducted using consecutive Ar^+ sputtering (75 s, 3 kV) and measuring cycles. Ir 4d and Mn 2p areas were used to calculate the content of Ir and Mn in the films. We used the Ir 4d peak instead of the more intense Ir 4f to avoid the overlap of the latter with the Ti 3s signal originating from exposure of the substrate after sputtering.

Scanning electron micrographs (SEM) were taken using a FEI Quanta 3D FEG microscope at an accelerating voltage of 5 kV without additional coating of the surface. Energy dispersive X-Ray (EDX) spectrometry was conducted on a Phenom Pro-X microscope at an accelerating voltage of 10 kV.

Raman spectra were acquired using a Witec Alpha 300R Raman microscope equipped with a monochromatic laser source (λ_{exc} = 532 nm). The laser was focused on the sample using a Zeiss 50x/0.55 lens. The spectra were acquired using a laser power of 10 mW and an accumulation time of 10 s. The reported spectra were obtained by averaging 10 accumulations to obtain a good signal to noise ratio.

4.3. Results

The OER performance of the Ir-Mn oxide films prepared by spin-coating supported on the Ti foil was determined by linear sweep voltammetry (LSV). The results are shown in Figure 4.1a. Compared to the pure Ir oxide sample Mn00, the incorporation of Mn significantly increased the current densities. Figure 4.1a demonstrates a cathodic shift of the

voltammograms and a decrease in the onset potential of the OER upon the addition of Mn. The highest current densities were obtained for samples Mn50 and Mn70. Further addition of Mn led to lower catalytic activity. These data and the negligible activity of the pure Mn sample (Mn100, Figure C1) point to a substantial synergy between Ir and Mn for the OER.

Tafel plots obtained by a step chronoamperometry for all the samples are reported in Figure 4.1b. The results of the Tafel plot analysis allow comparing the intrinsic activity of the different samples. The data summarized in Table 4.1 confirm the enhanced catalytic activity upon Mn addition. In the low-current density region (*i.e.* at $j < 1$ mA cm^{-2}), the Tafel slope of Mn00 is 54 mV dec^{-1}, which is in keeping with the typically reported values of IrO_2 (~ 50-65 mV dec^{-1}).[11,31–34] The Tafel slope of Mn25 is slightly lower (51 mV dec^{-1}) than that of Mn00 sample, while the samples with higher Mn contents exhibit lower slopes (44-49 mV dec^{-1}), pointing to faster OER kinetics or more favorable adsorptive properties of the electrode with respect to oxygen intermediates. The sample with the highest concentration of Mn, Mn85, shows a higher Tafel slope than the other samples (60 mV dec^{-1}).

The Tafel plots of IrO_2-based catalysts usually display a second Tafel region at higher current densities. The observed change in the slope can be interpreted as a change in the reaction mechanism.[32] As we observed this behavior for all samples, we also evaluated the Tafel slopes in this second Tafel region. Lower Tafel slopes were also found upon Mn addition in the high current density region. The decrease is only minor for sample Mn25 with a slope of 122 mV dec^{-1} as compared with 128 mV dec^{-1} for Mn00. Mn50 and Mn70 exhibit even lower slopes (93 mV dec^{-1} and 74 mV dec^{-1}, respectively), while an increase was observed again for sample Mn85 (101 mV dec^{-1}). In summary, the lower slopes in the two Tafel regions recorded for samples with intermediate Mn content confirm their favorable OER kinetics in a wide range of current densities. However, it is difficult to derive firm conclusions about the reaction mechanism based on these slopes as different coverages of adsorbed species can influence them.

Table 4.1. Slopes of all the catalysts in the two linear regions of Tafel plots.

Sample ID	Tafel slope ($j < 1$mA cm^{-2}), mV dec^{-1}	Tafel slope ($j > 1$mA cm^{-2}), mV dec^{-1}
Mn00	54	128
Mn25	51	122
Mn50	44	93
Mn70	49	74
Mn85	60	101

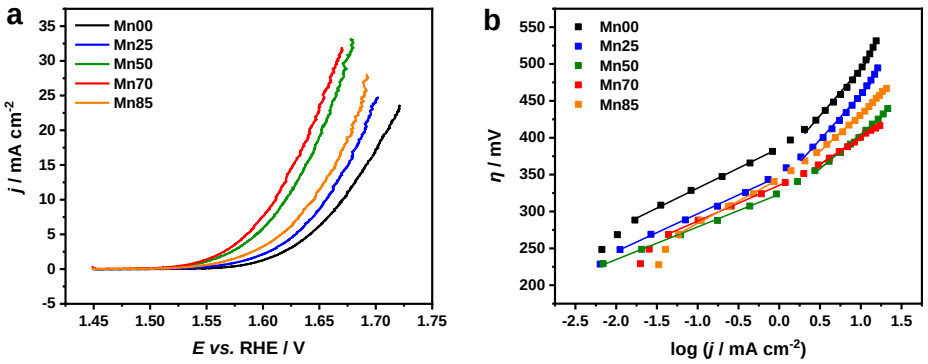

Figure 4.1. a) Linear sweep voltammetry (LSV) of Ir-Mn films recorded in 0.1 M H_2SO_4; b) Tafel plots: experimental data (points) and linear fits (lines).

The overall catalytic activity of the samples can also be evaluated by analyzing the geometric current densities recorded at a fixed overpotential. Figure 4.2a shows the current densities recorded at η = 350 mV during the LSV measurements. The data are normalized to the geometric surface area of the films. Clearly, the addition of Mn substantially improved the overall activity, especially for intermediate Mn loadings. The most active sample Mn70 reached an 8-times higher current density than the IrO_2 reference (Mn00). Mixed Ir-Ni oxide anodes also showed a similar increase in intrinsic activity compared to pure IrO_2.[18]

In order to compare the specific activity of the samples, we need to know their electrochemically active surface areas. For this purpose, we determined the anodic charge q^*, which represents the charge spent in surface modifications. The anodic charge is considered to be proportional to the accessible electrode surface area.[35,36] This approach has been used before to normalize the electrochemical activity of Ir-based catalysts.[8,18,35] Typically, the anodic charge is determined from the integration of the voltammograms in the potential range of 0.4-1.4 V_{RHE}.[16,18,37] Figure 4.2b shows the anodic charge q^* for the various samples. The maximum with respect to the Mn content is obtained for Mn70. Qualitatively similar trends were observed for bimetallic Ir-Mn oxides[23] and Ir-Ni oxides.[18] We used these values to normalize the current densities recorded at η = 350 mV during the LSV measurements and compared these data to the current densities normalized on the geometric area of the films (Figure 4.2a). The current density normalized on the anodic charge is a measure of the electrochemically active surface-specific activity of the samples. These values increased upon Mn addition, reaching a maximum for samples Mn50 and

Mn70. Their specific activities were roughly 2.5 times higher than that of Mn00. This increase is of the same order of magnitude as observed for Ni doping of IrO_2.[18] Increasing the Mn content to 85 at% resulted in a lowering of the specific activity. We validated the surface-normalization of the current densities by the anodic charge method by determining the double-layer capacitance (C_{dl}) obtained from EIS measurements. The double-layer capacitance is also assumed to be proportional to the electrochemical surface area.[38–41] The trends of C_{dl} and specific current densities as a function of the Mn content (Figure C2a, b) are qualitatively similar to those shown in Figure 4.2a, b, thus further confirming the substantial intrinsic synergy between Ir and Mn in mixed oxides.

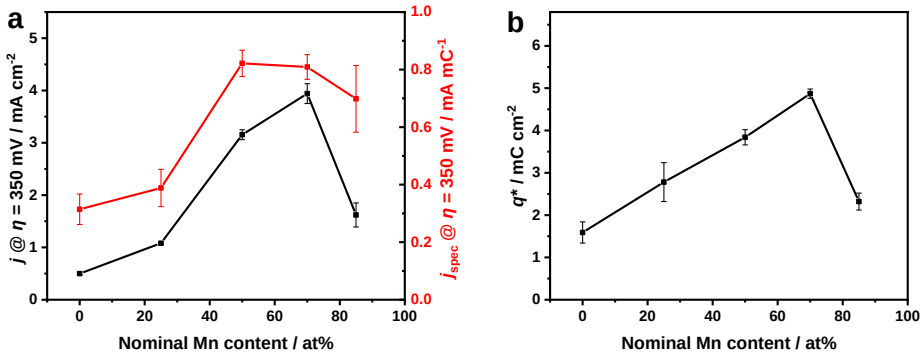

Figure 4.2. Influence of Mn content on a) current densities at η = 350 mV obtained from LSV normalized to the geometric area of the films (in black) and the anodic charge (in red) of the electrodes; b) anodic charge q^* determined by integration of cyclic voltammograms from 0.4 to 1.4 V_{RHE}.

We next evaluated the stability of the tested anodes by chronopotentiometry at a (geometric) current density of 10 mA cm^{-2}. Compared to the Mn00 reference, Mn25, Mn50, and Mn70 samples operated at a lower potential (Figure 4.3a), in agreement with the higher activity reported above. However, while the samples with concentration up to 50 at% of Mn displayed nearly similar increases in the potential during the 16 h stability test, the most active catalyst Mn70 showed a larger potential increase to maintain the current density. This difference points to a lower stability of the Mn70 sample. The response of the Mn85 sample was different in the sense that a sharp increase in the potential occurred already in the first few hours of tests, indicating a very low stability in the OER. We analyzed the Ir content of the used electrolytes by ICP-OES analysis to determine the amount of Ir dissolved

due to the prolonged anodic polarization. The data are collected in Figure 4.3b. The amount of Ir dissolved was highest for Mn50 and Mn70 when normalized to the geometric area of the films. Nevertheless, when normalized to the anodic charge q^*, the amount of Ir dissolved is nearly the same within the accuracy of the measurements. Thus, differences in Ir dissolved during the stability test are mainly due to the differences in the electrochemically active surface area. This, however, cannot explain the stability differences observed in Figure 4.3a. The sharp deactivation observed for sample Mn85 could be due to the low amount of stable IrO_2 phase, insufficient to provide adequate scaffolding and thus to stabilize the films,[42] or to particle agglomeration, detachment, passivation, or blocking of active sites by oxygen bubbles, all leading to a potential increase in the chronopotentiometry.[43] The analysis of dissolved Mn species by ICP-OES in the used electrolytes (Figure C3) showed low values of Mn dissolution (~7 $nmol_{Mn}$ cm^{-2}) for samples Mn25, Mn50, and Mn70. The amount of Mn dissolved for sample Mn85 was about three times higher than for the other samples. A similar ICP-OES measurement using a fresh sample Mn70 for reference showed a substantially higher Mn dissolution. Thus, Mn dissolution from the fresh catalyst is much higher (87 $nmol_{Mn}$ cm^{-2}) than from the used catalyst (7 $nmol_{Mn}$ cm^{-2}), indicating that substantial Mn leaching and surface modifications occurred during the initial stages of electrolysis.

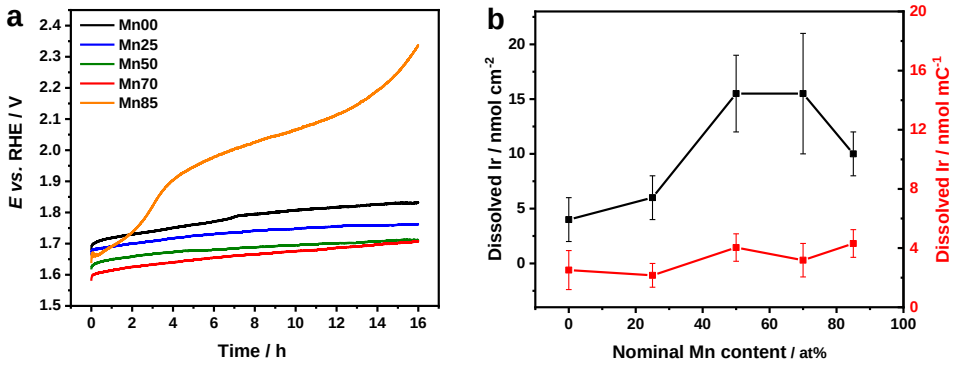

Figure 4.3. a) Chronopotentiometry of the samples recorded at 10 mA cm^{-2} for 16 h in 0.1 M H_2SO_4; b) Amount of dissolved Ir in the used electrolytes measured by ICP-OES analysis normalized to the geometric area (in black) and the anodic charge q^* (in red) of the electrodes.

The structure and phase composition of the catalysts were investigated by XRD. The XRD patterns of all the samples and the bare Ti substrate are reported in Figure 4.4. Sample Mn00 shows the expected XRD pattern of rutile IrO_2. At low Mn loadings, *i.e.* for samples Mn25 and Mn50, we can observe a shift of the IrO_2 peaks toward higher diffraction angles, indicative of a contraction of the unit cell of IrO_2. The shift can be caused by the insertion of Mn cations in the lattice of IrO_2, similarly to what was observed for rutile RuO_2.[26–28] Such substitution of Mn for Ir can involve different oxidation states of Mn. For instance, low-spin Mn^{2+} and high-spin Mn^{3+} have similar radii as tetravalent Ir in octahedral coordination, while Mn^{4+} is slightly smaller. We applied Vegard's law using the IrO_2(110) peak at $2\theta \approx 28°$ to determine the substitution level, assuming for simplicity substitution with MnO_2 (see Appendix C for more details). The results reported in Table 4.2 show a higher degree of substitution of Ir with Mn cations for sample Mn50 (33 at%) than for sample Mn25 (22 at%). The finding that the substitution level is not proportional to the Mn loading suggests the formation of segregated Mn oxide at higher Mn content.

No reflections that can be ascribed to Mn oxide phases are observed in the diffractograms of the bimetallic samples, indicative of the poor crystallinity of the MnO_x phases in these electrodes. Only for the MnO_x sample Mn100, reflections due to Mn_3O_4 can be observed. At high Mn contents, *i.e.* for samples Mn70 and Mn85, the IrO_2 peaks are hardly distinguishable anymore. To check whether the absence of IrO_2-related peaks in samples Mn70 and Mn85 was caused by a lack of crystallinity or simply by an insufficient amount of crystalline phase, we prepared two thicker samples for XRD analysis (synthesis details can be found in Appendix C). The XRD patterns of thick Mn70 and Mn85 samples show the presence of IrO_2-related peaks (Figure C4), which means that the IrO_2 maintains its crystalline structure also at high Mn loadings. Nevertheless, the maximum substitution level was reached at a Mn content of 50 at% (Table 4.2). Thus, the samples with a higher Mn content contain also separate Mn oxides. Finally, we found that the crystalline structure of the samples was unaffected by the electrochemical treatment, as the diffractograms of the used samples were similar to those for the fresh electrodes (Figure C5). This indicates that the samples are relatively stable.

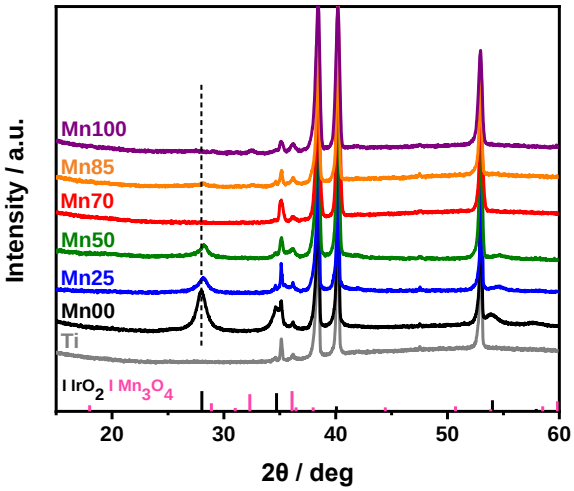

Figure 4.4. X-ray diffractograms of Ti-supported catalysts. Reference patterns of IrO_2 (PDF #15-0870) and Mn_3O_4 (PDF #24-0734) are reported in the bottom part of the figure.

Table 4.2. Degree of Ir substitution by Mn in crystalline IrO_2 according to Vegard's law applied to (110) reflection with respect to Mn00.

Sample ID	Substitution IrO_2 with MnO_2, at%
Mn25	22 ± 2
Mn50	33 ± 2
Mn70[a]	31 ± 2
Mn85[a]	30 ± 2

[a] Determined using thicker films.

The electronic state of the surface was investigated by XPS. XPS spectra of the Ir 4f region of the fresh anodes are reported in Figure 4.5. These spectra were fitted in accordance with the recent model of Freakley *et al.*,[44] using asymmetric line shapes for all the main photoemission peaks because of the conductive metallic nature of IrO_2 and with satellite features to account for different screened and unscreened final states. With increasing the Mn content, broader Ir 4f peaks are observed, which points to the presence of Ir in different oxidation states. Deconvolution showed that Ir^{3+} was present in the Mn-containing samples.

The Ir^{3+} spectral features are located at binding energies (BE) 0.5 eV higher than the main Ir^{4+} features.[44] While Ir^{3+} states in Mn00 could hardly be detected, the amount of Ir^{3+} increased with rising Mn content. The presence of Ir^{3+} at the surface is usually associated with oxygen vacancies in amorphous IrO_2 and has also been linked to an increased activity of amorphous IrO_2 in comparison with crystalline IrO_2.[12,45]

Changes upon Mn addition were also observed in the O 1s XPS spectra (Figure 4.6). The fitting model comprised three O^{2-} components, which can be ascribed to oxygen anions of the IrO_2 lattice (BE ≅ 529.9 eV), of hydroxyl groups (BE ≅ 531.2 eV), and of adsorbed water (BE ≅ 533 eV).[44] An additional shoulder at lower binding energy (BE ≅ 529.2 eV) was used to fit the spectra of Mn-containing anodes properly. This feature was also reported by Reier et al. in O 1s XPS spectra of mixed Ir-Ni oxides and assigned to oxygen atoms bridging between Ir and Ni.[18] A pre-edge feature in O K-edge NEXAFS spectra of amorphous IrO_x was associated with the presence of electrophilic O^- species, which find their origin in the O 2p hole states.[12] Similarly, Zaman et al. attributed the shift of the O 1s peak toward lower BE in Ni-Co co-doped IrO_2 as compared to pure IrO_2 to the presence of oxygen vacancies.[46] Although we cannot firmly attribute the low-BE shoulder in the O 1s spectra of the mixed Ir-Mn samples to electrophilic O^- species or oxygen bridging between Ir and Mn atoms, the changes in the O 1s spectra support the formation of different O species upon Mn addition to IrO_2. To verify that the low BE component was not due to O^{2-} species of lattice MnO_x, we measured the O 1s spectrum of the Mn100 sample (Figure C6). The lattice oxygen peak appeared at similar BE (529.9 eV) as that of IrO_2; thus, the low BE component in the mixed oxide anodes is related to the simultaneous presence of Ir and Mn and possibly relates to O^- ions close to defects.

Ir 4f XPS spectra of the samples after the stability tests are reported in Figure C7a-e. These spectra did not show substantial differences compared to those recorded for the fresh samples. Thus, the additional Ir surface state present before the electrochemical tests in the Mn-containing samples was maintained during anodic testing. The O 1s spectra of the used samples (Figure C7f-j) showed an increase in the amount of adsorbed hydroxyl groups and adsorbed water (except for Mn85). This can be linked to the applied electrochemical treatment in water.

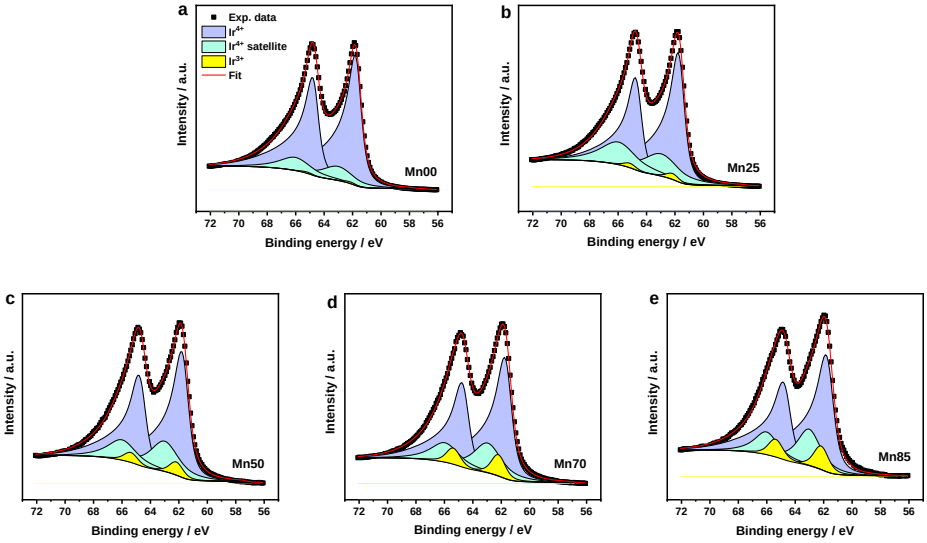

Figure 4.5. Ir 4f XPS spectra of fresh anodes: a) Mn00, b) Mn25, c) Mn50, d) Mn70, and e) Mn85.

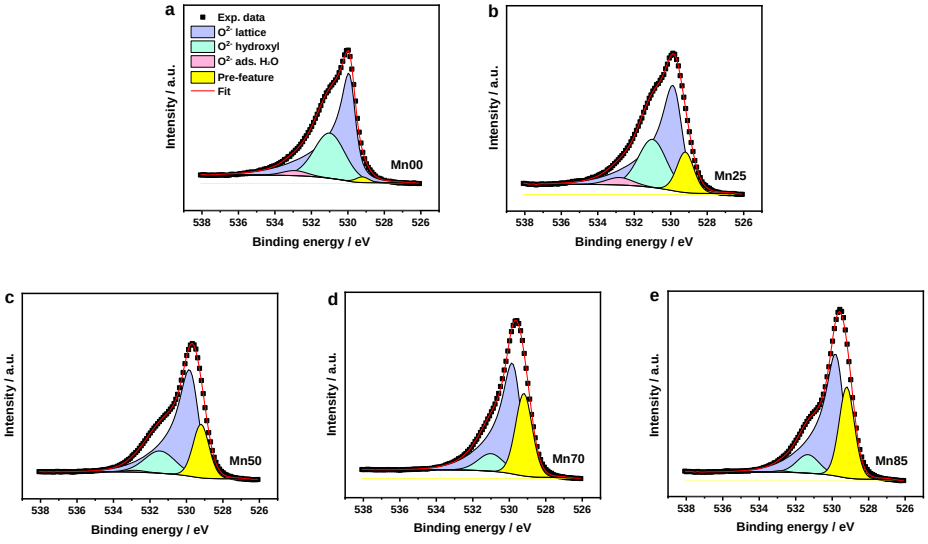

Figure 4.6. O 1s XPS spectra of fresh anodes: a) Mn00, b) Mn25, c) Mn50, d) Mn70, and e) Mn85.

The oxidation state of Mn was also investigated by XPS. As Mn 2p peaks of mixed MnO_x samples present overlapping features at similar BEs,[47] the splitting of the Mn 3s peaks was used to determine the oxidation state of Mn. The splitting of Mn 3s peaks (spectra are reported in Figure C8) originates from the exchange coupling of 3s holes and 3d electrons of Mn.[48] Its value can be used to determine the average oxidation state of Mn, with the advantage of being insensitive to surface charging and independent on spectrometer calibration. Reference values from the literature fall in the range of 4.5-4.8 eV for MnO_2, 5.3-5.4 eV for Mn_2O_3, 5.5-5.6 eV for Mn_3O_4, and 5.6-5.8 for MnO.[49–51] The Mn 3s splitting of our samples (Table 4.3) became larger with increasing Mn content, indicating a lower Mn oxidation state in more Mn-rich samples. The trends can be explained by the predominance of Mn^{3+} and Mn^{4+} species in IrO_2, and Mn^{2+} and Mn^{3+} species in segregated Mn_3O_4, which is a spinel oxide of Mn^{2+} and Mn^{3+}. The higher Mn 3s peak splitting values at high Mn loadings indicate that the fraction of segregated Mn_3O_4 increased with Mn content. Based on the XRD and XPS results, we can conclude that Mn is partially inserted as Mn^{3+} and Mn^{4+} in rutile IrO_2 and partially segregates as Mn_3O_4. The amount of segregated Mn oxide strongly increases with the Mn content of the samples. We also evaluated the splitting of the Mn100 sample, which was found to be equal to 5.6 eV, consistent with the presence of Mn in the mixed valence state spinel Mn_3O_4. This is also in line with the presence of Mn^{2+} and Mn^{3+} in the Ir-Mn samples with a higher Mn content. A similar analysis of the Mn oxidation state for the used anodes was not possible due to their lower Mn content (low signal-to-noise ratio).

Table 4.3. Peak splitting of the Mn 3s peaks determined from the Mn 3s XPS spectra of the fresh anodes.

Sample ID	Δ Mn 3s (eV)
Mn25	5.18
Mn50	5.26
Mn70	5.30
Mn85	5.44
Mn100	5.60

The composition of the samples before and after electrochemical tests was also investigated by depth-profiling XPS (Figure 4.7). The composition at the surface is represented in this figure by the data at sputtering cycle 0. All the samples exhibited a surface enrichment in Ir with the surface Mn content correlating to the nominal composition (Figure 4.7a). The surface enrichment of Ir in first-row transition metal-doped IrO_2 was also observed for Ni-Co co-doped IrO_2.[46] The preferential exposure of Ir was mentioned to improve the electrochemical performance. Sputtering shows that, deeper into the film, the Mn content gradually increased to the nominal composition. For the used samples, the Mn content at the surface was similar (16 at%) for samples Mn25, Mn50, and Mn70, while that of Mn85 was slightly higher (21 at%). The Mn content at the surface was significantly lower than at the surface of fresh anodes, particularly for samples with high nominal Mn loadings. This finding suggests that especially segregated Mn oxide, whose presence is more pronounced in the anodes with a higher Mn content, could be easily removed by the electrochemical treatment. The Mn content of the used anodes increased deeper into the samples, although it remained lower than in the fresh samples, even after the last sputtering cycle. This finding indicates that for the used anodes a compositional change with an overall decrease in Mn content both at the surface and in the bulk of the electrodes occurred, as result of the applied electrochemical testing protocol.

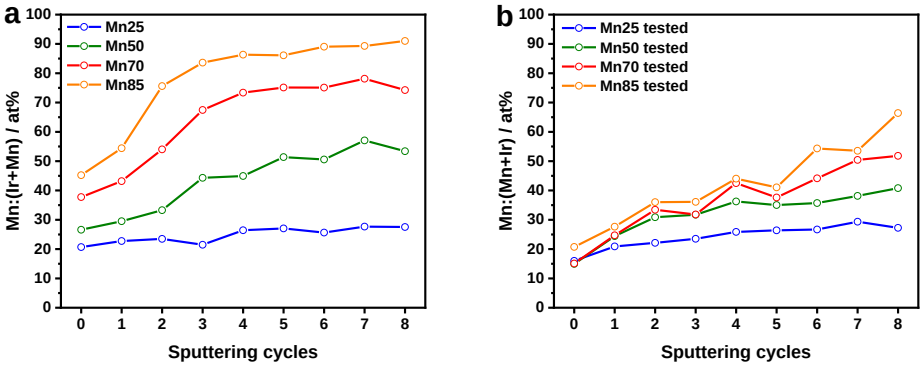

Figure 4.7. Composition of a) fresh and b) used electrodes derived from XPS depth-profiles. Sputtering cycle 0 corresponds to the XPS measurement at the surface of the samples before any sputtering.

The morphology of the electrodes was further investigated by SEM. Figure C9 shows representative micrographs acquired for fresh and used anodes. Fresh Mn00 exhibited a relatively smooth surface, while the Mn25 and Mn50 samples exhibited a similar morphology with small grains visible at the surface. At higher Mn loadings (Mn70 and Mn85), the morphology of the electrodes changed. The formation of larger grains and micrometer-sized agglomerates was apparent. EDX mapping conducted on sample Mn70 (Figure C10) showed that these agglomerates are Mn-rich, which are therefore most likely segregated Mn oxides. Similar morphologies were observed for the used anodes, with no significant changes except for fewer agglomerates on the surfaces of tested Mn70 and Mn85 samples.

Raman spectroscopy was used to characterize the structure of fresh and used samples (Figure 4.8). The fresh sample Mn00 exhibited the typical Raman features of rutile IrO_2, with bands appearing at ~ 550 cm^{-1} (E_g), 720 cm^{-1} (B_{2g}), and 745 cm^{-1} (A_{1g}).[52] The latter two features were visible as a single broad feature in the spectra [22]. Upon increasing the Mn content, the intensity of the IrO_2-related bands decreased and a new feature at 645 cm^{-1} became visible. This band is associated with the symmetric Mn-O stretching mode (A_{1g}), which is due to the motion of oxygen atoms inside the MnO_6 unit of manganese oxides.[53,54] The spectrum of Mn100 sample exhibited an intense band at ~645 cm^{-1} and an additional broad band at ~360 cm^{-1}, which are both characteristic features of Mn_3O_4.[55,56] After the stability tests, the intensity ratio between the bands related to IrO_2 and Mn oxide increased, particularly for samples with high nominal Mn contents (Mn70 and Mn85). This finding indicates that the used samples were enriched in Ir as a result of the electrochemical testing, in agreement with the results of XPS depth profiling. Moreover, the Raman spectra indicate that the Ir enrichment is in the form of IrO_2.

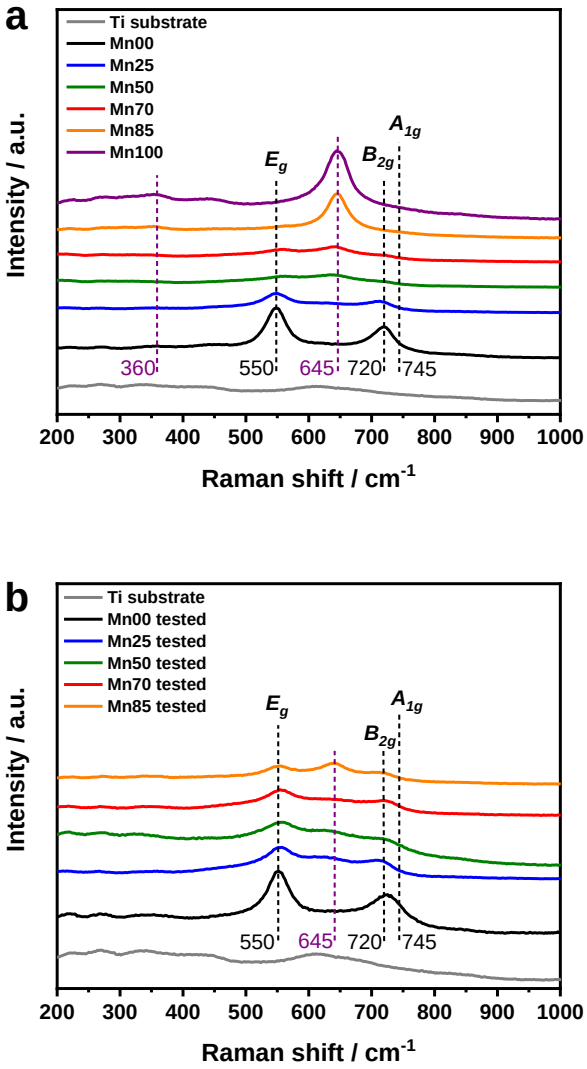

Figure 4.8. Raman spectra of a) fresh and b) used anodes.

4.4. Discussion

The activity and stability of IrO_2-based electrocatalysts for acidic OER can be improved by the addition of Mn. Both the overall activity based on the geometric electrode surface areas as well as the intrinsic activity based on the electrochemical surface area of Mn-containing samples are increased compared to pure IrO_2 due to Mn. The promoting effect can be estimated by comparing the overpotential needed to reach a current density of 10 mA/cm^2 (η_{10}). The optimal sample Mn70 exhibited an overpotential that was 58 mV lower compared to IrO_2. The η_{10} for Mn70 was 383 mV, while that of Mn00 was 441 mV. A direct comparison of overpotentials to literature is hampered by the dependence of overpotential on the catalyst loading, testing protocols (e.g., standard *vs.* rotating disk-electrode configuration), and electrolytes. Nevertheless, a similar trend of decreased overpotential was achieved by the addition of Cr to an Ir catalyst (η_{10} for Ir: 430 mV, η_{10} for IrCr: 395 mV).[21] Ir-Ni oxides presented different results: Reier et al. reported a η_{10} of ~300 mV,[18] while in other works bimetallic catalysts did not perform better than pure IrO_2 (i.e., η_{10} for Ir: 430 mV, η_{10} for IrNi: 433 mV).[21] Similar contradicting results were also found in alkaline OER.[22,57] We can infer from this comparison that the Mn promoting effect is highly relevant to the application of IrO_2-based oxygen-evolving anodes operating in acidic electrolytes.

We determined that the synergy between Ir and Mn has several origins. The increased roughness of the surface leads to a higher electrochemically active surface area and thereby increases the overall activity of the Mn-doped IrO_2 electrocatalysts. Evaluation by means of anodic charges showed that the samples with intermediate Mn content, Mn50 and Mn70, had the highest active surface area. We speculate that the higher surface area is brought about at the formation stage of the films and involves the formation of smaller crystals and the partial segregation of dopant oxides as earlier observed for Co-doped IrO_2.[58] Depth-profiling XPS of fresh anodes showed a surface enrichment in Ir for all the bimetallic samples. Thus, we expect an optimal amount of exposed Ir active sites at intermediate Mn contents, because a too high Mn content likely covers part of the electrochemically active surface.

Our data also show that the intrinsic electrocatalytic properties of the active materials were changed by Mn. Surface-normalized current densities and Tafel slopes provide insight into the intrinsic kinetic aspects of the various anodes. The surface-normalized current density at η = 350 mV increased with Mn content and leveled off at 50 at% Mn. A qualitatively similar trend was obtained by normalization of the current densities to the values of double-layer capacitance of the samples instead of the anodic charges. These results provide strong evidence for the intrinsic promoting effect that Mn has on IrO_2 in the OER. From the

characterization point of view, we can correlate the improved performance to the substitution of Ir by Mn. This most likely occurs via insertion of Mn^{3+} and/or Mn^{4+} ions into rutile IrO_2. While the substitution of Ir^{4+} by Mn^{4+} in rutile IrO_2 has been reported,[23,25] XPS results show that a significant part of the substitutions involves Mn^{3+}. We cannot exclude that also Mn^{2+} can be included in the IrO_2 lattice. Previous works showed that doping of IrO_2 by Ni, Co, and Cu in different oxidation states than 4 is also possible.[46,58,59]

As to the nature of the active sites, XPS showed that the amount of Ir^{3+} species increases upon Mn addition. Such species have also been observed in amorphous Ir oxides,[12,13] which typically exhibits higher activity than crystalline IrO_2 for the OER. In this respect, flexible Ir oxidation state and electrophilic surface oxygen species have been mentioned to facilitate nucleophilic attack by water.[60] We demonstrate that the introduction of Mn in the rutile IrO_2 lattice results in more Ir defects, which are likely involved in the OER. This could be relevant for the further development of iridium-based anodes because our results indicate that Ir^{3+} can benefit the OER reaction not only in amorphous but also in crystalline IrO_2. The presence of lower valent ions such as Ir^{3+} and Mn^{3+} in rutile IrO_2 leads to oxygen vacancies that neutralize the charge of the hosting crystal structure.[46,61] Note that oxidation of Mn^{2+} to a higher oxidation state during introduction into IrO_2 can also cause the reduction of Ir^{4+} to Ir^{3+}.

Tafel slopes can provide insight into the OER kinetics.[23,62] In the low-current density region, Mn00 exhibited a Tafel slope of 54 mV dec^{-1}. Doping with Mn led to lower values of Tafel slopes (except for Mn85), as a result of a change in the OER mechanism and/or in the adsorptive properties of the catalysts. The lowest Tafel slope was found for sample Mn50 (44 mV dec^{-1}). For instance, similar low Tafel slopes of 40 and 45 mV dec^{-1} were previously reported for pyrolyzed $IrCoO_x$ and $Bi_2Ir_2O_7$, respectively.[63,64] The enhanced intrinsic catalytic performance of the Ir-Mn catalysts is not only limited to the low current density regime. At high current densities, different Tafel slopes are observed due to higher surface coverages and a different OER mechanism. Low Tafel slopes at high current density are desirable in industrial applications, where generally high potentials and high current densities are used.[65] The Tafel slopes of all Mn-containing samples were significantly lower, with the lowest value of 74 mV dec^{-1} observed for Mn70. These changes can be due to either a different rate-determining step or a change in the coverage of adsorbed species on the electrode surface. A change in the adsorptive properties upon first-row transition metal addition was previously explored by DFT calculations for Cr-doped IrO_2. The results indicated that weaker binding energy of oxygen intermediates on the doped surface is beneficial for the OER.[21] Notably, a Tafel slope of 83 mV dec^{-1} was reported in the high-current density region, close to the values for samples Mn50 (93 dec^{-1}) and Mn70 (74 mV dec^{-1}).

From an application point of view, stability is also very important, and especially leaching of the expensive Ir component is a concern. Ir dissolution occurred during electrochemical polarization of all the anodes. Normalization on the geometric area showed that more Ir dissolved in the Ir-Mn samples, especially at intermediate and high Mn content. The changes in Ir dissolution were however much less pronounced than for Ir-Ni oxides.[18] When normalized to the active surface area, it was observed that the amount of Ir dissolved was similar for pure IrO_2 and Ir-Mn oxides. Thus, Mn promotion provides a way to increase the electrochemically active surface area and the intrinsic surface reactivity of IrO_2 OER catalysts without impeding severely the anode stability. However, durability is adversely affected by a too high Mn content, as observed for sample Mn85.

Finally, the characterization of the used anodes showed the extensive compositional changes at and below the surface of the anodes. Specifically, significant dissolution of Mn oxides takes place during electrochemical polarization as followed from depth-profiling XPS and Raman spectroscopy. Regardless of the differences between fresh and used bimetallic anodes, an important characteristic of the most active bimetallic samples was a high amount of Ir^{3+} species.

4.5. Conclusions

Bimetallic Ir-Mn oxide films deposited on a Ti foil substrate exhibited higher electrocatalytic performance for the OER compared to pure IrO_2 in 0.1 M H_2SO_4. The best performance was achieved at intermediate Mn content (Mn50 and Mn70). The most active sample showed an 8-fold higher geometric current density at η = 350 mV compared to pure IrO_2. The synergy can be attributed to an increased electrochemically active surface area as well as higher intrinsic catalytic activity. Low Tafel slopes of 44-49 mV dec^{-1} and 74-93 mV dec^{-1} were recorded in the low- and high-current density region, respectively, for the promoted anodes. A 2.5-fold increase of the surface specific current density as compared to pure IrO_2 evidenced the synergy between Ir and Mn in these bimetallic oxide electrocatalysts. Mixed Ir-Mn oxide catalysts were found stable during a chronopotentiometric test, except when th Mn content was too high (Mn85). The increased Ir dissolution for bimetallic films could be mostly attributed to the higher exposed surface area.

Mn addition was found to affect the electronic structure of rutile IrO_2. Mn partially entered the lattice of IrO_2 as Mn^{3+} and Mn^{4+} ions, and partially segregated as separate Mn_3O_4. The latter phase was easily removed during the initial stages of anodic polarization. The presence of segregated Mn oxide was found more abundant in the high Mn content

samples. In all the Ir-Mn oxide catalysts, XPS revealed the presence of Ir^{3+} species, previously associated with the higher OER activity of amorphous IrO_x. The amount of these Ir^{3+} species, which was negligible in pure IrO_2, increased with Mn content. Ir^{3+} and associated oxygen vacancies can be linked to the introduction of Mn in the IrO_2 rutile lattice and might stem from insertion as Mn^{3+}. The strongly improved electrocatalytic performance and the lower noble metal content of these bimetallic Ir-Mn oxides can be used to maximize the efficiency of IrO_2-based electrocatalysts for water oxidation in acid electrolyte.

4.6. References

(1) Tahir, M.; Pan, L.; Idrees, F.; Zhang, X.; Wang, L.; Zou, J. J.; Wang, Z. L. *Nano Energy* **2017**, *37*, 136–157.

(2) Suen, N.-T.; Hung, S.-F.; Quan, Q.; Zhang, N.; Xu, Y.-J.; Chen, H. M. *Chem. Soc. Rev.* **2017**, *46* (2), 337–365.

(3) Fabbri, E.; Habereder, A.; Waltar, K.; Kötz, R.; Schmidt, T. J. *Catal. Sci. Technol.* **2014**, *4* (11), 3800–3821.

(4) Carmo, M.; Fritz, D. L.; Mergel, J.; Stolten, D. *Int. J. Hydrogen Energy* **2013**, *38* (12), 4901–4934.

(5) Feng, Q.; Yuan, X. Z.; Liu, G.; Wei, B.; Zhang, Z.; Li, H.; Wang, H. *J. Power Sources* **2017**, *366*, 33–55.

(6) Lee, B. S.; Ahn, S. H.; Park, H. Y.; Choi, I.; Yoo, S. J.; Kim, H. J.; Henkensmeier, D.; Kim, J. Y.; Park, S.; Nam, S. W.; Lee, K. Y.; Jang, J. H. *Appl. Catal. B Environ.* **2015**, *179*, 285–291.

(7) Vesborg, P. C. K.; Jaramillo, T. F. *RSC Adv.* **2012**, *2* (21), 7933–7947.

(8) Geiger, S.; Kasian, O.; Shrestha, B. R.; Mingers, A. M.; Mayrhofer, K. J. J.; Cherevko, S. *J. Electrochem. Soc.* **2016**, *163* (11), F3132–F3138.

(9) Cherevko, S.; Reier, T.; Zeradjanin, A. R.; Pawolek, Z.; Strasser, P.; Mayrhofer, K. J. J. *Electrochem. commun.* **2014**, *48*, 81–85.

(10) Gottesfeld, S.; Srinivasan, S. *J. Electroanal. Chem. Interfacial Electrochem.* **1978**, *86* (1), 89–104.

(11) Reier, T.; Teschner, D.; Lunkenbein, T.; Bergmann, a; Selve, S.; Kraehnert, R.; Schlögl, R.; Strasser, P. *J. Electrochem. Soc.* **2014**, *161* (9), F876–F882.

(12) Pfeifer, V.; Jones, T. E.; Velasco Vélez, J. J.; Massué, C.; Greiner, M. T.; Arrigo, R.; Teschner, D.; Girgsdies, F.; Scherzer, M.; Allan, J.; Hashagen, M.; Weinberg, G.; Piccinin, S.; Hävecker, M.; Knop-Gericke, A.; Schlögl, R. *Phys. Chem. Chem. Phys.* **2016**, *18* (4), 2292–2296.

(13) Pfeifer, V.; Jones, T. E.; Wrabetz, S.; Massué, C.; Velasco Vélez, J. J.; Arrigo, R.; Scherzer, M.; Piccinin, S.; Hävecker, M.; Knop-Gericke, A.; Schlögl, R. *Chem. Sci.* **2016**, *7* (11), 6791–6795.

(14) da Silva, G. C.; Perini, N.; Ticianelli, E. A. *Appl. Catal. B Environ.* **2017**, *218*, 287–297.

(15) Bernicke, M.; Ortel, E.; Reier, T.; Bergmann, A.; Ferreira De Araujo, J.; Strasser, P.; Kraehnert, R. *ChemSusChem* **2015**, *8* (11), 1908–1915.

(16) Oellers, T.; Fruchter, L.; Pizzutilo, E.; Geiger, S.; Kasian, O.; Ledendecker, M.; Mingers, A. M.; Cherevko, S.; Koper, M. T. M.; Mayrhofer, K. J. J.; Li, Z.; Diaz-Morales, O.; Ludwig, A.; Fu, W. T. *Nat. Catal.* **2018**, *1* (7), 508–515.

(17) Kim, Y.; Lopes, P. P.; Park, S.; Lee, A.; Lim, J.; Lee, H.; Back, S.; Jung, Y.; Danilovic, N.; Stamenkovic, V.; Erlebacher, J.; Snyder, J.; Markovic, N. M. *Nat. Commun.* **2017**, *8*, 1449.

(18) Reier, T.; Pawolek, Z.; Cherevko, S.; Bruns, M.; Jones, T.; Teschner, D.; Selve, S.; Bergmann, A.; Nong, H. N.; Schlögl, R.; Mayrhofer, K. J. J.; Strasser, P. *J. Am. Chem. Soc.* **2015**, *137* (40), 13031–13040.

(19) Nong, H. N.; Oh, H. S.; Reier, T.; Willinger, E.; Willinger, M. G.; Petkov, V.; Teschner, D.; Strasser, P. *Angew. Chemie - Int. Ed.* **2015**, *54* (10), 2975–2979.

(20) Lim, J.; Yang, S.; Kim, C.; Roh, C. W.; Kwon, Y.; Kim, Y. T.; Lee, H. *Chem. Commun.* **2016**, *52* (32), 5641–

5644.

(21) Strickler, A. L.; Flores, R. A.; King, L. A.; Nørskov, J. K.; Bajdich, M.; Jaramillo, T. F. *ACS Appl. Mater. Interfaces* **2019**, *11* (37), 34059–34066.

(22) Lee, H.; Kim, J. Y.; Lee, S. Y.; Hong, J. A.; Kim, N.; Baik, J.; Hwang, Y. J. *Sci. Rep.* **2018**, *8* (1), 2–9.

(23) Ye, Z. G.; Meng, H. M.; Chen, D.; Yu, H. Y.; Huan, Z. S.; Wang, X. D.; Sun, D. B. *Solid State Sci.* **2008**, *10* (3), 346–354.

(24) Ghadge, S. D.; Patel, P. P.; Datta, M. K.; Velikokhatnyi, O. I.; Kuruba, R.; Shanthi, P. M.; Kumta, P. N. *RSC Adv.* **2017**, *7* (28), 17311–17324.

(25) Ghadge, S. D.; Velikokhatnyi, O. I.; Datta, M. K.; Shanthi, P. M.; Tan, S.; Damodaran, K.; Kumta, P. N. *ACS Catal.* **2019**, *9* (3), 2134–2157.

(26) Browne, M. P.; Nolan, H.; Duesberg, G. S.; Colavita, P. E.; Lyons, M. E. G. *ACS Catal.* **2016**, *6* (4), 2408–2415.

(27) Fernandez, J. L.; Chialvo, M. R. G. DE; Chialvo, A. C. *J. Appl. Electrochem.* **2002**, *2* (3), 513–520.

(28) Etzi Coller Pascuzzi, M.; Goryachev, A.; Hofmann, J. P.; Hensen, E. J. M. *Appl. Catal. B Environ.* **2020**, *261*, 118225.

(29) Sun, W.; Cao, L. M.; Yang, J. *J. Mater. Chem. A* **2016**, *4* (32), 12561–12570.

(30) Zaharieva, I.; Chernev, P.; Risch, M.; Klingan, K.; Kohlhoff, M.; Fischer, A.; Dau, H. *Energy Environ. Sci.* **2012**, *5* (5), 7081–7089.

(31) Martelli, G. N.; Ornelas, R.; Faita, G. *Electrochim. Acta* **1994**, *39* (11–12), 1551–1558.

(32) Hu, J. M.; Zhang, J. Q.; Cao, C. N. *Int. J. Hydrogen Energy* **2004**, *29* (8), 791–797.

(33) Diaz-Morales, O.; Raaijman, S.; Kortlever, R.; Kooyman, P. J.; Wezendonk, T.; Gascon, J.; Fu, W. T.; Koper, M. T. M. *Nat. Commun.* **2016**, *7*, 12363.

(34) Rondinini, S.; Achilli, E.; Vertova, A.; Ghigna, P.; Lugaresi, O.; Locatelli, C.; Minguzzi, A. *Chem. Sci.* **2014**, *5* (9), 3591.

(35) Trasatti, S. *Electrochim. Acta* **1984**, *29* (11), 1503–1512.

(36) Ardizzone, S.; Carugati, A.; Trasatti, S. *J. Electroanal. Chem.* **1981**, *126*, 287–292.

(37) Reier, T.; Teschner, D.; Lunkenbein, T.; Bergmann, A.; Selve, S.; Kraehnert, R.; Schlögl, R.; Strasser, P. *J. Electrochem. Soc.* **2014**, *161* (9), F876–F882.

(38) McCrory, C. C. L.; Jung, S.; Peters, J. C.; Jaramillo, T. F. *J. Am. Chem. Soc.* **2013**, *135* (45), 16977–16987.

(39) Zhang, J. J.; Hu, J. M.; Zhang, J. Q.; Cao, C. N. *Int. J. Hydrogen Energy* **2011**, *36* (9), 5218–5226.

(40) Goryachev, A.; Etzi Coller Pascuzzi, M.; Carlà, F.; Weber, T.; Over, H.; Hensen, E. J. M.; Hofmann, J. P. *Electrochim. Acta* **2020**, *336*, 135713.

(41) Etzi Coller Pascuzzi, M.; Man, A. J. W.; Goryachev, A.; Hofmann, J. P.; Hensen, E. J. M. *Catal. Sci. Technol.* **2020**, *10*, 5593–5601.

(42) Huynh, M.; Ozel, T.; Liu, C.; Lau, E. C.; Nocera, D. G. *Chem. Sci.* **2017**, *8* (7), 4779–4794.

(43) Geiger, S.; Kasian, O.; Mingers, A. M.; Nicley, S. S.; Haenen, K.; Mayrhofer, K. J. J.; Cherevko, S. *ChemSusChem* **2017**, *10* (21), 4140–4143.

(44) Freakley, S. J.; Ruiz-Esquius, J.; Morgan, D. J. *Surf. Interface Anal.* **2017**, *49* (8), 794–799.

(45) Pfeifer, V.; Jones, T. E.; Velasco Vélez, J. J.; Massué, C.; Arrigo, R.; Teschner, D.; Girgsdies, F.; Scherzer, M.; Greiner, M. T.; Allan, J.; Hashagen, M.; Weinberg, G.; Piccinin, S.; Hävecker, M.; Knop-Gericke, A.; Schlögl, R. *Surf. Interface Anal.* **2016**, *48* (5), 261–273.

(46) Zaman, W. Q.; Wang, Z.; Sun, W.; Zhou, Z.; Tariq, M.; Cao, L.; Gong, X. Q.; Yang, J. *ACS Energy Lett.* **2017**, *2* (12), 2786–2793.

(47) Biesinger, M. C.; Payne, B. P.; Grosvenor, A. P.; Lau, L. W. M.; Gerson, A. R.; Smart, R. S. C. *Appl. Surf. Sci.* **2011**, *257* (7), 2717–2730.

(48) Galakhov, V. R.; Demeter, M.; Bartkowski, S.; Neumann, M.; Ovechkina, N. A.; Kurmaev, E. Z.;

Lobachevskaya, N. I.; Mukovskii, Y. M.; Mitchell, J.; Ederer, D. L. *Phys. Rev. B - Condens. Matter Mater. Phys.* **2002**, *65* (11), 1–4.

(49) Chigane, M.; Ishikawa, M. *J. Electrochem. Soc.* **2000**, *147* (6), 2246.

(50) Nelson, A. J.; Reynolds, J. G.; Roos, J. W. *J. Vac. Sci. Technol. A* **2000**, *18* (4), 1072–1076.

(51) Huynh, M.; Shi, C.; Billinge, S. J. L.; Nocera, D. G. *J. Am. Chem. Soc.* **2015**, *137* (47), 14887–14904.

(52) Liao, P. C.; Chen, C. S.; Ho, W. S.; Huang, Y. S.; Tiong, K. K. *Thin Solid Films* **1997**, *301* (1–2), 7–11.

(53) Julien, C. M.; Massot, M.; Poinsignon, C. *Spectrochim. Acta - Part A Mol. Biomol. Spectrosc.* **2004**, *60* (3), 689–700.

(54) Etzi Coller Pascuzzi, M.; Selinger, E.; Sacco, A.; Castellino, M.; Rivolo, P.; Hernández, S.; Lopinski, G.; Tamblyn, I.; Nasi, R.; Esposito, S.; Manzoli, M.; Bonelli, B.; Armandi, M. *Electrochim. Acta* **2018**, *284*, 294–302.

(55) Bernard, M.-C.; Hugot-le Goff, A.; Vu Thi, B. *J. Electrochem. Soc.* **1993**, *140* (11), 3065–3070.

(56) Buciuman, F.; Patcas, F.; Craciun, R.; Zahn, D. R. T. *Phys. Chem. Chem. Phys.* **1999**, *1* (1), 185–190.

(57) Özer, E.; Sinev, I.; Mingers, A.; Araujo, J.; Kropp, T.; Mavrikakis, M.; Mayrhofer, K.; Cuenya, B.; Strasser, P. *Surfaces* **2018**, *1* (1), 165–186.

(58) Von Dreifus, D.; De Oliveira, A. J. A.; Do Rosario, A. V.; Pereira, E. C. *J. Supercond. Nov. Magn.* **2013**, *26* (6), 2319–2321.

(59) Sun, W.; Song, Y.; Gong, X. Q.; Cao, L. M.; Yang, J. *Chem. Sci.* **2015**, *6* (8), 4993–4999.

(60) Pfeifer, V.; Jones, T. E.; Velasco Vélez, J. J.; Arrigo, R.; Piccinin, S.; Hävecker, M.; Knop-Gericke, A.; Schlögl, R. *Chem. Sci.* **2017**, *8* (3), 2143–2149.

(61) Shao, G. *J. Phys. Chem. C* **2008**, *112* (47), 18677–18685.

(62) Doyle, R. L.; Godwin, I. J.; Brandon, M. P.; Lyons, M. E. G. *Phys. Chem. Chem. Phys.* **2013**, *15* (33), 13737–13783.

(63) Hu, W.; Zhong, H.; Liang, W.; Chen, S. *ACS Appl. Mater. Interfaces* **2014**, *6* (15), 12729–12736.

(64) Sardar, K.; Ball, S. C.; Sharman, J. D. B.; Thompsett, D.; Fisher, J. M.; Smith, R. A. P.; Biswas, P. K.; Lees, M. R.; Kashtiban, R. J.; Sloan, J.; Walton, R. I. *Chem. Mater.* **2012**, *24* (21), 4192–4200.

(65) Schalenbach, M.; Zeradjanin, A. R.; Kasian, O.; Cherevko, S.; Mayrhofer, K. J. J. *Int. J. Electrochem. Sci.* **2018**, *13* (2), 1173–1226.

Appendix C

Supporting Information for Chapter 4

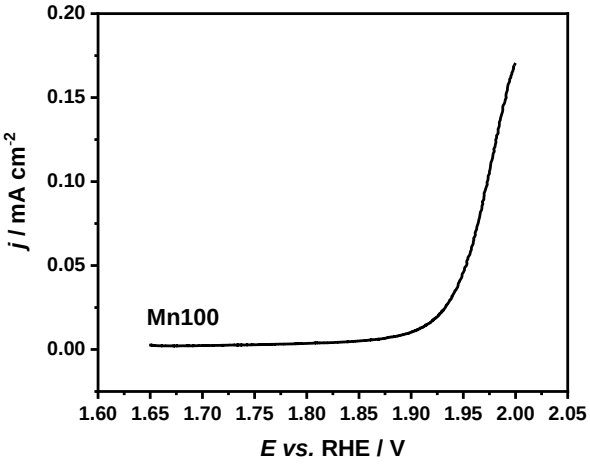

Figure C1. Linear Sweep Voltammetry (LSV) of a pure MnO_x sample (Mn100).

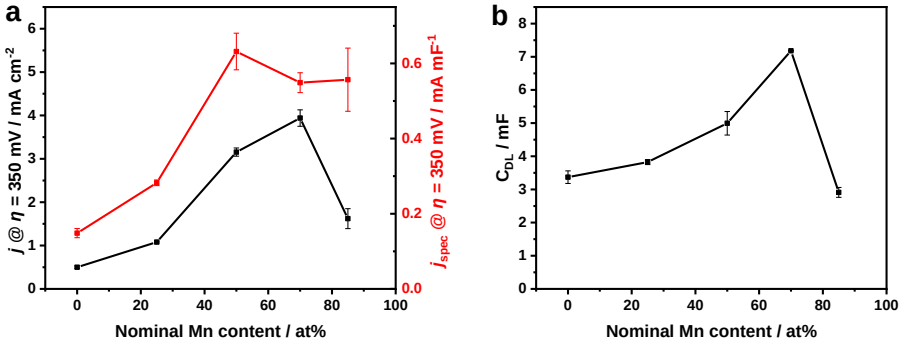

Figure C2. a) Current densities recorded at η = 350 mV in the LSV normalized to the geometric areas (black) and C_{dl} (red) of the anodes; b) values of double-layer capacitances.

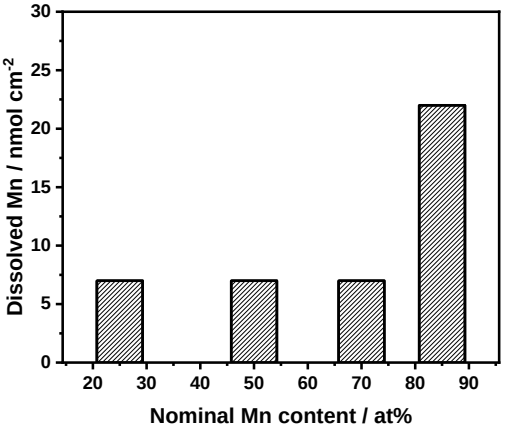

Figure C3. Amount of dissolved Mn during chronopotentiometry at 10 mA cm^{-2} for 16 h in 0.1 M H_2SO_4.

Preparation of thick samples for XRD analysis

Thick samples with the highest Mn contents were prepared in order to check whether they exhibited IrO_2-related peaks. These samples were not used for any other purpose. The samples were prepared by three consecutive depositions of the mixed Ir-Mn solutions on the substrates with intermediate calcination at 400 °C for 10 min. A final treatment at the same temperature for 1 h was applied.

Calculation of the degree of MnO_2 substitution in IrO_2

From the 2θ position of the (110) peak in the diffractograms of fresh samples we evaluated the d-spacing by the following equation:

$\lambda = 2d \sin(\vartheta)$

with λ = 1.5406 Å for Cu K-Alpha radiation.

For a rutile structure (a = b) → $\frac{1}{d^2} = \frac{h^2+k^2}{a^2} + \frac{l^2}{c^2}$

We calculated the values of the lattice parameter *a* ($a_{calc.}$) for all the samples and used the following equation to evaluate the degree of substitution:

$$x = \frac{a_{calc.\ sample} - a_{calc.\ IrO_2}}{a_{ref.MnO_2} - a_{calc.\ IrO_2}}$$

With $a_{ref.MnO_2}$ = 4.398 Å.

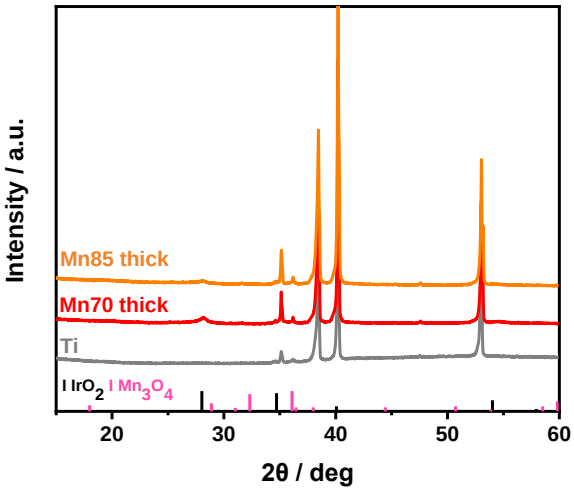

Figure C4. XRD diffractograms of thick Mn70 and Mn85 samples.

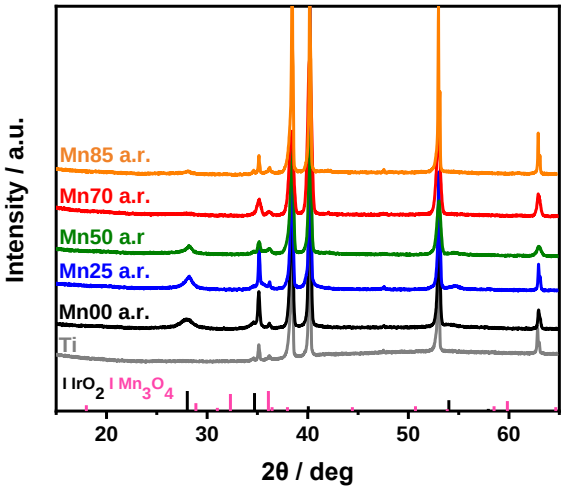

Figure C5. XRD patterns of samples after reaction (a.r.).

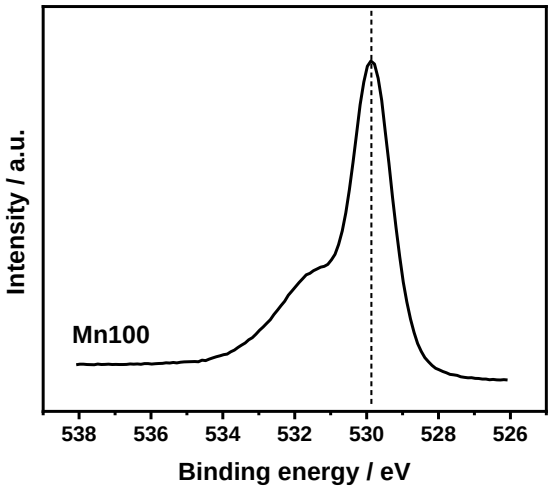

Figure C6. O 1s XPS spectrum recorded for sample Mn100.

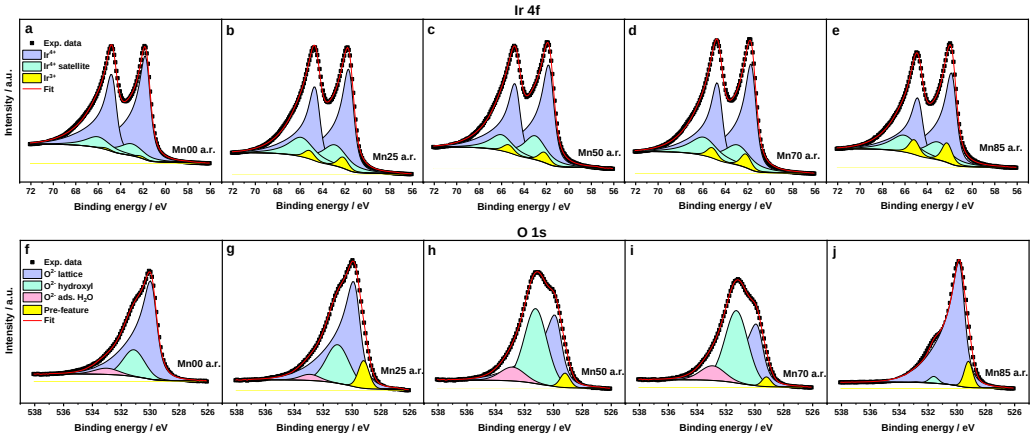

Figure C7. a-e) Ir 4f and f-j) O 1s XPS spectra of the samples after reaction (a.r.).

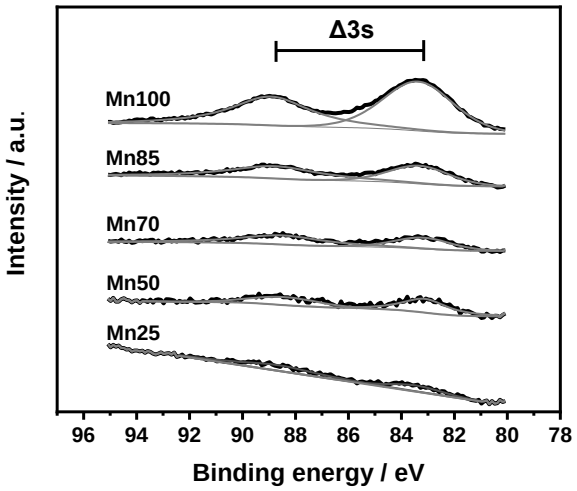

Figure C8. Mn 3s XPS spectra of fresh anodes.

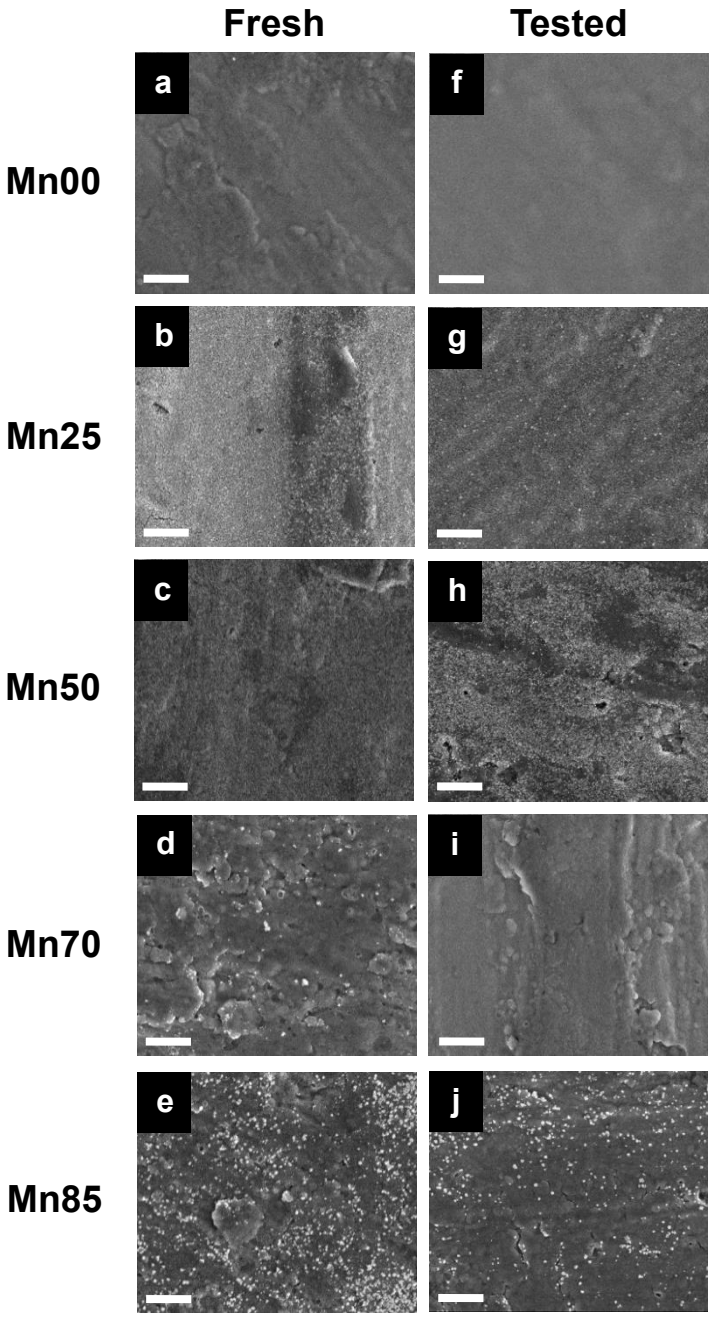

Figure C9. SEM images of as-prepared (left) and tested (right) anodes. Scale bar is equal to 1 µm.

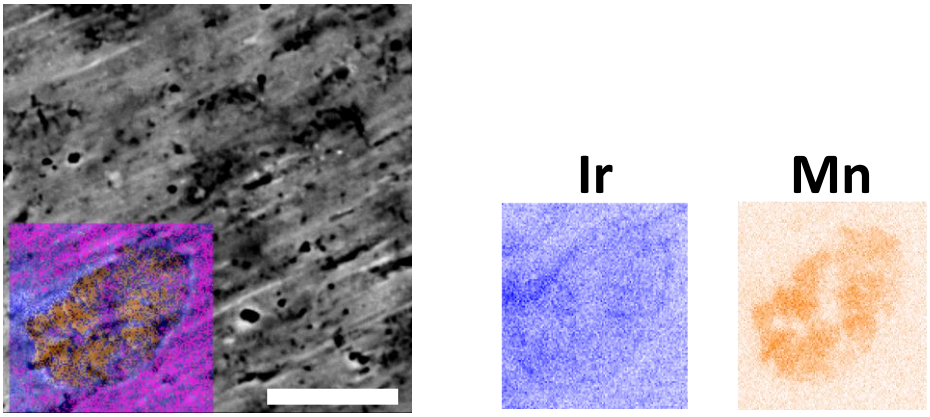

Figure C10. EDX mapping of a selected area of sample Mn70. Scale bar is equal to 10 µm.

Chapter 5

Investigation of the stability of NiFe-(oxy)hydroxide anodes in alkaline water electrolysis under industrially relevant conditions

Abstract

NiFe-(oxy)hydroxide is one of the most active electrocatalysts for the oxygen evolution reaction (OER) in alkaline conditions. Herein we investigated the stability of NiFe-(oxy)hydroxide anodes at high current densities (100 mA cm^{-2}) at different temperatures (25, 75 °C) and base concentrations (1, 5, 10 M KOH). While polarization led to minor structural and compositional changes under standard conditions (25 °C, 1 M KOH), the anodes were severely impacted at higher temperature (75 °C) and base concentrations (5, 10 M KOH). Overall leaching and preferential leaching of Fe (resulting in a lower Fe/Ni ratio) led to decreased OER performance and increased charge transfer resistance for the samples tested at industrially relevant conditions. A dramatic loss in the catalytic activity occurred for the sample polarized at 75 °C in 10 M KOH: besides extensive leaching, a transformation of $Ni(OH)_2$ into NiO was noted in this case. For pure NiO_xH_y, incorporation of Fe impurities from the electrolyte during polarization at 75 °C in 5 M KOH led to an improvement in the catalytic activity and charge-transfer properties, approaching the performance of $NiFeO_xH_y$.

This chapter has been published as:
Etzi Coller Pascuzzi, M.; Man, A. J. W.; Goryachev, A.; Hofmann, J. P.; Hensen, E. J. M. *Catal. Sci. Technol.* **2020,** *10,* 5593-5601**.**

5.1. Introduction

Electrochemical water splitting is a promising technology to convert excess electricity produced by intermittent renewable energy sources into a chemical fuel (hydrogen).[1] The anodic oxygen evolution reaction (OER), being a counter reaction to the H_2 evolution, constitutes a major bottleneck due to its sluggish kinetics.[2] Electrocatalysts are therefore needed to overcome kinetic limitations and to increase the overall efficiency of electrochemical water splitting devices. An ideal OER catalyst should combine high catalytic activity and stability with earth-abundancy and low price. First-row transition metal oxides and hydroxides offer interesting opportunities to enhance the rate of the OER, especially in the alkaline regime, without the use of expensive and scarce metals such as Ir or Ru.[3–6]

Fe-doped Ni oxides, and especially (oxy)hydroxides,[7] are the most active among noble-metal-free OER catalysts.[8–11] Some have reported that the alkaline OER activity of such anodes can be higher than those based on IrO_2 and RuO_2.[12–16] Fe impurities were found to enhance the OER activity of Ni-oxide already in 1987.[17] Subsequently, most efforts were directed towards understanding the role of Fe and the synthesis of highly active and porous anodes to maximize the activity.[18] Some reports mention that Fe enhances the activity of Ni sites by altering their redox properties,[19,20] while others propose that Fe atoms are the active sites for the OER.[21–24] Recent findings have pointed to the formation of mixed phase in which bridging Ni–O–Fe motifs are responsible for the enhanced catalytic activity.[25] Although the exact role of Fe is still debated, various synthetic strategies were developed to maximize the catalytic performance.[18]

Despite the efforts made to enhance the activity and to understand the role of Fe in NiFe-(oxy)hydroxide, the stability aspect of this material has not been extensively studied yet. Stability tests are usually conducted under standard conditions (T = 25 °C, [KOH] = 1 M), whereas the industrial alkaline water electrolysis requires much higher temperatures and base concentrations (T = 70-80 °C, [KOH] = 25-30 wt%).[26] These harsh conditions may cause structural changes in the electrodes and their premature degradation. These aspects are usually not captured in electrocatalyst evaluation protocols under standard conditions. However, performing experiments under such harsh conditions becomes challenging at the lab scale.

Recently, Andronescu et al. reported that NiFe layered double hydroxide (LDH) is sensitive to the applied anodic treatment: operation in 5 M KOH at 60 °C transforms the LDH into a mixture of NiO and $NiFe_2O_4$.[27] The same authors also studied the structural changes of a NiFe-LDH electrode upon immersion in 7.5 M KOH at 80 °C.[28] Even without electrochemical

polarization, the activity decreased considerably due to chemical degradation. We can thus expect that electrochemical polarization in harsh conditions could considerably affect anode stability.

Given the relevance of NiFe-(oxy)hydroxide for the alkaline OER, we investigated herein the stability of this material under electrochemical treatments conducted in non-standard, industrially relevant temperature and basicity regimes. The catalysts were comprehensively characterized by a combination of X-ray photoelectron spectroscopy (XPS), scanning electron microscopy (SEM), energy-dispersive X-ray spectroscopy (EDX), Raman spectroscopy, X-ray diffraction (XRD), and cyclic voltammetry (CV) to gain understanding into the structural, morphological, compositional, and activity change induced by anodic polarization under non-standard conditions.

5.2. Experimental

5.2.1. Anode preparation

NiFe-(oxy)hydroxide films were prepared on Au-coated Si substrates (Sigma-Aldrich, 100 nm) *via* electrodeposition, in accordance with previous literature.[19,29] The substrates were cleaned with absolute ethanol and then rinsed with copious amounts of Milli-Q water prior to the deposition to remove contaminants. The solution for electrodeposition was prepared by dissolving 5 mM nickel(II) sulfate hexahydrate (≥99.0%, Merck) and 0.5 mM iron(II) sulfate heptahydrate (≥99.0%, Sigma Aldrich) in Milli-Q water (18.2 MΩ cm). Before dissolving the metal salts, the water was purged by N_2 bubbling for 30 min to prevent the oxidation of Fe^{2+} into Fe^{3+}. Each deposition was carried out from the fresh solution (20 mL) by applying a constant cathodic current density of 50 µA cm^{-2} for 1125 s.[19] The geometric areas of the samples (in the range of 1.0-1.8 cm^2) were evaluated from digital photographs using ImageJ software.[30] The reproducibility of the preparation method was validated by XPS analysis of the fresh samples, which showed maximal deviations in the relative atomic Ni and Fe percentages of ± 3%. An iron-free Ni-(oxy)hydroxide anode (NiO_xH_y) was prepared using the same synthetic procedure but without the addition of iron salts to the electrodeposition bath. The as-prepared anodes were subjected to the stability tests described in the following section or tested for activity evaluation.

5.2.2. Electrochemical characterization

Electrochemical measurements were performed using an Autolab PGSTAT30N potentiostat (Metrohm Autolab B.V.). The stability tests were conducted in a two-electrode Teflon cell

under vigorous stirring, using a Pt foil (area 5 cm^2) as counter electrode. A total of 6 $NiFeO_xH_y$ anodes were used for the stability evaluation in different conditions. Each sample was subjected to a chronopotentiometry at 100 mA cm^{-2} for 1 h at different temperatures (25 °C or 75 °C) and base concentrations (1, 5, or 10 M KOH).

Activity evaluation of fresh and used samples was performed in 1 M KOH (KOH, Alfa Aesar, ACS reagent ≥85.0%) at room temperature. Milli-Q water (18.2 MΩ cm) was used in all the dilution and cleaning steps. The tests were conducted in a standard three-electrode configuration. A platinum wire and an XR440 Red Rod Electrode (Ag/AgCl without KCl, Radiometer Analytical, E = +0.48 V_{SHE}) were used as counter and reference electrodes, respectively. Cyclic voltammetry (CV) was conducted with a scan rate of 50 mV s^{-1}. Five cycles were applied in order to obtain stable voltammograms. The fifth cycle is reported in the graphs shown throughout the manuscript. Electrochemical Impedance Spectroscopy (EIS) measurements were conducted at E = +1.54 V_{RHE} in a frequency range from 10^{-1} to 10^3 Hz with an AC amplitude of 10 mV. Step chronoamperometry was conducted by increasing the potential in 20 mV steps and applying a hold time of 30 s: the values of current densities measured at the end of each step were plotted versus the iR-corrected values of overpotential to construct Tafel plots. Tafel slopes were evaluated by linear fits of the experimental data with an error of ±1 mV dec^{-1}.

5.2.3. Materials characterization

XPS measurements were performed on a K-alpha XPS spectrometer (Thermo Scientific) equipped with a monochromatic Al Kα (1486.6 eV) X-ray source. The spot size was 400 µm and the pass energy was set at 200 eV and 50 eV for survey and high-resolution spectra, respectively. A flood gun was used for charge compensation. Binding energy calibration of the spectra was applied by setting the C 1s binding energy of the adventitious sp^3 carbon component at 284.8 eV. Ni 2p and Fe 3p regions were used to determine the metal content at the surface of the electrodes. All the spectra were processed using CasaXPS software version 2.3.22 (Casa Software Ltd.).

Scanning electron micrographs (SEM) were acquired on a FEI Quanta 3D FEG microscope at an accelerating voltage of 5 kV. Energy dispersive X-Ray (EDX) spectroscopy was performed on a Phenom Pro-X microscope with an accelerating voltage of 10 kV.

Raman spectra were acquired on a Witec Alpha 300R Raman microscope with λ_{exc} = 532 nm using a Zeiss 50x, NA = 0.55 objective. Spectra were acquired at a power of 10 mW, with a collection time of 10 s, averaging 10 accumulations for each spectrum.

X-ray diffraction (XRD) patterns were acquired using a Bruker D2 Phaser diffractometer equipped with a Cu K_α radiation source, using a step size of 0.02° and acquisition time of 1 s per step.

Inductively coupled plasma optical emission spectrometry (ICP-OES) measurements of catalytic films and used electrolytes were conducted on a SPECTROBLUE spectrometer equipped with an axial plasma source (Ar). The films were dissolved by immersing the coated substrates overnight in 1 mL of concentrated nitric acid (HNO_3 65%, Sigma) under standard conditions and sealing with parafilm to prevent evaporation. Then, the solutions were diluted 20 times to reach a HNO_3 concentration of ≈3% to prevent damage of the instrument. Four independent samples were measured using this protocol. For ICP-OES analysis of used electrolytes, as KOH concentrations exceeding 0.1 M could damage the instrument, the solutions were diluted to this concentration prior to the analysis. Quantities below 5 µg L^{-1} could not be detected because of the sensitivity limit of the instrument.

5.3. Results and discussion

NiFe-(oxy)hydroxide films ($NiFeO_xH_y$) were deposited *via* cathodic electrodeposition from an aqueous solution of Ni(II) and Fe(II) sulfates. The deposition method is expected to form predominantly a $Ni(OH)_2$ phase, with Fe^{3+} ions substituting Ni^{2+}.

Elemental analysis of four independent samples measured by ICP-OES revealed total metal loadings of 13.5 (± 2.6) µg cm^{-2}, with Ni and Fe contents of 73 at% and 27 at% (± 5 at%), respectively.

Surface analysis of the films was conducted by means of XPS. Ni 2p, Fe 2p, and O 1s XP spectra are reported in Figure 5.1. The Ni 2p spectrum reveals a major contribution from Ni^{2+} species in a $Ni(OH)_2$ environment with the Ni $2p_{3/2}$ and Ni $2p_{1/2}$ contributions located at binding energies (BE) of 855.5 eV and 873.0 eV, respectively.[14,15,31,32] Satellite peaks at higher binding energies than the main photoemission lines are an additional fingerprint of Ni^{2+} species and originate from the interaction of unpaired core electrons with unpaired electrons in the valence band.[32,33] A small contribution of Ni^{3+} species (BE(Ni $2p_{3/2}$) = 857.3 eV) indicates a minor presence of NiOOH in the fresh films.[15] The fraction of Ni^{3+} was in the range of 9 – 20 % for the fresh samples. The Fe 2p spectrum shows two main peaks located at 711.7 eV (Fe $2p_{3/2}$) and 725.4 eV (Fe $2p_{1/2}$) and broad satellite features identified as shake-up peaks. These peaks are a clear sign of the presence of Fe^{3+} in the fresh samples.[31,34,35] It is however difficult to identify and quantify the presence of different Fe phases (oxides,

hydroxides) from the Fe 2p spectrum because of the multiple overlapping components in a narrow binding energy range.[33] The O 1s spectrum was fitted with three components located at binding energies of 529.4 eV, 531.0 eV, and 533.1 eV, which can be ascribed to lattice oxygen, oxygen in hydroxides, and adsorbed water, respectively.[32,36]

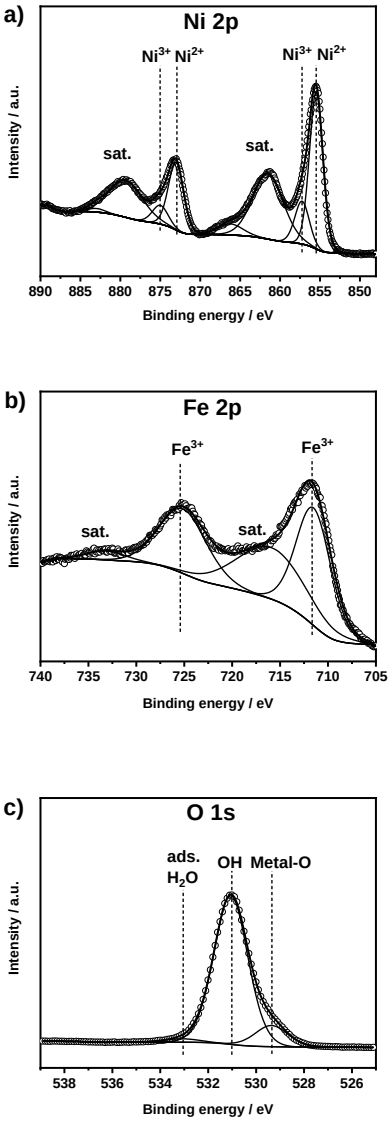

Figure 5.1. a) Ni 2p, b) Fe 2p, and c) O 1s XPS spectra of as-prepared $NiFeO_xH_y$ films. The circles represent the experimental data, the lines represent the fittings.

The Ni:Fe ratio of the as-prepared samples was evaluated by XPS and EDX in order to determine the surface and bulk composition of the films, respectively. Both techniques revealed similar Ni:Fe ratios (74:26 by XPS *vs.* 70:30 by EDX), which is an indication of the absence of surface enrichment in any of the metals; the results are also in agreement with those of ICP-OES elemental analysis of the films (Ni:Fe ratio of 73:27). The composition evaluated by EDX can be considered as the bulk composition because the probing depth of EDX is higher than the thickness of the films. This assumption is confirmed by the strong signal arising from the underlying Au-coated Si substrate (Figure D1). The Fe content at the surface (26% as determined by XPS) of our samples is in the range reported to be optimum for the OER (15-50%).[8,17,19,29] XRD revealed no other peaks than those arising from the Au-coated Si substrate (Figure D2). The electrodes were then subjected to an anodic polarization at different temperatures and KOH concentrations (Figure D3). The impact of these electrochemical tests on the electrodes will be discussed in the following.

As anodic polarization can lead to dissolution of the active metals, we analyzed the compositional changes of the anodes after the electrochemical treatment in terms of Ni:Fe ratio at the surface and in the bulk using XPS and EDX. XPS analysis (Figure 5.2a) shows the changes in the surface composition of the anodes upon electrochemical treatment under different conditions. After treatment at 25 °C, a very small increase in the Ni:Fe ratio at the surface is noted by XPS. The influence of the base concentration is very small. Similar treatment at 75 °C led to more substantial changes in the surface composition, which became larger with increased basicity. The sample anodically polarized in 10 M KOH at 75 °C shows a very high Ni content (97%). The results of EDX analysis (Figure 5.2b) are in line with the XPS results. While the samples tested at 25 °C show a slightly higher Ni:Fe ratio as compared to fresh samples, the changes are more substantial for the samples tested at 75 °C. These changes are also larger at higher KOH concentration, especially for the sample tested at 75 °C in 10 M KOH. The XPS and EDX results show preferential Fe leaching due to the electrochemical treatment. There is no large difference between these compositional changes at the surface and in the bulk, suggesting that the changes are uniform. This is likely because the films are very thin and composed of small particles. The overall changes before and after anodic testing are very minor in 1 M KOH, regardless of the temperature, showing that at low base concentration the electrodes are stable. Preferential Fe leaching is substantial for samples tested at 75 °C in 5 M KOH and 10 M KOH. As the films are very thin, it was not possible to quantitatively determine absolute leaching ratios by elemental analysis and, in this way, to establish how much Ni was leached. Fe leaching is most likely due to the applied electrochemical treatment rather than chemical dissolution, as no

significant changes in the Ni:Fe ratio were observed by XPS after 1 hour of electrode immersion in 10 M KOH at 75 °C (data reported in Figure D4).

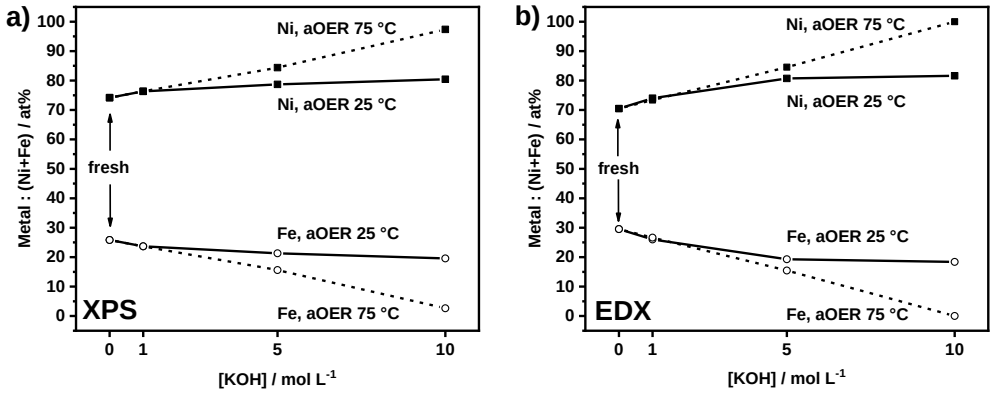

Figure 5.2. a) XPS and b) EDX analysis of $NiFeO_xH_y$ films before and after OER polarization (aOER) conducted at j = 100 mA cm^{-2} for 1 h at different temperatures and KOH concentrations.

The Ni 2p, Fe 2p, and O 1s XPS spectra of the used samples reported in Figure D5, D6, and D7, respectively, do not show significant changes as compared to those of fresh samples, except for the sample polarized in 10 M KOH at 75 °C. For this latter sample, the Ni $2p_{3/2}$ region contains an additional component at lower binding energy (BE = 853.9 eV) corresponding to NiO.[32,37] Its appearance goes together with an increasing signal of the lattice O component observed in the O 1s XPS spectrum. Notably, the Fe signal in this sample was very weak (Ni:Fe ratio = 97:3). We can infer from this that part of Ni-hydroxide was converted into Ni-oxide during electrochemical treatment at the most severe conditions (10 M KOH, 75 °C). This finding is in keeping with a previous study where NiFe-LDH was found to transform into a mixture of NiO and Ni_2FeO_4 after prolonged electrolysis (100 h) in 5 M KOH at 60 °C.[27] The transformation of Ni-(oxy)hydroxide into Ni-oxide could negatively affect the anode performance because NiO has a lower OER activity than $Ni(OH)_2$.[38]

Moreover, after electrochemical polarization at 75 °C in 10 M KOH, the loss of active phase led to the exposure and corrosion of the underlying Au coating on the substrate. The XPS survey spectrum (Figure D8) showed an increase in the intensity of the Au peaks and the

appearance of Si peaks arising from the substrate after polarization at the harshest conditions.

Changes in film morphology upon electrochemical treatment were investigated by SEM (Figure 5.3). The micrograph of the bare substrate is reported in Figure D9 as reference. The as-deposited sample exhibits a platelet-like morphology, characteristic of NiFe-(oxy)hydroxide films,[39] with some thicker agglomerates on the electrode surface. There were no substantial changes upon anodic polarization of the samples in 1 M KOH irrespective of the temperature. This is in line with the small chemical changes evident from XPS and EDX analyses under these conditions. Testing in 5 M KOH did not lead to morphological changes at 25 °C, although the number of platelets was lower after anodic polarization at 75 °C. Most of the platelets disappeared after anodic polarization at 10 M KOH. At 25 °C, the platelets were changed into small and compact flakes, while the sample obtained after testing at 75 °C only contained fine round grains on a flat surface. The absence of platelet-like features points toward a structural instability of the layered $NiFeO_xH_y$ phase under electrochemical conditions relevant to the OER. The severe changes are consistent with a loss of material during the stability tests at high temperatures and KOH concentrations.

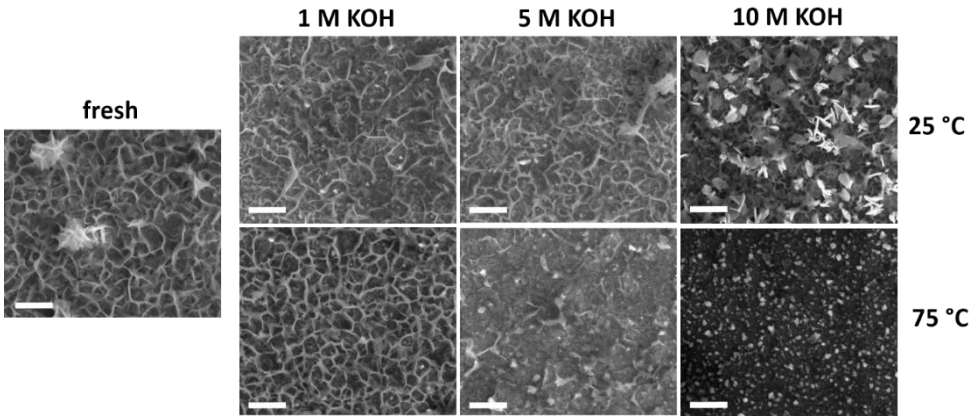

Figure 5.3. SEM images of fresh and used $NiFeO_xH_y$ films after the stability tests conducted at different temperatures and electrolyte concentrations (scale bars 500 nm).

The structure and phase composition of the $NiFeO_xH_y$ films were also investigated by Raman spectroscopy (Figure 5.4). The Raman spectra of $NiFeO_xH_y$ exhibit three characteristic bands at 458 cm^{-1}, 540 cm^{-1}, and 675 cm^{-1}. The band at 458 cm^{-1} is ascribed to α-$Ni(OH)_2$ and β-$Ni(OH)_2$ phases, which have Ni-O bands at similar frequencies (α-$Ni(OH)_2$: 460-465 cm^{-1}, β-$Ni(OH)_2$: 445-449 cm^{-1}).[19,21,40,41] The band at 540 cm^{-1} is ascribed to Ni-O vibrations in defective or highly disordered $Ni(OH)_2$ with a low degree of crystallinity.[19,40,41] The position of this band was found to be dependent on the amount of incorporated Fe in the $Ni(OH)_2$ films, shifting toward higher wavenumber at higher Fe incorporations.[19] The feature at 675 cm^{-1}, due to the presence of Fe, can be attributed to Fe_3O_4, γ-Fe_2O_3, and γ-FeOOH, which all exhibit a band at nearly similar frequencies.[42–44] The spectrum of $NiFeO_xH_y$ after activity evaluation (CV) exhibits similar but more intense features compared to fresh $NiFeO_xH_y$, which can be attributed to enhanced Raman scattering on a roughened surface. The spectra of $NiFeO_xH_y$ samples after anodic polarization in 1 M and 5 M KOH show some changes compared to the spectrum of $NiFeO_xH_y$. The lower intensity of the band at 458 cm^{-1} indicates a loss of $Ni(OH)_2$, while the shift of the band from 540 cm^{-1} to 530 cm^{-1} implies a lower substitution degree of Fe in the $Ni(OH)_2$ structure. These changes are in line with the preferential leaching of Fe as discussed above. To confirm this hypothesis, we compared the position of this band with a NiO_xH_y measured as a reference. We used the Raman spectrum of a NiO_xH_y after the activity test (cyclic voltammetry) for this purpose because we could not identify any Raman feature in the spectrum of fresh sample, possibly because of the low roughness of the as-deposited material. NiO_xH_y showed the presence of the feature at 515 cm^{-1}, confirming that the position of this band is sensitive to the amount of Fe. The negative shift occurred for $NiFeO_xH_y$ after the stability tests is, therefore, an indication of lower Fe incorporation as a result of the electrochemical treatment. The lower amount of Fe in the tested samples is also reflected in the lower intensity of the band at 675 cm^{-1}, related to Fe oxide/oxyhydroxide. For the sample tested in 10 M KOH, we can observe differences depending on the temperature used in the electrochemical test. In the spectrum of the sample tested at 25 °C, in addition to the previous changes, we can also distinguish a broad band appearing at ~580 cm^{-1}, potentially due to the oxidation of the underlying Au.[45] This can be due to a lower amount of catalytic phase resulting in parts of the substrate left uncovered. This band appears as a very broad feature grouped with the Ni-O band in the Raman spectrum of the sample tested at 75 °C in 10 M KOH, resulting in a very weak and large band extending from 500 cm^{-1} to 600 cm^{-1}. The decrease in band intensity suggests that a massive film leaching occurred during the electrochemical treatment at the harshest condition (75 °C and 10 M KOH).

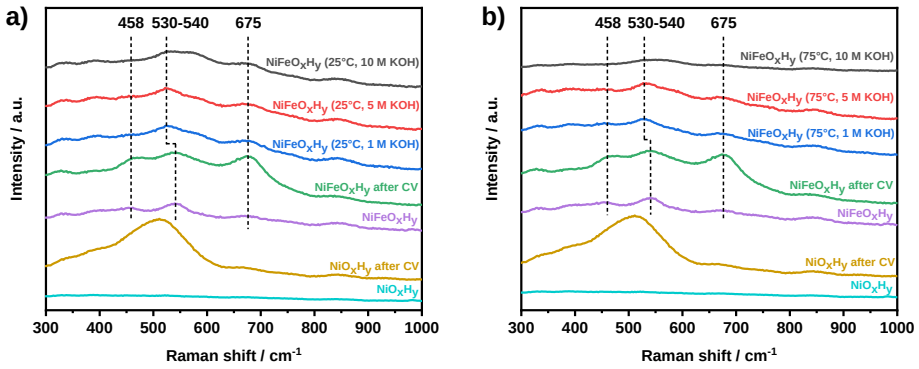

Figure 5.4. Raman spectra of fresh NiO_xH_y, NiO_xH_y after CV, fresh $NiFeO_xH_y$, $NiFeO_xH_y$ after CV, and $NiFeO_xH_y$ after anodic polarization at j = 100 mA cm^{-2} at a) 25 °C and b) 75 °C.

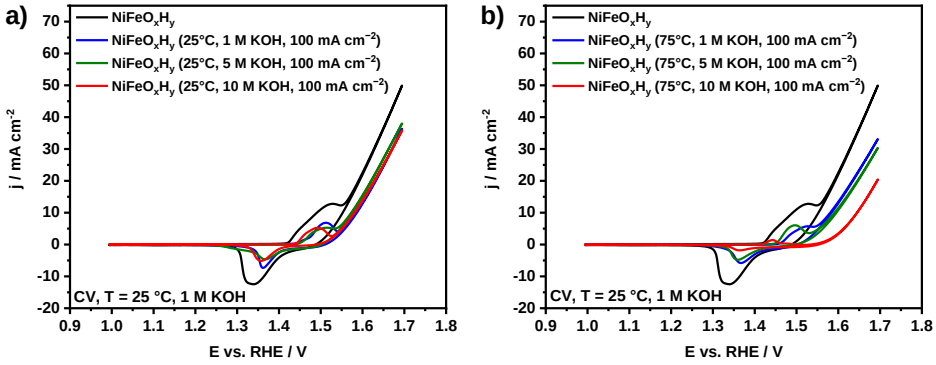

Figure 5.5. Cyclic voltammetry (CV) recorded at 25 °C in 1 M KOH at a scan rate of 50 mV s^{-1} of $NiFeO_xH_y$ before and after anodic polarization at j = 100 mA cm^{-2} in alkaline conditions at a) 25 °C and b) 75 °C.

The OER activity and redox properties of the samples before and after the electrochemical polarization were evaluated by cyclic voltammetry (Figure 5.5). The voltammogram of fresh $NiFeO_xH_y$ anode contains a redox peak associated with $Ni^{2+} \rightarrow Ni^{3+}$ oxidation, followed by an increase of the current density ascribed to oxygen evolution at higher potentials. The split of the redox peak can be associated with the presence of α-$Ni(OH)_2$ and β-$Ni(OH)_2$ phases in the fresh films, which respectively oxidize to γ-NiOOH and β-NiOOH. The conversion of α-$Ni(OH)_2$ to γ-NiOOH occurs at a lower potential than the conversion of β-$Ni(OH)_2$ to β-

NiOOH.[21,39,46]. The cyclic voltammograms of $NiFeO_xH_y$ samples previously subjected to anodic polarization at 25 °C are reported in Figure 5.5a. The catalytic activity of the used anodes at 25 °C is lower than that of the fresh $NiFeO_xH_y$ films, regardless of the different KOH concentration used in the stability test. We can also observe a decrease in the redox peak areas compared to the fresh anode, which is most likely due to dissolution of part of the active phase in the electrode. For samples previously tested at 75 °C (Figure 5.5b), the decrease in the catalytic activity is more pronounced than for samples tested at 25 °C. This is consistent with the more pronounced Fe leaching in the samples tested under more severe conditions. The KOH concentration in the stability test also affects the catalytic activity, a higher base concentration resulting in a lower OER activity, especially after treatment in 10 M KOH. Similar to the samples tested at 25 °C, the redox peak area of the samples tested at 75 °C is lower, which is also due to film degradation. In fact, for the most severely tested sample, the redox peak is hardly visible in the voltammogram.

The important result is that anodic polarization at elevated temperature and increased base concentration leads to loss of the active metals with a preferential removal of Fe, negatively affecting the OER performance of $NiFeO_xH_y$ anodes. Under the most severe testing conditions (75 °C, 10 M KOH), the conversion of Ni-(oxy)hydroxide to Ni-oxide was also observed, which will also contribute to the lowered activity.

We next compared the stability of $NiFeO_xH_y$ with that of NiO_xH_y after 1 hour of anodic polarization at 75 °C in 5 M KOH, similar to the conditions applied in commercial alkaline electrolyzers (Figure D10). The effect on the redox properties and electrocatalytic activity is shown in Figure 5.6a. In accordance with previous findings, the redox peak ascribed to the transformation Ni^{2+}/Ni^{3+} in the voltammogram of NiO_xH_y is cathodically shifted and the catalytic activity is significantly lower as compared to $NiFeO_xH_y$.[17,19,47] After anodic polarization at 75 °C in 5 M KOH, differently than in the case of $NiFeO_xH_y$, the activity of NiO_xH_y increased. The electrochemical test conducted at high temperature and molar concentration was thus beneficial for the performance of NiO_xH_y.

The electrocatalytic behavior of the anodes was also evaluated by Tafel analysis (Figure D11). The values of Tafel slopes (summarized in Table 5.1) of fresh $NiFeO_xH_y$ and NiO_xH_y clearly show the beneficial effect of Fe on the kinetics of OER on $Ni(OH)_2$, resulting in a lower Tafel slope for the Fe-doped sample (37 mV dec^{-1}) as compared to pure NiO_xH_y (48 mV dec^{-1}). The values of Tafel slopes are in agreement with previous findings available in literature;[19,48] Tafel slopes of around 40 mV dec^{-1} indicate that a second-electron transfer is rate-determining in the OER reaction pathway.[48,49] After an electrochemical treatment conducted at 75 °C in 5 M KOH, $NiFeO_xH_y$ maintained the same Tafel slope (37 mV dec^{-1}),

indicating that the reaction mechanism and the rate-determining step were unchanged by the applied electrochemical treatment. On the other hand, the Tafel slope of NiO_xH_y decreased after anodic polarization at 75 °C in 5 M KOH (to 39 mV dec^{-1}), exhibiting a slope comparable to that of $NiFeO_xH_y$ (37 mV dec^{-1}). This finding indicates improved kinetics for NiO_xH_y after anodic polarization.

To further investigate the electrochemical properties of the samples, electrochemical impedance spectroscopy was applied (Figure 5.6b). Each point in the Nyquist plot represents the real (*Z'*) and imaginary (*Z''*) part of the impedance determined at different frequencies (decreasing from left to right) of a sinusoidal electrochemical perturbation of the voltage.[50] The Nyquist plots of the fresh and tested samples show typical semicircles attributed to the charge-transfer resistance (R_{ct}) at the electrode surface.[13,51,52] The real value of impedance at low Z' (*i.e.*, at high frequencies) corresponds to the resistance of the electrolyte and the circuit (R_s). The spectra were fitted with an $R_s(R_{ct}C_{dl})$ circuit, to account for the series resistance, the charge-transfer resistance, and the double-layer capacitance of the samples.[50,53] The results are summarized in Table 5.1. Analysis of the values of R_{ct} shows that the charge-transfer resistance of the Fe-doped sample increased by a factor of three after anodic polarization, while for pure NiO_xH_y the values of R_{ct} were significantly lower after polarization. While the electrochemical test detrimentally affected the charge-transfer properties of $NiFeO_xH_y$, improved charge transfer was found for NiO_xH_y. We also evaluated the double-layer capacitances (C_{dl}) of the samples, which are proportional to the electrochemical surface area of the samples.[53–56] The values of C_{dl} of NiO_xH_y were higher than for $NiFeO_xH_y$ before the electrochemical test; after anodic polarization, the values for both samples were roughly halved, indicating that a loss of surface area occurred due to applied electrochemical treatment. The lower electrochemical surface areas could be due to lower catalyst loading after the electrochemical treatment because of leaching. SEM images of NiO_xH_y after anodic polarization at 75 °C in 5 M KOH reveal a loss of active phase compared to fresh sample (Figure D12), similar to what we previously observed for $NiFeO_xH_y$.

NiO_xH_y is known to incorporate Fe impurities present in KOH, which results in an activity enhancement.[21,39,57] We thus evaluated the surface composition on fresh and used NiO_xH_y by means of XPS analysis. The results reported in Figure 5.6c conducted on NiO_xH_y show that after anodic polarization at 75 °C in 5 M KOH the NiO_xH_y sample incorporated a small amount of Fe during the electrochemical treatment, responsible for the increase in catalytic activity compared to fresh NiO_xH_y. These results indicate that differences in Fe content and electrocatalytic properties of NiO_xH_y and $NiFeO_xH_y$ become small after electrochemical polarization at 75 °C in 5 M KOH, because of the similar final low Fe content.

Table 5.1. Summary of Tafel slopes (derived by step chronoamperometry) and values of R_{ct} and C_{dl} obtained by fitting the EIS spectra of fresh and used NiO_xH_y and $NiFeO_xH_y$.

Sample ID	Tafel slope, mV dec^{-1}	R_{ct}, Ω cm^2	C_{dl}, mF cm^{-2}
$NiFeO_xH_y$	37	3.14	7.05
$NiFeO_xH_y$ (75 °C , 5 M KOH, j = 100 mA cm^{-2})	37	10.29	3.20
NiO_xH_y	48	61.2	20.8
NiO_xH_y (75 °C, 5 M KOH, j = 100 mA cm^{-2})	39	26.8	12.0

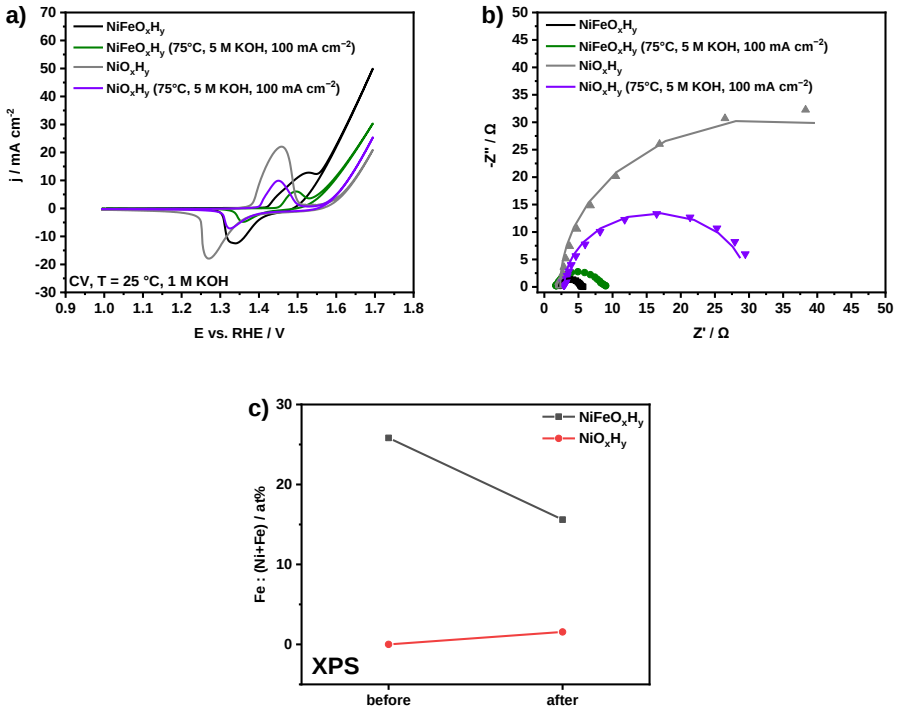

Figure 5.6. a) Cyclic voltammetry (CV) recorded in 1 M KOH with a scan rate of 50 mV s^{-1} of NiO_xH_y and $NiFeO_xH_y$ before and after anodic polarization at 75 °C in 5 M KOH, j = 100 mA cm^{-2}; b) experimental (points) and fitted (lines) Nyquist plots recorded at 25 °C in 1 M KOH at E = +1.54 V_{RHE}; c) atomic Fe percentage out of the total (Ni+Fe) content measured by XPS before and after anodic polarization at 75 °C in 5 M KOH, j = 100 mA cm^{-2}.

5.4. Conclusions

We investigated the stability of thin NiFe-(oxy)hydroxide films upon alkaline water oxidation at a current density of 100 mA cm^{-2} at different temperatures and KOH concentrations, close to conditions prevalent in industrial alkaline water electrolyzers. Depending on the temperature and KOH concentration, the anodes were affected in terms of structure and performance. While anodic polarization at 25 °C did not significantly impact the anodes, a higher temperature (75 °C) caused faster degradation of the anodes, especially in 5 or 10 M KOH. XPS, EDX, and Raman characterization pointed to preferential leaching of Fe over Ni, especially when high temperatures and KOH concentrations were applied. The platelet-like morphology characteristic of $NiFeO_xH_y$ disappeared during polarization at the harshest conditions, suggesting a loss of active phase, which was confirmed by a decreased electrochemical surface area. These changes also impacted the catalytic activity of the samples, which was decreased after electrochemical testing at high temperature and base concentrations. For the sample tested under the harshest conditions (75 °C, 10 M KOH), a conversion from $Ni(OH)_2$ to NiO was observed, resulting in further deterioration of the catalytic properties of this sample. On the other hand, pure NiO_xH_y easily incorporates Fe from the KOH electrolyte impurities during anodic polarization at 75 °C in 5 M KOH, which leads to an increase of its catalytic activity despite the loss of surface area during the electrochemical test. The Fe content, electrocatalytic activity, and Tafel slope of NiO_xH_y approached those of $NiFeO_xH_y$ after electrochemical treatment at industrially relevant conditions. These results highlight the importance of conducting stability tests at more realistic conditions to evidence degradation mechanisms of the electrodes during industrial operations.

5.5. References

(1) Seh, Z. W.; Kibsgaard, J.; Dickens, C. F.; Chorkendorff, I.; Nørskov, J. K.; Jaramillo, T. F. *Science* **2017**, *355*, eaad4998.

(2) Schalenbach, M.; Zeradjanin, A. R.; Kasian, O.; Cherevko, S.; Mayrhofer, K. J. J. *Int. J. Electrochem. Sci.* **2018**, *13* (2), 1173–1226.

(3) Du, P.; Eisenberg, R. *Energy Environ. Sci.* **2012**, *5* (3), 6012–6021.

(4) Lyu, F.; Wang, Q.; Choi, S. M.; Yin, Y. *Small* **2019**, *15* (1), 1–17.

(5) Burke, M. S.; Zou, S.; Enman, L. J.; Kellon, J. E.; Gabor, C. A.; Pledger, E.; Boettcher, S. W. *J. Phys. Chem. Lett.* **2015**, *6* (18), 3737–3742.

(6) Hunter, B. M.; Gray, H. B.; Müller, A. M. *Chem. Rev.* **2016**, *116* (22), 14120–14136.

(7) Gong, M.; Dai, H. *Nano Res.* **2015**, *8* (1), 23–39.

(8) Landon, J.; Demeter, E.; Nilay, I.; Keturakis, C.; Wachs, I. E.; Vasic, R.; Frenkel, A. I.; Kitchin, J. R. *ACS Catal.* **2012**, *2*, 1793–1801.

(9) Dionigi, F.; Strasser, P. *Adv. Energy Mater.* **2016**, *6*, 1600621.
(10) Corrigan, D. A.; Bendert, R. M. *J. Electrochem. Soc.* **1989**, *136* (3), 723–728.
(11) Lu, X.; Zhao, C. *Nat. Commun.* **2015**, *6*, 6616.
(12) Trotochaud, L.; Ranney, J. K.; Williams, K. N.; Boettcher, S. W. *J. Am. Chem. Soc.* **2012**, *134* (41), 17253–17261.
(13) Gao, M.; Sheng, W.; Zhuang, Z.; Fang, Q.; Gu, S.; Jiang, J.; Yan, Y. *J. Am. Chem. Soc.* **2014**, *136* (19), 7077–7084.
(14) Zhou, T.; Cao, Z.; Zhang, P.; Ma, H.; Gao, Z.; Wang, H.; Lu, Y.; He, J.; Zhao, Y. *Sci. Rep.* **2017**, *7* (46154), 1–9.
(15) He, K.; Cao, Z.; Liu, R.; Miao, Y.; Ma, H.; Ding, Y. *Nano Res.* **2016**, *9* (6), 1856–1865.
(16) Gong, M.; Li, Y.; Wang, H.; Liang, Y.; Wu, J. Z.; Zhou, J.; Wang, J.; Regier, T.; Wei, F.; Dai, H. *J. Am. Chem. Soc.* **2013**, *135*, 8452–8455.
(17) Corrigan, D. A. *J. Electrochem. Soc.* **1987**, *134* (2), 377–384.
(18) Hall, D. S.; Lockwood, D. J.; Bock, C.; MacDougall, B. R. *Proc. R. Soc. A* **2015**, *471*, 2174.
(19) Louie, M. W.; Bell, A. T. *J. Am. Chem. Soc.* **2013**, *135* (33), 12329–12337.
(20) Li, N.; Bediako, D. K.; Hadt, R. G.; Hayes, D.; Kempa, T. J.; von Cube, F.; Bell, D. C.; Chen, L. X.; Nocera, D. G. *Proc. Natl. Acad. Sci.* **2017**, *114* (7), 1486–1491.
(21) Klaus, S.; Cai, Y.; Louie, M. W.; Trotochaud, L.; Bell, A. T. *J. Phys. Chem. C* **2015**, *119* (13), 7243–7254.
(22) Stevens, M. B.; Trang, C. D. M.; Enman, L. J.; Deng, J.; Boettcher, S. W. *J. Am. Chem. Soc.* **2017**, *139* (33), 11361–11364.
(23) Ahn, H. S.; Bard, A. J. *J. Am. Chem. Soc.* **2016**, *138* (1), 313–318.
(24) Friebel, D.; Louie, M. W.; Bajdich, M.; Sanwald, K. E.; Cai, Y.; Wise, A. M.; Cheng, M. J.; Sokaras, D.; Weng, T. C.; Alonso-Mori, R.; Davis, R. C.; Bargar, J. R.; Nørskov, J. K.; Nilsson, A.; Bell, A. T. *J. Am. Chem. Soc.* **2015**, *137* (3), 1305–1313.
(25) Görlin, M.; Chernev, P.; Paciok, P.; Tai, C. W.; Ferreira de Araújo, J.; Reier, T.; Heggen, M.; Dunin-Borkowski, R.; Strasser, P.; Dau, H. *Chem. Commun.* **2019**, *55* (6), 818–821.
(26) Zeng, K.; Zhang, D. *Prog. Energy Combust. Sci.* **2010**, *36* (3), 307–326.
(27) Andronescu, C.; Barwe, S.; Ventosa, E.; Masa, J.; Vasile, E.; Konkena, B.; Möller, S.; Schuhmann, W. *Angew. Chemie - Int. Ed.* **2017**, *56* (37), 11258–11262.
(28) Andronescu, C.; Seisel, S.; Wilde, P.; Barwe, S.; Masa, J.; Chen, Y. T.; Ventosa, E.; Schuhmann, W. *Chem. - A Eur. J.* **2018**, *24* (52), 13773–13777.
(29) Klaus, S.; Louie, M. W.; Trotochaud, L.; Bell, A. T. *J. Phys. Chem. C* **2015**, *119* (32), 18303–18316.
(30) Schneider, C. A.; Rasband, W. S.; Eliceiri, K. W. *Nature Methods*. Nat Methods July 2012, pp 671–675.
(31) Hunter, B. M.; Hieringer, W.; Winkler, J. R.; Gray, H. B.; Müller, A. M. *Energy Environ. Sci.* **2016**, *9* (5), 1734–1743.
(32) Mcintyre, N. S.; Cook, M. G. *Anal. Chem.* **1975**, *47* (13), 2208–2213.
(33) Biesinger, M. C.; Payne, B. P.; Grosvenor, A. P.; Lau, L. W. M.; Gerson, A. R.; Smart, R. S. C. *Appl. Surf. Sci.* **2011**, *257* (7), 2717–2730.
(34) Roy, C.; Sebok, B.; Scott, S. B.; Fiordaliso, E. M.; Sørensen, J. E.; Bodin, A.; Trimarco, D. B.; Damsgaard, C. D.; Vesborg, P. C. K.; Hansen, O.; Stephens, I. E. L.; Kibsgaard, J.; Chorkendorff, I. *Nat. Catal.* **2018**, *1* (11), 820–829.
(35) Etzi Coller Pascuzzi, M.; Selinger, E.; Sacco, A.; Castellino, M.; Rivolo, P.; Hernández, S.; Lopinski, G.; Tamblyn, I.; Nasi, R.; Esposito, S.; Manzoli, M.; Bonelli, B.; Armandi, M. *Electrochim. Acta* **2018**, *284*, 294–302.
(36) Sun, T.; Xu, L.; Yan, Y.; Zakhidov, A. A.; Baughman, R. H.; Chen, J. *ACS Catal.* **2016**, *6* (3), 1446–1450.
(37) Casella, I. G.; Guascito, M. R.; Sannazzaro, M. G. *J. Electroanal. Chem.* **1999**, *462* (2), 202–210.

(38) Stern, L. A.; Hu, X. *Faraday Discuss.* **2014**, *176*, 363–379.
(39) Trotochaud, L.; Young, S. L.; Ranney, J. K.; Boettcher, S. W. *J. Am. Chem. Soc.* **2014**, *136* (18), 6744–6753.
(40) Kostecki, R.; McLarnon, F. *J. Electrochem. Soc.* **1997**, *144* (2), 485–493.
(41) Desilvestro, J.; Corrigan, D. A.; Weaver, M. J. *J. Electrochem. Soc.* **1988**, *135* (4), 885–892.
(42) Thierry, D.; Persson, D.; Leygraf, C.; Boucherit, N.; Hugot-le Goff, A. *Corros. Sci.* **1991**, *32* (3), 273–284.
(43) Slavov, L.; Abrashev, M. V.; Merodiiska, T.; Gelev, C.; Vandenberghe, R. E.; Markova-Deneva, I.; Nedkov, I. *J. Magn. Magn. Mater.* **2010**, *322* (14), 1904–1911.
(44) de Faria, D. L. A.; Venâncio Silva, S.; de Oliveira, M. T. *J. Raman Spectrosc.* **1997**, *28* (11), 873–878.
(45) Yeo, B. S.; Klaus, S. L.; Ross, P. N.; Mathies, R. A.; Bell, A. T. *ChemPhysChem* **2010**, *11* (9), 1854–1857.
(46) Lyons, M. E. G.; Brandon, M. P. *Int. J. Electrochem. Sci.* **2008**, *3* (12), 1386–1424.
(47) Li, X.; Walsh, F. C.; Pletcher, D. *Phys. Chem. Chem. Phys.* **2011**, *13* (3), 1162–1167.
(48) Pérez-Alonso, F. J.; Adán, C.; Rojas, S.; Peña, M. A.; Fierro, J. L. G. *Int. J. Hydrogen Energy* **2014**, *39* (10), 5204–5212.
(49) Guerrini, E.; Piozzini, M.; Castelli, A.; Colombo, A.; Trasatti, S. *J. Solid State Electrochem.* **2008**, *12* (4), 363–373.
(50) Bredar, A. R. C.; Chown, A. L.; Burton, A. R.; Farnum, B. H. *ACS Appl. Energy Mater.* **2020**, *3*, 66–98.
(51) Merrill, M.; Dougherty, R. *J. Phys. Chem. C* **2008**, *112* (10), 3655–3666.
(52) Weng, B.; Xu, F.; Wang, C.; Meng, W.; Grice, C. R.; Yan, Y. *Energy Environ. Sci.* **2017**, *10* (1), 121–128.
(53) McCrory, C. C. L.; Jung, S.; Peters, J. C.; Jaramillo, T. F. *J. Am. Chem. Soc.* **2013**, *135* (45), 16977–16987.
(54) Etzi Coller Pascuzzi, M.; Goryachev, A.; Hofmann, J. P.; Hensen, E. J. M. *Appl. Catal. B Environ.* **2020**, *261*, 118225.
(55) Zhou, F.; Izgorodin, A.; Hocking, R. K.; Armel, V.; Spiccia, L.; MacFarlane, D. R. *ChemSusChem* **2013**, *6* (4), 643–651.
(56) Goryachev, A.; Etzi Coller Pascuzzi, M.; Carlà, F.; Weber, T.; Over, H.; Hensen, E. J. M.; Hofmann, J. P. *Electrochim. Acta* **2020**, *336*, 135713.
(57) Smith, A. M.; Trotochaud, L.; Burke, M. S.; Boettcher, S. W. *Chem. Commun.* **2015**, *51* (25), 5261–5263.

Appendix D

Supporting Information for Chapter 5

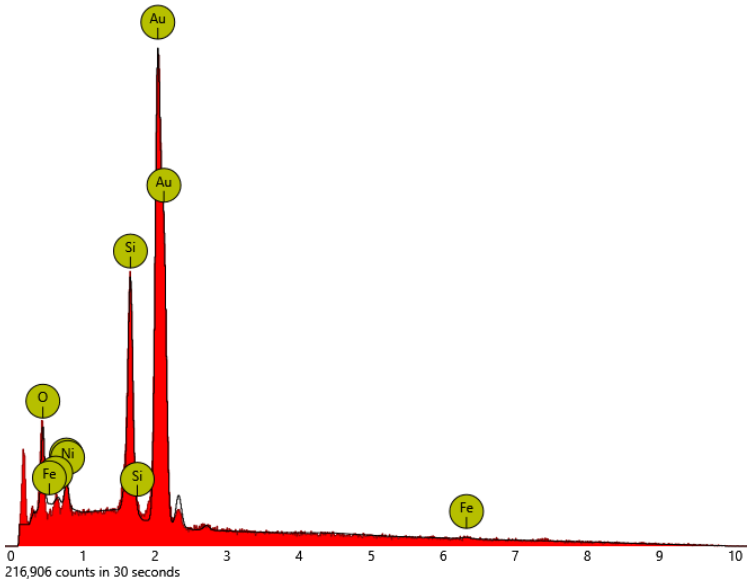

Element Symbol	Atomic Conc.	Weight Conc.
Au	58.9	91.6
O	18.5	2.3
Si	18.3	4.1
Ni	3.0	1.4
Fe	1.3	0.6

Figure D1. EDX analysis of as-deposited $NiFeO_xH_y$ sample.

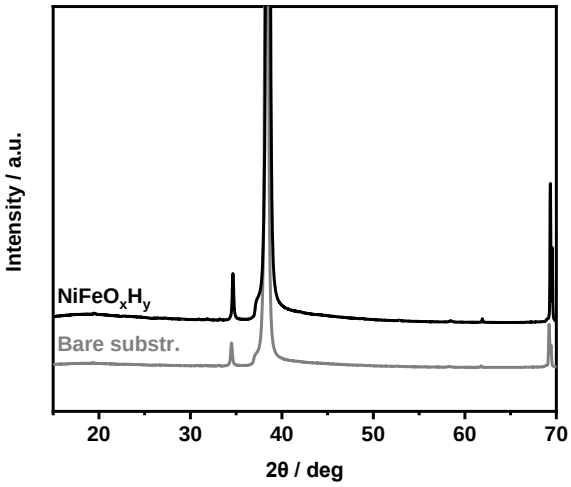

Figure D2. XRD patterns of fresh supported NiFeO$_x$H$_y$ sample and bare Au-coated Si substrate.

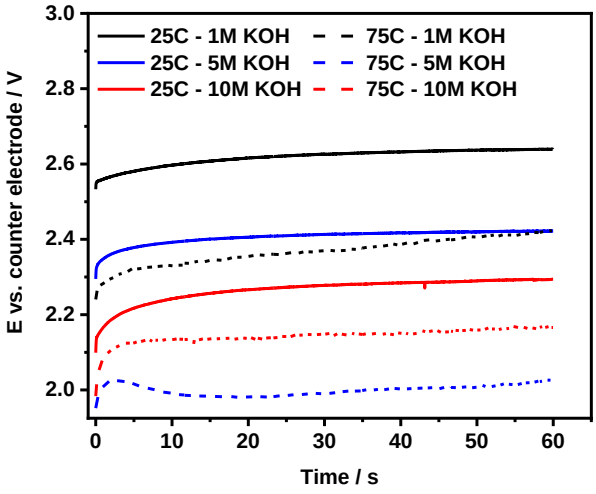

Figure D3. Chronopotentiograms of NiFeO$_x$H$_y$ conducted at j = 100 mA cm^{-2} at different temperatures and KOH concentrations.

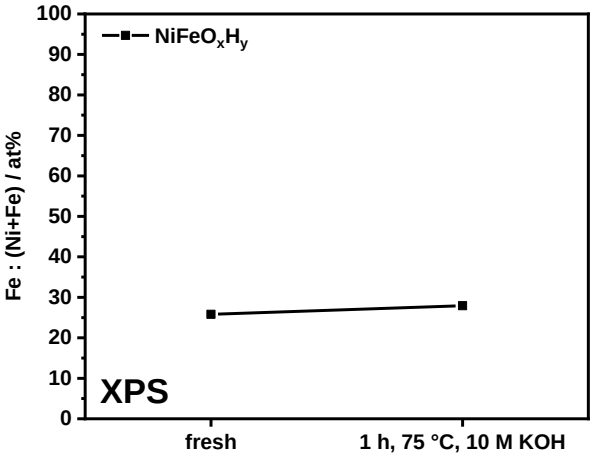

Figure D4. XPS analysis of fresh $NiFeO_xH_y$ and after 1 hour of immersion in 10 M KOH at 75 °C without anodic polarization.

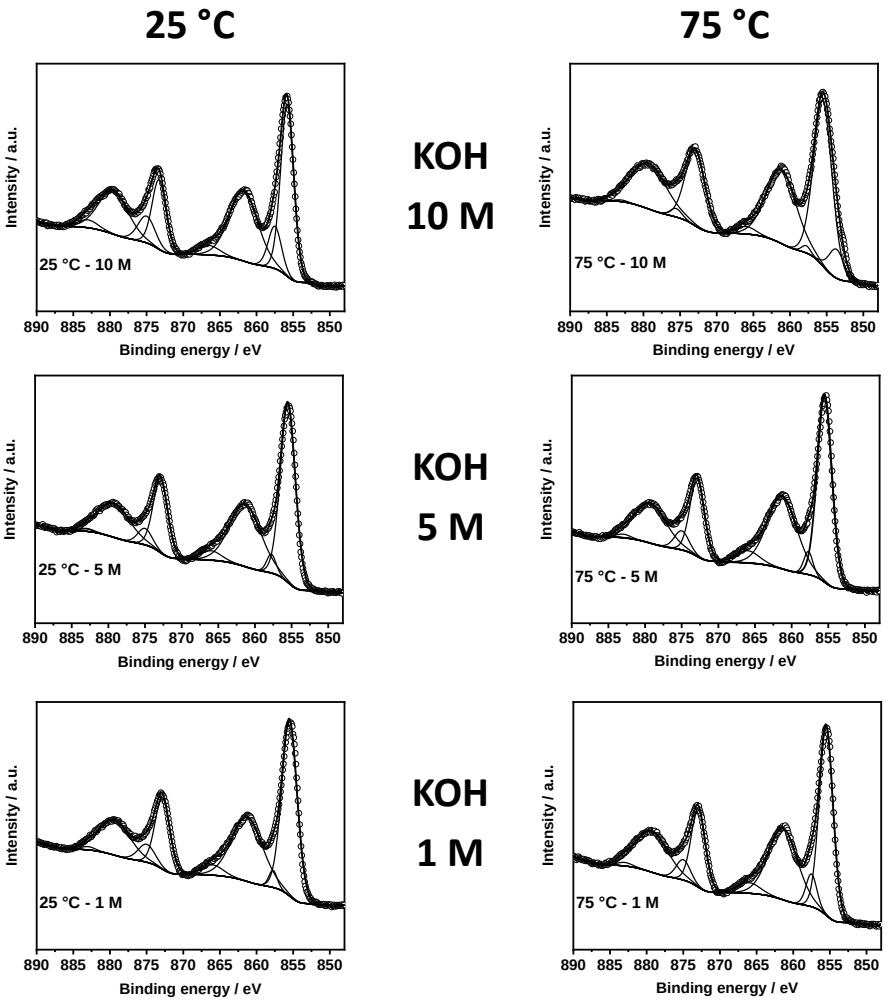

Figure D5. Ni 2p spectra of $NiFeO_xH_y$ samples after the stability tests performed under different conditions.

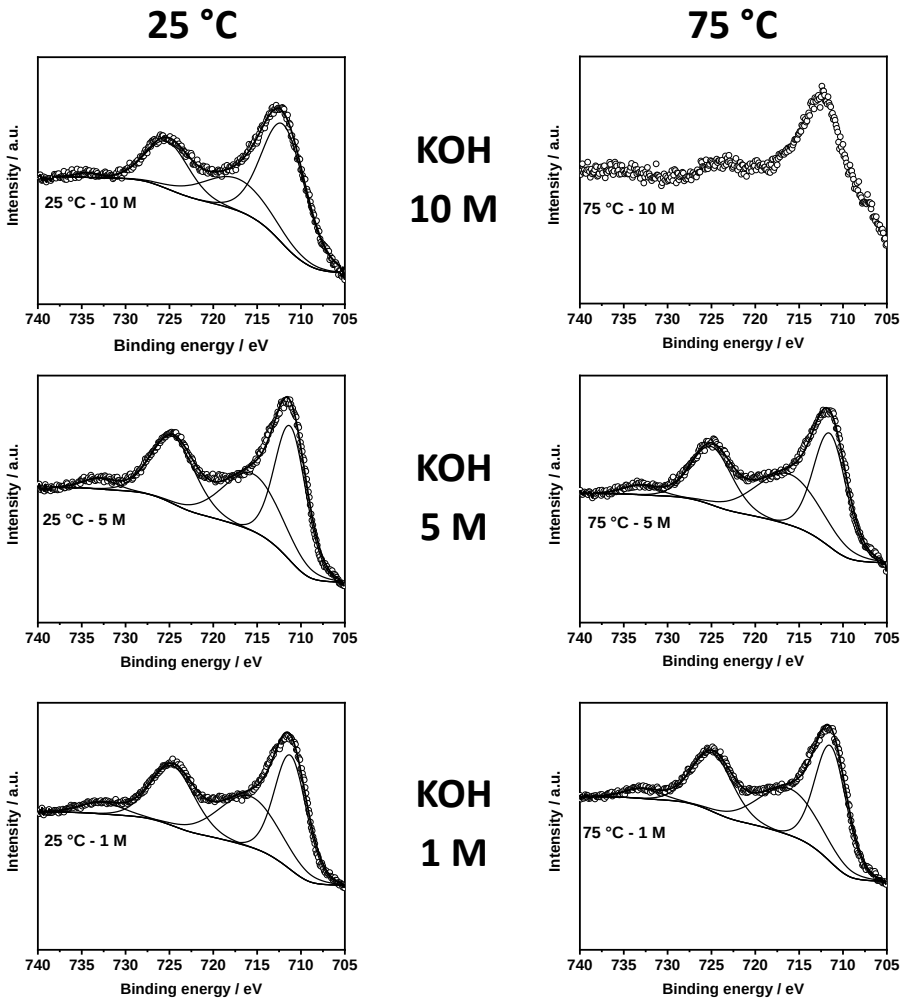

Figure D6. Fe 2p spectra of $NiFeO_xH_y$ samples after the stability tests performed under different conditions. For the sample tested at 75 °C in 10 M KOH, no peak fitting was performed, because of the strong intensity of the Ni Auger LMM feature overlapping with the weak Fe $2p_{3/2}$ peak for this low Fe-containing sample.

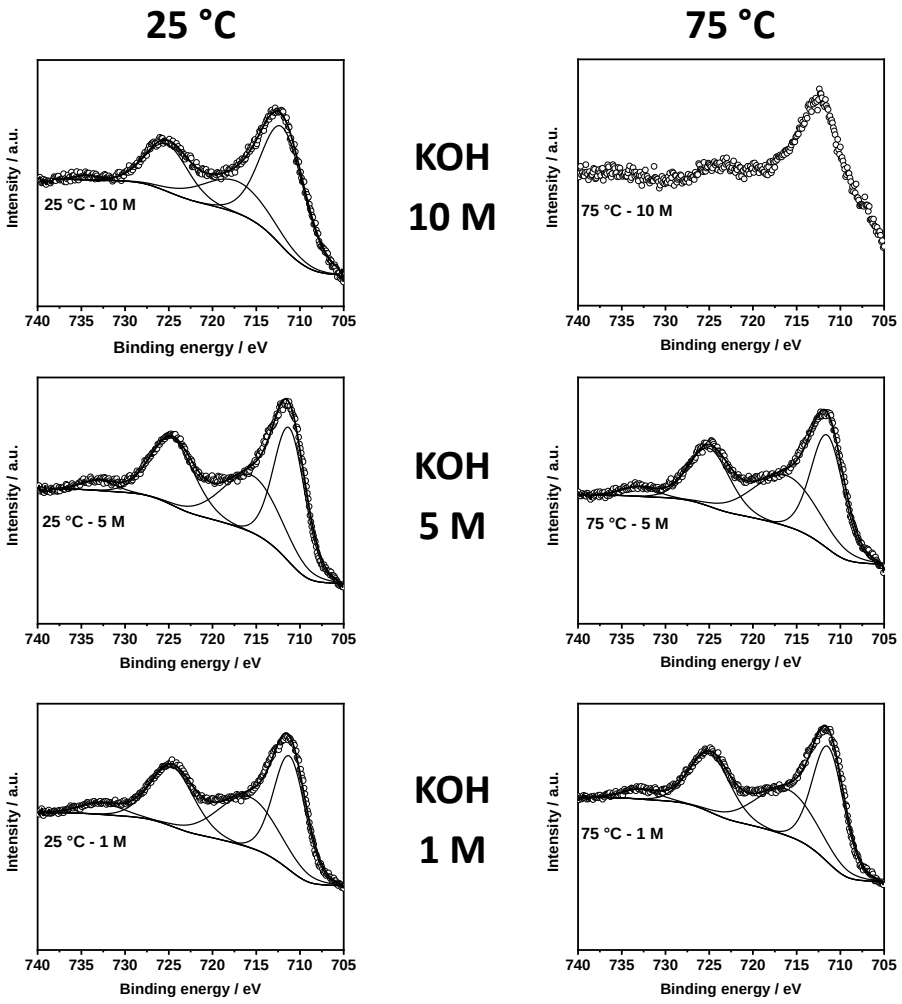

Figure D7. O 1s spectra of $NiFeO_xH_y$ samples after the stability tests performed under different conditions.

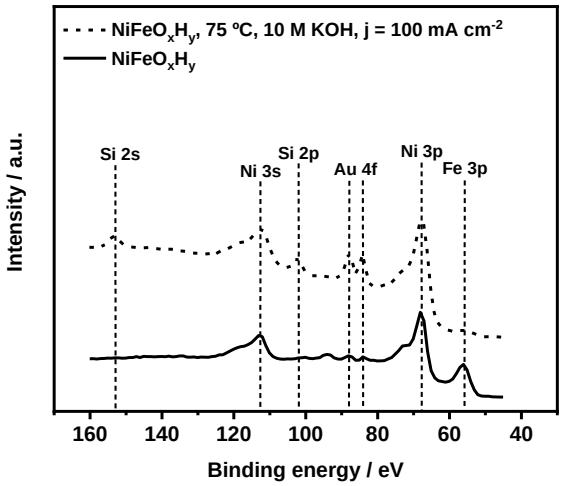

Figure D8. Low-binding energy region of XPS survey scan of $NiFeO_xH_y$ before and after anodic polarization at 75 °C in 10 M KOH, j = 100 mA cm^{-2}.

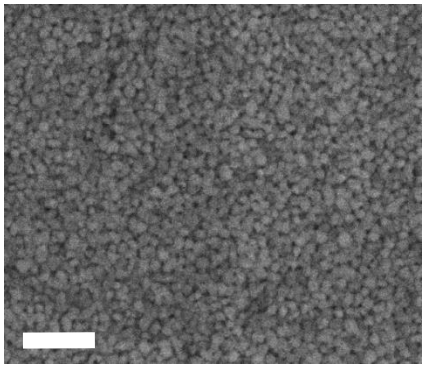

Figure D9. SEM image of the bare substrate, prior to film deposition. Scale bar is equal to 500 nm.

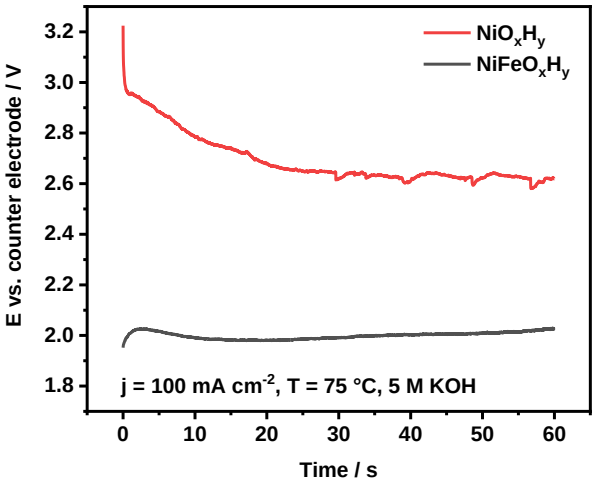

Figure D10. Chronopotentiograms of NiO_xH_y (red) and $NiFeO_xH_y$ (black) conducted at j = 100 mA cm^{-2}, 75 °C, 5 M KOH.

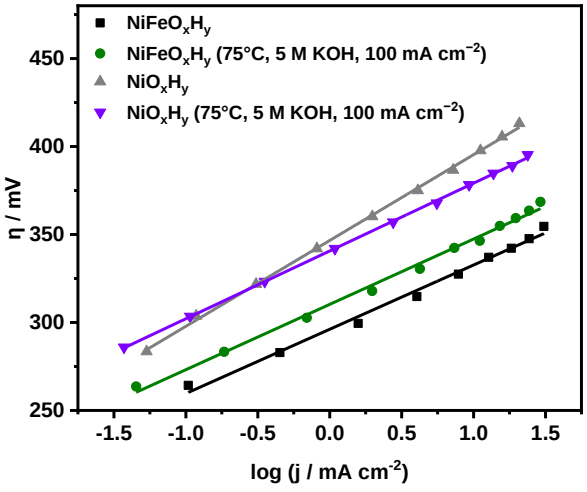

Figure D11. iR-corrected Tafel plots of NiO_xH_y and $NiFeO_xH_y$ before and after anodic polarization at 75 °C in 5 M KOH, j = 100 mA cm^{-2}. Measurements were carried out in 1 M KOH at 25 °C; the dots represent the experimental data, the lines represent the fittings.

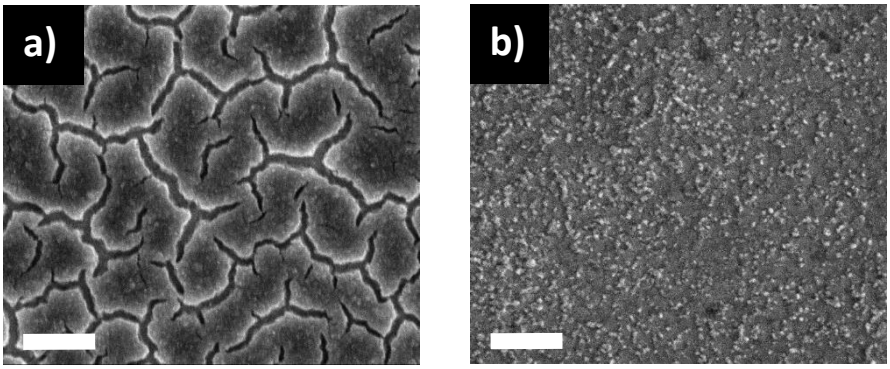

Figure D12. SEM images of NiO_xH_y a) before and b) after anodic polarization at 75 °C in 5 M KOH, j = 100 mA cm^{-2}, 1 h. Scale bars are equal to 500 nm.

Chapter 6

On the stability of Co_3O_4 oxygen evolution electrocatalysts in acid

Abstract

Oxygen evolution reaction (OER) electrocatalysts suitable to work in acid are typically restricted to platinum group noble metal oxides because of their high activity and, especially, stability. Co_3O_4 is currently explored as an alternative OER catalyst. We herein prepared Co_3O_4 films on fluorine-doped Sn oxide (FTO) glass and Ti foil via thermal decomposition of nitrate salts and evaluated their activity and stability in 0.05 M H_2SO_4. Crystalline Co_3O_4 films deposited on FTO were stable during chronopotentiometry at 10 mA cm^{-2} for over 16 hours. The dissolution rate was 61 ng_{Co} cm^{-2} min^{-1}. The choice of a stable support such as FTO is essential to ensure the stability of the catalyst-substrate interface and to prevent substrate passivation under OER conditions. Doping Co_3O_4 with Li resulted in a higher OER activity under acidic conditions to be attributed to the larger electrochemical surface area, although the stability was impeded compared to undoped Co_3O_4.

This chapter has been published as:
Etzi Coller Pascuzzi, M.; van Velzen, M.: Hofmann, J. P.; Hensen, E. J. M. *ChemCatChem* **2020**, DOI: 10.1002/cctc.202001428.

6.1. Introduction

Concerns about climate change have already led to a larger share of renewable energy to cover the global energy demand.[1] To increase this share further, challenges related to the intermittent nature of renewable energy sources such as wind and solar need to be overcome, requiring effective energy storage. Water splitting is a technology to store excess electricity into chemical fuels such as H_2, which can later be used to generate electricity back in a fuel cell, to generate work by combustion, or as a reactant.[2] In an electrolyzer, water is split into H_2 and O_2 over cathodic and anodic catalysts, respectively, separated by a membrane or a diaphragm. Among the different technologies available, proton-exchange membrane (PEM) electrolyzers have been developed to an advanced stage and allow for flexible operation under dynamic conditions (e.g., frequent start-and-stops, partial load), which makes them ideally suited for coupling with solar panels or wind turbines.[3,4] Between the two half-reactions involved in water splitting, the oxygen evolution reaction (OER) is the most energy-demanding because of its sluggish kinetics.[5] OER catalysts are thus required to decrease the kinetic limitations and to increase the overall efficiency of water splitting.[6] The acidic environment present in PEM electrolyzers poses serious limitations in terms of catalyst activity and, especially, stability. IrO_2 is the state-of-the-art OER catalyst because of its activity and, especially, long durability in acidic media.[7] Unfortunately, the scarcity and high price of Ir represent a major limitation for scaling up PEM electrolyzer technology to a size relevant to the storage of large amounts of renewable energy.[8,9]

Mn- and Co-based catalysts have been investigated as potential alternative water oxidation catalysts under acidic conditions. Mn-based catalysts are moderately active and stable OER catalysts at low (~0.1 mA cm^{-2}) and moderate (~1 mA cm^{-2}) current densities in strongly acidic electrolytes.[10,11] At high potentials, however, Mn rapidly dissolves in the form of permanganates and is therefore unsuitable for operation under the high current densities needed in a commercial electrolyzer.[10] As Co-oxides and -hydroxides[12,13] are more active than Mn-based catalysts in a wide range of pH and moderately stable at low pH, Co is considered a candidate to replace Ir as an OER catalyst in acid.[14,15] Huynh et al. improved the stability of CoO_x by the addition of Fe and Pb, that is to say that $CoFePbO_x$ deposited on FTO glass exhibited long-term acid stability (over 50 h at 1 mA cm^{-2}, pH 2) with an activity comparable to that of CoO_x.[16] The authors highlighted the beneficial effect of combining an active metal (Co) with structural promoters (Fe and Pb), which ensured a sufficient scaffolding around the active sites. Highly crystalline Co_3O_4 prepared by electron-beam evaporation was also successively tested in 0.5 M H_2SO_4 for more than 12 h at 10 mA cm^{-2}.[17] The authors emphasized the importance of a robust interface between the catalyst and

the substrate to ensure high durability. Besides assessing stability based on the chronopotentiogram, their study also determined the amount of Co leached into the electrolyte. Such an approach is important because high Co loadings can obscure deactivation effects.[18]

In this work, we present a simple method to obtain Co_3O_4 films that are stable for over 16 h at a relevant current density of 10 mA cm^{-2} under acidic conditions (0.05 M H_2SO_4). Catalyst optimization included (i) the selection of suitable and stable support materials, (ii) tailoring the thickness and crystallinity of Co_3O_4 to maximize its durability, and (iii) doping of the most promising Co_3O_4 sample with Li, which was previously reported to increase the OER activity of Co_3O_4 in the alkaline regime.[19,20] Various electrochemical, spectroscopic, and structural characterization tools helped us establish and clarify the roles of catalyst dissolution and substrate passivation in the electrode deactivation.

6.2. Experimental

6.2.1. Synthesis

Films of Co_3O_4 were prepared by thermal decomposition of metal salts deposited by spin coating on conductive substrates, being either Ti foil or fluorine-doped tin oxide (FTO) glass. The substrates were firstly sonicated in acetone for 15 min, following by rinsing with ethanol and Milli-Q water to ensure the removal of organic/inorganic contaminants. The precursor solution was prepared by dissolving $Co(NO_3)_2{\cdot}6H_2O$ (>99%, Merck) in absolute ethanol at a concentration of 0.5 M. For Li-doped samples, a solution was prepared with $LiNO_3$ (>98%, Merck), which was then mixed with the Co-containing solution in a proportion to give the desired atomic Li/Co ratio. The precursor solution was then spin-coated on the substrate at 1500 rpm for 10 s, followed by a high-speed rotation (4000 rpm) for 60 s to complete the deposition process. One-layer samples (1L) were then directly calcined in air at 300 °C for 1 hour. Three-layer samples (3L) were prepared via three cycles of deposition followed by 10 minutes calcination at 300 °C. The samples were then finally annealed at 300 °C for 1 hour.

6.2.2. Characterization

X-ray diffraction (XRD) was carried out on a Bruker D2 Phaser diffractometer equipped with a Cu K_α radiation source. XRD patterns were recorded in the 2θ range of 25-50° using a step size of 0.02° and a step time of 3 s.

X-ray photoelectron spectroscopy (XPS) measurements were performed on a K-alpha XPS spectrometer (Thermo Scientific) equipped with a monochromatic Al Kα (1486.6 eV) X-ray source. The spot size was 400 µm and the pass energy was set at 200 eV and 50 eV for survey and high-resolution spectra, respectively. All the spectra were processed in CasaXPS (v2.3.23, Casa Software Ltd) using a Shirley background. Binding energy calibration was performed by setting the position of the C 1s peak of adventitious sp^3 carbon to 284.6 eV. XPS depth profiles were obtained by consecutive Ar^+ sputtering (75 s, 3 kV) and measuring cycles. Co 2p, Ti 2p, or Sn 3d regions were used to determine the metal content as a function of the depth of probing. The depth profiles of each element were normalized to the highest intensity.

Field-emission Scanning Electron Microscopy (SEM) images were acquired using a FEI Quanta 3D FEG microscope at an accelerating voltage of 5 kV.

Raman spectra were acquired on a Witec Alpha 300R Raman microscope with λ_{exc} = 532 nm using a Zeiss 50x, NA = 0.55 objective. Spectra were acquired using a laser power of 10 mW, a collection time of 10 s, and by averaging 10 accumulations.

6.2.3. Electrochemical characterization

All the electrochemical tests were performed in a standard three-electrode cell using an Autolab PGSTAT30 potentiostat (Metrohm Autolab). Supported catalytic films with a geometric area of 1 cm^2 were used as working electrodes (WE). A Pt foil (area ≈ 5 cm^2) and an Ag/AgCl electrode were used as counter and reference electrodes, respectively. All the electrochemical tests were conducted in a 0.05 M H_2SO_4 solution (H_2SO_4 99.999%, Sigma-Aldrich). Milli-Q water (18.2 MΩ·cm) was used in all the cleaning and dilution steps.

Electrochemical impedance spectroscopy measurements were conducted at E = +1.78 V_{RHE} in the frequency range 10^{-1} to 10^3 Hz with an AC amplitude of 10 mV. The spectra were fitted with an $R_s(R_{ct}C)$ circuit, to account for the series resistance, the charge-transfer resistance, and the capacitance of the samples.[21–23] The catalytic activity was evaluated by linear sweep voltammetry (LSV) recorded at a scan rate of 10 mV s^{-1}. Cyclic voltammetry (CV) was conducted with a scan rate of 50 mV s^{-1}: five cycles were applied to obtain stable voltammograms, and the fifth cycle is shown in the graphs. The stability of the catalysts was assessed by chronopotentiometry conducted at different current densities, 1 or 10 mA cm^{-2}, under vigorous stirring. Elemental analysis of the electrolytes was performed to quantify the metal dissolution during the stability tests. The potentials reported in the voltammograms and chronopotentiograms were *iR*-corrected using the values of series

resistance obtained by impedance spectroscopy conducted prior to each measurement and reported versus the reversible hydrogen electrode (RHE) scale.

The double-layer capacitance (C_{dl}) of the samples was evaluated by performing cyclic voltammetries in a non-faradaic region (0.70-0.90 V_{RHE}) at different scan rates (10, 20, 40, 60 mV s^{-1}). The anodic and cathodic charging currents recorded in the middle of the potential window were plotted versus the scan rate, where the slope is equal to the C_{dl} of the samples.[22,24,25]

6.2.4. Elemental analysis of electrolytes and films

Inductively coupled plasma optical emission spectrometry (ICP-OES) measurements were conducted on a SPECTROBLUE EOP spectrometer equipped with an axial plasma source (Ar). Elemental analysis of the used electrolytes was performed without any additional preparation. The evaluation of the loadings of the 1L catalysts was performed by dissolving the uncalcined samples in 0.05 M H_2SO_4. The calcined 3L catalysts were dissolved in concentrated nitric acid by immersing the coated substrates in 5 mL of HNO_3 65% (Sigma) for 2 hours under heating. The solutions were then transferred into a 50 mL flask and diluted with Milli-Q water (18.2 MΩ·cm).

6.3. Results and discussion

Co_3O_4 films deposited on different substrates were initially screened for stability at 1 mA cm^{-2} for 16 h in 0.05 M H_2SO_4 (Figure 6.1a). The sample deposited on Ti (1L/Ti) slowly deactivates during the first 8 hours of the test. Thereafter, a sharper increase in the potential to maintain the set current density was observed. Increasing the number of layers (3L/Ti) or depositing the sample on FTO glass (1L/FTO) results in more stable samples as evident from the nearly unchanged chronopotentiograms after the initial activation period.

We determined the amount of Co dissolved in the used electrolytes and compared it with the initial Co loadings using elemental analysis (ICP-OES). Figure 6.1b shows that the amount of Co dissolved during the stability test for 16 h is similar, regardless of the substrate or thickness. The fraction of dissolved Co is roughly 20-30% for the thin samples independent of the substrate. For the 3L/Ti sample, the dissolved Co amount represents a lower fraction of the initial loading (6%). We determined the Co:Ti and Co:Sn ratios at the surface of the electrodes by XPS to gain insight into the coverage of the substrate by the catalytic film. The results reported in Figure 6.1c show a decrease in the Co surface ratio for the 1L samples deposited on Ti and FTO glass after electrochemical treatment. This shows

that cobalt dissolution results in the exposure of the substrate in some areas. On the other hand, the 3L/Ti sample does not show any change in the Co:Ti ratio, indicating that the film is completely covering the substrate, even after the stability test. As this sample showed similar dissolution as the 1L/FTO sample but drastically different stability in the chronopotentiometry, these results suggest that the dissolution of the active phase is not the only responsible factor for the deactivation of the 1L/Ti sample. Despite metal dissolution is often regarded as the main cause of deactivation of non-noble metal-based catalysts in acid, other factors can also contribute to the activity loss such as mechanical layer detachment, sintering of the active phase, formation of a less active form of the active phase, and support passivation. Support passivation can result in the formation of an insulating layer at the catalyst-substrate interface.[18]

To gain more insight into the deactivation mechanism of the 1L/Ti sample, we performed a detailed characterization comprising XPS, SEM, and Raman spectroscopy. The Co 2p XPS spectral region shows the typical features of Co_3O_4 (Figure 6.2a). The fitting procedure included components for Co^{3+} (binding energy, BE Co $2p_{3/2}$: 779.6 ± 0.2 eV) and Co^{2+} (BE Co $2p_{3/2}$: 781.4 ± 0.2 eV). The inverse shift in the BE position of Co^{2+} and Co^{3+} components is due to the higher ionic character of the Co^{2+}–O bond than that of Co^{3+}–O, which results in a higher binding energy of Co^{2+} peak as compared to Co^{3+}.[26,27] The O 1s spectrum (Figure 6.2b) shows two main components at 529.7 ± 0.2 eV and 531.0 ± 0.2 eV, which can be ascribed to oxygen in the lattice and surface hydroxyl groups, respectively.[28] The Co 2p spectrum of the deactivated catalyst shows the same spectral features of the fresh sample. In the O 1s spectrum, we can observe an increase in the intensity of the component ascribed to hydroxyl, which can be explained by the applied electrochemical treatment in water.

The morphology of the fresh and used sample was investigated by SEM (Figure 6.2c, d). The fresh sample appears as a compact film with some cracks, possibly originating from tensile stress during the thermal treatment. This may leave already some parts of the Ti foil substrate uncovered. A similar morphology can be observed for the used sample, except for a slightly larger exposed area of the Ti foil. The Raman spectra of fresh and used samples (Figure E1) show similar Raman active modes at 190 cm^{-1} (F_{2g}), 470 cm^{-1} (E_g), 515 cm^{-1} (F_{2g}), 610 cm^{-1} (F_{2g}), 675 cm^{-1} (A_{1g}), which are typical features of Co_3O_4.[29–32] There are no substantial differences in the spectra of fresh and used catalysts.

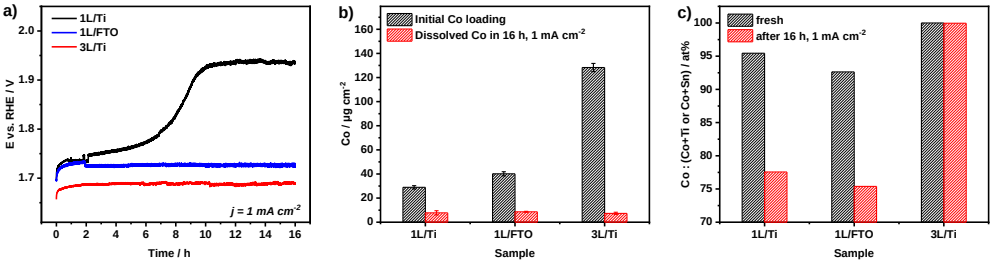

Figure 6.1. a) Chronopotentiometry of supported Co_3O_4 samples conducted at j = 1 mA cm^{-2} in 0.05 M H_2SO_4; b) amount of leached Co in the electrolyte during the tests measured by ICP-OES compared to the initial Co loadings; c) surface metal ratio determined by XPS.

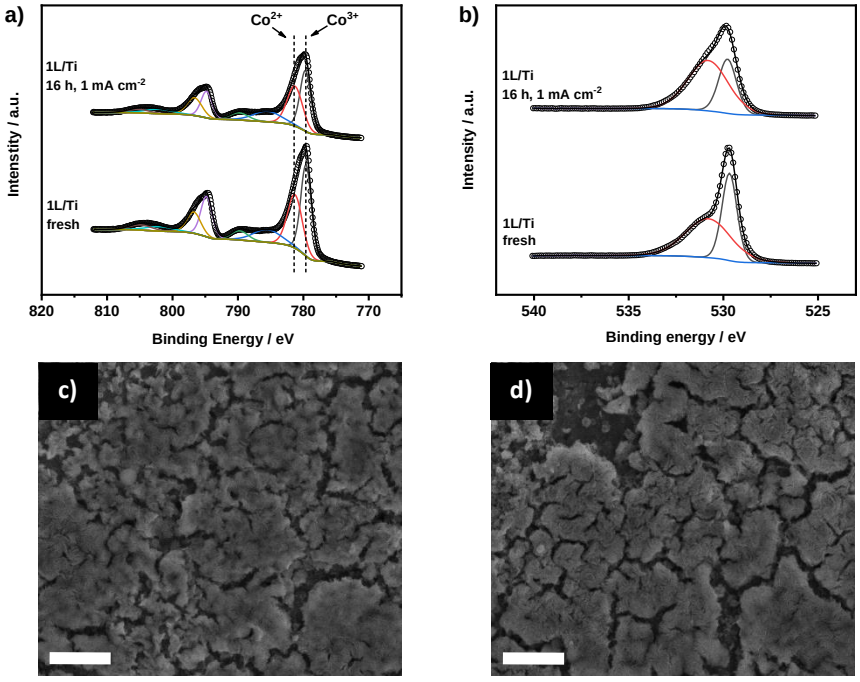

Figure 6.2. a) Co 2p and b) O 1s XPS spectra of fresh and used (16 h, 1 mA cm^{-2}) 1L/Ti samples; SEM images of c) fresh and d) used 1L/Ti samples (scale bars are equal to 1 µm).

Given the absence of clear indications of changes in the active phase, we speculate that deactivation is caused by exposure and passivation of the Ti substrate. Typically, for Ti-supported RuO_2 and IrO_2 catalysts, the passivation of Ti is not an issue as TiO_2 forms an electrically conductive solid solution with these rutile oxides.[33,34] For spinel Co_3O_4, the passivation of Ti to TiO_2 under reaction conditions can be prevented by depositing the sample on FTO glass, which is known to be stable under OER acidic conditions,[16] or by the deposition of multiple layers of active phase, ensuring complete coverage of the substrate. It is, however, difficult to unambiguously identify the presence of an electrochemically grown layer of TiO_2, because a thin layer of TiO_2 is usually formed on Ti foil during exposure to air. The Ti 2p region (Figure E2) reveals, for both fresh and used Co_3O_4 1L/Ti samples, TiO_2-related peaks (BE $Ti2p_{3/2}$ = 458.9 eV).[35] The higher intensity of the peaks in the used catalysts is due to a larger area of the substrate exposed in the used sample resulting from the partial dissolution of the active phase. To verify the influence of a layer of TiO_2 on the electrocatalytic performances of supported Co_3O_4 catalysts, we annealed a Ti substrate at 600 °C for 1 hour and then deposited a layer of Co_3O_4 on the pre-annealed substrate. This sample showed a much lower activity than the fresh 1L/Ti sample. The activity of this sample deposited on pre-annealed Ti was similar to that of the used 1L/Ti sample (Figure E3). The decrease in the activity of 1L/Ti after the stability test could be due to a higher resistance at the catalyst-substrate interface. Electrochemical impedance spectroscopy experiments (results reported in Figure E3b and Table E1) show that the charge-transfer resistances for the tested 1L/Ti sample (915 Ω cm^2) and the fresh 1L sample deposited on the preannealed substrate (18.8 kΩ cm^2) are significantly higher than for fresh 1L/Ti sample (14.4 Ω cm^2). This finding indicates that the electron transfer process at the catalyst surface for these samples is significantly slower than for fresh 1L/Ti.

The following step was to investigate the stability of Co_3O_4 anodes at 10 mA cm^{-2}, which corresponds to the benchmark value of current density typically used in literature for comparing the performance of OER catalysts.[22] For this purpose, we prepared three-layer (3L) samples deposited on Ti or FTO glass, in order to ensure the full coverage of the substrates. The activity of 3L samples is higher than that of 1L samples, as a result of the better coverage of the substrates (Figure E4).

The chronopotentiometry of the samples conducted at 10 mA cm^{-2} (Figure 6.3a) shows that the 3L/Ti and 3L/FTO samples have significantly different stabilities. While 3L/FTO is stable for the entire duration of the test (16 hours), 3L/Ti exhibits a two-step deactivation behavior. We suspect that the first potential increase is due to the substrate passivation, while the second is related to dissolution. We analyzed the dissolution of Co during the tests by ICP-OES conducted on the used electrolytes (Figure 6.3b). After 16 hours of prolonged

electrolysis at 10 mA cm^{-2}, 3L/Ti exhibits higher Co dissolution (91 μg_{Co} cm^{-2}) than 3L/FTO (59 μg_{Co} cm^{-2}).

We also analyzed the catalyst dissolution for samples subjected to 5 hours of anodic polarization at 10 mA cm^{-2}: the difference in dissolution between 3L/Ti and 3L/FTO samples is smaller. Also, the dissolution rate (*i.e.* the slope in Figure 6.3b) for 3L/Ti in the first 5 hours is lower than in the following 9 hours of testing. This increase can be related to the higher potential needed to maintain the same current density in the second part of the test, where the substrate is eventually passivated. On the other hand, the dissolution rate of the 3L/FTO sample is nearly constant during the duration of the test. We evaluated the Co dissolution rate of the 3L/FTO sample in order to compare it with previously reported values in literature. The average Co dissolution rate for this sample during 16 hours of anodic polarization at 10 mA cm^{-2} is 61 ng_{Co} cm^{-2} min^{-1} (at pH 1.3). Mondschein et al. reported dissolution rates of 100 ng_{Co} cm^{-2} min^{-1} and 50 ng_{Co} cm^{-2} min^{-1} for a 300 nm thick crystalline Co_3O_4 prepared by electron-beam evaporation during 12 hours of polarization at 10 mA cm^{-2} at pH 1 and 2, respectively.[17] The value that we found for our 3L/FTO sample prepared by thermal decomposition is falling in that range: we thus conclude that our facile synthesis method fully accomplishes the goal of making Co_3O_4 anodes with state-of-the-art stability in acid.

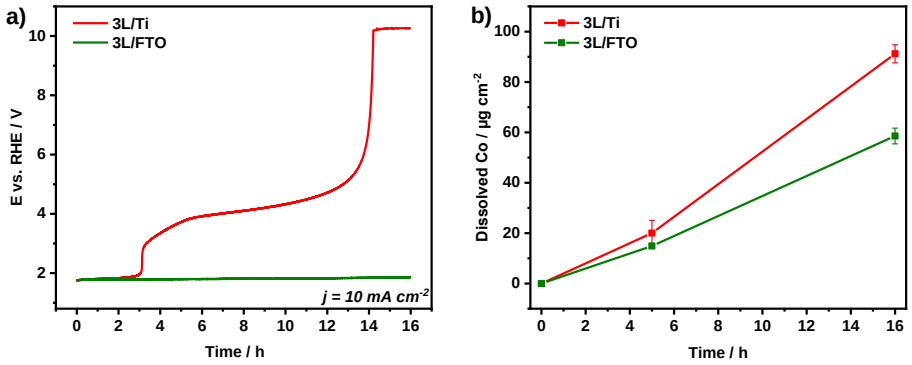

Figure 6.3. a) Chronopotentiometry of 3L/Ti and 3L/FTO samples conducted at j = 10 mA cm^{-2} in 0.05 M H_2SO_4; b) amount of leached Co in the electrolyte during the tests measured by ICP-OES.

We then characterized the fresh and used samples to understand further the deactivation mechanism. The Co 2p XPS spectral regions (Figure E5a, c) show the features of Co_3O_4 for all fresh and used 3L/Ti and 3L/FTO samples. In the O 1s spectra (Figure E5b, d), the used samples show a slight increase in the component related to the hydroxyl groups as compared to lattice oxygen, as the polarization was conducted in an aqueous solution.

We used depth profiling XPS to investigate the element distribution at different probing depths of fresh and used samples (Figure 6.4). The number of sputtering cycles is proportional to the probing depth of the sample. As the layer thickness removed in each sputtering cycle (or sputtering time) can be evaluated only for materials with known sputtering constant, the thickness is typically given in terms of sputtering cycles.[34,36] We used the number of cycles where the Co signal was < 2 % (with respect to its highest intensity) to compare the Co_3O_4 film thicknesses. For 3L/Ti, we can observe a significant change in the distribution of the elements between fresh and used catalysts. The depth profile of the used sample exhibits a sharp decrease in the Co content already after a few sputtering cycles, meaning that the layer is thinner. A lower thickness is also shown by a lower number of cycles to extinguish the Co signal for the used sample (≈20) than for the fresh sample (≈40). For the fresh 3L/FTO sample, the depth profile shows that the Co signal does not extinguish even after SnO_2 has been reached (sputter cycles > 30). This indicates deep penetration of Co_3O_4 among SnO_2 grains. The used 3L/FTO sample shows a similar decrease of the Co signal in the first sputtering cycles. At higher sputtering cycles (> 20), *i.e.* at higher probing depths, the Co signal in the used sample decreases faster than for the fresh sample, indicating a lower overall film thickness.

Raman spectroscopy was also used to characterize fresh and used 3L/Ti and 3L/FTO catalysts (Figure 6.5). The spectra of fresh samples exhibit the vibrations of Co_3O_4.[29–31] In the spectrum of 3L/FTO after 16 hours of reaction (at 10 mA cm^{-2}), we can observe a decrease in the intensity of the peaks, as part of the film has dissolved during the anodic polarization. A similar treatment conducted on 3L/Ti also leads to a lower peak intensity as compared to the fresh sample. Moreover, new peaks appear at 150 cm^{-1}, 397 cm^{-1}, 513 cm^{-1}, 632 cm^{-1}. These Raman modes can be identified with the E_g, B_{1g}, A_{1g}, E_g vibrations of anatase TiO_2.[37–39] The formation of TiO_2 can be related to prolonged exposure to anodic conditions, which leads to the oxidation of the Ti substrate after the Co_3O_4 film has dissolved. This finding suggests that the substrate is severely impacted by prolonged electrochemical treatment.

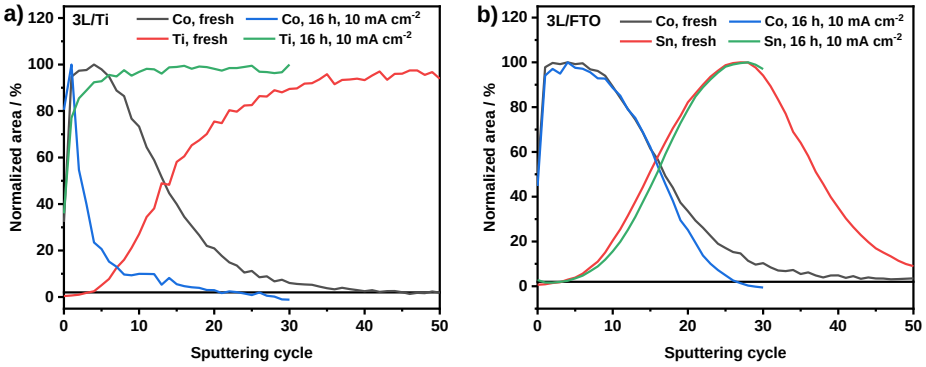

Figure 6.4. XPS depth profiles of a) 3L/Ti and b) 3L/FTO samples before and after anodic polarization at j = 10 mA cm^{-2} for 16 h. Horizontal lines placed at 2% were drawn to enable a better comparison of the Co_3O_4 thickness.

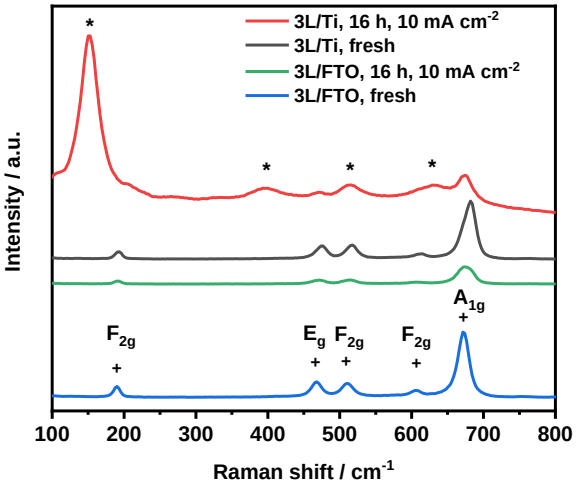

Figure 6.5. Raman spectra of 3L/Ti and 3L/FTO samples before and after anodic polarization conducted at j = 10 mA cm^{-2} for 16 hours. (+) peaks correspond to Co_3O_4-related vibrations, (*) correspond to anatase TiO_2-related vibrations.

The morphology of fresh and used samples was investigated by SEM. Both fresh 3L/Ti and 3L/FTO samples (Figure 6.6a, d) exhibit a morphology characterized by sub-micrometer spherical agglomerates. After the electrochemical tests, these agglomerates are hardly visible in some areas of the 3L/Ti sample (Figure 6.6b), while in other areas they have completely disappeared (Figure 6.6c). For used 3L/FTO, the active phase has largely maintained its structure and morphology (Figure 6.6e), although in some places the film has dissolved leaving cracks where grains of the underlying FTO are visible (Figure 6.6f). Changes in morphology in the used catalysts are caused by the partial dissolution of active phase during the applied electrochemical treatment.

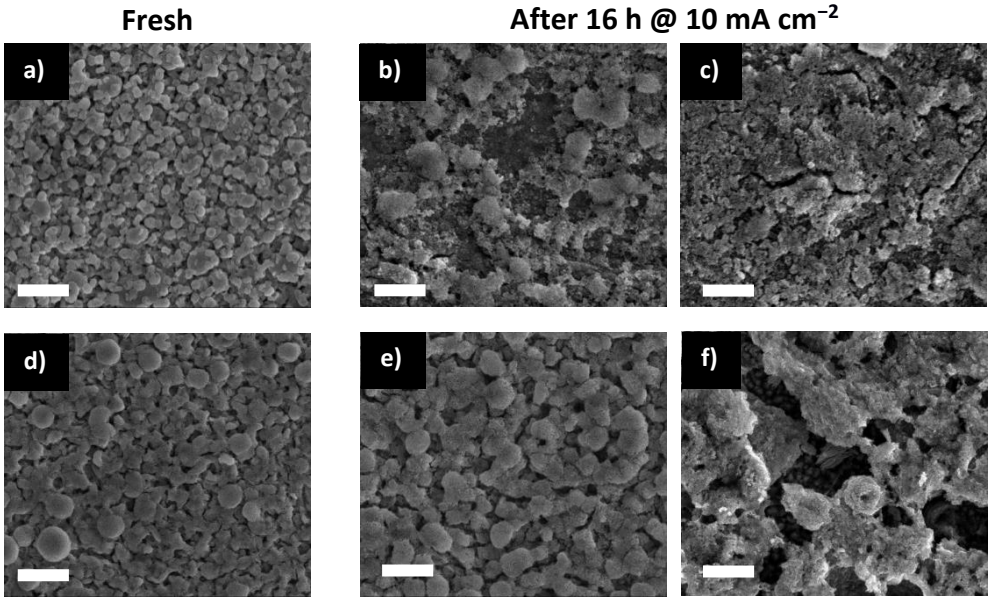

Figure 6.6. SEM images of fresh and used (16 h, 10 mA cm^{-2}) 3L/Ti (top) and 3L/FTO samples (bottom). Scale bars are equal to 1 µm.

To further optimize the electrochemical performance of the 3L/FTO catalyst, we explored the effect of Li doping on the structure and catalytic performances of Co_3O_4. Higher OER activities were previously observed for Li-doped Co_3O_4 as compared to pure Co_3O_4 under alkaline conditions.[19,20,40,41] The higher electrical conductivity and the distortion of the crystalline lattice upon Li addition contribute to increase catalytic activity.[19,20,40]

We prepared samples with Li doping amounts in the range of 5 at% - 10 at% (out of the total metal content). Changes in the structure can be observed by analysis of the XRD patterns of pure and Li-doped Co_3O_4 samples (Figure 6.7a). Upon addition of Li, the intensities of Co_3O_4-related peaks are lower relative to those of the SnO_2 peaks that originate from the substrate. This points to a lower crystallinity of Li-doped samples as compared to pure Co_3O_4. The spinel Co_3O_4 consists of Co^{2+} and Co^{3+} ions occupying tetrahedral and octahedral sites, respectively. Upon addition of Li^+ ions, the charge can be balanced by replacement of Co^{2+} with Co^{3+} in the tetrahedral sites or by the formation of Co^{4+} in the octahedral sites,[19,20] thus increasing the average Co valence state.[42]

The influence of Li doping on the catalytic activity is shown in Figure 6.7b. Li doping results in a slightly higher electrocatalytic activity with the maximum being reached at a 5 at% level of Li doping. The current densities recorded at a fixed overpotential (η = 500 mV) normalized to the geometric areas (Table 6.1) provide an estimate of the overall activity. Clearly, Li doping benefits the electrocatalytic activity. We also normalized the current densities to the C_{dl} values (Figure E6) measured in a non-faradaic region of CV to estimate the intrinsic catalytic activity,[24,43,44] as the values of C_{dl} are proportional to the electrochemical surface areas of the samples.[22] The intrinsic activity of Li-doped samples decreased upon Li addition, especially at high Li doping levels. This finding suggests that the main reason for the higher activity of Li-doped samples was the larger surface area, resulting in a higher number of active sites for OER.

The redox properties of the samples were studied using cyclic voltammetry (Figure E7). Upon Li addition, we can observe a shift toward more negative potentials of the anodic and cathodic peaks related to the Co^{3+}-Co^{4+} transition,[19,20,40] indicating that Li addition promotes the oxidation of Co^{3+} to Co^{4+}. The formation of Co^{4+} contributes to enhancing the electrocatalytic activity of the Li-doped samples, as Co^{4+} species were previously identified as the active sites for OER.[19,42]

Table 6.1. Normalization of the current densities recorded at η = 500 mV in the LSV to the geometric areas and C_{dl} of undoped and Li-doped 3L FTO samples.

Sample ID	C_{dl}, mF cm^{-2}	*j* at η = 500 mV, mA cm^{-2}	j_{spec} at η = 500 mV , mA mF^{-1}
3L/FTO	0.90	5.56	6.18
Li 5 at% 3L/FTO	1.34	7.91	5.93
Li 7.5 at% 3L/FTO	1.78	6.89	3.87
Li 10 at% 3L/FTO	1.99	6.20	3.12

We then investigated the stability of Li-doped 3L/FTO catalysts during prolonged electrolysis in acid at 10 mA cm^{-2} for the two most active Li-doped samples (5 at% and 7.5 at% Li). While undoped Co_3O_4 is stable for 16 h with a slight increase in the potential observed, Li-doped samples exhibit lower stability with more pronounced increases of the potential (Figure 6.7c). This is more visible at the highest Li doping level. We next evaluated the Co dissolution into the electrolyte by ICP-OES (Figure 6.7d). Upon Li addition, the amount of dissolved Co increases: for the 7.5 at% Li sample, the increase is around 30% compared to pure Co_3O_4. This indicates that Li addition has a negative impact on the stability of the samples by accelerating Co dissolution. This behavior can be attributed to a lower degree of crystallinity[45] or higher electrochemical surface areas of the Li-doped Co_3O_4 electrodes. We cannot exclude that also changes in the electronic structure might be responsible for the lower stability: in this regard, it was recently suggested that a higher amount of Co^{4+} species could lead to lower durability during prolonged OER treatment.[42] The high crystallinity of pure Co_3O_4 and the presence of a stable support such as FTO can explain the high stability of Co_3O_4 3L/FTO sample under prolonged polarization in acid environment. Highly crystalline materials are usually more stable than less crystalline and amorphous materials.[45–47] This behavior is common to many oxides used as OER catalysts and has been ascribed (for IrO_2) to the lower number of oxygen vacancies and low-coordinated sites susceptible to fast dissolution in amorphous oxide rather than in crystalline oxide.[45]

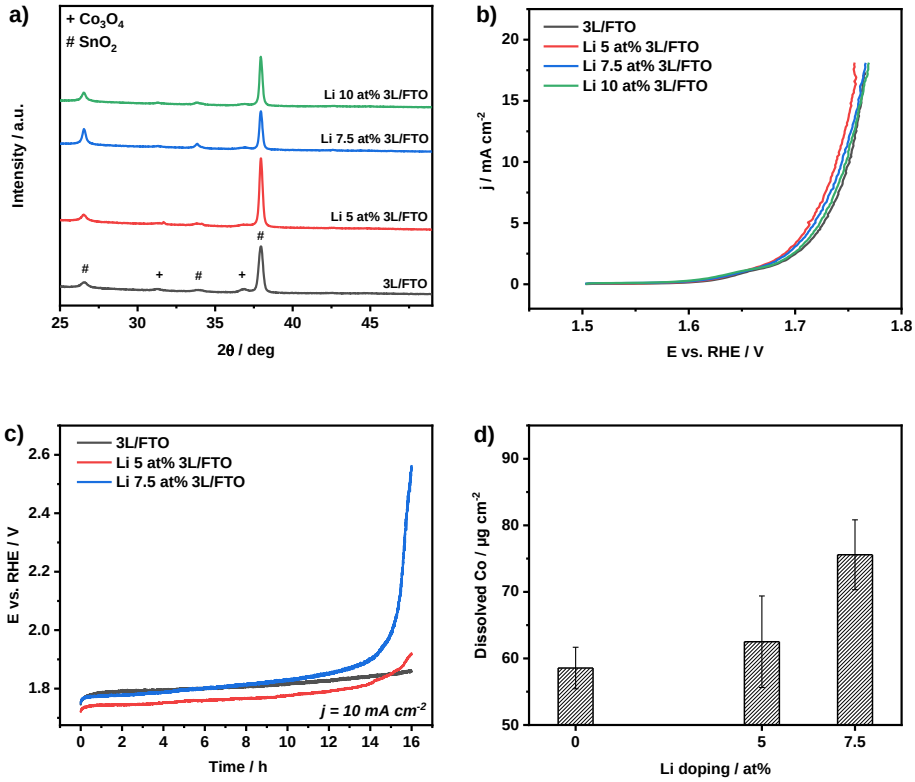

Figure 6.7. Effect of Li doping on the structure and acidic OER activity and stability of 3L/FTO sample: a) XRD; b) Linear Sweep Voltammetry; c) Chronopotentiometry; d) c) Chronopotentiometry conducted at j = 10 mA cm^{-2}; d) amount of leached Co in the electrolyte during the chronopotentiometry measured by ICP-OES.

6.4. Conclusions

We investigated the electrochemical stability of Co_3O_4 catalysts for the oxygen evolution reaction in acid. The anodes were prepared by thermal decomposition of a solution containing the metal precursors deposited by spin-coating on different substrates, Ti foil or FTO glass. When tested at 1 mA cm^{-2}, one-layer (1L) sample deposited on Ti foil deactivated rapidly. Depositing the sample on FTO or increasing the number of layers leads to increased stability, despite similar Co dissolution rates. We attributed this behavior to Ti substrate exposure and possible passivation upon reaction conditions. Tests at higher current densities were done for thicker samples to ensure complete coverage of the substrates. Analogously, 3L/Ti and 3L/FTO samples exhibit different stabilities in chronopotentiometric tests conducted at 10 mA cm^{-2}: while 3L/Ti deactivated in a two-step fashion, 3L/FTO sample was stable for the entire duration of the test (16 hours). The instability of the 3L/Ti sample is due to substrate passivation, *i.e.* the formation of a TiO_2 layer, as shown by Raman spectroscopy. An increase in the potential and a faster Co dissolution occurred as a result of the formation of the insulating interlayer. The 3L/FTO sample exhibits higher stability with lower Co dissolution than the 3L/Ti catalyst. Co dissolution for this sample, prepared by a simple and scalable method, is in line with that of other state-of-the-art Co_3O_4 catalysts reported in the literature. Further optimization of the 3L/FTO catalyst included doping with Li: although an increase in the catalytic activity was found, the stability of Li-doped samples was lower than that of pure Co_3O_4. The reason for this lowered stability can be found in a lower crystallinity, higher electrochemical surface area, and/or electronic modifications induced by Li doping, such as the stabilization of Co^{4+} species.

6.5. References

(1) Nocera, D. G.; Lewis, N. S. *Proc. Natl. Acad. Sci. U. S. A.* **2006**, *103* (43), 15729–15735.

(2) Yan, Z.; Hitt, J. L.; Turner, J. A.; Mallouk, T. E. *Proc. Natl. Acad. Sci.* **2020**, *117* (23), 12558–12563.

(3) Carmo, M.; Fritz, D. L.; Mergel, J.; Stolten, D. *Int. J. Hydrogen Energy* **2013**, *38* (12), 4901–4934.

(4) Babic, U.; Suermann, M.; Büchi, F. N.; Gubler, L.; Schmidt, T. J. *J. Electrochem. Soc.* **2017**, *164* (4), F387–F399.

(5) Katsounaros, I.; Cherevko, S.; Zeradjanin, A. R.; Mayrhofer, K. J. J. *Angew. Chemie - Int. Ed.* **2014**, *53* (1), 102–121.

(6) Tahir, M.; Pan, L.; Idrees, F.; Zhang, X.; Wang, L.; Zou, J. J.; Wang, Z. L. *Nano Energy* **2017**, *37*, 136–157.

(7) Ledendecker, M.; Geiger, S.; Hengge, K.; Lim, J.; Cherevko, S.; Mingers, A. M.; Göhl, D.; Fortunato, G. V.; Jalalpoor, D.; Schüth, F.; Scheu, C.; Mayrhofer, K. J. J. *Nano Res.* **2019**, *12* (9), 2275–2280.

(8) Kibsgaard, J.; Chorkendorff, I. *Nat. Energy* **2019**, *4* (6), 430–433.

(9) Vesborg, P. C. K.; Jaramillo, T. F. *RSC Adv.* **2012**, *2* (21), 7933–7947.

(10) Huynh, M.; Shi, C.; Billinge, S. J. L.; Nocera, D. G. *J. Am. Chem. Soc.* **2015**, *137* (47), 14887–14904.

(11) Huynh, M.; Bediako, D. K.; Nocera, D. G. *J. Am. Chem. Soc.* **2014**, *136* (16), 6002–6010.
(12) Deng, X.; Tuysuz, H. *ACS Catal.* **2014**, *4*, 3701–3714.
(13) Wang, J.; Cui, W.; Liu, Q.; Xing, Z.; Asiri, A. M.; Sun, X. *Adv. Mater.* **2016**, *28* (2), 215–230.
(14) Burke, M. S.; Zou, S.; Enman, L. J.; Kellon, J. E.; Gabor, C. A.; Pledger, E.; Boettcher, S. W. *J. Phys. Chem. Lett.* **2015**, *6* (18), 3737–3742.
(15) Kanan, M. W.; Nocera, D. G. *Science* **2008**, *321* (5892), 1072–1075.
(16) Huynh, M.; Ozel, T.; Liu, C.; Lau, E. C.; Nocera, D. G. *Chem. Sci.* **2017**, *8* (7), 4779–4794.
(17) Mondschein, J. S.; Callejas, J. F.; Read, C. G.; Chen, J. Y. C.; Holder, C. F.; Badding, C. K.; Schaak, R. E. *Chem. Mater.* **2017**, *29* (3), 950–957.
(18) Spöri, C.; Kwan, J. T. H.; Bonakdarpour, A.; Wilkinson, D. P.; Strasser, P. *Angew. Chemie - Int. Ed.* **2017**, *56* (22), 5994–6021.
(19) Nikolov, I.; Darkaoui, R.; Zhecheva, E.; Stoyanova, R.; Dimitrov, N.; Vitanov, T. *J. Electroanal. Chem.* **1997**, *429*, 157–168.
(20) Wu, X.; Scott, K. *Int. J. Hydrogen Energy* **2013**, *38* (8), 3123–3129.
(21) Bredar, A. R. C.; Chown, A. L.; Burton, A. R.; Farnum, B. H. *ACS Appl. Energy Mater.* **2020**, *3*, 66–98.
(22) McCrory, C. C. L.; Jung, S.; Peters, J. C.; Jaramillo, T. F. *J. Am. Chem. Soc.* **2013**, *135* (45), 16977–16987.
(23) Etzi Coller Pascuzzi, M.; Man, A. J. W.; Goryachev, A.; Hofmann, J. P.; Hensen, E. J. M. *Catal. Sci. Technol.* **2020**, *10*, 5593–5601.
(24) Etzi Coller Pascuzzi, M.; Selinger, E.; Sacco, A.; Castellino, M.; Rivolo, P.; Hernández, S.; Lopinski, G.; Tamblyn, I.; Nasi, R.; Esposito, S.; Manzoli, M.; Bonelli, B.; Armandi, M. *Electrochim. Acta* **2018**, *284*.
(25) Browne, M. P.; Nolan, H.; Duesberg, G. S.; Colavita, P. E.; Lyons, M. E. G. *ACS Catal.* **2016**, *6* (4), 2408–2415.
(26) Fradette, N.; Marsan, B. *J. Electrochem. Soc.* **1998**, *145* (7), 2320.
(27) Chuang, T. J.; Brundle, C. R.; Rice, D. W. *Surf. Sci.* **1976**, *59* (2), 413–429.
(28) La Rosa-Toro, A.; Berenguer, R.; Quijada, C.; Montilla, F.; Morallón, E.; Vázquez, J. L. *J. Phys. Chem. B* **2006**, *110* (47), 24021–24029.
(29) Rashad, M.; Rusing, M.; Berth, G.; Lischka, K.; Pawlis, A. *J. Nanomater.* **2013**, *714853*.
(30) George, G.; Anandhan, S. *RSC Adv.* **2015**, *5* (99), 81429–81437.
(31) Li, Y.; Qiu, W.; Qin, F.; Fang, H.; Hadjiev, V. G.; Litvinov, D.; Bao, J. *J. Phys. Chem. C* **2016**, *120* (8), 4511–4516.
(32) Fan, X.; Balogun, M. S.; Huang, Y.; Tong, Y. *ChemElectroChem* **2017**, *4* (10), 2453–2459.
(33) Trasatti, S. *Electrochim. Acta* **2000**, *45* (15–16), 2377–2385.
(34) Etzi Coller Pascuzzi, M.; Goryachev, A.; Hofmann, J. P.; Hensen, E. J. M. *Appl. Catal. B Environ.* **2020**, *261*, 118225.
(35) Saied, S.; Sullivan, J.; Choudhury, T.; Pearce, C. *Vacuum* **1988**, *38* (8–10), 917–922.
(36) Reier, T.; Pawolek, Z.; Cherevko, S.; Bruns, M.; Jones, T.; Teschner, D.; Selve, S.; Bergmann, A.; Nong, H. N.; Schlögl, R.; Mayrhofer, K. J. J.; Strasser, P. *J. Am. Chem. Soc.* **2015**, *137* (40), 13031–13040.
(37) Chen, X.; Mao, S. S. *Chem. Rev.* **2007**, *107* (7), 2891–2959.
(38) Wypych, A.; Bobowska, I.; Tracz, M.; Opasinska, A.; Kadlubowski, S.; Krzywania-Kaliszewska, A.; Grobelny, J.; Wojciechowski, P. *J. Nanomater.* **2014**, *2014* (March).
(39) Lubas, M.; Jasinski, J. J.; Sitarz, M.; Kurpaska, L.; Podsiad, P.; Jasinski, J. *Spectrochim. Acta - Part A Mol. Biomol. Spectrosc.* **2014**, *133*, 867–871.
(40) Švegl, F.; Orel, B.; Grabec-Švegl, I.; Kaučič, V. *Electrochim. Acta* **2000**, *45* (25–26), 4359–4371.
(41) Hamdani, M.; Pereira, M. I. S.; Douch, J.; Ait Addi, A.; Berghoute, Y.; Mendonça, M. H. *Electrochim. Acta* **2004**, *49* (9–10), 1555–1563.
(42) Zhou, J.; Zhang, L.; Huang, Y. C.; Dong, C. L.; Lin, H. J.; Chen, C. Te; Tjeng, L. H.; Hu, Z. *Nat. Commun.* **2020**,

11, 1984.

(43) Strickler, A. L.; Flores, R. A.; King, L. A.; Nørskov, J. K.; Bajdich, M.; Jaramillo, T. F. *ACS Appl. Mater. Interfaces* **2019**, *11* (37), 34059–34066.

(44) Zhou, F.; Izgorodin, A.; Hocking, R. K.; Armel, V.; Spiccia, L.; MacFarlane, D. R. *ChemSusChem* **2013**, *6* (4), 643–651.

(45) Oellers, T.; Fruchter, L.; Pizzutilo, E.; Geiger, S.; Kasian, O.; Ledendecker, M.; Mingers, A. M.; Cherevko, S.; Koper, M. T. M.; Mayrhofer, K. J. J.; Li, Z.; Diaz-Morales, O.; Ludwig, A.; Fu, W. T. *Nat. Catal.* **2018**, *1* (7), 508–515.

(46) Tsuji, E.; Imanishi, A.; Fukui, K. I.; Nakato, Y. *Electrochim. Acta* **2011**, *56* (5), 2009–2016.

(47) Cherevko, S.; Reier, T.; Zeradjanin, A. R.; Pawolek, Z.; Strasser, P.; Mayrhofer, K. J. J. *Electrochem. commun.* **2014**, *48*, 81–85.

Appendix E

Supporting Information for Chapter 6

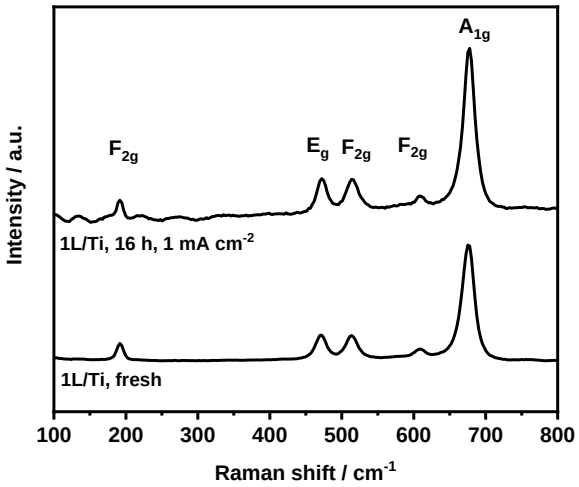

Figure E1. Raman spectra of fresh and used (16 h, 1 mA cm^{-2}) 1L/Ti samples.

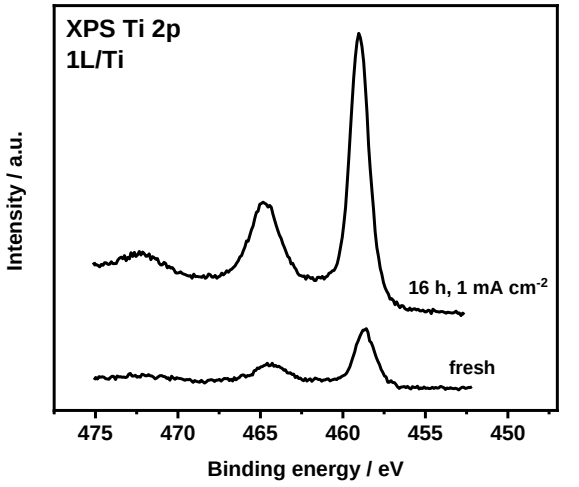

Figure E2. XPS of Ti 2p region for spectra of fresh and used (16 h, 1 mA cm^{-2}) 1L/Ti samples.

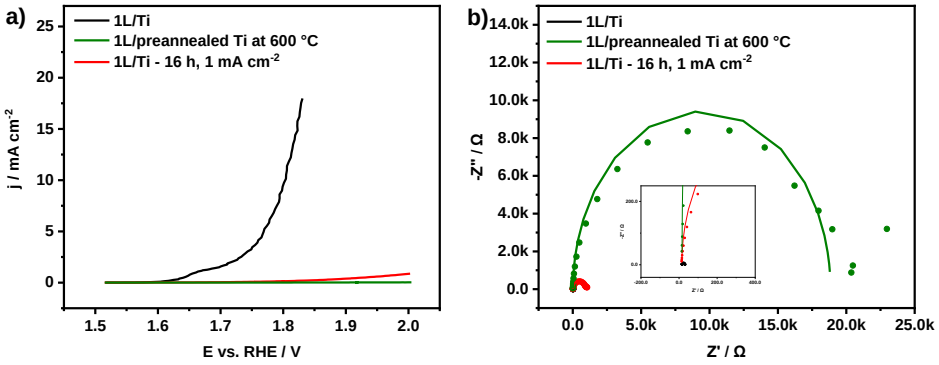

Figure E3. a) Linear Sweep Voltammetry (LSV) and b) experimental (points) and fitted (lines) Nyquist plots recorded at E = +1.78 V_{RHE} for fresh and used (16 h, 1 mA cm^{-2}) 1L/Ti samples and 1L sample deposited on preannealed Ti substrate (600 °C).

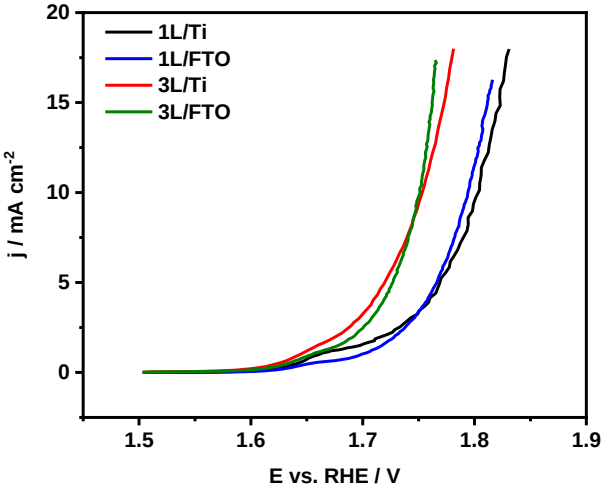

Figure E4. Linear Sweep Voltammetry of 1L and 3L samples deposited on Ti and FTO-glass substrates.

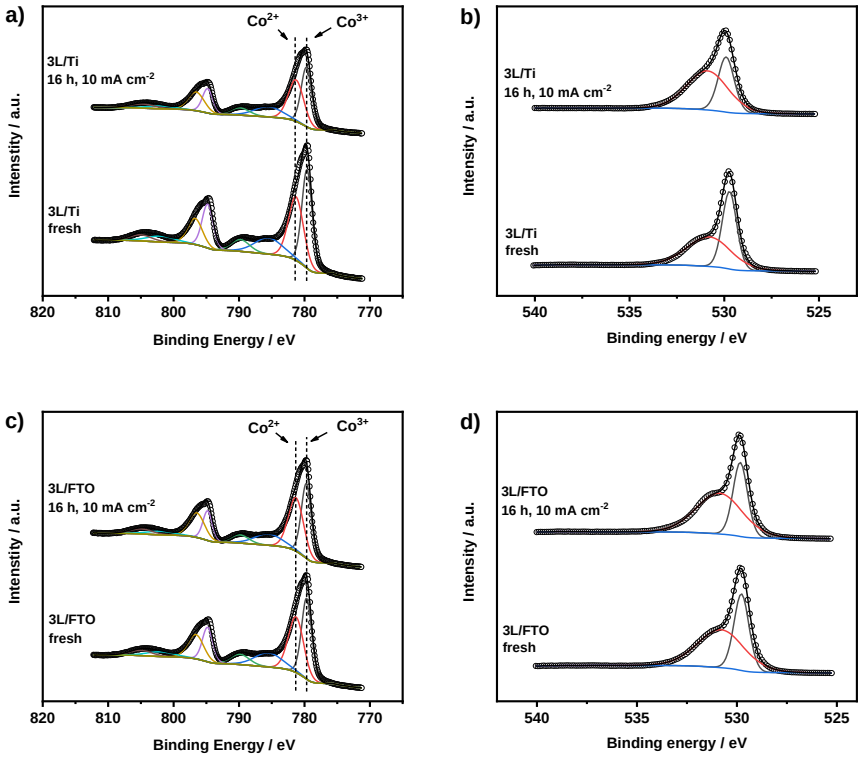

Figure E5. XPS Co 2p and O 1s spectra of fresh and used (16 h, 10 mA cm^{-2}) 3L samples deposited on a, b) Ti and c,d) FTO-glass.

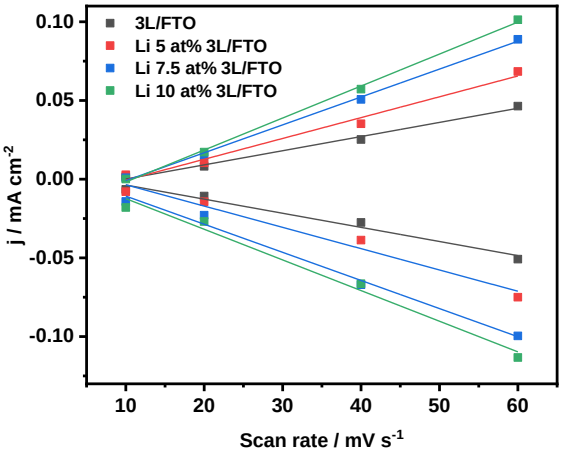

Figure E6. Charging currents measured in the middle of the potential window (0.70-0.90 V_{RHE}) plotted versus the scan rate used in the cyclic voltammetries. The slopes are equal to the values of C_{dl} of the electrodes.

Table E1. Values of R_{ct} obtained from the fitting of EIS spectra recorded at E = +1.78 V_{RHE}.

Sample ID	R_{ct}
1L/Ti	14.4 Ω cm^2
1L/preannealed Ti at 600 °C	18.8 kΩ cm^2
1L/Ti – 16 h, 1 mA cm^{-2}	915 Ω cm^2

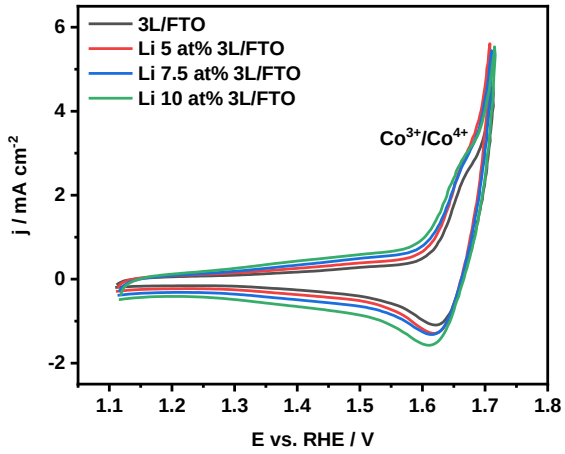

Figure E7. Cyclic voltammetry (CV) of pure and Li-doped Co_3O_4 3L/FTO samples.

Chapter 7

Summary and outlook

Tailoring the activity and stability of oxygen evolution electrocatalysts

Electricity will play a key role in the future energy market, driven by the boost in the production of renewable energy from solar and wind. Efficient solutions for energy storage are needed to overcome the fluctuating nature of these renewable energy sources. Electrochemical water splitting is a candidate to store electricity into H_2, which can be later used as a fuel or reactant. In this process, water is dissociated and molecular hydrogen and oxygen are produced in the cathodic and anodic compartments, respectively. Between the two half-reactions, the oxygen evolution reaction (OER) is the most energy-demanding, as it involves the transfer of four electrons and four protons for the formation of one O_2 molecule. The development of Earth-abundant, active, and stable OER catalysts is thus a primary target for the large-scale implementation of electrolyzers. The two main types of electrolyzers are the alkaline electrolyzer and proton-exchange membrane (PEM) electrolyzer. The employed OER catalysts are different depending on the application. In the alkaline electrolyzers, first-row transition metal (e.g. Ni, Fe) oxides and (oxy)hydroxides can be used as OER catalysts as they are active and stable in basic environment. In PEM electrolyzers, due to the acidic environment, only noble metal oxides (especially IrO_2) provide sufficient activity and stability. The scarcity and high price of Ir is a major limitation for the spread of PEM technology, which is considered to be ideal for coupling with solar or wind power generation. In this context, the development of highly active and stable OER catalysts, with reduced noble metal content, is a key challenge for the large spread of PEM technology.

To overcome the sluggish OER kinetics, the chlorine evolution reaction (CER) could be an alternative reaction to replace the OER at the anode, as in the case of seawater electrolysis. Currently, Cl_2 is an industrially more attractive intermediate than O_2, but the high toxicity and corrosiveness of Cl_2 imply that expensive materials for its handling and storage must be used. Thus, oxygen evolution is preferred in small-scale devices. The chlor-alkali process is worldwide used for the large-scale production of Cl_2, NaOH, and H_2 from salt-water brine.

The anodes consist of a solid solution of rutile TiO_2 and RuO_2 (typically in a 70:30 molar ratio), also called Dimensionally Stable Anodes (DSA®). These anodes are very active in both CER and OER: high chloride concentrations and low pH are thus required to maximize the CER selectivity. Although the presence of TiO_2 contributes to increasing the stability by providing a structural matrix, RuO_2 is prone to dissolution at anodic potentials. The stability issue of RuO_2 at anodic potentials is crucial for both chlorine and oxygen evolution reactions. This aspect was investigated in **Chapter 2**, where a RuO_2(110)/Ru(0001) was selected as a model electrode to study the electrochemical stability under pure OER (in 0.5 M H_2SO_4) or CER-OER (in 0.5 M HCl) conditions. The use of a well-defined system allowed to precisely monitor the impact of electrochemical treatment on the structural, morphological, and compositional changes of the anode. The presence of chloride ions shifted anodically the onset of OER due to the competition between CER and OER. The onset potential of RuO_2 dissolution and the degradation mechanism were however similar in both electrolytes. When the electrodes were subjected to a potential higher than the onset potential of RuO_2 dissolution (*i.e.* oxidation of RuO_2 to RuO_4), corrosion of the RuO_2(110) film occurred in some areas. Consequently, the Ru(0001) substrate was exposed to the electrolyte which led to rapid dissolution of Ru. The corroded areas formed pits surrounded by randomly-oriented petals, with higher oxygen content due to the electrochemical growth of a hydrous oxide. The degree of corrosion was found to be dependent on the main reaction taking place at the anode. The treatment in HCl was less severe than in H_2SO_4 due to the competition between RuO_2 oxidation with the kinetically favorable CER. The RuO_2(110) film was however intact to a great extent (with similar thickness and oxygen contents), thus protecting the underlying substrate from fast corrosion. The results of this chapter showed that the anode corrosion rate can be tailored by changing the selectivity although the degradation mechanism remains unchanged.

As mentioned above, DSA® anodes are also active in the oxygen evolution reaction and can be used as anodes in fresh-water electrolysis. In **Chapter 3** we proposed a strategy to increase the activity in acidic media and reduce the Ru content of DSA® anodes. We explored the effect of Mn addition on the structure, catalytic activity, and stability of DSA® anodes. A drastic increase in the catalytic activity was observed, with our best-performing anode made of TiO_2-RuO_2-MnO_x needing only 386 mV overpotential to reach a current density of 10 mA cm^{-2}. Mn was found responsible for the formation of a porous structure with high surface area and for the distortion of the rutile structure due to the insertion of Mn cations in the host lattice. This strategy allowed reducing the Ru content in the anode up to 17 at% together with a higher activity than both DSA® anodes and pure RuO_2.

Although the presence of TiO_2 in DSA® anodes increases the durability, RuO_2 still suffers from lower durability issues as compared to IrO_2, which is the state-of-the-art OER catalyst in acid because of its excellent stability. As RuO_2 and IrO_2 crystallize in the same rutile structure, we studied the influence of Mn addition on IrO_2 as well. In **Chapter 4**, the use of IrO_2-MnO_x electrocatalysts for the acidic water oxidation was investigated. Similar to TiO_2-RuO_2, the addition of Mn to IrO_2 enhanced both the overall and intrinsic activities. Other than the substitution of Mn for Ir cations in the rutile lattice, we first showed a change in the electronic structure of IrO_2 induced by Mn. X-ray photoelectron spectroscopy evidenced the presence of Ir^{3+} in all mixed Ir-Mn oxide electrocatalysts; these species were previously argued to be responsible for the higher OER activity of amorphous IrO_2 with respect to crystalline IrO_2. The stability of the catalysts was good, except at very high Mn contents. Ir dissolution was mostly dependent on the exposed electrochemical surface areas. The results of Chapter 3 and Chapter 4 demonstrated that the addition of first-row transition metal oxides to DSA® anodes and IrO_2 can be used to boost the electrochemical performance of oxygen evolution catalysts in acid, relevant for PEM electrolyzers. This provides a strategy to decrease the noble metal content.

Compared to PEM electrolysis, alkaline electrolysis is more mature and poses fewer limitations in the choice of suitable Earth-abundant OER catalysts. Fe-doped Ni(oxy)hydroxide is among the most investigated OER catalyst due to its excellent activity and the large availability of Ni and Fe. Although the activity aspect has been examined in-depth, the stability of $NiFeO_xH_y$ under industrially relevant conditions has not been well established. In **Chapter 5** we studied the effect of anodic polarization conducted at high temperatures and KOH concentrations on the structure and performance of $NiFeO_xH_y$ supported on Au/Si wafers. The impact of harsh electrochemical treatments on NiO_xH_y and $NiFeO_xH_y$ were also compared. A decrease in the Fe content occurred for $NiFeO_xH_y$ when tested under severe conditions, together with a decrease in the catalytic activity. On the other hand, NiO_xH_y incorporated Fe traces present in the electrolyte during anodic polarization at industrially relevant conditions (75 °C, 5 M KOH), leading to an activity improvement after the electrochemical treatment for NiO_xH_y. For both NiO_xH_y and $NiFeO_xH_y$, a loss in the electrochemical surface area occurred after electrochemical testing in harsh conditions. High temperature, KOH concentration, and current density do not only accelerate the deactivation process of $NiFeO_xH_y$ but can also lead to different degradation phenomena than those observed at milder conditions: for the $NiFeO_xH_y$ sample subjected to polarization at the harshest conditions (75 °C, 10 M KOH), a transformation of Ni-(oxy)hydroxide into Ni-oxide also took place. These results indicate that a careful evaluation of the stability is of great importance for scaling-up catalysts from lab-based to practical

applications. Also, anodes with different compositions and activities could display more similar structure and performance after electrochemical treatments in severe conditions.

In **Chapter 6,** we explored the behavior of Co_3O_4 as an Earth-abundant OER catalyst in acid. The anodes were prepared by thermal decomposition of metal precursors spin-coated on Ti foil or FTO glass substrates. Although the dissolution of active phase is often the reason for the fast degradation of non-noble-metal catalysts in acid, we showed that also the substrate plays an important role in the catalyst deactivation. A layer of TiO_2 can be formed during anodic polarization in the case of Co_3O_4/Ti, leading to a sharp increase in the required potential during a chronopotentiometric stability test. On the other hand, Co_3O_4 films deposited on FTO glass were stable for more than 16 hours at 10 mA cm^{-2}. Co dissolution for this catalyst was lower than for Co_3O_4/ Ti and similar to what was previously reported for Co_3O_4 prepared with other synthesis techniques. We also tailored the electrocatalytic OER performance of Co_3O_4 in acid by Li doping. The activity of Li-doped samples was higher than for pure Co_3O_4, mainly because of the larger electrochemical surface area (ECSA). On the other hand, the long-term stability decreased, as a result of the lower crystallinity, higher ECSA, and electronic modifications of Co_3O_4 (formation of Co^{4+} species) induced by Li doping.

The results of this thesis provide directions for the development of active and stable oxygen evolution catalysts, needed to face the upcoming electrification of the energy market at a GW scale. Altering the selectivity, changing the level of transition-metal doping, selecting the optimal substrate are tools to tailor the electrocatalytic activity and stability of the anodes. The synthesis of nanoparticles and their deposition on high surface area supports are additional strategies that can be used to further enhance the electrocatalytic activity. These approaches can be combined in order to reduce and eventually replace the use of noble metals in the anodes of PEM electrolyzers, where IrO_2 currently remains the only suitable choice. *In situ/operando* studies could better reveal changes in the catalyst structure and oxidation state and provide deeper insight into the dissolution mechanism. Successive testing of the catalysts in lab-based electrolyzers and pilot plants would provide additional understanding about their performance under more realistic conditions. The results could be used to further optimize the structure and morphology of the catalysts in view of their industrial application.

Acknowledgments

These four years have made me grow both at a scientific and personal level, teaching me not only how to conduct research, but also how to face challenges and to interact with people from many countries and backgrounds. This special journey wouldn't have been possible without all the people with whom I talked, worked, and spent time together.

Emiel, thank you for the supervision and guidance during my PhD. I appreciated the freedom that you gave me in conducting my research, yet providing me with ideas and directions during our meetings and discussions. Your inputs in the writing process contributed to improving the level of my manuscripts. I wish you to preserve your enthusiastic attitude in the supervision of the next generations of PhD students at IMC!

Jan Philipp, thank you for always being ready to discuss with me my research progress, and for dealing with NAP-XPS and surface science issues closely. I also appreciated the opportunity you gave me to train my teaching skills in the Inorganic Chemistry bachelor course. I wish you good luck with your future and career in Darmstadt!

I would also like to thank my committee members prof. Paolo Pescarmona, dr. Thijs de Groot, prof. John Van der Schaaf, prof. Herbert Over, and dr. Marta Figueiredo for the time spent reading my thesis and for taking part in the defense ceremony.

I would then like to thank my two paranymphs: Andrey, your help and suggestions on how to deal with failing experiments and obstacles encountered in the PhD life were unique. Thanks for all the times you contributed to solving issues on a wide variety of topics, such as XPS fitting, the setting of experiments, and many others; your generous attitude is incredible. The conversations that we had during our coffee breaks were a nice remedy to release the stress of the PhD life. I wish you a lot of success and happiness in your life! Yue, it has been a pleasure for me to share with you not only the office but also electrochemistry- and life-related talks during these years. You were always ready to help deal with every kind of issues encountered in the lab and in the office. I hope that I did the same with you! Your kind nature and your humor made it very easy to talk with you about our work, Chinese culture, or plans for the upcoming trips. I hope you will also defend your thesis and start the next chapter of your life soon!

Freddy, I appreciated all the funny moments that we had together during your stay in Eindhoven. Our common Latin cultural background made it very easy to interact when we

arrived in Eindhoven. Your expertise in XPS and thin films was also very helpful to me, you were able to explain to me photochemistry and semiconductor-related concepts in clear and effective words. Lu, you have been a pillar of all the PhD students working in the electrochemistry lab. Your knowledge in the field was really deep and you were able to fix most of the issues with the potentiostats readily. Thanks for explaining to me how impedance spectroscopy works. Thank you Longfei, for your cheerful presence in the electrochemistry lab!

This thesis would not have been possible without my students. Sahasra, even if the results of your work didn't end up in this thesis, you have been a very tenacious and motivated student. I hope the best for your future life and career. Alex, I supervised you only for half of your project. Your ambitions were always very high, I hope I kept your motivation that high during your internship! Thank you for your dedication to the NiFe project, your efforts were finally compensated by a nice publication together. Matthijs, I enjoyed working with you and supervising you during your internship at TU/e. We had day-to-day discussions, experiments, and it was very nice to see your efforts and enthusiasm in stabilizing Co_3O_4 catalysts in acid that led to our joint publication! It was great to have such a team composed of you and Alex at the same time, I wish you good luck in successfully finishing your studies. Ivo, it was a pity that your project could not be completed because of the Coronavirus restrictions, even if you were very dedicated to it. It was awesome that you enjoyed electrochemistry so much that you were seeking an electrochemistry-related job after your graduation.

Tiny, thank you for fixing every kind of issues in the lab, you take care of all the instruments (and users!) of the group, ensuring that every PhD student has everything that might be needed to successfully reach his/her research goals. Adelheid, I appreciated your assistance in the ICP measurements, you made sure that we were able to get high-quality results. Ingeborg, I am grateful to you for always helping solve big and small microscope-related problems, and for your instructions on how to take proper SEM pictures for publications. I am also grateful to Mark Ledendecker and Andreas Mingers from Max Planck Institute in Dusseldorf for performing some preliminary ICP-MS experiments.

Emma, your easy-going attitude and willingness to have a talk (and a laugh) about life, sport, etc. in your office and outside are amusing! Thank you for taking care of the administrative matters of my promotion. I wish you to spend several happy moments with your family and grandchildren!

Thank you, Gabriella, for the nice moments spent together after you first arrived as a guest postdoc in our group; I am pleased to have met you and talked with you about every aspect

of life. I wish you plenty of happiness in the future! Michele, it was very funny to spend so many coffee-breaks with you (in the rare moments you were leaving your chair in the 3.79 lab)! I have good memories of funny and cheerful moments outside of the university too! Giulia, I enjoyed the coffee-breaks that we had together, sharing our daily experiences at work; thank you also for providing me with advice about how to deal with life in the Netherlands as an Italian expat after my arrival! Elisabet, your solar attitude and humor are great! Aleksei, your talent in making funny movies and in dancing are even more incredible than the length of your beard! Thank you for the help in the lab whenever I needed any. Yanan, you have been my roommate at many NCCC conferences, I appreciated exchanging ideas with you! Tobias, we also shared a room during the last NCCC, I wish you will be able to get your PhD soon!

Francesco, I enjoyed the drinks and dinners together as well as our talks during the coffee-breaks! I wish you good luck for your PhD and your future! Maurilio, you deserve a prize for the best pizza in Eindhoven, I appreciated all the chances to have great food and nice evenings together! Nicolo', it was a pleasure to spend time together in Eindhoven, and to talk with you about life and future! Teresa, the parties at your place have always been awesome! Davide, it was a pleasure to spend time talking with you and having dinners at our places!

Thanks to all the people met in the IMC group: Nitin, Xiaofeng, Valery, Floriane, Sasha, Miao, Jiadong, Jiachun, Dimitra, Ferdy, Yuije, Shaoje, Rim, Tan, Anna, Luke, Aleksei P., Mengyan, Jerome, Bianca, Tim, Qianqian, Hao, Xianhong, Gabriela, Geert, Nikolay, Ivo, Long, Bart Sr. and Jr., Robin, Lulu, Zhaochun, Ming-Wen, Brahim, Robert, Dannie, Panos, Peng, Liang, Douglas, Roderigh, Lennart, Jan, Arno, Wilbert, Monica, Evgeny Sr. and Jr., Xiaoming, Kaituo, Farshid, Lingqian, Xuefang, Georgy, Johan, Tamas, Yaqiong, Chong, and all our former and current group members who contributed to creating a stimulating environment.

Many people contributed to keeping my spirits up throughout these years. Mom, thanks for always supporting me and help me deal with the obstacles in my life. Marco, your stimulus and interest in what I was doing have been precious to face the challenges of the (PhD) life. Guido, your enthusiasm about my achievements has always boosted me. Carlo, you always gave me proper support and good advice when I looked for them. Lilia, even if we have met only from time to time during the last years, you were always keen to know how I was doing. Dada, you were always present when I needed anything in these years. Enzo, you taught me how to face challenges remaining objective. And finally, to those who are not among us anymore, I hope you that you can also celebrate this special moment wherever you are. Thanks to all of you for everything you have done for me.

List of publications

Publications within the scope of this thesis

- A. Goryachev, M. Etzi Coller Pascuzzi, F. Carlà, T. Weber, H. Over, E. J. M. Hensen, J. P. Hofmann, Electrochemical stability of RuO_2(110)/Ru(0001) model electrodes in the oxygen and chlorine evolution reactions, *Electrochim. Acta* **2020**, *336*, 135713.
- M. Etzi Coller Pascuzzi, A. Goryachev, J. P. Hofmann, E. J. M. Hensen, Mn promotion of rutile TiO_2-RuO_2 anodes for water oxidation in acidic media, *Appl. Catal. B Environ.* **2020**, *261*, 118225.
- M. Etzi Coller Pascuzzi, J. P. Hofmann, E. J. M. Hensen, Promoting oxygen evolution of IrO_2 in acid electrolyte by Mn, *Electrochim. Acta* **2020**, accepted.
- M. Etzi Coller Pascuzzi, A. J. W. Man, A. Goryachev, J. P. Hofmann, E. J. M. Hensen, Investigation of the stability of NiFe-(oxy)hydroxide anodes in alkaline water electrolysis under industrially relevant conditions, *Catal. Sci. Technol.* **2020**, *10*, 5593-5601.
- M. Etzi Coller Pascuzzi, M. van Velzen, J. P. Hofmann, E. J. M. Hensen, On the stability of Co_3O_4 oxygen evolution electrocatalysts in acid, *ChemCatChem* **2020**, DOI: 10.1002/cctc.202001428.

Publications outside the scope of this thesis

- M. Etzi Coller Pascuzzi, E. Selinger, A. Sacco, M. Castellino, P. Rivolo, S. Hernández, G. Lopinski, I. Tamblyn, R. Nasi, S. Esposito, M. Manzoli, B. Bonelli, M. Armandi, Beneficial effect of Fe addition on the catalytic activity of electrodeposited MnO_x films in the water oxidation reaction, *Electrochim. Acta.* **2018**, *284*, 294-302.

Conference contributions

- M. Etzi Coller Pascuzzi, J. P. Hofmann, E. J. M. Hensen, "Ir-Mn oxides as bimetallic electrocatalysts for the Oxygen Evolution Reaction in Acidic Medium", *The Netherlands' Catalysis and Chemistry Conference (NCCC) XXI,* Noordwijkerhout, The Netherlands, **March 2020** (oral).

- M. Etzi Coller Pascuzzi, A. Goryachev, J. P. Hofmann, E. J. M. Hensen, "MnOx-modified mixed rutile TiO_2-RuO_2 as active and stable water oxidation catalysts in acid**"**, *Chains 2019,* Veldhoven, The Netherlands, **December 2019** (poster).

- M. Etzi Coller Pascuzzi, A. Goryachev, J. P. Hofmann, E. J. M. Hensen, "MnO_x-modified mixed rutile TiO_2-RuO_2 as water oxidation electrocatalysts with enhanced activity and stability in acidic media", *The Netherlands' Catalysis and Chemistry Conference (NCCC) XX,* Noordwijkerhout, The Netherlands, **March 2019** (poster).

- M. Etzi Coller Pascuzzi, A. Goryachev, F. Carla', J. Pfrommer, H. Over, E. J. M. Hensen, J. P. Hofmann, "Electrochemical stability of RuO_2 (110)/Ru(0001) model electrodes in the oxygen and chlorine evolution reactions", *The Netherlands' Catalysis and Chemistry Conference (NCCC) XIX,* Noordwijkerhout, The Netherlands, **March 2018** (poster).

Curriculum Vitae

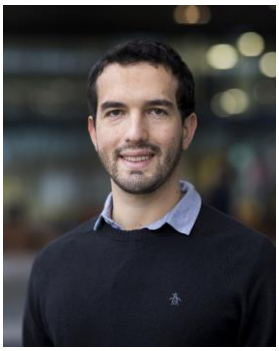

Marco Etzi Coller Pascuzzi was born in Torino, Italy, in 1991. After finishing high school in 2009, he studied Chemical Engineering at Politecnico di Torino, Italy. During his Bachelor studies, he made an internship at Presblock S.p.A., a company producing valves and connectors, focusing on the suitability of polymeric materials for use in food-contact applications. In 2013 he completed his BSc and enrolled in the MSc in Chemical and Sustainable Processes Engineering at the same university. Between August 2014 and January 2015 he spent a semester following courses at the Eindhoven University of Technology through an Erasmus exchange program. In 2016 he obtained his Master's Degree at Politecnico di Torino, graduating with a thesis on electrocatalytic water oxidation over manganese oxide films under the supervision of prof. Marco Armandi. In October 2016 he started a Ph.D. project at the Eindhoven University of Technology in the Inorganic Materials and Catalysis group chaired by prof. Emiel Hensen, focusing his research on electrocatalysts for the water oxidation reaction. The main results are presented in this dissertation.